Title
Elucidating Structural Motifs in β-Amyloid Peptide with Sub-molecular Resolution via Scanning Tunneling Microscopy

Author
Yugay, Diana

Publication Date
2019

Peer reviewed|Thesis/dissertation

UNIVERSITY OF CALIFORNIA

Los Angeles

Elucidating Structural Motifs in β-Amyloid Peptide with Sub-molecular Resolution *via* Scanning Tunneling Microscopy

A dissertation submitted in partial satisfaction of the

requirements for the degree Doctor of Philosophy

in Chemistry

by

Diana Yugay

2019

ABSTRACT OF THE DISSERTATION

Elucidating Structural Motifs in β-Amyloid Peptide with Sub-molecular Resolution *via* Scanning Tunneling Microscopy

by

Diana Yugay

Doctor of Philosophy in Chemistry

University of California, Los Angeles, 2019

Professor Paul S. Weiss, Chair

β-Amyloid aggregates in the brain play critical roles in Alzheimer's disease, a chronic neurodegenerative condition. Amyloid-associated metal ions, particularly zinc and copper ions, have been implicated in disease pathogenesis. Despite the importance of such ions, the binding sites on the β-amyloid peptide remain poorly understood. Due to the conformational flexibility of the peptide, conventional techniques such as X-ray crystallography are not able to determine the important nonperiodic structures of this system. This work addresses these structural resolution

issues of this non-crystalline biomolecule, as well as its interactions with metal ions *via* scanning tunneling microscopy (STM), spectroscopic imaging, and image segmentation tools.

Our findings reveal critical interactions of an initially disordered region of *β*-amyloid ($A\beta_{1-16}$) with copper and zinc ions. Based on our analyses of the STM images, we elucidate and outline similarities and differences between Cu^{2+} and Zn^{2+} interactions with $A\beta_{1-16}$ with sub-molecular resolution. We show that both metal ions participate in inter-strand $A\beta_{1-16}$ binding by coordinating with the two histidine residues at positions 13 and 14 (His_{13} and His_{14}) on adjacent strands and not intra-strand binding, as it had been hypothesized previously.

We found that the non-periodic binding of both types of metal ions results in more ordered peptide assemblies, but pristine β-sheets are formed only in the presence of copper. These results indicate that the bound copper has strong, long-range stabilizing effects on the assembly, whereas zinc ions are associated with local destabilizing effects. We also identified several amino acids within the peptide, which are more strongly influenced by metal ion binding, suggesting possible targets for pharmacological intervention.

Finally, we address the interactions of the remaining β-amyloid fragment, containing the last 26 residues of the full length β-amyloid peptide (p3 or $A\beta_{17-42}$), with copper ions. Because it is generated in the non-amyloidogenic pathway, $A\beta_{17-42}$ has been considered a non-pathogenic peptide, and, until now, its function and its role remain undetermined. Recent reports suggest that the segment may be involved in Alzheimer's disease and Down syndrome. However, the production of $A\beta_{17-42}$ as well as its dependence and involvement in metal ion misbalance have not been well studied. Thus, herein, we address structural changes in $A\beta_{17-42}$ due to its interaction with Cu^{2+} ions. Our results based on techniques such as cyclic voltammetry indicate interaction between Cu^{2+} ions and $A\beta_{17-42}$; furthermore, results based on surface-enhanced Raman

spectroscopy, atomic force microscopy, and scanning tunneling microscopy suggest that the interaction between Cu^{2+} ions and $A\beta_{17-42}$ ultimately leads to changes in $A\beta_{17-42}$ secondary structure, shifting it from less to more β-sheet content, and its aggregation state, shifting it from a less aggregated to a more aggregated state.

The dissertation of Diana Yugay is approved.

Jorge Z. Torres

Z. Hong Zhou

Paul S. Weiss, Committee Chair

University of California, Los Angeles

2019

For my family

Table of Contents

List of Figures……*xi*

List of Abbreviations and Symbols……..*xxvi*

Acknowledgments……..*xxxiii*

VITA……...*xxxvi*

CHAPTER 1

β-Amyloid and Scanning Tunneling Microscopy as the Ultimate Tool to Study Its Structure and Metal Ion Binding Site

1.1 Introduction: Importance of Studying Biomolecular Structures……..2

1.2 Conventional Techniques Used to Decipher Biomolecular Structures……3

1.3 Importance of Studying β-Amyloid and Theories Regarding Amyloid Toxicity……4

1.3.1 Tau Hypothesis……4

1.3.2 Amyloid Hypothesis……5

1.4 β-Amyloid Facts…….....6

1.4.1 β-Sheet Characteristics of β-Amyloid Peptides……...7

1.5 Probable Causes of β-Amyloid Toxicity……7

1.5.1 Toxicity of β-Amyloid Due to Interaction with Metal Ions……8

1.5.2 Relationship between Metal Ions and β-Amyloid: *In Vitro* and *in Vivo* Results……9

1.5.3 β-Amyloid Toxicity Due to Production of Reactive Oxygen Species……...10

1.5.4 β-Amyloid and Its Interactions with Zinc, Copper, and Iron…….10

1.6 Structural Characterization of β-Amyloid: Techniques and Recent Advances…….12

1.6.1 Results of Amyloid-β Structural Research……13

1.7 Scanning Tunneling Microscopy as the Ultimate Tool To Study Structures of Intrinsically Disordered Biomolecules....14
1.7.1 Working Principles of Scanning Tunneling Microscopy....14
1.7.2 Scanning Tunneling Microscopy and Biomolecules with Metal Centers....16
1.8 Dissertation Overview....16
1.9 References....24

CHAPTER 2

Copper Ion Binding Site in β-Amyloid Peptide

2.1 Introduction....36
2.2 Circular Dichroism....38
2.3 Surface-Enhanced Raman Spectroscopy....39
2.4 Scanning Tunneling Microscopy....40
2.5 Materials and Methods....45
2.5.1 Scanning Probe Microscopy and Surface-Enhanced Raman Spectroscopy Sample Preparation....45
2.5.2 Scanning Tunneling Microscopy Measurements....45
2.5.3 Atomic Force Microscopy Measurements....46
2.5.4 Scanning Tunneling Microscopy and Atomic Force Microscopy Image Processing....46
2.5.5 Surface-Enhanced Raman Spectroscopy Measurements....46
2.5.6 Circular Dichroism Sample Preparation....47
2.5.7 Circular Dichroism Measurements....47
2.5.8 Surface-Enhanced Raman Spectroscopy and Circular Dichroism Spectral Analyses....47
2.6 References....58

CHAPTER 3

Metal-Ion-Induced Structural Rearrangements of β-Amyloid Peptides

3.1 Introduction....66

3.2 Results and Discussion....68

3.3 Conclusions and Prospects....75

3.4 Materials and Methods....78

3.4.1 Scanning Tunneling Microscopy Sample Preparation....78

3.4.2 Scanning Tunneling Microscopy Measurements....78

3.4.3 Scanning Tunneling Microscopy Image Processing....79

3.4.4 Scanning Tunneling Microscopy Image Analysis....79

3.5 References....98

CHAPTER 4

Copper Ion Interactions with the C-terminus of the β-Amyloid Peptide

4.1 Introduction....104

4.2 Results and Discussion....105

4.2.1 Cyclic Voltammetry....105

4.2.2 Surface-Enhanced Raman Spectroscopy....107

4.2.3 Atomic Force Microscopy....108

4.2.4 Scanning Tunneling Microscopy....110

4.2.5 X-Ray Photoelectron Spectroscopy....112

4.3 Conclusions and Prospects....112

4.4 Materials and Methods....114

4.4.1 Cyclic Voltammetry Sample Preparation....114

4.4.2 Cyclic Voltammetry Measurements....114
4.4.3 Surface-Enhanced Raman Spectroscopy Sample Preparation....115
4.4.4 Surface-Enhanced Raman Spectroscopy Measurements....115
4.4.5 Atomic Force Microscopy Sample Preparation....116
4.4.6 Atomic Force Microscopy Measurements....116
4.4.7 Scanning Tunneling Microscopy Sample Preparation....117
4.4.8 Scanning Tunneling Microscopy Measurements....117
4.4.9 X-Ray Photoelectron Spectroscopy Sample Preparation....117
4.4.10 X-Ray Photoelectron Spectroscopy Measurements....117
4.5 References....126

CHAPTER 5

Summary and Outlook

5.1 Scanning Tunneling Microscopy: Past and Future....136
5.2 Visualization of Buried Metal Ion-Binding Sites....137
5.3 Detection of Buried Metal Ion-Binding Sites....138
5.4 Resolving Structures and Interactions between Post-Translationally Modified Amyloidogenic Peptides....139
5.5 References....144

Appendix A

A.1 Chapter 2 MATLAB Code....147
A.2 Chapter 3 MATLAB Code and Computation....149

List of Figures

Figure 1.1 Amyloidogenic and non-amyloidogenic pathways of amyloid precursor protein (APP). In the amyloidogenic pathway (top of the diagram) APP is cleaved by β-secretase at position 672 (right before Glu1 in Aβ) and by γ-secretase (between amino acids 39 and 43 of Aβ). γ-Secretase is non-specific and thus, cleaves Aβ anywhere between amino acids 39 and 43. Asterisks (∗) next to γ-secretase indicate Aβ segments which are not found in abundant quantity in Aβ plaques and thus, those segments are considered to be less toxic than the cut at the position 42. In the non-amyloidogenic pathway (bottom of the diagram), APP is cleaved by α-secretase at position 688 (between amino acids 16 and 17 of Aβ) and similarly to amyloidogenic pathways later it is cleaved by γ-secretase (between amino acids 39 and 43 of Aβ). The end product of the α-secretase cleavage is a peptide that is 16 amino acids shorter than the peptide produced in the amyloidogenic pathway – $A\beta_{17-42}$, as well known as P3. 18

Figure 1.2 (a) Transmission electron micrograph image of amyloid fibrils. (b) The schematic diagram of the amyloidogenic β-strands which are in parallel arrangement with the β-strand spacing (interstrand spacing) of ~4.7 Å. In fibrils, strands run perpendicular to the fiber x-axis, whereas sheets continue their growth towards z-axis. The distance between sheets in the z-axis direction is 6-11 Å, whereas the total filament diameter is 60-120 Å. Adapted from ref. 52. Copyright 2010, Structure. 19

Figure 1.3 β-Amyloid sequence illustrating possible amino acid residues that could be involved in Aβ toxicity. Amongst the most hypothesized reasons of Aβ toxicity that have emerged are interactions of Aβ with transition metal ions, involvement of Aβ in oxidative stress, dysregulation of Aβ due to its familial mutations, interaction and aggregation of Aβ with cholesterol molecules, and toxicity of Aβ due to its various post-translational modifications. 20

Figure 1.4 Diagram illustrating Aβ interaction with copper (Aβ-Cu) and iron (Aβ-Fe) and production of ROS. It is hypothesized that in the process of redox cycling, Aβ acts as an electron donor, upon which it becomes Aβ radical (Aβ•). The Aβ radical is thought to extract protons from surroundings such as DNA, lipids, and proteins, which act as reducing agents. As a consequence of proton extraction, hydroxy-2-nonenal (HNE) and carbonyls that are detrimental for healthy brain activity are generated. Afterwards, Aβ• gets returned to its normal state, *i.e.*, Aβ. Furthermore, during Aβ-Cu and Aβ-Fe interaction, both metal ions undergo cycling between oxidized (Cu^{2+}, Fe^{3+}) and reduced (Cu^{+}, Fe^{2+}) states. Upon metal ion reduction, molecular oxygen (O_2) is reduced to peroxide (H_2O_2). The latter is directly involved in generation of ROS (in the form of •OH and $^{-}$OH). Reactive oxygen species are detrimental for healthy brain activity due to DNA and mitochondrial damage, lipid peroxidation, and protein aggregation. Adapted from ref. 62. Copyright 2007, Biochimica et Biophysica Acta. 21

Figure 1.5 Various discovered Aβ arrangements in fibrils. (a,b) Structural organization of $A\beta_{1-42}$ fibrils *via* ssNMR examined by Griffin and co-workers.[104] Findings indicate that Aβ, in the region of residues 15-42, folds twice onto itself into an S-like shape. Furthermore, residues 1-14 linearly extend and are adjacent to the C-terminus of another amyloid unit (not shown). (b) In a fiber two amyloid units contact through Met35 (M35) (residue in yellow color), Leu17 (L17), and Gln15 (Q15) (residues in the dashed ovals). (c,d) Structural characterization of $A\beta_{1-40}$ involving single deletion at Glu22 (known as the Osaka mutant). In this study Schütz *et al.*, reported that the Osaka mutant organizes in the vicinity of N-terminus into an inverted L structure with a bend at Tyr10 (pink circle). Furthermore, the Osaka mutant was reported to fold onto itself into an S-like shape between amino acid residues 20 and 40 (pink shaded rectangles).[105] (e) Gremer *et al.* visualized structure of $A\beta_{1-42}$ using cryo-EM.[13] In the study he showed that $A\beta_{1-42}$ has an LS-shape topology (lower dimer) while dimers from both sides of the reported structure make contact at Lys28 (upper dimer) and Asp1 (lower dimer). Adapted from refs: 13. Copyright 2017, Science; 104. Copyright 2016, Journal of the American Chemical Society; 105. Angewandte Chemie International Edition. 22

Figure 2.1 Circular dichroism spectrum of $A\beta_{1-16}$ at pH 7.4 with the negative band at 197 nm and the positive band at 222 nm. $A\beta_{1-16}$-Cu^{2+} (blue) and $A\beta_{1-16}$ (red). 48

Figure 2.2 Substrate arrangement and results of the surface-enhanced Raman spectroscopy experiments. (a) (Top) Photograph of the substrate used in SERS experiments. (Bottom) Schematic of the substrate and its components: (I) silicon wafer, (II) gold film with gold pyramids, (III) graphene, (IV) deposited $A\beta_{1-16}$ peptides. (b) SERS spectrum of $A\beta_{1-16}$-Cu^{2+} (blue) and $A\beta_{1-16}$ (red). The black dashed box (~1449 cm^{-1}) indicates the C–H bending mode that signifies $A\beta_{1-16}$ peptides lack structural homogeneity in comparison to $A\beta_{1-16}$-Cu^{2+}. 49

Figure 2.3 Atomic force microscopy images of $A\beta_{1-16}$ at pH 7.4 deposited on HOPG, 500 nm × 500 nm (a) $A\beta_{1-16}$-Cu^{2+} (b) $A\beta_{1-16}$. Protrusions indicate $A\beta_{1-16}$ aggregates. Measurements were done to test if we continuously produced laminated monolayers of $A\beta_{1-16}$ and $A\beta_{1-16}$-Cu^{2+} over large surface areas. 50

Figure 2.4 Distributions of the strand lengths for $A\beta_{1-16}$ (red) and $A\beta_{1-16}$-Cu^{2+} (blue) with bin numbers 7 and 8, and means 4.76 nm and 5.1 nm, respectively. Sample size: 50. 51

Figure 2.5 (a) $A\beta_{1-16}$ sequence with the highlighted Phe4 and His13/His14 amino acids. Ideal distance from β-sheet boundary to Phe4 is 0.975 nm (purple arrow), to His13 is 0.975 nm (blue arrow), and to His14 is 0.65 nm (blue arrow). (b) Average interstrand separation bar graph for $A\beta_{1-16}$ vs $A\beta_{1-16}$-Cu^{2+}. Interstrand separation for $A\beta_{1-16}$ is 5.8 ± 0.4 Å, and $A\beta_{1-16}$-Cu^{2+} is 4.6 ± 0.3 Å (from n = 42 and 120 measurements, respectively). (c) Scanning tunneling microscopy image of

$A\beta_{1-16}$-Cu^{2+}. The regular protruding features in the purple box indicate the positions of the Phe4, whereas irregular protruding features in the blue box indicate the positions of His13/His14 binding Cu^{2+} in the peptide β-sheet assembly. Imaging conditions: V_{sample} = 0.55 V, I_{tunnel} = 10 pA. (d) Average distance between amino acids with the corresponding number of amino acids to the specified distance. Phe4 (purple) distance, 1.0 ± 0.1 nm; number of amino acids, 3.1 ± 0.4; His13/His14 (blue) distance, 0.9 ± 0.1 nm; number of amino acids, 2.7 ± 0.4; and ideal distance vs number of amino acids (black) (from n = 92 and 145 measurements, respectively). 52

Figure 2.6 (a) Average β-sheet inter-strand separation values for Aβ1-16, Aβ1-16-Cu^{2+}, and full length Aβ ($A\beta_{1-42}$): 5.8 ± 0.4 Å, 4.6 ± 0.25 Å, and 4.7 ± 0.3 Å, respectively. $A\beta_{1-42}$ inter-strand separation was previously reported elsewhere;[89] thus, the measurements on Aβ were performed and compared against $A\beta_{1-16}$ and $A\beta_{1-16}$-Cu^{2+} to verify if the large inter-strand separation for $A\beta_{1-16}$ was not due to the instrumental error. (b) (I) Average strand length vs number of amino acids for $A\beta_{1-16}$-Cu^{2+}: 5.09 ± 0.33 nm and 15.67 ± 1.01 amino acids, respectively. (II) Average length from protruding features to β-sheet boundary vs number of amino acids: 0.85 ± 0.11 nm *vs* 2.6 ± 0.36 amino acids, respectively. 53

Figure 2.7 Scanning tunneling microscopy images of (a,b) $A\beta_{1-16}$-Cu^{2+} and (c,d) $A\beta_{1-16}$. Imaging conditions: (a,b) 10 nm × 10 nm, V_{sample} = 0.55 V, I_{tunnel} = 10 pA; (c)

10 nm × 10 nm, V_{sample} = 0.25 V, I_{tunnel} = 17 pA; (d) 10 nm × 10 nm, V_{sample} = 0.30 V, I_{tunnel} = 14 pA. 54

Figure 2.8 Scanning tunneling microscope images of $A\beta_{1-16}$-Cu^{2+}. Scanning parameters: size: 10 nm ×10 nm, V_{sample}=0.55 V, I_{tunnel}=10 pA. Images demonstrate a consistent protrusion pattern in the vicinity of the β-sheet boundary. 55

Figure 2.9 Schematic of the structure determined for $A\beta_{1-16}$-Cu^{2+}. Cu^{2+} interstrand binding to His13 and His14 forms a brace between strands (blue dashed box). In this schematic, we depict copper coordinated with water. It is also possible that copper coordinates with the substrate surface; our data do not distinguish which scenario is more likely. Regular protrusions on STM micrographs that we attribute to be Phe4 are illustrated as a purple dashed box. 56

Table 2.1 Vibrational peak positions and corresponding band assignments for the surface-enhanced Raman spectroscopy spectra recorded. 57

Figure 3.1 Scanning tunneling micrographs of assemblies of the 1-16 amino acid fragment of β-Amyloid ($A\beta_{1-16}$) coordinated with (a) Zn^{2+} metal ions and (b) Cu^{2+} metal ions. Blue circles highlight the non-periodic, high-intensity protrusions indicative of bound metal ions. Blue arrows highlight the boundaries of the $A\beta_{1-16}$ strands. The average interstrand distance of the assemblies was 5.17 ± 0.03 Å in the presence

of Zn^{2+} and 4.82 ± 0.01 Å in the presence of Cu^{2+}, indicating that metal ion binding induces β-sheet formation in the case of Cu^{2+}, but not in the case of Zn^{2+}. 80

Figure 3.2 Scanning tunneling micrographs of assemblies of the 1-16 amino acid fragment of β-Amyloid ($A\beta_{1-16}$) coordinated with (a) Zn^{2+} metal ions and (b) Cu^{2+} metal ions. Blue circles highlight the non-periodic, high-intensity protrusions indicative of bound metal ions. Blue arrows highlight the boundaries of the $A\beta_{1-16}$ strands. ...81

Scheme 3.1 Schematic of the study design. To analyze structural changes in $A\beta_{1-16}$ due to interactions with Zn^{2+} and Cu^{2+} ions (M^{2+}), the lamellar arrangement of the peptides was categorized into three distinct groups. The first group ($A\beta_{1-16}$-M^{2+}, shaded box on the left) consists of strands with bound metal ions in an interstrand arrangement. The histidines at position 13 (His_{13}) and 14 (His_{14}) (yellow) are the residues with a propensity to bind metal ions (M^{2+}) with an interstrand bridge. The second group (M^{2+}-Adj, dashed box in the middle) consists of pairs of strands with one strand in direct contact with M^{2+} and the second strand in an adjacent location, but not directly bound. The third group (M^{2+}-Aff, clear box on the right) consists of strands that are affiliated but lack direct contact with M^{2+} and placed a minimum of one strand away from $A\beta_{1-16}$-M^{2+}. 82

Figure 3.3 Effects of metal ions on interstrand distance in each category of $A\beta_{1-16}$ (Scheme 3.1) as measured *via* scanning tunneling microscopy. $A\beta_{1-16}$-M^{2+} (square-solid

line) and M^{2+}-Adj (square-dashed line) are compared for (a) Cu^{2+} and (b) Zn^{2+}. The distinguishing feature of M^{2+}-Adj and $A\beta_{1-16}$-M^{2+} is the marginal fluctuation in interstrand distance between Asp_1 and Val_{12} followed by the pronounced increase (M^{2+}-Adj) and decrease ($A\beta_{1-16}$-M^{2+}) in interstrand separations after Val_{12}. This observation is consistent with Zn^{2+} and Cu^{2+} binding to $A\beta_{1-16}$ in interstrand fashion at the His_{13} and His_{14} positions. The ideal interstrand distance of β-sheet secondary structure is 4.5−5.0 Å (purple region).[18,21-24,26,52] Interstrand distance measurements were collected from at least three independent experiments. Error bars represent standard error (S.E.); Tukey's HSD test was used in conjunction with one-way Anova to determine significance. Significance in $A\beta_{1-16}$-M^{2+} between specific amino acids and His_{13} (13) and His_{14} (14) are indicated (Table 3.1). Results are shown as *, $p < 0.05$; **, $p < 0.01$; and ***, $p < 0.001$. (c) Interstrand distances of $A\beta_{1-16}$ affiliated with Zn^{2+} (triangle-blue line) and Cu^{2+} (triangle-red line). Due to the absence of direct interaction with metal ions these peptides lack structural homogeneity. (d) $A\beta_{1-16}$ intercalated with Zn^{2+} (circle-blue line) and Cu^{2+} (circle-red line) metal ions. Global interstrand distance as average of $A\beta_{1-16}$-M^{2+}, M^{2+}-Adj, and M^{2+}-Aff interstrand distances. Previous studies found that the interstrand distance of $A\beta_{1-16}$ without the presence of metal ions is 5.8 ± 0.4 Å (brown region).[20] 83

Table 3.1 Tukey's HSD test was used to determine statistical significance of interstrand distances between amino acid pairs of $A\beta_{1-16}$-Zn^{2+} and $A\beta_{1-16}$-Cu^{2+}. In $A\beta_{1-16}$-Zn^{2+} – Asp_1, Glu_3, Phe_4, Arg_5, His_6, Ser_8, Gly_9, Tyr_{10}, Glu_{11} are

significantly different to His_{13} and His_{14}; while in $A\beta_{1-16}$-Cu^{2+} – Asp_1, Ala_2, Phe_4, Arg_5, Asp_7, Ser_8, Gly_9, Tyr_{10}, Glu_{11}, Val_{12} are significantly different to His_{14}. Underlined values represent confidence interval of 0.01, red values represent confidence intervals of 0.05. 85

Table 3.2 Statistical results (Mean, standard deviation, S.D., of the mean, and standard error, S.E., of the mean) of interstrand distance measurements per each amino acid for all studied $A\beta_{1-16}$ categories. 87

Table 3.3 Comparison of interstrand distance measurements of different $A\beta_{1-16}$ categories per each amino acid pair *via* one-way Anova; amino acids with significant difference are outlined in red. Measurements were collected from at least three independent sets of experiments. Results are shown as *, $p < 0.05$; **, $p < 0.01$; and ***, $p < 0.001$. 88

Table 3.4 Comparison of average interstrand distance values of the full length $A\beta_{1-16}$ peptide (1-16), first 11 residues from the N-terminus (1-11), last 4 residues of C-terminus (12-16), His13 and His 14 to ideal interstrand distance (upper 5.0 Å and lower values 4.5 Å), average of 1-16 and 1-11 residues of $A\beta_{1-16}$ peptide. Positive values represent increases in interstrand distance while negative values represent decreases in interstrand distance between examined pairs. 89

Figure 3.4 (a) Scheme of $A\beta_{1-16}$ sequence with a bound metal ion. Predicted distance from the metal ion binding site to the C-terminus is 8.12 Å. (b) Comparison between length from the metal ion binding site to the C-terminus of predicted (P) $A\beta_{1-16}$ (black) and measured $A\beta_{1-16}$-Zn^{2+} (blue) and $A\beta_{1-16}$-Cu^{2+} (red). Total length of $A\beta_{1-16}$-Zn^{2+} is significantly ($p = 0.0117$) greater in comparison to $A\beta_{1-16}$-Cu^{2+}, 9.52 ± 0.3 Å and 8.14 ± 0.2 Å, respectively. (c) Comparison of inter-residue distances of the three $A\beta_{1-16}$ strand categories (Scheme 3.1) and two segments based on deformation due to ion binding (residues 1-13 *vs.* residues 14-16). Residues that are not in direct contact with M^{2+} show compact, less than ideal, inter-residue separations of 3.25 Å – dashed black line (Panels 1-3). Residues adjacent to M^{2+} binding site show distorted, larger than ideal residue-residue distances. This distortion is most likely due to vacancies created by the metal ion binding between strands of $A\beta_{1-16}$-M^{2+} and M^{2+}-Adj. These peptides, in the residue 14-16 segment, show higher than ideal inter-residue separations (Panel 4). Zn^{2+} (blue) and Cu^{2+} (red) have different effects on the C-terminus of $A\beta_{1-16}$-M^{2+} (Panel 5). This difference can be observed from significantly larger ($p = 0.0117$) inter-residue distances of $A\beta_{1-16}$-Zn^{2+} than $A\beta_{1-16}$-Cu^{2+} in residues 14-16. Zn^{2+} ions create a strong, local effect on the C-terminus of $A\beta_{1-16}$-M^{2+}, which ultimately leads to a distortion of the C-terminus. Cu^{2+} ions, in contrast to Zn^{2+}, show a strong and long-range effect on $A\beta_{1-16}$-M^{2+}. This effect ultimately contributes to the stabilizing interactions between neighboring peptide strands that results in the overall greater β-sheet character. Measurements were collected from

at least three independent sets of experiments. Error bars represent standard error (S.E.); to determine significance one-way Anova was used. Results are shown as *, $p < 0.05$; **, $p < 0.01$; and ***, $p < 0.001$. 91

Figure 3.5 (a) $A\beta_{1-16}$ sequence; upon Cu^{2+} (red) and Zn^{2+} (blue) binding to $A\beta_{1-16}$ in interstrand fashion between His_{13} and His_{14} the highlighted amino acids undergo structural deformation acquiring interstrand distances smaller (≤4.4 Å) than the ideal β-sheet range (4.5−5.0 Å). Both metal ions have prominent structural effects on certain residues (highlighted), which ultimately lead to global ordering of $A\beta_{1-16}$ peptides (for more details see Figure 3.6 and Table 3.5). (b) Residues prone to structural deformation upon $A\beta_{1-16}$ interaction with Zn^{2+}, besides His_{13} and His_{14}, are Asp_7 and Gln_{15}. (c) Affected residues, besides His_{13} and His_{14}, in $A\beta_{1-16}$ due to Cu^{2+} binding are Glu_3, His_6, $Gln_{15,}$ and Lys_{16}. Compared to Cu^{2+}-Aff these residues undergo significant strand-to-strand deformation towards adapting small (≤4.4 Å) interstrand distance with similar residues from adjacent strands. Measurements were collected from at least three independent experiments. Error bars represent standard error (S.E.); to determine significance, one-way Anova was used. Results are shown as *, $p < 0.05$; **, $p < 0.01$; and ***, $p < 0.001$. 93

Figure 3.6 Amino acid frequencies in three interstrand distance categories: small (≤4.4 Å), ideal β-sheet range (4.5−5.0 Å), and large (≥5.1 Å) for $A\beta_{1-16}$ categories and their corresponding frequencies of residues in those categories. Error bars represent standard error (S.E.). 95

Table 3.5 Comparison of interstrand distance frequencies (Figures 3.5 and 3.6) of different $A\beta_{1-16}$ categories per each amino acid pair *via* one-way Anova; amino acids with significant difference are outlined in red. Measurements were collected from at least three independent experiments. Results are shown as *, $p < 0.05$; **, $p < 0.01$; and ***, $p < 0.001$. 97

Figure 4.1 An overlay of the redox potentials measured by cyclic voltammetry. Cyclic voltammetric responses represent: substrate – gold on silica (dashed orange line), free Cu^{2+} (dotted blue line), $A\beta_{17-42}$ (dashed blue line), and $A\beta_{17-42}$ with Cu^{2+} (solid blue line). Bands with positive current in the range of 0.2 V to 0.7 V represent oxidized state of copper (Cu^{2+}; $Cu \rightarrow Cu^{2+} + 2e^-$) while bands with negative current in the range of -0.1 V to 0.3 V represent reduced state of copper (Cu^+; $Cu^{2+} + 2e^- \rightarrow Cu$). 119

Figure 4.2 Surface-enhanced Raman spectrum of $A\beta_{17-42}$ (bottom spectra) and $A\beta_{17-42}$-Cu^{2+} (top spectra) obtained by depositing $A\beta_{17-42}$ and $A\beta_{17-42}$-Cu^{2+} solutions on the SERS substrate composed of silver–coated gold nanostars. Amide I and Amide III indicate structural differences between $A\beta_{17-42}$ and $A\beta_{17-42}$-Cu^{2+}. $A\beta_{17-42}$ is more in α-helical configuration because it lacks bands that would indicate β-sheet component in Amide III region. 120

Table 4.1 Surface-Enhanced Raman Spectroscopy Band Assignment for Acquired Spectra of $A\beta_{17-42}$ and $A\beta_{17-42}$-Cu^{2+} at 633 nm excitation. 121

Figure 4.3 Atomic force microscopy images of $A\beta_{17-42}$ (a) and $A\beta_{17-42}$-Cu^{2+} (b) incubated for 1 hr in the absence and in the presence of Cu^{2+} ions, respectively. Both conditions result in aggregation of the peptide, however, in contrast to $A\beta_{17-42}$, aggregates of $A\beta_{17-42}$-Cu^{2+} are larger in size and result in denser surface coverages than $A\beta_{17-42}$. In addition, $A\beta_{17-42}$ and $A\beta_{17-42}$-Cu^{2+} images were analyzed for average surface roughness (see Figure 4.4 for more details). Average surface roughness of $A\beta_{17-42}$ is lower than for $A\beta_{17-42}$-Cu^{2+} specifically, 0.364 nm and 0.524 nm, respectively. This result indicates that $A\beta_{17-42}$ results in smoother surface than $A\beta_{17-42}$-Cu^{2+}. Overall, AFM results signify that Cu^{2+} ions enhance aggregation of $A\beta_{17-42}$ segment. 122

Figure 4.4 Atomic force microscopy analyses of average surface roughness (Ra) of (a) $A\beta_{17-42}$ and (b) $A\beta_{17-42}$-Cu^{2+}. Average surface roughness of $A\beta_{17-42}$ and $A\beta_{17-42}$-Cu^{2+} is 0.364 nm and 0.524 nm, respectively. (a,c) Diagonal lines represent (b,d) the cross sections of the Ra analysis. (b,d) Corresponding graphs of the Ra analysis of $A\beta_{17-42}$ and $A\beta_{17-42}$-Cu^{2+}, respectively. 123

Figure 4.5 Scanning tunneling micrograph of $A\beta_{17-42}$-Cu^{2+}. Blue arrows signify boundaries of laminated $A\beta_{17-42}$-Cu^{2+} peptides. For clarity, two $A\beta_{17-42}$-Cu^{2+} strands are

outlined as blue dashed lines. (a) Measured average strand length is 54.8 ± 1.3 Å while, (b) measured average interstrand separation is 5.5 ± 0.2 Å (b). 124

Figure 4.6 X-ray photoelectron spectroscopy of (a) $A\beta_{17-42}$ (b) $A\beta_{17-42}$ incubated with excess of Cu^{2+} (c) HOPG washed with excess of Cu^{2+}. All conditions show negative results for presence of Cu^{2+}. Copper band (Cu $2p_{1/2}$) was expected at ~957 eV (dashed line).[96-98] 125

Figure 5.1 Scanning tunneling microscopy image showing molecular polarizability of highly polarizable 4,4'-di(ethynylphenyl)-1-benzenethiol (OPE) molecules inserted into dodecanethiolate (C12) self-assembled monolayer (SAM). In the ACSTM microwave image, OPE molecules appear as high-contrast protruding features (numbered 1–5) against a dark background (C12 SAM); contrast between OPE and C12 is more intense in the ACSTM image than in the STM topography image. Adapted from ref. 2. Copyright 2010, ACS Nano. 141

Figure 5.2 Primary structure of glycosylated $A\beta_{1-15}$. The R group on the tyrosine residue indicates an α-linked glycan attachment (bottom, left) or a β-linked glycan attachment (bottom, right). Adapted from ref. 15. Copyright 2014, Chemical Communications. 142

Figure 5.3 Images of adhesion measurements with atomic force microscopy (a) $A\beta_{1-15}$ without Cu^{2+} and (b) $A\beta_{1-15}$ incubated with Cu^{2+} ions. $A\beta_{1-15}$ without Cu^{2+} has

higher adhesive properties; therefore, laminated β-sheets are more flexible ("sticky") compared to β-sheets of $A\beta_{1-15}$ when incubated with Cu^{2+} ions. 143

List of Abbreviations and Symbols

Aβ	β-amyloid
Aβ•	β-amyloid radical
$A\beta_{1-15}$	β-amyloid segment containing the first 15 amino acid residues
$A\beta_{1-16}$	β-amyloid segment containing the first 16 amino acid residues
$A\beta_{17-42}$	β-amyloid segment composed of the last 26 amino acid residues (also known as p3)
$A\beta_{18-41}$	β-amyloid segment between amino acid at the position 18 and amino acid at the position 41
$A\beta_{1-40}$	β-amyloid isoform that is 40 amino acids in length
$A\beta_{1-42}$	β-amyloid isoform that is 42 amino acids in length
$A\beta_{1-16}$-Cu^{2+}	β-amyloid segment containing the first 16 amino acid residues in association with copper ion
$A\beta_{1-16}$-M^{2+}	β-amyloid strands with bound metal ions in an interstrand arrangement
$A\beta_{17-42}$-Cu^{2+}	β-amyloid segment composed of the last 26 amino acid residues in association with copper ion
Aβ-Cu	β-amyloid associated with copper
Aβ-Fe	β-amyloid associated with iron
$A\beta_{rat}$	Rat β-amyloid
ACSTM	Alternating current coupled to the scanning tunneling microscopy (also known as microwave scanning tunneling microscopy)
A	Amp
AD	Alzheimer's disease

AFM	Atomic force microscopy
Ala_{21}	Alanine at position 21 in β-amyloid peptide
Ala_{42}	Alanine at position 42 in β-amyloid peptide
Anova	Statistical test used to analyze significant differences between means
APP	Amyloid precursor protein
Arg_{13}	Arginine at position 13 in rat β-amyloid peptide
Asp_{1}	Aspartic acid at position 1 in β-amyloid peptide
Asp_{7}	Aspartic acid at position 7 in β-amyloid peptide
Asp_{23}	Aspartic acid at position 23 in β-amyloid peptide
Asp_{23}-Lys_{28}	β-amyloid segment between aspartic acid at position 23 and lysine at position 28
C12	Dodecanethiolate
CD	Circular dichroism
cm	Centimeter
cryo-EM	Cryo-electron microscopy
Cu^{2+}	Copper – divalent cation
Cu^{2+}-$C_{term}{}^{M}$	Measured length from copper ion to C-terminus of β-amyloid
Cu^{2+}-$C_{term}{}^{P}$	Predicted length from copper ion to C-terminus of β-amyloid
Cu^{2+}-Global	Self-assembly of β-amyloid ($A\beta_{1-16}$) peptides in the presence of copper ions
CV	Cyclic voltammetry
DNA	Deoxyribonucleic acid
DS	Down syndrome

ECSTM	electrochemical scanning tunneling microscopy
EM	Electron microscopy
EPR	Electron paramagnetic resonance
Fe^{2+}	Iron – divalent cation
Gln_{15}	Glutamine at position 15 in β-amyloid peptide
Glu_{1}	Glutamic acid at position one in β-amyloid peptide
Glu_{22}	Glutamic acid at position 22 in β-amyloid peptide
Glu_{22}-Lys_{28}	β-amyloid segment between glutamic acid at position 22 and lysine at position 28
Glu_{3}	Glutamic acid at position three in β-amyloid peptide
Gly_{1}	Glycine at position one in rat β-amyloid peptide
Gly_{32}	Glycine at position 32 in β-amyloid peptide
H_2O_2	Hydrogen peroxide
He−Ne	Helium−Neon (acronym associated with a laser that is commonly used in surface-enhanced Raman spectroscopy)
His	Histidine
His_{6}	Histidine at position 6 in β-amyloid peptide
His_{13}	Histidine at position 13 in β-amyloid peptide
His_{14}	Histidine at position 14 in β-amyloid peptide
HOPG	Highly oriented pyrolytic graphite
hr	Hour
IDP	Intrinsically disordered protein

Ile_{32}-Ile_{41}	β-amyloid segment between isoleucine at position 32 and isoleucine at position 41
IR	Infrared spectroscopy
kDa	Kilodalton
L	Liter
Lys_1	Lysine at position 1 in β-amyloid peptide
Lys_{16}	Lysine at position 16 in β-amyloid peptide
Leu_{17}	Leucine at position 17 in β-amyloid peptide
Lys_{28}	Lysine at position 28 in β-amyloid peptide
M	Molar
m	Meter
M^{2+}	Divalent metal ion used to describe either Zinc (Zn^{2+}) or copper ion (Cu^{2+})
M^{2+}-Adj	Pair of β-amyloid strands with one strand in direct contact with metal ion and the second strand in an adjacent location to the strand which is in direct contact with metal ion
M^{2+}-Aff	Pair of β-amyloid strands that are affiliated but lack direct contact with metal ion. These β-amyloid strands placed a minimum of one strand away from a pair of strands that are in direct contact with metal ion
M^{2+}-C_{term}	β-amyloid length from metal ion to C-terminus
M^{2+}-$C_{term}{}^{M}$	Measured length from metal ion to C-terminus of β-amyloid
M^{2+}-Global	Self-assembly of β-amyloid ($A\beta_{1-16}$) peptides in the presence of metal ions
(MAS) NMR	Magnetic angle spinning nuclear magnetic resonance spectroscopy
MD	Molecular dynamics

mdeg	Millidegree
Met_{35}	Methionine at position 35 in β-amyloid peptide
mg	Milligram
min	Minute
mm	Millimeter
mW	Milliwatt
nm	Nanometer
N	Newton
NMR	Nuclear magnetic resonance
OPE	4,4'-di(ethynylphenyl)-1-benzenethiol
p	Probability value (indicates significance of the performed statistical test)
p3	β-amyloid segment composed of the last 26 amino acid residues (also known as $A\beta_{17-42}$)
PET	Positron emission tomography
pH	Measure of acidity or alkalinity of a solution
Phe_4	Phenylalanine at position 4 in β-amyloid peptide
Phe_5	Phenylalanine at position 5 in rat β-amyloid peptide
Phe_{20}	Phenylalanine at position 20 in β-amyloid peptide
PPII	Polyproline type II helix
Pt−Ir	Platinum−Iridium
PTM	Post-translational modification
Ra	Roughness average
ROS	Reactive oxygen species

s	Second
S.D.	Standard deviation
S.E.	Standard error
SAM	Self-assembled monolayer
SERS	Surface-enhanced Raman spectroscopy
SPM	Scanning probe microscopy
ssNMR	Solid-state nuclear magnetic resonance
STM	Scanning tunneling microscopy
Sup35	Prion protein
Tyr_{10}	Tyrosine at position ten
US	United States
V	Volts
Val_{12}	Valine at position 12 in β-amyloid peptide
Val_{18}-Ile_{31}	β-amyloid segment between valine at position 18 and isoleucine at position 31
XPS	X-ray photoelectron spectroscopy
XRD	X-ray powder diffraction
Zn^{2+}	Zinc – divalent cation
Zn^{2+}-C_{term}^{M}	Measured length from zinc ion to C-terminus of β-amyloid
Zn^{2+}-C_{term}^{P}	Predicted length from zinc ion to C-terminus of β-amyloid
Zn^{2+}-Global	Self-assembly of β-amyloid ($A\beta_{1-16}$) peptides in the presence of zinc ions
μL	Microliter
μM	Micromolar

μm	Micrometer
Å	Ångstrom
τ	Tau (protein)
%	Percent

Acknowledgments

It seems like it was yesterday when I started graduate studies at the University of California, Los Angeles (UCLA) yet, *that yesterday* was 2012, and *today* is 2019. Upon admission to UCLA, I joined Professor Paul S. Weiss's group – and thus started my journey of my Ph.D. career and β-amyloid research. Writing this dissertation, I realize I am not the same person I was when I joined the group. Knowledge and training obtained throughout Ph.D. years would not have been possible without the mentorship and guidance of Professor Paul S. Weiss. *I am* and *always will be* endlessly thankful to Professor Paul S. Weiss for creating a stimulating and learning environment that made me the professional that I am today, about to graduate with a Doctorate in Chemistry and Biochemistry.

Also, I want to thank oral qualifying exam committee members: Professor Z. Hong Zhou, Professor James W. Gober, and Professor Jorge Z. Torres for their time, guidance, and comments on how I can improve as a graduate student. Professor James W. Gober and Professor Jorge Z. Torres in addition to being committee members, were teaching instructors of biochemistry courses I took as a graduate student. Thus, I would like to thank them for teaching me graduate courses in Biocatalysis and Bioenergetics, and Biomolecular Structure, Catalysis, and Regulation.

Furthermore, I want to thank experts of amyloidogenic biomolecules – Professor David S. Eisenberg and Professor Jose Rodriguez that are UCLA faculty members. They contributed to the research and this dissertation by providing insightful conversations about β-amyloid peptides and their interaction with metal ions.

Upon joining Professor Paul S. Weiss's group, I worked closely with a postdoctoral fellow Shelley Claridge who is today a Professor at Purdue University. I want to thank Shelley

Claridge for her help and guidance during my first year. Also, I want to thank Professor Jérôme Gilles of the San Diego State University for a great collaboration. He created image segmentation tools, which we used to learn about similarities and differences of β-amyloid interaction with zinc and copper ions. The research investigations of this dissertation would not have been possible without help and support of group members specifically: Dr. Dominic P. Goronzy, Dr. Xiaobin Xu, Dr. Qing Yang, Lisa M. Kawakami, and Kevin M. Cheung. I am tremendously thankful to them for their help, time, and contribution to this dissertation.

Additionally, I would like to thank CNSI scientific staff – Dr. Adam Z. Stieg and Dr. Shivani Sharma, for providing training and addressing issues of scanning probe microscopy techniques (atomic force microscopy) used in this work.

Furthermore, I thank and acknowledge financial support from the Department of Energy Grant (# DE-SC-1037004) for the experiments conducted and imaging methods developed, and the W. M. Keck Foundation for the analytical methods developed and applied. Additionally, I thank support from the Eugene V. Cota-Robles Fellowship from UCLA, and support from the UCLA Department of Chemistry and Biochemistry.

During my Ph.D. career, a great time has been spent assisting in teaching various biochemistry courses. Professor Richard L. Weiss and Professor Stacie S. Nakamoto were both lecturers with whom I spent multiple quarters teaching undergraduate students. They were both role models for me who exemplified teaching and qualities that a lecturer must have. I want to thank them for their hard work, dedication to education and teaching me the skills required to work with undergraduate students.

Thinking about graduate studies and graduate research work, I recognize that multiple people contributed to this dissertation. Yet, Professor Larry R. Dalton and Dr. Denise Bale, from

the University of Washington, were the ones who opened doors to the research field for me by accepting me to their research group as an undergraduate assistant. It has been a life-changing experience. Without them, my research career and advancement to graduate studies would not have been possible. I want to thank both of them for their time, patience, and for teaching me the skills required to become a scientist.

Last but not least, I would like to thank my family and friends for supporting me throughout the journey of this academic work. I am proud to say that I am the first one in my family to receive a doctorate degree; however, this would not have been possible without the support and love of my mom. She was the one who gave me full freedom of choosing my pathway, and she was the one who supported, helped, and encouraged me in every step. My brother was a role model for me on how to be strong in any circumstance. My mom's and brother's unconditional love helped me to go through the thin and thick of the Ph.D. program, and I am endlessly thankful to them. As well, I want to thank my partner, Shahryar Hashemi, for his help and support. I could not have wished for a better partner than him. He is the one with whom I go through obstacles and worries, as well as with whom I share moments of happiness and joy. My Ph.D. program began in 2012, as a newly admitted student, I was invited to visit the UCLA campus. I visited the campus with my family and my friend Iryna Burich. Irina is not only a friend whom I have known for more than a decade, she is the person who like all the people above have supported and helped me throughout the Ph.D. program – a Ph.D. program that ends by completing this dissertation.

VITA

Diana Yugay obtained her BA in Biochemistry at the University of Washington in 2012, while performing research in the field of organic electro-optic, nonlinear optical, and electronic materials in the lab of Professor Larry R. Dalton. She began her graduate studies at the University of California, Los Angeles in 2012 under the mentorship of Professor Paul S. Weiss in the Department of Chemistry and Biochemistry. At the University of California, Los Angeles, she has been supported under a Cota Robles Fellowship and the departmental award for Commitment and Dedication to Teaching. Her graduate thesis focuses on elucidating structural motifs in β-amyloid peptide with sub-molecular resolution *via* scanning tunneling microscopy and spectroscopic imaging. Throughout her graduate career, she not only proposed and led research projects, but she also taught various chemistry and biochemistry classes, and mentored undergraduate students.

CHAPTER 1

β-Amyloid and Scanning Tunneling Microscopy as the Ultimate Tool to Study Its Structure and Metal Ion Binding Sit

1.1 Introduction: Importance of Studying Biomolecular Structures

X-ray powder diffraction (XRD) is an analytical technique developed in 1912 by Max von Laue.[1,2] The technique is used in structural identification and characterization of molecules biomolecular assemblies, and solids. Development of XRD led to advances in organic/inorganic chemistry and structural biology. Today, advantages of XRD include high resolution, versatile software packages (intensity extraction and space group determination, crystal structure solution, crystal structure refinement from powder data and etc.), and a vast library of molecules available for identification and characterization of unknown materials.[2,3] In order to employ XRD, it is vital to crystallize the molecule of interest. The crystals are exposed to an X-ray beam, which creates a diffraction pattern in scattering through the solid. From the diffraction pattern, the positions of atoms in the crystals are deduced by software and accordingly, structures of molecules are reconstructed or refined.[2-4]

Since 1912, various organic and biological molecules and macromolecules have been discovered. The interest in studying different types of structures of organic and biological molecules stems from their structure-function relationships. Particularly, a biological molecule with a specific sequence has a specific structure, which often corresponds to a specific function. Thus, by studying the structure-function relationships, we can compare molecules/biomolecules that have similar sequences and similar structures and thus, differentiate between pathogenic and nonpathogenic biomolecules.[5-7]

A significant disadvantage of XRD is its inability to elucidate the structures of amorphous molecules and materials, *i.e.*, molecules that cannot be crystallized.[3,8] Thus, some biological molecules impose a challenge in structural biology owing to their non-crystalline properties.[3] Often, proteins have disordered structures; however, it is theorized that each

disordered structure is unique in its disorder, and thus, it is a type of structure that carries a specific function.[5-7]

Proteins that are known to be difficult or impossible to crystallize include transmembrane and membrane proteins, proteins with post-translational modifications (PTM), intrinsically disordered proteins (IDP), and proteins with intrinsically disordered regions.[6,9,10] Some proteins with intrinsically disordered regions are known to be involved in deteriorating diseases in humans. Examples of these proteins include, but are not limited to, α-fetoprotein, p53, and, BRCA-1, which are involved in cancer; hirudin and thrombin, which are involved in cardiovascular diseases; α-synuclein, which is involved in synucleinopathies; tau and β-amyloid (Aβ), which are involved in Alzheimer's disease; prion protein, which is involved in prion diseases; and amylin and islet amyloid polypeptide, which are involved in type II diabetes.[11]

1.2 Conventional Techniques Used to Decipher Biomolecular Structures

Apart from XRD, other conventional techniques used in studying secondary structures of biomolecules and their interactions with ligands are solid-state nuclear magnetic resonance (ssNMR) and cryo-electron microscopy (cryo-EM).[3,8] Although non-crystallinity remains an issue in XRD and cryo-EM techniques, these structural characterization techniques have had tremendous recent advances in studying structures of non-crystalline biomolecules. For example, in 2006, Nelson *et al.* resolved the first atomic structure of amyloid-like fibrils using XRD. These fibrils were made up of a seven-residue peptide segment from Sup35 – a prion protein.[12] In 2017, Gremer *et al.* were the first to identify and to report the fibril structure of Aβ containing 42 residues using cryo-EM.[13] Thus, in the recent years, we have learned important structural information about amyloidogenic and Aβ peptides and their organization in fibrils. However,

structural information about Aβ in oligomeric form – the form considered to be neurotoxic[14,15] – is still missing.

1.3 Importance of Studying β-Amyloid and Theories Regarding Amyloid Toxicity

Alzheimer's disease (AD) is a deteriorating neurodegenerative disorder characterized by dementia and memory loss. Anyone who is around the age of 65 is at the risk of AD.[16,17] Although the disease progression ultimately leads to death, currently, no treatment is available for AD. Two neuropathological characteristics of AD brains are diseased neurons and plaques.[18,19] Diseased neurons are made up of paired helical filaments of hyperphosphorylated tau (τ) protein. The aggregates of hyperphosphorylated τ are called tangles. Plaques are made up of Aβ peptide aggregated into fibrils.[20,21] Since the discovery of neurofibrillary tangles and plaques, there were two main hypotheses regarding AD: Aβ hypothesis and τ hypothesis. The two hypotheses differ in opinion about the possible cause of neurodegeneration, and therefore, the two hypotheses have two different fundamental research approaches regarding AD and neurodegeneration. However, recently, the two hypotheses have started to merge and neuronal loss is considered to be a result of both Aβ and τ dysregulation.[22]

1.3.1 Tau Hypothesis

The tau hypothesis advocates that the cause of AD is dysregulation of cytosolic τ protein. Normal τ is bound to microtubules, and its identified functions include assembly and stabilization of microtubules and regulation of motor-driven axonal transport.[22,23] However, to date, not all functions and roles of τ have been determined. Dysregulation of τ is hypothesized to be due to various mutations and interaction with Zn^{2+} ions that lead to its

hyperphosphorylation.[23,24] Hyperphosphorylated τ disassembles from microtubules. Ultimately, it causes microtubules to lose their function. Additionally, hyperphosphorylated τ protein sequesters normal τ and causes it to aggregate. This process ultimately results in neurofibrillary tangles, which consist of hyperphosphorylated τ, different types of microtubule-associated proteins, and ubiquitin.[22-24]

1.3.2 Amyloid Hypothesis

The amyloid hypothesis advocates that the cause of dementia is miscleavage of the amyloid precursor protein (APP), which results in a flexible, sticky, and aggregation-prone peptide known as β-amyloid. The amyloid precursor protein is a transmembrane protein;[25,26] its amyloidogenic and non-amyloidogenic pathways have similarities as well as striking differences.

As illustrated in Figure 1.1, the similarity between the two pathways is that the transmembrane part of APP – C-terminus of Aβ – is cleaved by γ-secretase (between amino acids 39 and 42 of Aβ). The difference between the two pathways is that the soluble, extracellular part of APP in the amyloidogenic pathway is cleaved by β-secretase at position 672 (right before Glu1 in Aβ). This cleavage results in $A\beta_{1\text{-}42}$ and its homologs. In the non-amyloidogenic pathway, APP is cleaved by α-secretase at position 688 (between amino acids 16 and 17 of Aβ).[27,28] The end product of the α-secretase cleavage is a peptide that is 16 amino acids shorter than the peptide produced in the amyloidogenic pathway – $A\beta_{17\text{-}42}$, as well known as p3. It is hypothesized that the amyloidogenic pathway becomes the predominant pathway of APP cleavage owing to various mutations.[25,26]

1.4 β-Amyloid Facts

β-Amyloid is ~4 kDa in size, and it varies in length from 38 to 43 amino acids.[29] The two most common Aβ isoforms are 40 amino acids ($A\beta_{1-40}$) and 42 amino acids ($A\beta_{1-42}$) in length. The isoform with 42 amino acids received significant attention due to its aggregation that proceeds more rapidly than other isoforms, as well as, owing to findings that showed that naturally occurring plaques in AD are predominantly composed of $A\beta_{1-42}$.[30-33]

Essentially, Aβ can be divided into two parts. The first part is an extracellular domain located in the vicinity of the N-terminus (Figure 1.1). The extracellular domain is hydrophilic and intrinsically disordered. In oligomeric form, specifically, the first 15 amino acids at the N-terminus of Aβ have a high propensity for disordered secondary structure.[34-36] We know that disordered structure of Aβ is unstable; it disintegrates with time and disappears entirely from Aβ fibrils. The extracellular domain also has a central hydrophobic core spanning from Leu17 to Ala21.[37,38]

The second part of Aβ is a transmembrane domain (Figure 1.1). It encompasses the rest of amino acids, and it is located in the vicinity of the C-terminus. The boundary between the extracellular and the transmembrane domain is not clearly established, but it is reported to be in the vicinity of amino acids 19 to 28.[27,28,39,40]

The transmembrane domain is more straightforward than its counterpart. It is a hydrophobic region with a high propensity to form β-sheet structures.[38,41,42] It is predominantly composed of hydrophobic amino acids, and it is known as the hydrophobic core of Aβ, with a highly hydrophobic region that spans from Gly32 to Ala42.[29,38] It is believed that a second metal ion-binding site could be located in the vicinity of the C-terminus.[43,44] Nevertheless, its involvement in metal ion binding is not known. Additionally, it is believed that the

transmembrane domain plays a significant role in cell oxidative damage due to Met35 and its ability to undergo redox cycling.[45-47]

1.4.1 β-Sheet Characteristics of β-Amyloid Peptides

The structure of β-Amyloid and amyloidogenic peptides was studied by electron microscopy (EM) and XRD.[12,13] Based on the results, it is widely accepted that amyloidogenic strands organize into cross-β-sheet motifs (Figure 1.2).[52] We also know that in fibrils, vertically stacked strands are in the β-strand conformation. These β-strands are in parallel arrangements with a β-strand spacing (interstrand spacing) of ~4.7 Å.[12,48-52] In fibrils, strands run perpendicular to the fiber x-axis, whereas sheets continue their growth towards z-axis. The distance between sheets in the z-axis direction is 6-11 Å (Figure 1.2), whereas the total filament diameter is 60-120 Å.[51,52]

Predominant forces that hold Aβ fibril structures together are hydrogen bonding, hydrophobic interactions, and van der Waals interactions.[53,54] Specifically, N-terminus is stabilized by hydrophobic and electrostatic interactions, whereas C-terminus is stabilized by hydrophobic and van der Waals interactions.[55]

1.5 Probable Causes of β-Amyloid Toxicity

In search of possible neurodegenerative treatments, probable causes of Aβ toxicity have been extensively investigated. Attention has shifted from Aβ fibrils to Aβ oligomers. Now, it is established that Aβ oligomers are pathogenic species with neuronal toxicity.[14,15] On the basis of mice/rat studies, the size of Aβ oligomers was determined to be ~56 kDa.[56-58] It is hypothesized that the size and toxicity of Aβ oligomers are inversely related.[57] Furthermore, toxicity depends

on the structure and conformation of the oligomer, yet the structures and conformations of the toxic oligomers remain to be determined.

In addition to the Aβ toxic-oligomer theory, other possible causes of Aβ toxicity that emerged are summarized in Figure 1.3. Amongst the most hypothesized reasons are interactions of Aβ with transition metal ions, involvement of Aβ in oxidative stress, dysregulation of Aβ due to its familial mutations, interaction and aggregation of Aβ with cholesterol molecules, and toxicity of Aβ due to its various post-translational modifications.[29,40,59-63]

1.5.1 Toxicity of β-Amyloid Due to Interaction with Metal Ions

Although numerous theories exist regarding Aβ toxicity, the following two theories are interconnected: the theory of Aβ toxicity due to Aβ interaction with metal ions and the theory of Aβ toxicity due to reactive oxygen species (ROS) production.[64,65] During early research on Aβ interactions with metal ions, two points were established – first, Aβ, in the vicinity of the N-terminus, has a binding site for transition metal ions such as Cu^{2+}, Zn^{2+}, and Fe^{2+};[66-69] second, transition metal ions speed up the aggregation process of Aβ, the result of which is Aβ fibrils.[70] In the case of metal ion interactions with Aβ, it is hypothesized that metal ions act as a seeding factor for Aβ aggregation.[71] Hence, in this pathway, owing to the bound metal ions, Aβ misbalances the metal ion distributions in the brain.[65,72] In addition, the other detrimental outcome of the interaction of Aβ with transition metal ions is believed to be ROS production, which will be covered below.

Interestingly, rat Aβ ($Aβ_{rat}$), which has Gly1, Phe5, and Arg13 instead of Asp1, Arg5, and His13 found in human Aβ (Figure 1.3), possesses properties very different from those of human Aβ. Unlike human Aβ, $Aβ_{rat}$ does not have a strong affinity to metal ions nor a high rate of

aggregation in the presence of metal ions, and it has lower rates of ROS production than human Aβ.[70] After extensive research, it has been concluded that $A\beta_{rat}$ is less toxic and thus, non-life-threatening.[73-75]

Even though considerable information is available today about Aβ and Aβ properties, we do not yet have a definite conclusion on which residues are involved in metal ion binding and thus which residues contribute to the aggregation of Aβ. One of the multiple reasons for slow research progress is the mechanical and conformational flexibility of Aβ.[34,36,76-78] Aβ is a polymorphic peptide, and various extrinsic factors influence its state of aggregation.[79] The extrinsic factors include, but are not limited to, concentration of peptides, presence of external molecules, pH, net charge, temperature, pressure, and agitation.[80,81] Another reason for slow research progress is the non-crystallinity of Aβ and thus, instrumental limitations, *i.e.*, conventional techniques such as XRD and cryo-EM may not be used to investigate structural aspects of Aβ, especially when Aβ is in oligomeric form.

1.5.2 Relationship between Metal Ions and β-Amyloid: *In Vitro* and *in Vivo* Results

In 2014, Johnson *et al.* collected high-resolution positron emission tomography (PET) images of brains corresponding to people with and without AD.[82] The goal of the study was to compare and to contrast clinically healthy brains with the brains of people diagnosed with AD. Based on the results of the study, healthy brains had little to no presence of Aβ and τ deposits, whereas the brains of people diagnosed with AD showed an abundance of both Aβ and τ.

Bush *et al.*, in 1998, performed a comprehensive *in vitro* study, which showed that Aβ aggregation depends on the presence, concentration, and type of metal ions in solution.[83] Subsequently, other groups confirmed their findings.[84] The relationship between metal ion

concentration and Aβ aggregation has also been studied *in vivo*. However, until now, the *in vivo* results are more controversial than the *in vitro* results, as the former are highly dependent on the studied tissue and the technique used by researchers. The general trend observed is that during AD, the concentration of metal ions in neuropil and gray matter tissues increases. Specifically, the normal/healthy concentrations of Cu^{2+}, Zn^{2+}, and Fe^{2+} in neuropil and gray matter tissues are ~79 μM, ~150 μM and ~340 μM, respectively, whereas in diseased tissues, the concentrations of these ions increase to ~400 μM, ~1000 μM, and ~1000 μM, respectively.[85-88]

1.5.3 β-Amyloid Toxicity Due to Production of Reactive Oxygen Species

Increased aggregation rate of Aβ upon its interaction with metal ions increases its toxicity. Toxicity of Aβ increases due to increased production of redox species. Redox species lead to oxidative stress, whereas oxidative stress is detrimental for healthy cell function.

1.5.4 β-Amyloid and Its Interactions with Zinc, Copper, and Iron

Zinc is an essential element with catalytic, structural, and regulatory functions in our bodies. Amongst its various roles are cellular signal transduction and modulation of synaptic neurotransmission. Zinc dysregulation is hypothesized to be involved in neurodegeneration. In case of AD and its interaction with Aβ, findings suggest that Zn^{2+} and Cu^{2+} have shared residues that participate in Aβ binding site.[87,89] Involvement of Zn^{2+} in neurodegeneration is different than that of Cu^{2+} or Fe^{2+}; it was not found to be directly involved in ROS production, but it is thought to be an agent that initiates amyloid deposition.[90]

The outcome of Aβ interaction with copper (Aβ-Cu) and iron (Aβ-Fe) is the production of ROS (Figure 1.4).[62] Reactive oxygen species are known to be detrimental to healthy brain activity owing to DNA damage, mitochondrial damage, and protein oxidation.[89,91]

In 1999, Bush *et al.* showed that during Aβ-Cu and Aβ-Fe interaction, both metal ions undergo cycling between oxidized (Cu^{2+}, Fe^{3+}) and reduced (Cu^{+}, Fe^{2+}) states.[92] Upon metal ion reduction, molecular oxygen is reduced to H_2O_2. The latter is directly involved in generation of ROS (in the form of •OH and $^{-}$OH; Figure 1.4).[62,93-95]

It is hypothesized that in the process of redox cycling, Aβ could itself act as an electron donor, upon which it becomes Aβ radical (Aβ•). The Aβ radical is thought to extract protons from surroundings such as DNA, lipids, and proteins, which act as reducing agents. At the end of the redox process, Aβ• gets returned to its normal state, *i.e.*, Aβ, whereas Cu^{+} and Fe^{2+} reduce to a more stable state—Cu^{2+} and Fe^{3+} (Figure 1.4).[62] The process of metal ion redox cycling and Aβ radicalization could occur several times, which ultimately leads to brain tissue damage.[62,96,97]

Residues believed to be involved in ROS production during Aβ-Cu interaction are Asp1, His6, His13, His14, Tyr10, Phe20, and Met35; and residues involved in Aβ-Fe interaction are Asp1, Glu3, His6, His13, and His14. Of the listed residues, Met35 in Aβ-Cu interaction received considerable attention. This residue is strongly correlated with the oxidative and neurotoxic properties of Aβ. Recent findings suggest that removal of this residue changed the properties of the peptide to non-oxidative and non-neurotoxic.[98-100]

Apart from Aβ interaction with metal ions, the toxicity is also attributed to Aβ interference with synaptic receptors. The interaction is noted to be *via* direct binding of Aβ to receptors or indirect interaction such as membrane association that results in modification of various receptor properties.[23]

1.6 Structural Characterization of β-Amyloid: Techniques and Recent Advances

This section discusses current advances and techniques used in the characterization of Aβ structure. Past research focused on overcoming the challenges of structural characterization of Aβ and amyloid-like peptides. Although research on Aβ has a long history, structural reports on amyloid fibrils started to emerge only recently. There is only slow progress towards structural characterization of amyloid-like peptides and Aβ because hydrophilic segments of these peptides have high mechanical, structural, and conformational flexibility.[34-36,77,78] This flexibility ultimately leads to the non-crystallinity of amyloid-like peptides and Aβ, and thus, the inability of techniques such as XRD to be employed to investigate the structure of these peptides.

In addition to non-crystallinity, the other challenge in determining structures of amyloids is the amyloidogenic property of having several different conformations. Before organizing into fibrils, amyloids nucleate and progress in their structure from monomers to dimers, trimers, and so on. The process creates versatile structural intermediates. The structures of those intermediates are affected by internal factors such as length and mutations, and external factors such as time of incubation, pH, and presence of metal ions.[81,101] Owing to this structural flexibility, amyloids are classified as polymorphic peptides.[76,79,102,103]

The structural dependence of amyloids on intrinsic properties and external factors make amyloids highly complicated systems. For example, based on conditions of sample preparation (external conditions), two different research groups would end up examining two different amyloid structures.

Techniques employed by structural biochemists to determine amyloid structure are ssNMR, mass-per-length exchange measurements, magnetic angle spinning (MAS) NMR, and

cryo-EM.[13,34,104,105] These techniques rely on scanning through the fibril structure of an amyloid, and their outcome is a visualization of the Aβ peptidyl arrangement in fibrils.

1.6.1 Results of Amyloid-β Structural Research

Reik-Loher, Griffin, and their co-workers examined the structural organization of $A\beta_{1-42}$ fibrils *via* ssNMR and mass-per-length exchange measurements, and MAS NMR, respectively.[34,104] Their findings indicate that Aβ, in the region of residues 15-42, folds twice onto itself into an S-like shape (Figure 1.5a,b). Furthermore, residues 1-14 linearly extend and are adjacent to the C-terminus of another amyloid unit. The N-terminus is partially ordered and in a β-strand conformation. However, the study by Reik-Loher and co-workers is less clear than the study by Griffin and co-workers on the N-terminus arrangement of $A\beta_{1-42}$; nevertheless, both studies agree that in a fiber, two amyloid units contact through Met35, Leu17, and Gln15 residues.

Another structural characterization study of $A\beta_{1-40}$ involved single deletion at Glu22 (known as the Osaka mutant). The study reported Aβ fibril organization different from that reported by Reik-Loher, Griffin, and their co-workers. In the study by Schütz *et al.*, the Osaka mutant was reported to organize in the vicinity of N-terminus into an inverted L structure with a bend at Tyr10 (Figure 1.5b,c).[105] Furthermore, the Osaka mutant was reported to fold onto itself into an S-like shape between amino acid residues 20 and 40.

The most recently reported Aβ structure was by Gremer *et al.*[13] Using cryo-EM, Gremer *et al.* examined the structure of fibrillar $A\beta_{1-42}$ (Figure 1.5e). Once again, the reported structural organization of fibrillar $A\beta_{1-42}$ was different from that in previous reports. The structure

visualized using cryo-EM showed that $A\beta_{1-42}$ has an LS-shape topology while dimers from both sides of the reported structure make contact at Lys28 and Lys1.

Based on the above studies, the consensus that the C-terminus of fibrillar Aβ is in an S-like shape, where the size of the S-shape, length of the N-terminus, and dimeric contacts depend strongly on the external conditions and intrinsic properties of Aβ such as sample preparation, Aβ length, and the mutations present.

1.7 Scanning Tunneling Microscopy as the Ultimate Tool To Study Structures of Intrinsically Disordered Biomolecules

Failure of conventional techniques to determine the structure of disordered biomolecules opened up doors to search for nonconventional techniques that would be able to do so. Scanning tunneling microscopy (STM) is a characterization method used by researchers to study atoms, molecules, and biomolecules.[106-112] By using STM, we can learn about atoms – their structure and surface arrangement;[107] inorganic and organic molecules – their structures, surface arrangements, and surface defects;[111] and small and large biomolecules – their structures and co-assembly with host molecules of various origins (guest/host interaction).[106,108-110,112]

1.7.1 Working Principles of Scanning Tunneling Microscopy

Scanning tunneling microscopy is a surface characterization technique. The working principle behind STM is mapping and processing the changes in tunneling current (created between a sample and an atomically sharp tip) into an image. One of the main requirements of STM is a conducting substrate.[113] Common conducting substrates include, but are not limited to, gold and highly oriented pyrolytic graphite (HOPG).[114] After choosing a substrate, a monolayer

of molecules of interest is deposited on top of the substrate. The process is followed by scanning the substrate with an ultra-sharp (atomically sharp) tip.

During scanning, the tip is brought into close proximity with the surface. The distance between the tip and the sample is usually 5-10 Å.[115] Subsequently, a voltage bias is applied. This bias voltage results in a tunneling current between the sample and the tip that depends strongly on the tip-sample separation. Changes in the tunneling current, which occur owing to sample topography, height, and/or sample/molecular surface arrangement are mapped and processed by a computer. The result is STM image with a lateral resolution of <1 Å and a depth of resolution < 0.1 Å.[115,116]

In addition to high image resolution, the versatility of the technique is another advantage of STM, *i.e.*, depending on the goals of the researchers, it can be operated under different conditions such as ultrahigh vacuum, in ambient/air, under liquids/chemicals/water, and in gases.[117-120] Another advantage is that the three-dimensional profile of the scanned surface allows examination of sample characteristics such as sample surface roughness, sample/surface defects, and size/structure of scanned molecules on the surface.[121] However, one of the disadvantages of STM is its speed. Scanning tunneling microscopy takes a long time to acquire a high-resolution image.[122-124] Finally, disadvantages regarding sample preparation and scanning include requirements of a clean sample/substrate surface (preferably a monolayer of deposited molecules of interest), an ultra-sharp scanning tip (atomically sharp/single-atom tip), and good vibrational control during operation.

1.7.2 Scanning Tunneling Microscopy and Biomolecules with Metal Centers

As mentioned above, the disadvantages of STM do not include biomolecular crystallizability, flexibility, and/or hydrophilicity. Thus, the technique is suitable for studying biomolecular structures that cannot be otherwise accessed by conventional techniques such as XRD.

In addition to studying structures of non-crystalline biomolecules with STM, it is possible to utilize the technique to study biomolecules with metal ion centers (metal ion-binding sites). In 2005, Chi *et al.* demonstrated an extensive potential of STM by studying azurin – a copper-binding electron transfer protein.[125] In the study, they showed that it is possible to not only study large biological molecules *via* STM but also to use the technique in order to identify proteins with a metal center.

Coordination of $A\beta_{1\text{-}42}$ with transition metal ions has long been debated in the scientific community.[126,127] Owing to the flexibility and non-crystallinity of Aβ, conventional techniques cannot access a metal ion-binding site. In this dissertation, STM is a primary characterization technique used to elucidate Aβ structure, its interactions with metal ions (specifically Cu^{2+} and Zn^{2+}), its metal ion-binding sites, and its residues participating in metal ion binding.

1.8 Dissertation Overview

This dissertation is organized as follows: Chapter 1 discusses the importance and current challenges in studying non-crystalline biomolecules, theories behind Aβ toxicity and current state of the art and advances in Aβ research, and finally, an alternative and non-conventional technique – scanning tunneling microscopy – and why we used it to access the structures and binding sites of Aβ. Chapter 2 presents investigations into and related results for copper

ion-binding sites in Aβ. Chapter 3 compares and contrasts the effects of copper and zinc ions on Aβ structure and its β-sheet self-assembly. Chapter 4 details structural changes in Aβ occurring in the vicinity of C-terminus upon its interaction with copper ions. Future prospects of this work are summarized in Chapter 5.

Chapter 2 has been reformatted from the following manuscript:

Yugay, D.; Goronzy, D.P.; Kawakami, L.M.; Claridge, S.A.; Song, T.B.; Yan, Z.; Xie Y.H.; Gilles, J.; Yang, Y.; Weiss, P.S. Copper Ion Binding Site in β-Amyloid Peptide. *Nano Lett.* **2016**, *16*, 6282–6289

Chapter 3 has been reformatted from a manuscript in preparation:

Yugay, D.; Goronzy, D.P.; Gilles, J.; Rouvier, T.; Weiss, P.S. Metal-Ion-Induced Structural Rearrangements of β-Amyloid Peptides. *In preparation* **2019**.

Chapter 4 has been reformatted from a manuscript in preparation:

Yugay, D.; Xu, X.; Yang, Q.; Weiss, P.S. Copper Ion Interactions with the C-terminus of the β-Amyloid Peptide. *In preparation* **2019**.

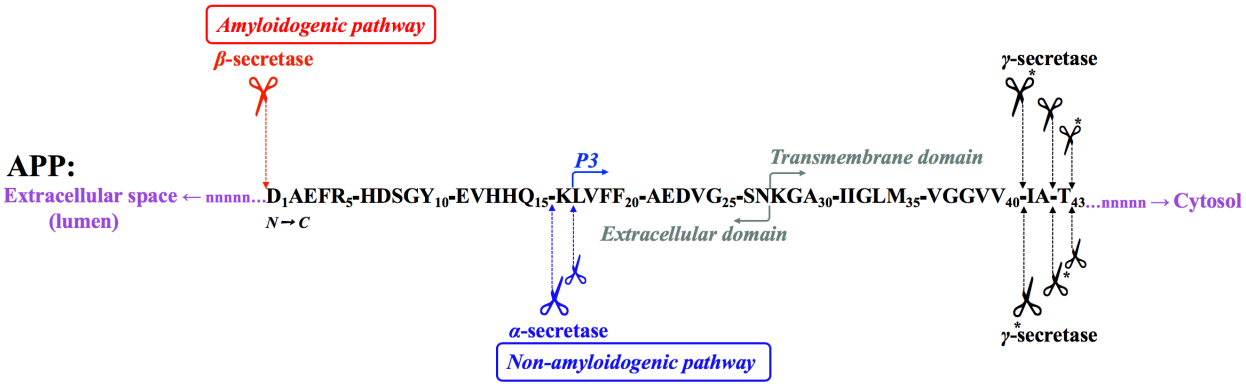

Figure 1.1. Amyloidogenic and non-amyloidogenic pathways of amyloid precursor protein (APP). In the amyloidogenic pathway (top of the diagram) APP is cleaved by β-secretase at position 672 (right before Glu1 in Aβ) and by γ-secretase (between amino acids 39 and 43 of Aβ). γ-Secretase is non-specific and thus, cleaves Aβ anywhere between amino acids 39 and 43. Asterisks (∗) next to γ-secretase indicate Aβ segments which are not found in abundant quantity in Aβ plaques and thus, those segments are considered to be less toxic than the cut at the position 42. In the non-amyloidogenic pathway (bottom of the diagram), APP is cleaved by α-secretase at position 688 (between amino acids 16 and 17 of Aβ) and similarly to amyloidogenic pathways later it is cleaved by γ-secretase (between amino acids 39 and 43 of Aβ). The end product of the α-secretase cleavage is a peptide that is 16 amino acids shorter than the peptide produced in the amyloidogenic pathway – $A\beta_{17-42}$, as well known as P3.

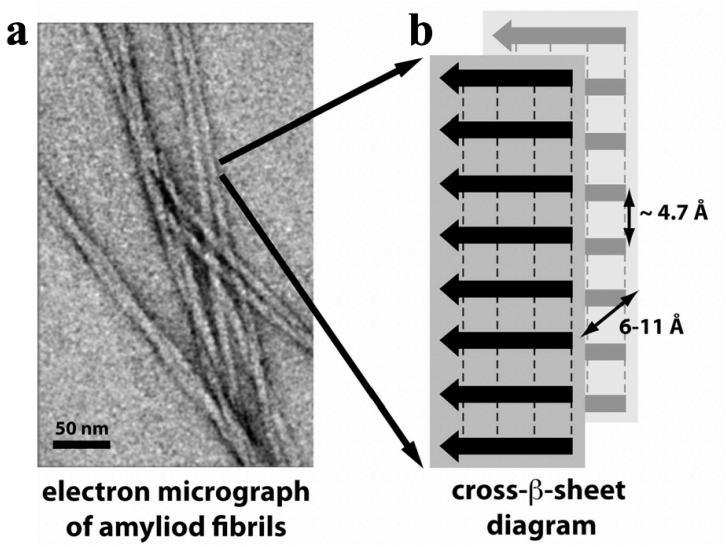

Figure 1.2. (a) Transmission electron micrograph image of amyloid fibrils. (b) The schematic diagram of the amyloidogenic β-strands which are in parallel arrangement with the β-strand spacing (interstrand spacing) of ~4.7 Å. In fibrils, strands run perpendicular to the fiber x-axis, whereas sheets continue their growth towards z-axis. The distance between sheets in the z-axis direction is 6-11 Å, whereas the total filament diameter is 60-120 Å. Adapted from ref. 52. Copyright 2010, Structure.

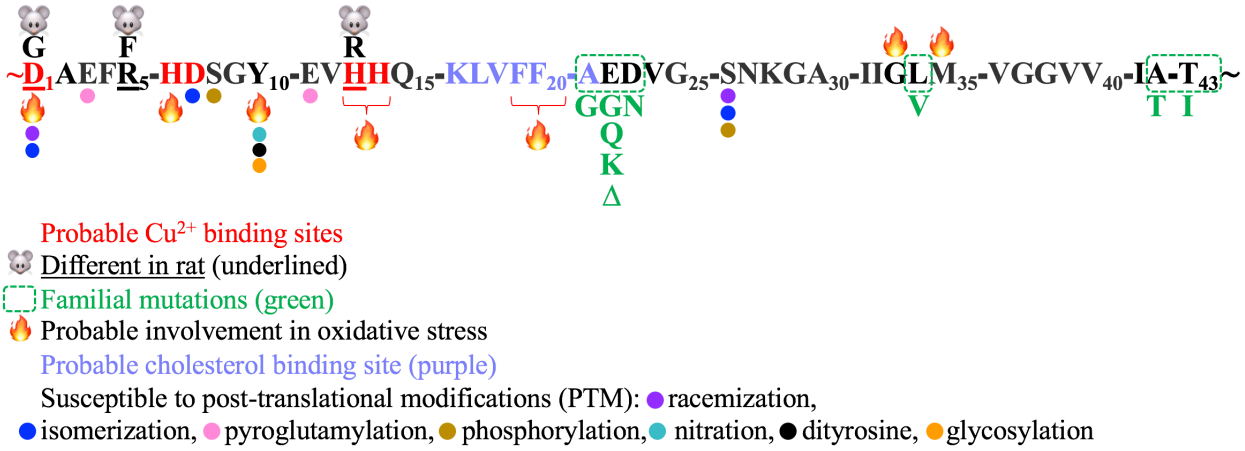

Figure 1.3. β-Amyloid sequence illustrating possible amino acid residues that could be involved in Aβ toxicity. Amongst the most hypothesized reasons of Aβ toxicity that have emerged are interactions of Aβ with transition metal ions, involvement of Aβ in oxidative stress, dysregulation of Aβ due to its familial mutations, interaction and aggregation of Aβ with cholesterol molecules, and toxicity of Aβ due to its various post-translational modifications.

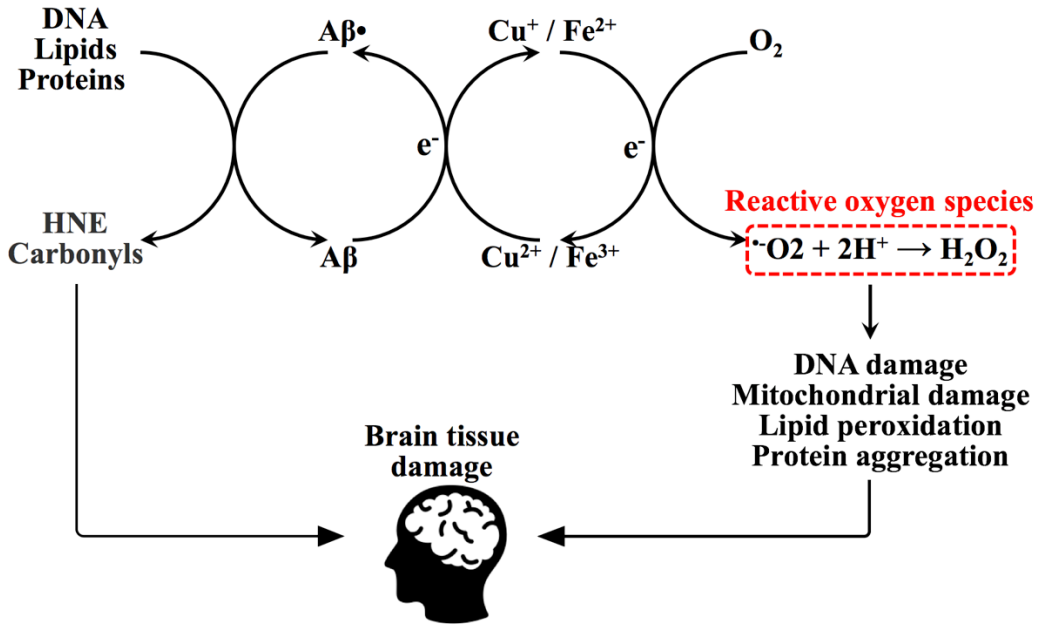

Figure 1.4. Diagram illustrating Aβ interaction with copper (Aβ-Cu) and iron (Aβ-Fe) and production of ROS. It is hypothesized that in the process of redox cycling, Aβ acts as an electron donor, upon which it becomes Aβ radical (Aβ•). The Aβ radical is thought to extract protons from surroundings such as DNA, lipids, and proteins, which act as reducing agents. As a consequence of proton extraction, hydroxy-2-nonenal (HNE) and carbonyls that are detrimental for healthy brain activity are generated. Afterwards, Aβ• gets returned to its normal state, *i.e.*, Aβ. Furthermore, during Aβ-Cu and Aβ-Fe interaction, both metal ions undergo cycling between oxidized (Cu^{2+}, Fe^{3+}) and reduced (Cu^{+}, Fe^{2+}) states. Upon metal ion reduction, molecular oxygen (O_2) is reduced to peroxide (H_2O_2). The latter is directly involved in generation of ROS (in the form of •OH and $^{-}$OH). Reactive oxygen species are detrimental for healthy brain activity due to DNA and mitochondrial damage, lipid peroxidation, and protein aggregation. Adapted from ref. 62. Copyright 2007, Biochimica et Biophysica Acta.

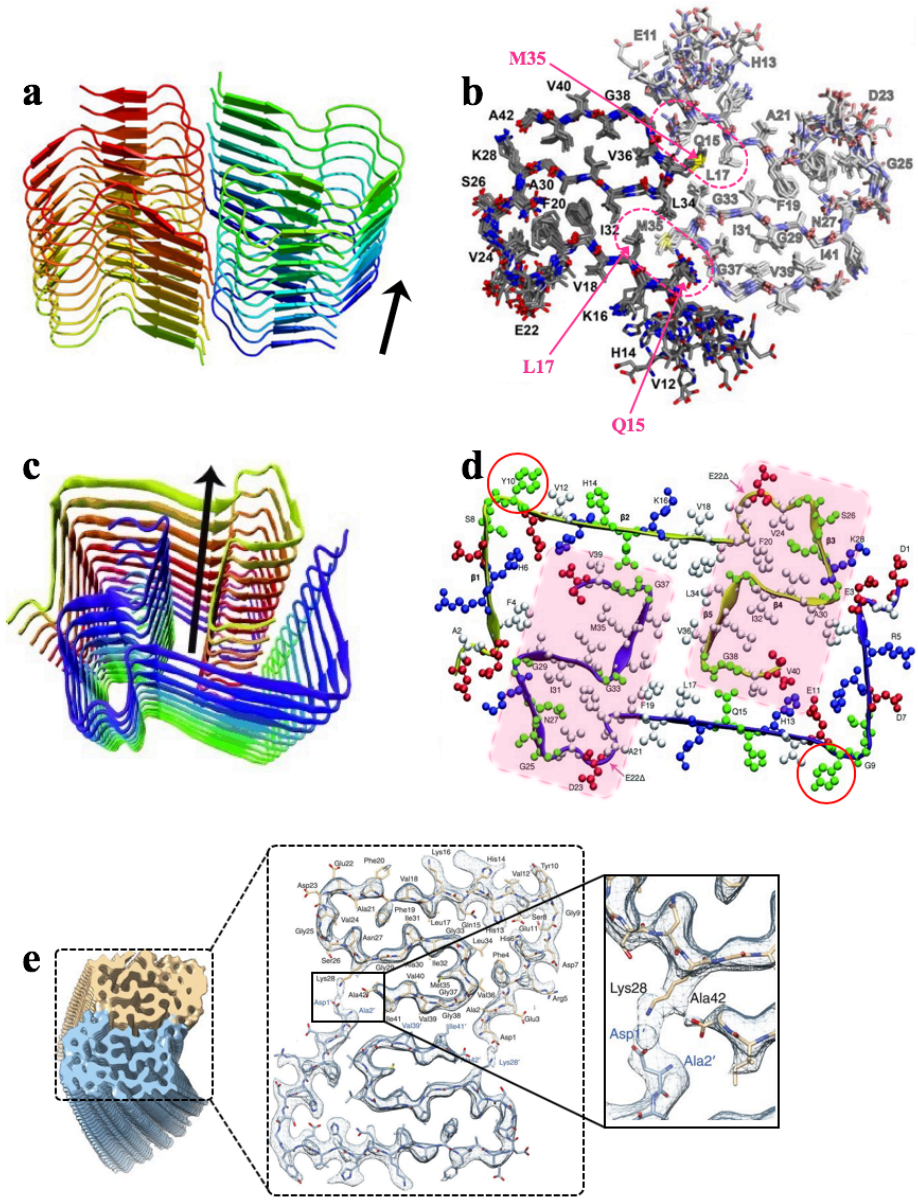

Figure 1.5. Various discovered Aβ arrangements in fibrils. (a,b) Structural organization of $A\beta_{1\text{-}42}$ fibrils *via* ssNMR examined by Griffin and co-workers.[104] Findings indicate that Aβ, in the region of residues 15-42, folds twice onto itself into an S-like shape. Furthermore, residues 1-14 linearly extend and are adjacent to the C-terminus of another amyloid unit (not shown). (b) In a fiber two amyloid units contact through Met35 (M35) (residue in yellow color), Leu17 (L17), and Gln15 (Q15) (residues in the dashed ovals). (c,d) Structural characterization of $A\beta_{1\text{-}40}$ involving single deletion at Glu22 (known as the Osaka mutant). In this study Schütz *et al.*,

reported that the Osaka mutant organizes in the vicinity of N-terminus into an inverted L structure with a bend at Tyr10 (pink circle). Furthermore, the Osaka mutant was reported to fold onto itself into an S-like shape between amino acid residues 20 and 40 (pink shaded rectangles).[105] (e) Gremer *et al.* visualized structure of $A\beta_{1-42}$ using cryo-EM.[13] In the study he showed that $A\beta_{1-42}$ has an LS-shape topology (lower dimer) while dimers from both sides of the reported structure make contact at Lys28 (upper dimer) and Asp1 (lower dimer). Adapted from refs: 13. Copyright 2017, Science; 104. Copyright 2016, Journal of the American Chemical Society; 105. Angewandte Chemie International Edition.

1.9 References

1. Eckert, M. Max Von Laue and the Discovery of X-Ray Diffraction in 1912. *Ann Phys-Berlin* **2012,** *524,* A83–A85.

2. Dutrow, B. L.; Clark, C. M. X-Ray Powder Diffraction (XRD). https://serc.carleton.edu/research_education/geochemsheets/techniques/XRD.html (July 26, 2019).

3. Creative Biostructure. Comparison of Crystallography, NMR and EM. https://www.creative-biostructure.com/comparison-of-crystallography-nmr-and-em_6.htm (July 26, 2019).

4. Wang, H. W.; Wang, J. W. How Cryo-Electron Microscopy and X-Ray Crystallography Complement Each Other. *Protein Sci* **2017,** *26,* 32–39.

5. Babu, M. M. The Contribution of Intrinsically Disordered Regions to Protein Function, Cellular Complexity, and Human Disease. *Biochem Soc T* **2016,** *44,* 1185–1200.

6. van der Lee, R.; Buljan, M.; Lang, B.; Weatheritt, R. J.; Daughdrill, G. W.; Dunker, A. K.; Fuxreiter, M.; Gough, J.; Gsponer, J.; Jones, D. T.; Kim, P. M.; Kriwacki, R. W.; Oldfield, C. J.; Pappu, R. V.; Tompa, P.; Uversky, V. N.; Wright, P. E.; Babu, M. M. Classification of Intrinsically Disordered Regions and Proteins. *Chem Rev* **2014,** *114,* 6589–6631.

7. Wright, P. E.; Dyson, H. J. Intrinsically Unstructured Proteins: Re-Assessing the Protein Structure-Function Paradigm. *J Mol Biol* **1999,** *293,* 321–331.

8. PDB-101. Methods for Determining Atomic Structures. https://pdb101.rcsb.org/learn/guide-to-understanding-pdb-data/methods-for-determining-structure (July 26, 2019).

9. Deller, M. C.; Kong, L.; Rupp, B. Protein Stability: A Crystallographer's Perspective. *Acta Crystallogr F Struct Biol Commun* **2016,** *72,* 72–95.

10. Sowadski, J. M. Introduction: Crystallization of Membrane Proteins – in Need of a New Focus? *J Bioenerg Biomembr* **1996,** *28,* 3–5.

11. Uversky, V. N.; Oldfield, C. J.; Dunker, A. K. Intrinsically Disordered Proteins in Human Diseases: Introducing the D^2 Concept. *Annu Rev Biophys* **2008,** *37,* 215–246.

12. Nelson, R.; Sawaya, M. R.; Balbirnie, M.; Madsen, A. O.; Riekel, C.; Grothe, R.; Eisenberg, D. Structure of the Cross-β Spine of Amyloid-Like Fibrils. *Nature* **2005,** *435,* 773–778.

13. Gremer, L.; Scholzel, D.; Schenk, C.; Reinartz, E.; Labahn, J.; Ravelli, R. B. G.; Tusche, M.; Lopez-Iglesias, C.; Hoyer, W.; Heise, H.; Willbold, D.; Schroder, G. F. Fibril Structure of Amyloid-β(1-42) by Cryo-Electron Microscopy. *Science* **2017,** *358,* 116–119.

14. Lublin, A. L.; Gandy, S. Amyloid-β Oligomers: Possible Roles as Key Neurotoxins in Alzheimer's Disease. *Mt Sinai J Med* **2010,** *77,* 43–49.

15. Rauk, A. Why Is the Amyloid Beta Peptide of Alzheimer's Disease Neurotoxic? *Dalton T* **2008,** 1273–1282.

16. Jahn, H. Memory Loss in Alzheimer's Disease. *Dialogues Clin Neurosci* **2013,** *15,* 445–454.

17. Kumar, A.; Tsao, J. W., Alzheimer Disease. In *Statpearls*, Treasure Island (FL), 2019.

18. Perl, D. P. Neuropathology of Alzheimer's Disease. *Mt Sinai J Med* **2010,** *77,* 32–42.

19. Serrano-Pozo, A.; Frosch, M. P.; Masliah, E.; Hyman, B. T. Neuropathological Alterations in Alzheimer Disease. *CSH Perspect Med* **2011,** *1*.

20. Bloom, G. S. Amyloid-β and Tau: The Trigger and Bullet in Alzheimer Disease Pathogenesis. *JAMA Neurol* **2014,** *71,* 505–508.

21. Goedert, M.; Spillantini, M. G. A Century of Alzheimer's Disease. *Science* **2006,** *314,* 777–781.

22. Ittner, L. M.; Gotz, J. Amyloid-β and Tau — a Toxic *Pas de Deux* in Alzheimer's Disease. *Nat Rev Neurosci* **2011,** *12,* 65–72.

23. Ghosh, R.; Alajbegovic, A.; Gomes, A. V. NSAIDs and Cardiovascular Diseases: Role of Reactive Oxygen Species. *Oxid Med Cell Longev* **2015,** *2015,* 536962.

24. Mudher, A.; Lovestone, S. Alzheimer's Disease-Do Tauists and Baptists Finally Shake Hands? *Trends Neurosci* **2002,** *25,* 22–26.

25. MacLeod, R.; Hillert, E. K.; Cameron, R. T.; Baillie, G. S. The Role and Therapeutic Targeting of α-, β- and γ-Secretase in Alzheimer's Disease. *Future Sci OA* **2015,** *1,* FSO11.

26. Muller, U. C.; Deller, T.; Korte, M. Not Just Amyloid: Physiological Functions of the Amyloid Precursor Protein Family. *Nat Rev Neurosci* **2017,** *18,* 281–298.

27. Hayne, D. J.; Lim, S.; Donnelly, P. S. Metal Complexes Designed to Bind to Amyloid-β for the Diagnosis and Treatment of Alzheimer's Disease. *Chem Soc Rev* **2014,** *43,* 6701–6715.

28. Suh, Y. H.; Checler, F. Amyloid Precursor Protein, Presenilins, and α-Synuclein: Molecular Pathogenesis and Pharmacological Applications in Alzheimer's Disease. *Pharmacol Rev* **2002,** *54,* 469–525.

29. Enache, T. A.; Chiorcea-Paquim, A. M.; Oliveira-Brett, A. M. Amyloid-β Peptides Time-Dependent Structural Modifications: AFM and Voltammetric Characterization. *Anal Chim Acta* **2016,** *926,* 36–47.

30. Attems, J.; Lintner, F.; Jellinger, K. A. Amyloid β Peptide 1–42 Highly Correlates with Capillary Cerebral Amyloid Angiopathy and Alzheimer Disease Pathology. *Acta Neuropathol* **2004,** *107,* 479–480.

31. Finder, V. H.; Vodopivec, I.; Nitsch, R. M.; Glockshuber, R. The Recombinant Amyloid-β Peptide Aβ1–42 Aggregates Faster and Is More Neurotoxic than Synthetic Aβ1–42. *J Mol Biol* **2010,** *396,* 9–18.

32. Roher, A. E.; Lowenson, J. D.; Clarke, S.; Woods, A. S.; Cotter, R. J.; Gowing, E.; Ball, M. J. β-Amyloid-(1-42) Is a Major Component of Cerebrovascular Amyloid Deposits: Implications for the Pathology of Alzheimer-Disease. *P Natl Acad Sci USA* **1993,** *90,* 10836–10840.

33. Tiiman, A.; Krishtal, J.; Palumaa, P.; Tougu, V. *In Vitro* Fibrillization of Alzheimer's Amyloid-β Peptide (1-42). *AIP Adv* **2015,** *5*.

34. Luhrs, T.; Ritter, C.; Adrian, M.; Riek-Loher, D.; Bohrmann, B.; Doeli, H.; Schubert, D.; Riek, R. 3D Structure of Alzheimer's Amyloid-β(1-42) Fibrils. *P Natl Acad Sci USA* **2005,** *102,* 17342–17347.

35. Miller, Y.; Ma, B. Y.; Nussinov, R. Zinc Ions Promote Alzheimer Aβ Aggregation via Population Shift of Polymorphic States. *P Natl Acad Sci USA* **2010,** *107,* 9490–9495.

36. Yu, X.; Zheng, J. Polymorphic Structures of Alzheimer's β-Amyloid Globulomers. *PLoS ONE* **2011,** *6*.

37. Boopathi, S.; Kolandaivel, P. Role of Zinc and Copper Metal Ions in Amyloid β-Peptides $A\beta_{1-40}$ and $A\beta_{1-42}$ Aggregation. *RSC Adv* **2014,** *4,* 38951–38965.

38. Serpell, L. C. Alzheimer's Amyloid Fibrils: Structure and Assembly. *Biochim Biophys Acta* **2000,** *1502,* 16–30.

39. Funamoto, S.; Morishima-Kawashima, M.; Tanimura, Y.; Hirotani, N.; Saido, T. C.; Ihara, Y. Truncated Carboxyl-Terminal Fragments of β-Amyloid Precursor Protein Are Processed to Amyloid β-Proteins 40 and 42. *Biochemistry* **2004,** *43,* 13532–13540.

40. Lovestone, S.; McLoughlin, D. M. Protein Aggregates and Dementia: Is There a Common Toxicity? *J Neurol Neurosur Psychiatry* **2002,** *72,* 152–161.

41. Cheon, M.; Hall, C. K.; Chang, I. Structural Conversion of Aβ17-42 Peptides from Disordered Oligomers to U-Shape Protofilaments via Multiple Kinetic Pathways. *PLoS Comput Biol* **2015,** *11,* e1004258.

42. Streltsov, V. A.; Varghese, J. N.; Masters, C. L.; Nuttall, S. D. Crystal Structure of the Amyloid-β P3 Fragment Provides a Model for Oligomer Formation in Alzheimer's Disease. *J Neurosci* **2011,** *31,* 1419–1426.

43. Danielsson, J.; Pierattelli, R.; Banci, L.; Graslund, A. High-Resolution NMR Studies of the Zinc-Binding Site of the Alzheimer's Amyloid β-Peptide. *FEBS Journal* **2007,** *274,* 46–59.

44. Jun, S.; Gillespie, J. R.; Shin, B. K.; Saxena, S. The Second Cu(II)-Binding Site in a Proton-Rich Environment Interferes with the Aggregation of Amylold-β(1-40) into Amyloid Fibrils. *Biochemistry* **2009,** *48,* 10724–10732.

45. Butterfield, D. A. Amyloid β-Peptide (1-42)-Induced Oxidative Stress and Neurotoxicity: Implications for Neurodegeneration in Alzheimer's Disease Brain. A Review. *Free Radical Res* **2002,** *36,* 1307–1313.

46. Hou, L. M.; Kang, I.; Marchant, R. E.; Zagorski, M. G. Methionine 35 Oxidation Reduces Fibril Assembly of the Amyloid Aβ-(1-42) Peptide of Alzheimer's Disease. *J Biol Chem* **2002,** *277,* 40173–40176.

47. Parthasarathy, S.; Yoo, B.; McElheny, D.; Tay, W.; Ishii, Y. Capturing a Reactive State of Amyloid Aggregates. *J Biol Chem* **2014,** *289,* 9998–10010.

48. Rambaran, R. N.; Serpell, L. C. Amyloid Fibrils: Abnormal Protein Assembly. *Prion* **2008,** *2,* 112–117.

49. Riek, R. The Three-Dimensional Structures of Amyloids. *Cold Spring Harb Perspect Biol* **2017,** *9,* a023572.

50. Stroud, J. C.; Liu, C.; Teng, P. K.; Eisenberg, D. Toxic Fibrillar Oligomers of Amyloid-β Have Cross-β Structure. *P Natl Acad Sci* **2012,** *109,* 7717–7722.

51. Al-Halifa, S.; Babych, M.; Zottig, X.; Archambault, D.; Bourgault, S. Amyloid Self-Assembling Peptides: Potential Applications in Nanovaccine Engineering and Biosensing. *Peptide Sci* **2019,** *111*.

52. Greenwald, J.; Riek, R. Biology of Amyloid: Structure, Function, and Regulation. *Structure* **2010,** *18,* 1244–1260.

53. Cheng, P. N.; Pham, J. D.; Nowick, J. S. The Supramolecular Chemistry of β-Sheets. *J Am Chem Soc* **2013,** *135,* 5477–5492.

54. Tsemekhman, K.; Goldschmidt, L.; Eisenberg, D.; Baker, D. Cooperative Hydrogen Bonding in Amyloid Formation. *Protein Sci* **2007,** *16,* 761–764.

55. Zheng, J.; Jang, H.; Ma, B.; Tsai, C. J.; Nussinov, R. Modeling the Alzheimer Aβ17-42 Fibril Architecture: Tight Intermolecular Sheet-Sheet Association and Intramolecular Hydrated Cavities. *Biophys J* **2007,** *93,* 3046–3057.

56. Lee, S. J.; Nam, E.; Lee, H. J.; Savelieff, M. G.; Lim, M. H. Towards an Understanding of Amyloid-β Oligomers: Characterization, Toxicity Mechanisms, and Inhibitors. *Chem Soc Rev* **2017,** *46,* 310–323.

57. Sengupta, U.; Nilson, A. N.; Kayed, R. The Role of Amyloid-β Oligomers in Toxicity, Propagation, and Immunotherapy. *EBioMedicine* **2016,** *6,* 42–49.

58. Viola, K. L.; Klein, W. L. Amyloid β Oligomers in Alzheimer's Disease Pathogenesis, Treatment, and Diagnosis. *Acta Neuropathol* **2015,** *129,* 183–206.

59. Arioz, C.; Wittung-Stafshede, P. Folding of Copper Proteins: Role of the Metal? *Q Rev Biophys* **2018,** *51*.

60. Kumar-Singh, S. Hereditary and Sporadic Forms of Aβ-Cerebrovascular Amyloidosis and Relevant Transgenic Mouse Models. *Int J Mol Sci* **2009,** *10,* 1872–1895.

61. Kummer, M. P.; Heneka, M. T. Truncated and Modified Amyloid-β Species. *Alzheimers Res Ther* **2014,** *6,* 28.

62. Smith, D. G.; Cappai, R.; Barnham, K. J. The Redox Chemistry of the Alzheimer's Disease Amyloid β Peptide. *Biochim Biophys Acta* **2007,** *1768,* 1976–1990.

63. Nelson, T. J. Alzheimer's Disease and Cholesterol. https://www.randombio.com/alzheimers.html (July 27, 2019).

64. Pedersen, J. T.; Chen, S. W.; Borg, C. B.; Ness, S.; Bahl, J. M.; Heegaard, N. H.; Dobson, C. M.; Hemmingsen, L.; Cremades, N.; Teilum, K. Amyloid-β and Alpha α-Synuclein Decrease the Level of Metal-Catalyzed Reactive Oxygen Species by Radical Scavenging and Redox Silencing. *J Am Chem Soc* **2016,** *138,* 3966–3969.

65. Plascencia-Villa, G.; Ponce, A.; Collingwood, J. F.; Arellano-Jimenez, M. J.; Zhu, X. W.; Rogers, J. T.; Betancourt, I.; Jose-Yacaman, M.; Perry, G. High-Resolution Analytical Imaging and Electron Holography of Magnetite Particles in Amyloid Cores of Alzheimer's Disease. *Sci Rep-UK* **2016,** *6*.

66. Boopathi, S.; Kolandaivel, P. Fe^{2+} Binding on Amyloid β-Peptide Promotes Aggregation. *Proteins* **2016,** *84,* 1257–1274.

67. Bousejra-ElGarah, F.; Bijani, C.; Coppel, Y.; Faller, P.; Hureau, C. Iron(II) Binding to Amyloid-β, the Alzheimer's Peptide. *Inorg Chem* **2011,** *50,* 9024–9030.

68. Ma, Q. F.; Hu, J.; Wu, W. H.; Liu, H. D.; Du, J. T.; Fu, Y.; Wu, Y. W.; Lei, P.; Zhao, Y. F.; Li, Y. M. Characterization of Copper Binding to the Peptide Amyloid-β(1-16) Associated with Alzheimer's Disease. *Biopolymers* **2006,** *83,* 20–31.

69. Zirah, S.; Kozin, S. A.; Mazur, A. K.; Blond, A.; Cheminant, M.; Segalas-Milazzo, I.; Debey, P.; Rebuffat, S. Structural Changes of Region 1-16 of the Alzheimer Disease Amyloid β-Peptide upon Zinc Binding and in Vitro Aging. *J Biol Chem* **2006,** *281,* 2151–2161.

70. Atwood, C. S.; Moir, R. D.; Huang, X. D.; Scarpa, R. C.; Bacarra, N. M. E.; Romano, D. M.; Hartshorn, M. K.; Tanzi, R. E.; Bush, A. I. Dramatic Aggregation of Alzheimer Aβ by Cu(II) Is Induced by Conditions Representing Physiological Acidosis. *J Biol Chem* **1998,** *273,* 12817–12826.

71. Derreumaux, P. Alzheimer's Disease Insights into Low Molecular Weight and Cytotoxic Aggregates from in Vitro and Computer Experiments Molecular Basis of Amyloid-β Protein Aggregation and Fibril Formation Preface. *Molec Med Medicin* **2013,** *7,* XVII–XIX.

72. Gamez, P.; Caballero, A. B. Copper in Alzheimer's Disease: Implications in Amyloid Aggregation and Neurotoxicity. *AIP Adv* **2015,** *5*.

73. Shivers, B. D.; Hilbich, C.; Multhaup, G.; Salbaum, M.; Beyreuther, K.; Seeburg, P. H. Alzheimer's Disease Amyloidogenic Glycoprotein: Expression Pattern in Rat Brain Suggests a Role in Cell Contact. *EMBO J* **1988,** *7,* 1365–1370.

74. Ueno, H.; Yamaguchi, T.; Fukunaga, S.; Okada, Y.; Yano, Y.; Hoshino, M.; Matsuzaki, K. Comparison between the Aggregation of Human and Rodent Amyloid β-Proteins in GM1 Ganglioside Clusters. *Biochemistry* **2014,** *53,* 7523–7530.

75. Syme, C. D.; Nadal, R. C.; Rigby, S. E. J.; Viles, J. H. Copper Binding to the Amyloid-β (Aβ) Peptide Associated with Alzheimer's Disease. Folding, Coordination Geometry, pH Dependence, Stoichiometry, and Affinity of Aβ-(1-28): Insights from a Range of Complementary Spectroscopic Techniques. *J Biol Chem* **2004,** *279,* 18169–18177.

76. Miller, Y.; Ma, B.; Nussinov, R. Polymorphism in Alzheimer Aβ Amyloid Organization Reflects Conformational Selection in a Rugged Energy Landscape. *Chem Rev* **2010,** *110,* 4820–4838.

77. Rasmussen, J.; Mahler, J.; Beschorner, N.; Kaeser, S. A.; Hasler, L. M.; Baumann, F.; Nystrom, S.; Portelius, E.; Blennow, K.; Lashley, T.; Fox, N. C.; Sepulveda-Falla, D.; Glatzel, M.; Oblak, A. L.; Ghetti, B.; Nilsson, K. P. R.; Hammarstrom, P.; Staufenbiel, M.; Walker, L. C.; Jucker, M. Amyloid Polymorphisms Constitute Distinct Clouds of Conformational Variants in Different Etiological Subtypes of Alzheimer's Disease. *P Natl Acad Sci USA* **2017,** *114,* 13018–13023.

78. Sachse, C.; Grigorieff, N.; Fandrich, M. Nanoscale Flexibility Parameters of Alzheimer Amyloid Fibrils Determined by Electron Cryo-Microscopy. *Angew Chem Int Edit* **2010,** *49,* 1321–1323.

79. Berhanu, W. M.; Alred, E. J.; Bernhardt, N. A.; Hansmann, U. H. E. All-Atom Simulation of Amyloid Aggregates. *Phys. Procedia* **2015,** *68,* 61–68.

80. Meisl, G.; Yang, X. T.; Frohm, B.; Knowles, T. P. J.; Linse, S. Quantitative Analysis of Intrinsic and Extrinsic Factors in the Aggregation Mechanism of Alzheimer-Associated Aβ-Peptide. *Sci Rep-UK* **2016,** *6*.

81. Zapadka, K. L.; Becher, F. J.; dos Santos, A. L. G.; Jackson, S. E. Factors Affecting the Physical Stability (Aggregation) of Peptide Therapeutics. *Interface Focus* **2017,** *7,* 20170030.

82. Sperling, R.; Mormino, E.; Johnson, K. The Evolution of Preclinical Alzheimer's Disease: Implications for Prevention Trials. *Neuron* **2014,** *84,* 608–622.

83. Atwood, C. S.; Moir, R. D.; Huang, X. D.; Scarpa, R. C.; Bacarra, N. M. E.; Romano, D. M.; Hartshorn, M. K.; Tanzi, R. E.; Bush, A. I. Dramatic Aggregation of Alzheimer Aβ by Cu(II) Is Induced by Conditions Representing Physiological Acidosis. *J Biol Chem* **1998,** *273,* 12817–12826.

84. Klug, G. M. J. A.; Losic, D.; Subasinghe, S. S.; Aguilar, M. I.; Martin, L. L.; Small, D. H. β-Amyloid Protein Oligomers Induced by Metal Ions and Acid pH Are Distinct from Those Generated by Slow Spontaneous Ageing at Neutral pH. *Eur J Biochem* **2003,** *270,* 4282–4293.

85. Gerber, H.; Wu, F.; Dimitrov, M.; Garcia Osuna, G. M.; Fraering, P. C. Zinc and Copper Differentially Modulate Amyloid Precursor Protein Processing by γ-Secretase and Amyloid-β Peptide Production. *J Biol Chem* **2017,** *292,* 3751–3767.

86. Lovell, M. A.; Robertson, J. D.; Teesdale, W. J.; Campbell, J. L.; Markesbery, W. R. Copper, Iron and Zinc in Alzheimer's Disease Senile Plaques. *J Neurol Sci* **1998,** *158,* 47–52.

87. Rana, M.; Sharma, A. K. Cu and Zn Interactions with Aβ Peptides: Consequence of Coordination on Aggregation and Formation of Neurotoxic Soluble Aβ Oligomers. *Metallomics* **2019,** *11,* 64–84.

88. Roberts, B. R.; Ryan, T. M.; Bush, A. I.; Masters, C. L.; Duce, J. A. The Role of Metallobiology and Amyloid-β Peptides in Alzheimer's Disease. *J Neurochem* **2012,** *120 Suppl 1,* 149–166.

89. Cheignon, C.; Tomas, M.; Bonnefont-Rousselot, D.; Faller, P.; Hureau, C.; Collin, F. Oxidative Stress and the Amyloid β Peptide in Alzheimer's Disease. *Redox Biol* **2018,** *14,* 450–464.

90. Yuan, Y.; Niu, F. L.; Liu, Y.; Lu, N. Zinc and Its Effects on Oxidative Stress in Alzheimer's Disease. *Neurol Sci* **2014,** *35,* 923–928.

91. Huang, W. J.; Zhang, X.; Chen, W. W. Role of Oxidative Stress in Alzheimer's Disease. *Biomed Rep* **2016,** *4,* 519–522.

92. Huang, X. D.; Atwood, C. S.; Hartshorn, M. A.; Multhaup, G.; Goldstein, L. E.; Scarpa, R. C.; Cuajungco, M. P.; Gray, D. N.; Lim, J.; Moir, R. D.; Tanzi, R. E.; Bush, A. I. The Aβ Peptide of Alzheimer's Disease Directly Produces Hydrogen Peroxide through Metal Ion Reduction. *Biochemistry* **1999,** *38,* 7609–7616.

93. Das, T. K.; Wati, M. R.; Fatima-Shad, K. Oxidative Stress Gated by Fenton and Haber Weiss Reactions and Its Association with Alzheimer's Disease. *Arch Neurosci* **2015,** *2*.

94. Tabner, B. J.; Mayes, J.; Allsop, D. Hypothesis: Soluble Aβ Oligomers in Association with Redox-Active Metal Ions Are the Optimal Generators of Reactive Oxygen Species in Alzheimer's Disease. *Int J Alzheimers Dis* **2010,** *2011,* 546380.

95. Uranga, R. M.; Salvador, G. A. Unraveling the Burden of Iron in Neurodegeneration: Intersections with Amyloid β Peptide Pathology. *Oxid Med Cell Longev* **2018,** 2850341.

96. Curtain, C. C.; Ali, F.; Volitakis, I.; Cherny, R. A.; Norton, R. S.; Beyreuther, K.; Barrow, C. J.; Masters, C. L.; Bush, A. I.; Barnham, K. J. Alzheimer's Disease Amyloid-β Binds Copper and Zinc to Generate an Allosterically Ordered Membrane-Penetrating Structure Containing Superoxide Dismutase-Like Subunits. *J Biol Chem* **2001,** *276,* 20466–20473.

97. Farooqui, A. A. Neurochemical Aspects of Alzheimer's Disease: Risk Factors, Pathogenesis, Biomarkers, and Potential Treatment Strategies. *Neurochemical Aspects of Alzheimer's Disease: Risk Factors, Pathogenesis, Biomarkers, and Potential Treatment Strategies* **2017,** 1–394.

98. Butterfield, D. A.; Sultana, R. Methionine-35 of Aβ(1-42): Importance for Oxidative Stress in Alzheimer Disease. *J Amino Acids* **2011,** *2011,* 198430.

99. Chauhan, V.; Chauhan, A. Oxidative Stress in Alzheimer's Disease. *Pathophysiology* **2006,** *13,* 195–208.

100. Hou, L.; Shao, H.; Zhang, Y.; Li, H.; Menon, N. K.; Neuhaus, E. B.; Brewer, J. M.; Byeon, I. J.; Ray, D. G.; Vitek, M. P.; Iwashita, T.; Makula, R. A.; Przybyla, A. B.; Zagorski, M. G. Solution NMR Studies of the Aβ(1-40) and Aβ(1-42) Peptides Establish That the Met35 Oxidation State Affects the Mechanism of Amyloid Formation. *J Am Chem Soc* **2004,** *126,* 1992–2005.

101. Meisl, G.; Yang, X.; Frohm, B.; Knowles, T. P.; Linse, S. Quantitative Analysis of Intrinsic and Extrinsic Factors in the Aggregation Mechanism of Alzheimer-Associated Aβ-Peptide. *Sci Rep* **2016,** *6,* 18728.

102. Fandrich, M.; Nystrom, S.; Nilsson, K. P. R.; Bockmann, A.; LeVine, H., 3ed; Hammarstrom, P. Amyloid Fibril Polymorphism: A Challenge for Molecular Imaging and Therapy. *J Intern Med* **2018,** *283,* 218–237.

103. Yates, E. A.; Legleiter, J. Preparation Protocols of Aβ(1-40) Promote the Formation of Polymorphic Aggregates and Altered Interactions with Lipid Bilayers. *Biochemistry* **2014,** *53,* 7038–7050.

104. Colvin, M. T.; Silvers, R.; Ni, Q. Z.; Can, T. V.; Sergeyev, I.; Rosay, M.; Donovan, K. J.; Michael, B.; Wall, J.; Linse, S.; Griffin, R. G. Atomic Resolution Structure of Monomorphic Aβ(42) Amyloid Fibrils. *J Am Chem Soc* **2016,** *138,* 9663–9674.

105. Schutz, A. K.; Vagt, T.; Huber, M.; Ovchinnikova, O. Y.; Cadalbert, R.; Wall, J.; Guntert, P.; Bockmann, A.; Glockshuber, R.; Meier, B. H. Atomic-Resolution Three-Dimensional Structure of Amyloid β Fibrils Bearing the Osaka Mutation. *Angew Chem Int Edit* **2015,** *54,* 331–335.

106. Claridge, S. A.; Thomas, J. C.; Silverman, M. A.; Schwartz, J. J.; Yang, Y. L.; Wang, C.; Weiss, P. S. Differentiating Amino Acid Residues and Side Chain Orientations in Peptides Using Scanning Tunneling Microscopy. *J Am Chem Soc* **2013,** *135,* 18528–18535.

107. Crommie, M. F.; Lutz, C. P.; Eigler, D. M. Confinement of Electrons to Quantum Corrals on a Metal-Surface. *Science* **1993,** *262,* 218–220.

108. Niu, L.; Ma, X. J.; Liu, L.; Mao, X. B.; Wu, D. X.; Yang, Y. L.; Zeng, Q. D.; Wang, C. Molecularly Tuned Peptide Assemblies at the Liquid-Solid Interface Studied by Scanning Tunneling Microscopy. *Phys Chem Chem Phys* **2010,** *12,* 11683–11687.

109. Tanaka, H.; Kawai, T. Partial Sequencing of a Single DNA Molecule with a Scanning Tunnelling Microscope. *Nat Nanotechnol* **2009,** *4,* 518–522.

110. Wang, J. H.; Zhang, L.; Hu, C.; Liu, Q. S.; Hou, Y. B.; Zhang, X.; Lu, Q. Y. Sub-Molecular Features of Single Proteins in Solution Resolved with Scanning Tunneling Microscopy. *Nano Res* **2016,** *9,* 2551–2560.

111. Weiss, P. S. Functional Molecules and Assemblies in Controlled Environments: Formation and Measurements. *Acc Chem Res* **2008,** *41,* 1772–1781.

112. Yugay, D.; Goronzy, D. P.; Kawakami, L. M.; Claridge, S. K.; Song, T. B.; Yan, Z. B.; Xie, Y. H.; Gilles, J.; Yang, Y.; Weiss, P. S. Copper Ion Binding Site in β-Amyloid Peptide. *Nano Lett* **2016,** *16,* 6282–6289.

113. Hornyak, G. L.; Peschel, S.; Sawitowski, T.; Schmid, G. TEM, STM and AFM as Tools to Study Clusters and Colloids. *Micron* **1998,** *29,* 183–190.

114. Bayburt, T.; Carlson, J.; Godfrey, B.; Shank-Retzlaff, M.; Sligar, S. G., Chapter 12 - Structure, Behavior, and Manipulation of Nanoscale Biological Assemblies. In *Handbook of Nanostructured Materials and Nanotechnology*, Nalwa, H. S., Ed. Academic Press: 2000; Vol. 5, pp 637–710.

115. Frenken, J.; Groot, I., Chapter 1 - Live Observations of Catalysts Using High-Pressure Scanning Probe Microscopy. In *Operando Research in Heterogeneous Catalysis*, Frenken, J.; Groot, I., Eds. Springer International Publishing Switzerland: 2017; pp 1–30.

116. Nasrollahzadeh, M.; Atarod, M.; Sajjadi, M.; Sajadi, S. M.; Issaabadi, Z., Chapter 6 - Plant-Mediated Green Synthesis of Nanostructures: Mechanisms, Characterization, and Applications. In *Interface Science and Technology*, Nasrollahzadeh, M.; Sajadi, S. M.; Sajjadi, M.; Issaabadi, Z.; Monireh Atarod, Eds. Elsevier: 2019; Vol. 28, pp 199–322.

117. Han, P.; Mantooth, B. A.; Sykes, E. C. H.; Donhauser, Z. J.; Weiss, P. S. Benzene on Au {111} at 4 K: Monolayer Growth and Tip-Induced Molecular Cascades. *J Am Chem Soc* **2004,** *126,* 10787–10793.

118. Kumar, A. S.; Ye, T.; Takami, T.; Yu, B. C.; Flatt, A. K.; Tour, J. M.; Weiss, P. S. Reversible Photo-Switching of Single Azobenzene Molecules in Controlled Nanoscale Environments. *Nano Lett* **2008,** *8,* 1644–1648.

119. Preuss, P. A Close Look: Exploring the Mystery of the Surface. https://www2.lbl.gov/Science-Articles/Archive/STM-under-pressure.html (July 30, 2019).

120. Stout, K. J.; Blunt, L., Part II - Instruments and Measurement Techniques of Three-Dimensional Surface Topography. In *Three Dimensional Surface Topography*, Stout, K. J.; Blunt, L., Eds. Butterworth-Heinemann: 2000; pp 19–94.

121. Guo, H.; Zhang, J., 11 - Scanning Probe Microscopy (SPM) of Epitaxial Oxide Thin Films. In *In Woodhead Publishing Series in Electronic and Optical Materials, Epitaxial Growth of Complex Metal Oxides*, Koster, G.; Huijben, M.; Rijnders, G., Eds. Woodhead Publishing: 2015; pp 295–328.

122. Hansma, P. K.; Tersoff, J. Scanning Tunneling Microscopy. *J Appl Phys* **1987,** *61,* R1–R23.

123. MicroscopeMaster. The Scanning Tunneling Microscope (STM). https://www.microscopemaster.com/scanning-tunneling-microscope.html (July 30, 2019).

124. Yee, S. Design of a Scanning Tunneling Microscope. Undergraduate Honors Thesis The Ohio State University, 2017.

125. Chi, Q. J.; Farver, O.; Ulstrup, J. Long-Range Protein Electron Transfer Observed at the Single-Molecule Level: In Situ Mapping of Redox-Gated Tunneling Resonance. *P Natl Acad Sci USA* **2005,** *102,* 16203–16208.

126. Miller, Y.; Ma, B. Y.; Nussinov, R. Metal Binding Sites in Amyloid Oligomers: Complexes and Mechanisms. *Coordin Chem Rev* **2012,** *256,* 2245–2252.

127. Barrio, M. d.; Borghesani, V.; Hureau, C.; Faller, P., Chapter 14 - Metal-Binding to Amyloid-β Peptide: Coordination, Aggregation, and Reactive Oxygen Species Production. In *Biometals in Neurodegenerative Diseases: Mechanisms and Therapeutics*, White, A. R.; Aschner, M.; Costa, L. G.; Bush, A. I., Eds. Academic Press: 2017; pp 265–281.

CHAPTER 2

Copper Ion Binding Site in β-Amyloid Peptide

2.1 Introduction

Alzheimer's disease (AD) is a worldwide health problem and the third most financially costly disease in the U.S. and Europe.[1] The dominant symptom of AD is anterograde amnesia and 60−80% of dementing illness is caused by AD.[2] A hallmark of AD is the aggregation of β-amyloid peptides (Aβ). Nevertheless, the body of knowledge around the disease pathogenesis is limited, the etiology remains poorly understood, and no curative interventions are available. It has been shown that people with AD exhibit abnormally high concentrations of transition metal ions (Cu^{2+} and Zn^{2+}) in Aβ aggregates and synaptic areas of the brain.[3,4] Fu *et al.* studied copper regulatory genes, in the study he and coworkers showed that there is a correlation between age and copper production while Singh *et al.* based on mouse studies showed that abnormal copper levels influence Aβ production and neuroinflammation.[5,6] Nonetheless, the significance of Aβ interaction with metal ions for the disease process remains largely unexplored, and there remains no cure for AD. Understanding the structure(s) of Aβ peptides, their interactions with transition metals, and more precise definitions of the metal-peptide binding sites promise improved insight into AD and may open new avenues for treatment.

Aβ oligomers are considered to be neurotoxic through a variety of mechanisms, that is, interactions with cell membranes and the production of reactive oxygen species.[7−9] The pathway of Aβ neurotoxicity remains unknown and is the subject of active research. In prior work, Aβ has been shown to bind Cu^{2+} ions in 1:1 stoichiometric ratios in the vicinity of the N-terminus.[10] A second low-affinity binding site has also been suggested due to the binding of Cu^{2+} to Aβ in 1:2 stoichiometric ratios in the vicinity of the C-terminus.[10,11] The structure and the binding site of Aβ oligomers in the presence of metal ions have been extensively studied using nuclear magnetic resonance,[14] X-ray absorption spectroscopy,[12,15] Fourier transform infrared spectroscopy,[13]

electron paramagnetic resonance,[16] and atomic force microscopy.[17,18] However, there is a paucity of experimental data with sub-molecular resolution because identifying exact amino acid involvement in metal ion binding is challenging due to the high mechanical and conformational flexibility of Aβ as well as the dramatic changes in conformation of the peptide based on metal ion valence.[5,19,20]

Previously, we have demonstrated the ability to resolve sub-molecular structures of biological molecules and to differentiate between side chains of individual amino acids and their orientations using scanning tunneling microscopy (STM) and related spectroscopic imaging methods.[21] In this study, we report structural elucidation of the first 16 amino acids (1−16) of the full length Aβ and its structural variation in the presence ($A\beta_{1-16}$-Cu^{2+}) and the absence ($A\beta_{1-16}$) of Cu^{2+} ions via STM, surface-enhanced Raman spectroscopy (SERS), and circular dichroism (CD). We chose Cu^{2+} for this study due to its biological significance in AD.[13,22] Although $A\beta_{1-16}$ has been reported as a disordered region of Aβ and therefore is often *omitted* from computational studies,[23−27] our findings indicate that upon co-deposition of Cu^{2+} and $A\beta_{1-16}$ on highly oriented pyrolytic graphite (HOPG), it laminates into structured β-sheet domains. We targeted this segment because preliminary data on $A\beta_{1-42}$ indicated binding of Cu^{2+} in this region.[10,13,18] Previous reports on the binding site of Cu^{2+} in this portion of the peptide are conflicting. Li and co-workers, based primarily on nuclear magnetic resonance (NMR) measurements, report the involvement of residues His6, His13, His 14, and Tyr10 in binding in $A\beta_{1-16}$, whereas Viles and co-workers, using a combination of NMR measurements and electron paramagnetic resonance (EPR) measurements, found that His13 is crucial for binding in $A\beta_{1-28}$ and there are indications of the involvement of His6 and His14, but not Tyr10.[28,29] Furthermore, these reports rely on conventional ensemble (*i.e.*, averaging) measurements (NMR and EPR), whereas STM can

provide definitive real-space images of non-crystalline, nonperiodic, and even dilute structures.[30] These results could significantly enhance our understanding of the biology of Aβ peptides *in vivo* and their morphological changes due to interactions with the synaptic cell membrane.[31–33] Most importantly, on the basis of the STM image analysis of the length and position of the protruding features, we determine and elucidate the specific interactions and binding of Cu^{2+} with $A\beta_{1-16}$. Here, we show that Cu^{2+} ions participate in interstrand $A\beta_{1-16}$ binding by coordinating with the two histidine residues at positions 13 and 14 (His13 and His14) on adjacent strands, and not intrastrand binding as had been hypothesized previously.[16,19,20]

2.2 Circular Dichroism

We used circular dichroism (CD) to determine whether Cu^{2+} ion binding onto $A\beta_{1-16}$ occurs readily in solution. In Figure 2.1, two bands (negative band at 197 nm and positive band at 222 nm) indicate that the polyproline type II (PPII) helix secondary structure conformation appears in the CD spectra of $A\beta_{1-16}$ at pH 7.4. The PPII helix structure is commonly found in many proteins in unfolded states.[34,35] The addition of Cu^{2+} to the solution decreased the CD spectra intensity in both bands. This indicates that Cu^{2+} weakens the PPII helical conformation and induces a partial β-sheet conformation in the peptide.[36,37] Because of its hydrophilicity, $A\beta_{1-16}$ is able to form hydrogen bonds with surrounding water molecules, which stabilizes the structure of the PPII helix.[34,38] A decrease in the number of water molecules around the PPII helix backbone causes the peptide to change its conformation from a PPII helix to a β-sheet.[39] Hence, the presence of Cu^{2+} around $A\beta_{1-16}$ may not only alter the $A\beta_{1-16}$ structure by binding but also cause the peptide to undergo a conformational change from a helix to a β-sheet by displacing water molecules around the peptide backbone.[40–43] The latter process is reported to be

highly entropically favorable.[39,40] Though CD data alone do not enable making definitive structural assignments, they do indicate that structural changes occur upon binding Cu^{2+}.

2.3 Surface-Enhanced Raman Spectroscopy

The challenge of many infrared spectroscopy (IR) techniques when used to study biomolecular conformation on surfaces is their limited ability to investigate the structures of biomolecules at low concentrations.[44] An additional challenge for peptides and proteins is that the amide bands, which are responsible for the secondary structure, are located in the same region as the strong absorption band of water.[45] The infrared spectroscopy dependence on concentration imposes a significant barrier to studying amyloid peptides because they exhibit structural polymorphism, which is greatly influenced by concentration.[42,46] To overcome the above-mentioned challenges of IR techniques, and to stay consistent with $A\beta_{1-16}$ concentrations used throughout the scanning probe microscopy experiments, surface-enhanced Raman spectroscopy (SERS)[47] was employed to study conformational changes of $A\beta_{1-16}$ in the presence and absence of Cu^{2+}. Furthermore, to increase the intensity of the SERS signal, specialized platforms that exhibit large electromagnetic enhancements ($\sim 10^{14}$) have been used, as shown in Figure 2.2a.[48–50] Surface-enhanced Raman spectra for $A\beta_{1-16}$ and $A\beta_{1-16}$-Cu^{2+} are shown in Table 2.1 and Figure 2.2b. Changes in the secondary structure of $A\beta_{1-16}$ upon addition of Cu^{2+} ions were assessed based on displacement and intensity of the amide bands and the C−H bending vibrations of the peptide. The Amide I band (1610−1700 cm^{-1})[51,52] was not resolved by SERS due to overlap with the strong G band ∼1585 cm^{-1},[53,54] which comes from the graphene coating of the substrate surface (Figure 2.2). Because of its weak Raman activity there is little information available about the Amide II band,[55–58] yet a few reports mention that its location at

~1529 cm^{-1} is associated with a β-sheet structure.[59,60] The Amide III band (1200−1340 cm^{-1}) showed a strong signal at ~1249 cm^{-1}, indicative of $A\beta_{1-16}$ forming either a hydrated β-sheet[61] or a PPII type helical structure[62−64] on the surface. The band at 1449 cm^{-1}, present in the $A\beta_{1-16}$ sample and absent in the $A\beta_{1-16}$-Cu^{2+} sample, belongs to the C−H bending mode vibration of the peptide.[65−68] Increased C−H vibrations in $A\beta_{1-16}$ indicate the lack of intermolecular hydrogen bonding within the peptide; together with increased amide band intensities, it demonstrates that $A\beta_{1-16}$ on the surface is more disordered than $A\beta_{1-16}$-Cu^{2+}.

2.4 Scanning Tunneling Microscopy

$A\beta_{1-16}$ is typically a disordered and hydrophilic portion of an extracellular domain of Aβ.[23,24,26,68] Because it is a disordered region it has often been omitted from computational studies.[23−27] However, we show here that upon $A\beta_{1-16}$ deposition on HOPG, individual peptide chains laminate into structured β-sheet domains (Figure 2.3). Previous reports indicate that Aβ has a parallel β-sheet arrangement with amino acids spacings of 0.325 nm.[31,69] For our image analysis, we assumed the same parallel β-sheet arrangement for $A\beta_{1-16}$. The average scanned length of $A\beta_{1-16}$ is 5.2 ± 0.4 nm; this value is consistent with the ideal $A\beta_{1-16}$ length of 4.9 nm. In addition, we noticed that $A\beta_{1-16}$ has higher structural polymorphism, with the strands' length being less uniform, than that of $A\beta_{1-16}$-Cu^{2+} (Figure 2.4). These STM studies relied on the deposition from solution of $A\beta_{1-16}$ raising the question of whether there are surface-induced structural changes. Previously, our group has shown that the peptide-surface interactions are relatively small in comparison to the peptide−peptide interactions within the assembly.[21] Furthermore, the transition from the hydrophilic regime to the hydrophobic HOPG surface may mimic the interaction of $A\beta_{1-16}$ with the cellular membrane in physiological conditions. Based on

our measurements, $A\beta_{1-16}$ and $A\beta_{1-16}$-Cu^{2+} vary significantly from one another in terms of their interstrand separations (Figure 2.5b). Free $A\beta_{1-16}$ peptides have an interstrand separation of 5.8 ± 0.4 Å; this value differs greatly from the interstrand separation in $A\beta_{1-16}$-Cu^{2+}, which is 4.6 ± 0.3 Å. The latter is in a good agreement with Aβ (Figure 2.6a) and earlier reported literature values for β-sheet separation, which is 4.5−5 Å.[21,69−74] A large interstrand separation value for $A\beta_{1-16}$, together with CD and SERS results, indicates that peptides in that system lack intermolecular hydrogen bonding and are either in a PPII helical configuration or are intrinsically disordered. Intrinsically disordered β-sheets have been identified and previously reported for amyloidogenic peptides.[75−77] However, to our knowledge, there are no structural reports of the interstrand separation for either PPII helices or intrinsically disordered β-sheets. Thus, we cannot determine which structural state the free $A\beta_{1-16}$ peptides have when deposited on HOPG; all structural characterizations in this study indicate that $A\beta_{1-16}$-Cu^{2+} peptides are in a β-sheet arrangement. This arrangement of $A\beta_{1-16}$-Cu^{2+} is apparently triggered by copper ion binding between adjacent $A\beta_{1-16}$ strands. Intercalation of copper ions between strands would cause neighboring β-strands to come into closer contact due to His^{+}−Cu^{2+} interactions, which are based on the repulsive electrostatic and attractive cation-π interactions between Cu^{2+} and imidazole rings.[78,79] Topographic examination of the $A\beta_{1-16}$-Cu^{2+} lamellae displayed almost evenly arranged protruding features from both sides of β -sheet boundaries, with one side being more uniform than the other. Such features were present only in $A\beta_{1-16}$-Cu^{2+} and were absent in $A\beta_{1-16}$ (without Cu^{2+}) (Figures 2.7 and 2.8; many areas of four independently prepared samples of each were measured; for each distance, the average, standard deviation, and number of measurements used are reported). Both the total lengths of the strands and the distances of the protruding features from both β-sheet boundaries have been measured (Figure 2.9). The measured distance

of the nonperiodic, site-specific protruding features from the boundary was 0.9 ± 0.1 nm, which corresponds to the protruding features being two to three amino acids away from the β-sheet boundary (Figure 2.5c,d). The only possible amino acids in the strand, which are two to three amino acids away from the ends of the peptide and can participate in Cu^{2+} binding, are His13 and His14 residues. Adjacent positions of His13 and His14 amino acids in the $A\beta_{1-16}$ strand make them unique in the sequence because only they can participate in binding copper between the strands. Therefore, based on STM image analysis of the protruding features, our results support the conclusion that Cu^{2+} ions bind to His13 and His14 residues forming a histidine brace between two strands. We did not observe nonsite specific protruding features, suggesting that there are no other Cu^{2+} ions bound on the surface. The measured distance of the more uniform protruding features from the boundary was 1.0 ± 0.1 nm, which corresponds to the protruding features being three amino acids residues away from the β-sheet boundary. Phenylalanine at the fourth position (Phe4) in the strand is three amino acids away from the beginning of the $A\beta_{1-16}$ strand. We infer that π stacking between the Phe4 ring and graphite leads it to protrude evenly throughout the whole β -sheet domain. Several previous computational and experimental studies have suggested that neighboring His residues in amyloid peptides or amyloid-like proteins participate in interstrand metal ion binding.[80−86] However, this type of metal ion interaction with Aβ has never previously been observed directly. In this study, based on the length and the position of protruding features of copper ions within $A\beta_{1-16}$ peptides, we show that copper ions participate in interstrand $A\beta_{1-16}$ binding by coordinating with two His residues from adjacent stands. In conclusion, metal ions are enriched in the β-amyloid aggregates typically found in patients with Alzheimer' s dementia, yet their functional role is largely unexplored. Here, we have identified the primary binding site of Cu^{2+} ions to $A\beta_{1-16}$ and have clarified how such Cu^{2+}

ions facilitate interstrand binding, implicating metal ions as critical stabilizers of pathogenic β-amyloid assemblies. Circular dichroism provided key insights into how Cu^{2+} ions interact with the $A\beta_{1-16}$ peptide in solution; inducing a conformational change from a disordered type II helix secondary structure to a secondary structure with β-sheet character. Based on strong C−H bending vibrations and higher PPII helical character in $A\beta_{1-16}$, SERS demonstrated that $A\beta_{1-16}$ peptides on the surface are less densely packed and more disordered than $A\beta_{1-16}$-Cu^{2+}. Finally, scanning tunneling microscopy enabled us to deduce the structural changes of $A\beta_{1-16}$ upon copper binding. In summary, $A\beta_{1-16}$ has a higher structural polymorphism than $A\beta_{1-16}$-Cu^{2+}, as indicated by the range in $A\beta_{1-16}$ strand lengths. When compared to $A\beta_{1-16}$-Cu^{2+}, strands in $A\beta_{1-16}$ are less uniform in the length, suggesting that they sometimes fold in upon themselves. Large interstrand separation in $A\beta_{1-16}$ indicate that such peptides lack hydrogen bonding between adjacent strands. Thus, on a surface, $A\beta_{1-16}$ laminates into either intrinsically disordered β-sheets or into a PPII-type helix. In contrast, our data provide strong evidence that $A\beta_{1-16}$-Cu^{2+} has a smaller interstrand separation and laminates into β-sheets on a surface. We conclude that the interaction of the $A\beta_{1-16}$ peptide with the Cu^{2+} ions is the driving force for this more ordered formation. Lastly, we observed features as apparent protrusions in STM images at the ends of the β-sheet boundaries in $A\beta_{1-16}$-Cu^{2+} but not in $A\beta_{1-16}$. These features are localized 2−3 amino acids away from the β -sheet boundaries, pointing to His13 and His14 as critical binding partners. The only possible amino acids that could participate in copper ion binding that are 2−3 amino acids away from the β-sheet boundary are His13 and His14. These data support the assignment that His13 and His14 represent primary binding sites for the copper ions, creating an interstrand histidine brace. β-Amyloid has been implicated as a primary pathogenic factor in Alzheimer's disease and the current work links metal ions, specifically copper, to the formation

and structure of the β-amyloid aggregates that are the signature of this disease. Understanding the structural features of β-amyloid and how it interacts and coassembles with other elements can open the door to studies of β-amyloid aggregates in the tissue environment and the identification of "drugable" targets that ultimately shape the deposition of neurotoxic peptides. Further, blocking metal ion binding could be utilized to destabilize the indigestible β-amyloid clusters in neurodegeneration. (NB—As noted above, there may also be Cu^{2+} binding sites near the C-terminus of $A\beta_{1-42}$.) This report establishes the capability of scanning tunneling microscopy as a methodology to determine structural characteristics and critical interaction sites in biologically relevant systems where traditional techniques that average or extract only periodic portions of structures have been unsuccessful.[12,21,30,31,72,87,88]

2.5 Materials and Methods

2.5.1 Scanning Probe Microscopy and Surface-Enhanced Raman Spectroscopy Sample Preparation

Solutions were prepared in a glass vial with a final total volume of 400 μL for both samples ($A\beta_{1-16}$ and $A\beta_{1-16}$-Cu^{2+}). $A\beta_{1-16}$ molarity was kept constant between samples: 2.5×10^{-7} M. In the $A\beta_{1-16}$-Cu^{2+} samples, the final Cu^{2+} concentration was 2.5×10^{-5} M. The $A\beta_{1-16}$ solution mixture was prepared by mixing 20 μL of phosphate-buffered saline at pH 7.4, 200 μL acetonitrile (Sigma-Aldrich Fluka Analytical, St. Louis, MO, purity >99.9%), 179 μL double-distilled water, and 1 μL of $A\beta_{1-16}$ (American Peptide Company, Inc., Sunnyvale, CA, 95.4% purity). Before depositing $A\beta_{1-16}$ solution onto HOPG (SPI supplies, size: 10 mm × 10 mm × 2 mm) the surface of HOPG was cleaved with scotch tape to clean the surface and to eliminate any preexisting flakes. $A\beta_{1-16}$ solution was deposited onto HOPG for 1 min and blown off using nitrogen gas. The $A\beta_{1-16}$-Cu^{2+} solution mixture was prepared by mixing 20 μL phosphate-buffered saline at pH 7.4, 10 μL Cu^{2+} (Sigma-Aldrich Fluka Analytical, Copper Standard for ICP 1001 ± 2 mg/L), 200 μL acetonitrile, 169 μL double-distilled water, and 1 μL $A\beta_{1-16}$ solution.

2.5.2 Scanning Tunneling Microscopy Measurements

For STM measurements, a mechanically cut Pt−Ir (80%−20%) (Goodfellow Corp., Oakdale, PA) wire was used as the STM tip. The STM observations were carried out on a Pico SPM microscope head (Molecular Imaging, now Agilent, Santa Clara, CA) controlled by a low noisecontroller (RHK Model R9, RHK Technology, Troy, MI) under ambient conditions.

2.5.3 Atomic Force Microscopy Measurements

All AFM measurements were performed under ambient conditions at the California NanoSystems Institute (NanoPico Characterization laboratory) using a Bruker High-Speed MultiMode 8 with ScanAsyst-HR instrument in peak force tapping mode with Bruker Nanoprobe (Model MPP-21100-10, Part RFESP, and nominal force constant 3 N/m).

2.5.4 Scanning Tunneling Microscopy and Atomic Force Microscopy Image Processing

Both STM and AFM images were processed by GWYDDION[88] (free scanning probe microscopy data analysis software). Scratch artifacts were removed from STM images by using MATLAB (Mathworks, Natick, MA) unstripping code (see Appendix A1).

2.5.5 Surface-Enhanced Raman Spectroscopy Measurements

Substrates were prepared as described previously.[48] Briefly, fabrication involved bottom-up templating technology where spin coating and hitting polystyrene (PS) film created PS spheres on Si/SiO_2. Polystyrene spheres were used as mask for further gold nanopyramids fabrication. Final gold nanopyramids were approximately 200 nm × 200 nm in size. Graphene was transferred on gold nanopyramids substrates as a final step by chemical vapor deposition. A Renishaw inVia Raman system (Renishaw, IL) operating under ambient conditions was employed for Raman analysis. A 632.8 nm He−Ne laser was used as the Raman excitation source to match the resonant wavelength of the substrate. Laser power and beam diameter were ∼5 mW and ∼1 μm, respectively. Spectra were acquired by mapping the substrate surface. Each measurement was a convolution of 20 sweeps in the wavelength range of interest with a set integration time of 1 s.

2.5.6 Circular Dichroism Sample Preparation

Solutions were prepared in a glass vial with final total volume of 300 μL for both samples ($A\beta_{1-16}$ and $A\beta_{1-16}$-Cu^{2+}). $A\beta_{1-16}$ molarity kept constant between samples: 7.5×10^{-5} M. In $A\beta_{1-16}$-Cu^{2+} samples, the final Cu^{2+} concentration was 2.5×10^{-5} M. The $A\beta_{1-16}$ solution mixture was prepared by mixing 15 μL of phosphate-buffered saline at pH 7.4, 52.5 μL acetonitrile, 7.5 μL double-distilled water, and 225 μL $A\beta_{1-16}$ solution. The $A\beta_{1-16}$-Cu^{2+} solution mixture was prepared by mixing 15 μL of phosphate-buffered saline at pH 7.4, 7.5 μL of Cu^{2+} solution, 52.5 μL acetonitrile, and 225 μL $A\beta_{1-16}$ solution.

2.5.7 Circular Dichroism Measurements

Circular dichroism (CD) spectra of $A\beta_{1-16}$ and $A\beta_{1-16}$-Cu^{2+} in the wavelength region from 250 to 190 nm were measured at room temperature using a JASCO (Easton, MD) J-715 Circular Dichrosim Spectrophotometer and cell with 1 mm path length. The spectra were recorded with a step resolution of 0.2 nm, scan speed 20 nm/min, bandwidth of 1 nm, sensitivity of 50 mdeg ellipticity, and response 4 s with ten spectra collected and averaged per sample.

2.5.8 Surface-Enhanced Raman Spectroscopy and Circular Dichroism Spectral Analyses

Both SERS and CD spectral analyses, peak assignments, and plotting were carried out using OriginPro software and Microsoft Office Excel.

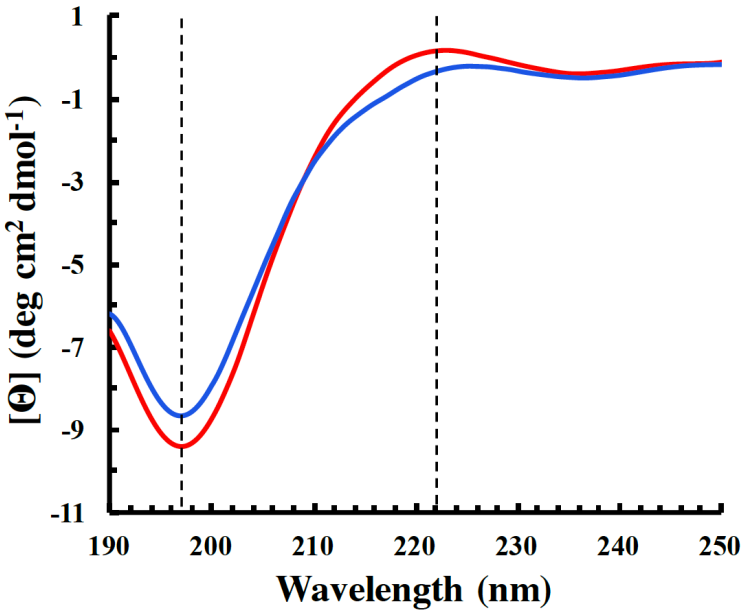

Figure 2.1. Circular dichroism spectrum of $A\beta_{1-16}$ at pH 7.4 with the negative band at 197 nm and the positive band at 222 nm. $A\beta_{1-16}$-Cu^{2+} (blue) and $A\beta_{1-16}$ (red).

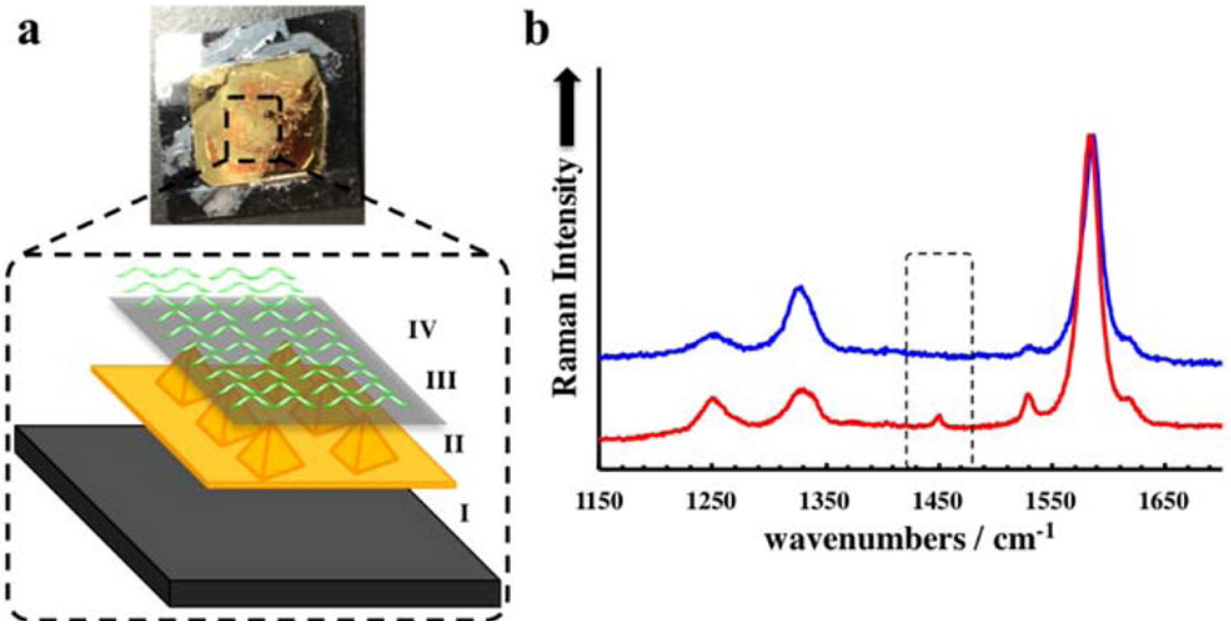

Figure 2.2. Substrate arrangement and results of the surface-enhanced Raman spectroscopy experiments. (a) (Top) Photograph of the substrate used in SERS experiments. (Bottom) Schematic of the substrate and its components: (I) silicon wafer, (II) gold film with gold pyramids, (III) graphene, (IV) deposited $A\beta_{1-16}$ peptides. (b) SERS spectrum of $A\beta_{1-16}$-Cu^{2+} (blue) and $A\beta_{1-16}$ (red). The black dashed box (~1449 cm^{-1}) indicates the C–H bending mode that signifies $A\beta_{1-16}$ peptides lack structural homogeneity in comparison to $A\beta_{1-16}$-Cu^{2+}.

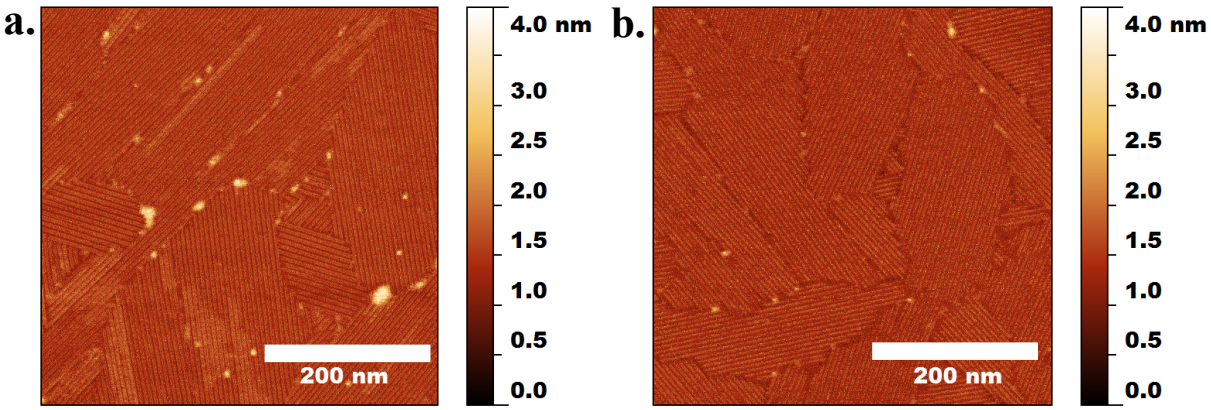

Figure 2.3. Atomic force microscopy images of $A\beta_{1-16}$ at pH 7.4 deposited on HOPG, 500 nm × 500 nm (a) $A\beta_{1-16}$-Cu^{2+} (b) $A\beta_{1-16}$. Protrusions indicate $A\beta_{1-16}$ aggregates. Measurements were done to test if we continuously produced laminated monolayers of $A\beta_{1-16}$ and $A\beta_{1-16}$-Cu^{2+} over large surface areas.

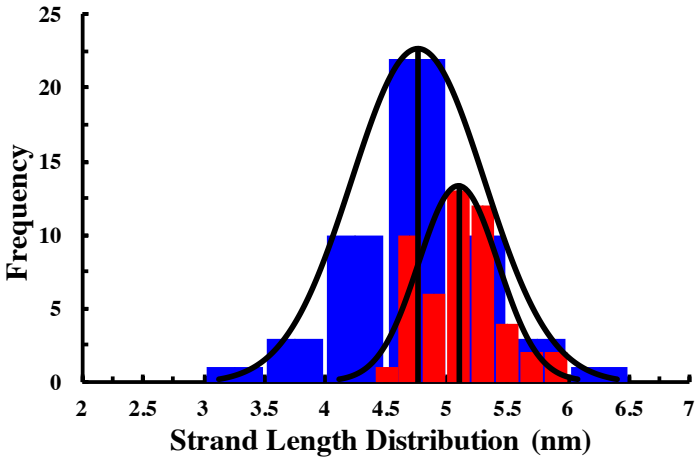

Figure 2.4. Distributions of the strand lengthss for $A\beta_{1-16}$ (red) and $A\beta_{1-16}$-Cu^{2+} (blue) with bin numbers 7 and 8, and mean 4.76 nm and 5.1 nm, respectively. Sample size: 50.

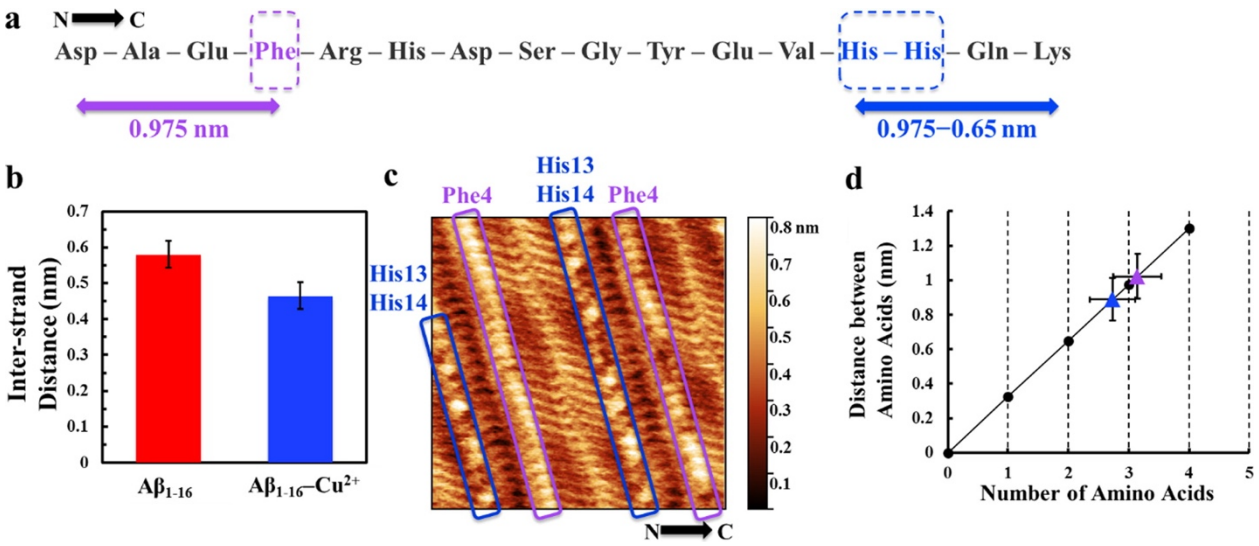

Figure 2.5. (a) $A\beta_{1–16}$ sequence with the highlighted Phe4 and His13/His14 amino acids. Ideal distance from β-sheet boundary to Phe4 is 0.975 nm (purple arrow), to His13 is 0.975 nm (blue arrow), and to His14 is 0.65 nm (blue arrow). (b) Average interstrand separation bar graph for $A\beta_{1–16}$ vs $A\beta_{1–16}$-Cu^{2+}. Interstrand separation for $A\beta_{1–16}$ is 5.8 ± 0.4 Å, and $A\beta_{1–16}$-Cu^{2+} is 4.6 ± 0.3 Å (from n = 42 and 120 measurements, respectively). (c) Scanning tunneling microscopy image of $A\beta_{1–16}$-Cu^{2+}. The regular protruding features in the purple box indicate the positions of the Phe4, whereas irregular protruding features in the blue box indicate the positions of His13/His14 binding Cu^{2+} in the peptide β-sheet assembly. Imaging conditions: V_{sample} = 0.55 V, I_{tunnel} = 10 pA. (d) Average distance between amino acids with the corresponding number of amino acids to the specified distance. Phe4 (purple) distance, 1.0 ± 0.1 nm; number of amino acids, 3.1 ± 0.4; His13/His14 (blue) distance, 0.9 ± 0.1 nm; number of amino acids, 2.7 ± 0.4; and ideal distance vs number of amino acids (black) (from n = 92 and 145 measurements, respectively).

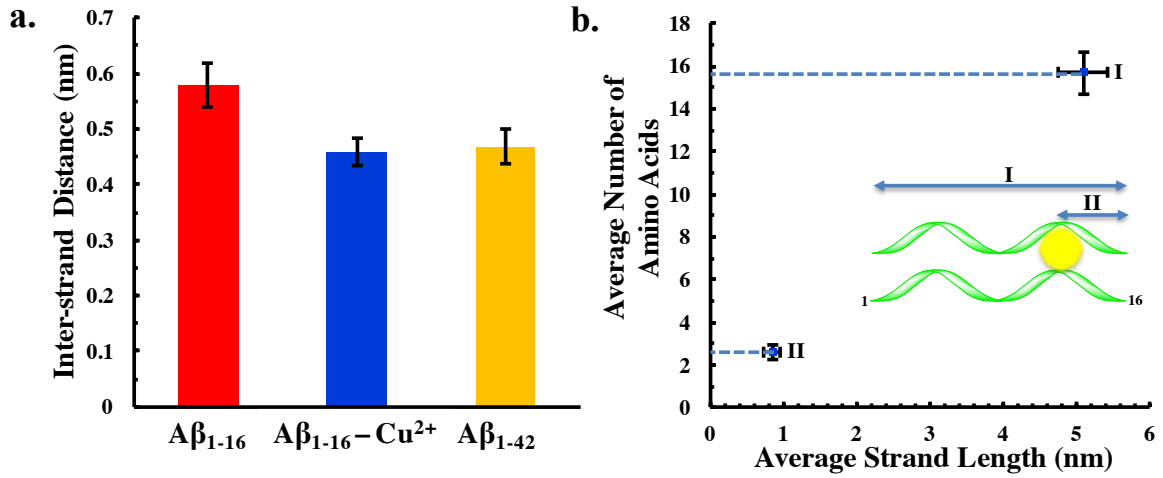

Figure 2.6. (a) Average β-sheet inter-strand separation values for Aβ1-16, Aβ1-16-Cu^{2+}, and full length Aβ ($Aβ_{1-42}$): 5.8 ± 0.4 Å, 4.6 ± 0.25 Å, and 4.7 ± 0.3 Å, respectively. $Aβ_{1-42}$ inter-strand separation was previously reported elsewhere;[89] thus, the measurements on Aβ were performed and compared against $Aβ_{1-16}$ and $Aβ_{1-16}$-Cu^{2+} to verify if the large inter-strand separation for $Aβ_{1-16}$ was not due to the instrumental error. (b) (I) Average strand length vs number of amino acids for $Aβ_{1-16}$-Cu^{2+}: 5.09 ± 0.33 nm and 15.67 ± 1.01 amino acids, respectively. (II) Average length from protruding features to β-sheet boundary vs number of amino acids: 0.85 ± 0.11 nm *vs* 2.6 ± 0.36 amino acids, respectively.

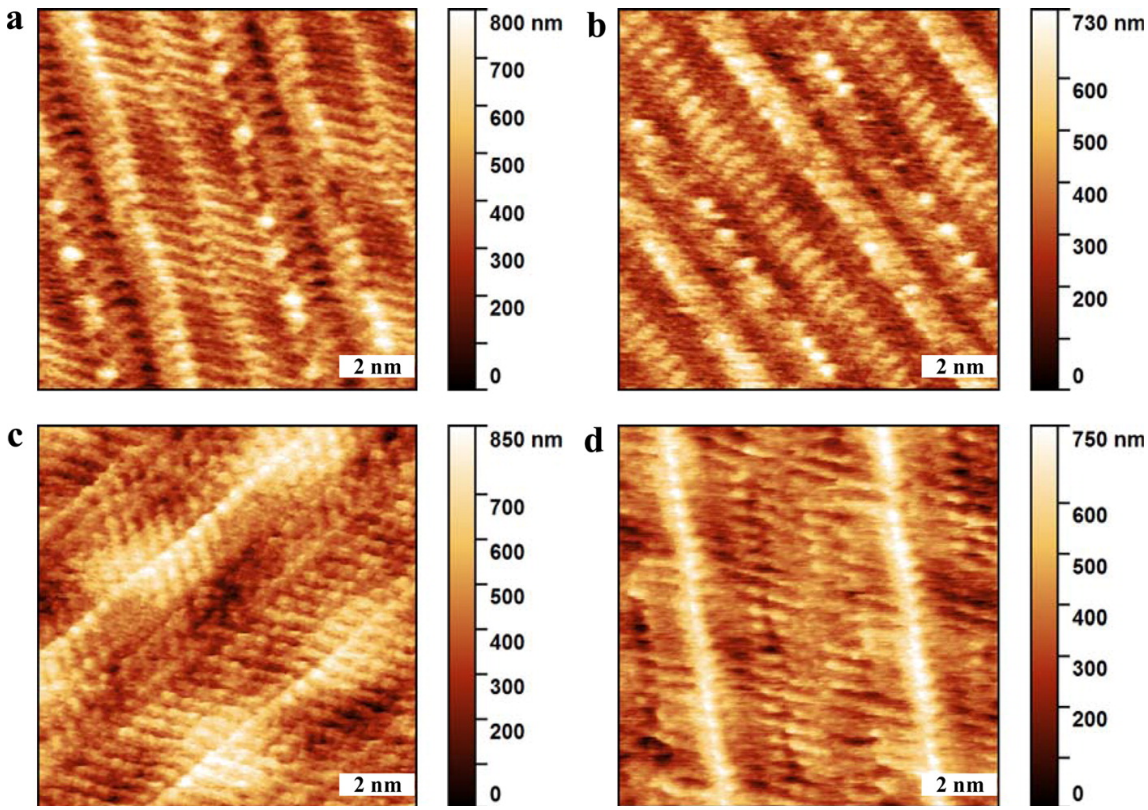

Figure 2.7. Scanning tunneling microscopy images of (a,b) $A\beta_{1-16}$-Cu^{2+} and (c,d) $A\beta_{1-16}$. Imaging conditions: (a,b) 10 nm × 10 nm, V_{sample} = 0.55 V, I_{tunnel} = 10 pA; (c) 10 nm × 10 nm, V_{sample} = 0.25 V, I_{tunnel} = 17 pA; (d) 10 nm × 10 nm, V_{sample} = 0.30 V, I_{tunnel} = 14 pA.

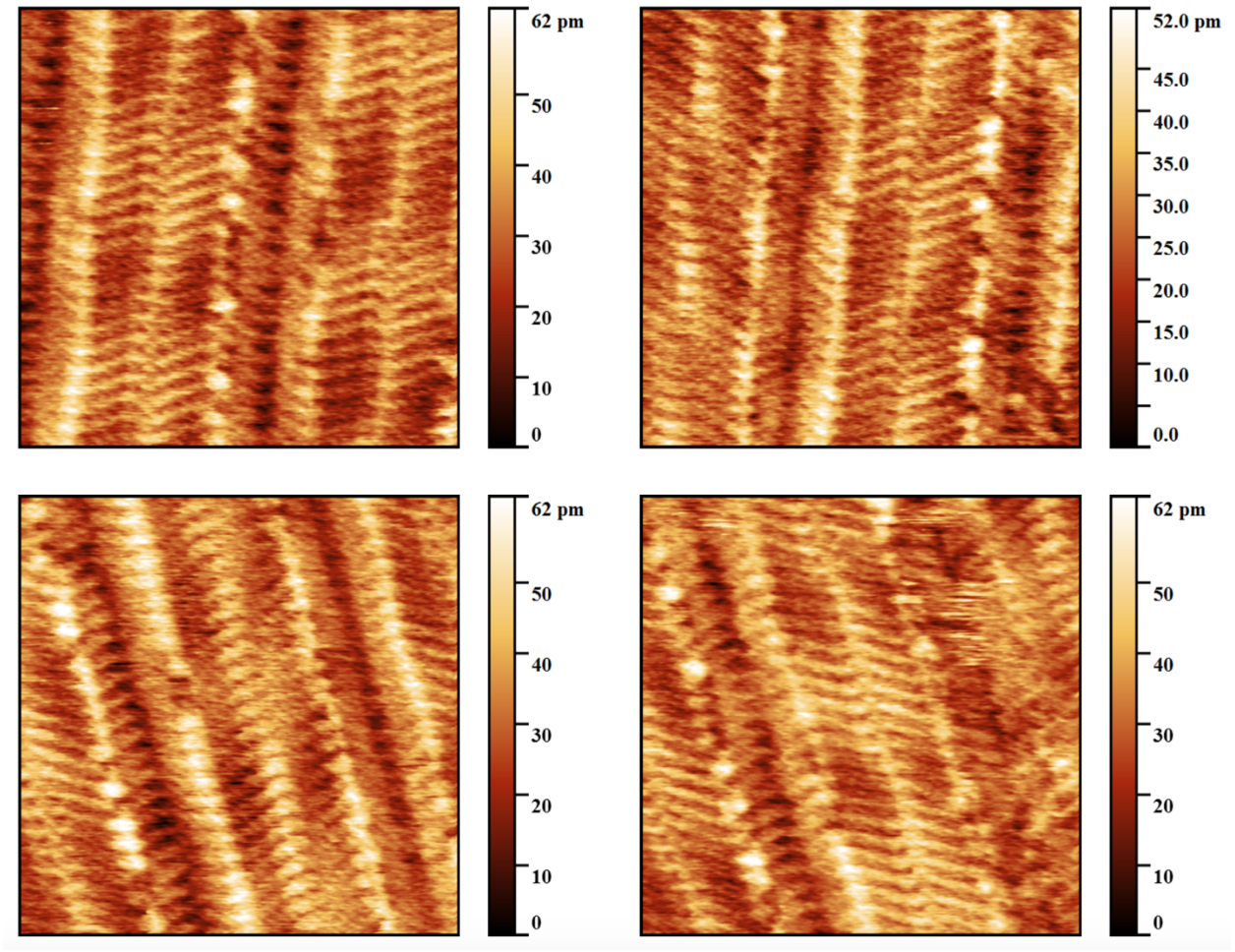

Figure 2.8. Scanning tunneling microscope images of $A\beta_{1\text{-}16}$-Cu^{2+}. Scanning parameters: size: 10 nm ×10 nm, V_{sample}=0.55 V, I_{tunnel}=10 pA. Images demonstrate a consistent protrusion pattern in the vicinity of the β-sheet boundary.

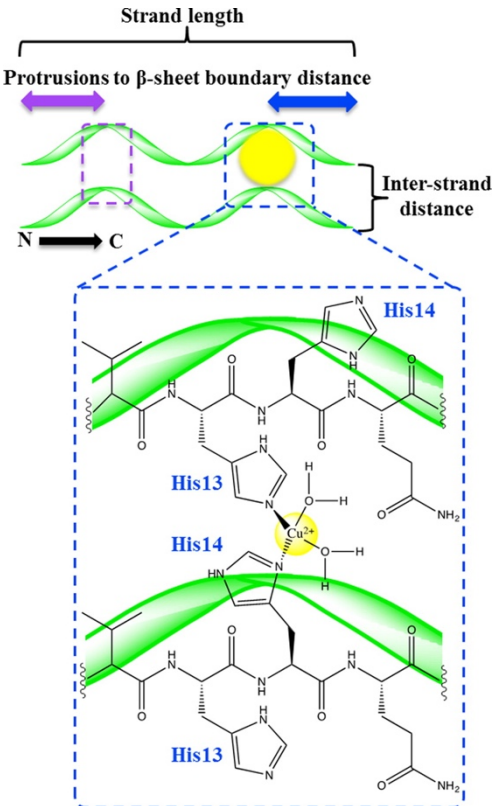

Figure 2.9. Schematic of the structure determined for $A\beta_{1\text{-}16}$-Cu^{2+}. Cu^{2+} interstrand binding to His13 and His14 forms a brace between strands (blue dashed box). In this schematic, we depict copper coordinated with water. It is also possible that copper coordinates with the substrate surface; our data do not distinguish which scenario is more likely. Regular protrusions on STM micrographs that we attribute to be Phe4 are illustrated as a purple dashed box.

Raman shift (cm−1)	assignment	reference
1585	Graphene G band	53, 54
1529	Amide II band	55−60
1449	C−H bending mode	65−68
1328	Graphene D band	53, 54
1250	Amide III band	61−64

Table 2.1. Vibrational peak positions and corresponding band assignments for the surface-enhanced Raman spectroscopy spectra recorded.

2.6 References

1. Zhu, C. W.; Sano, M. Economic Considerations in the Management of Alzheimer's Disease. *Clin. Interv. Aging* **2006**, *1*, 143–154.

2. Goldman, L.; Schaffer, A. I. *Goldman's Cecil Medicine*; Elsevier Saunders: Philadelphia, PA, 2011; Chapter 402, pp 2274–2279.

3. Malakooti, N.; Pritchard, M. A.; Adlard, P. A.; Finkelstein, D. I. Role of Metal Ions in the Cognitive Decline of Down Syndrome. *Front. Aging Neurosci*. **2014**, *6*, 136.

4. Hyman, B. T.; Van Hoesen, G. W.; Kromer, L. J.; Damasio, A. R. Perforant Pathway Changes and the Memory Impairment of Alzheimer's Disease. *Ann. Neurol*. **1986**, *20*, 472–481.

5. Fu, S.; Jiang, W.; Zheng, W. Age-dependent Increase of Brain Copper Levels and Expressions of Copper Regulatory Proteins in the Subventricular Zone and Choroid Plexus. *Front. Mol. Neurosci.* **2015,** *8*, 1–22

6. Singh, I.; Sagare, P.A.; Coma, M.; Perlmutter, D.; Gelein, R.; Bell, D.R.; Deane, J.R.; Zhong, E.; Parisi, M.; Ciszewski, R.J.; Kasper, T.; Deane, R. Dysregulation of Brain Aβ Homeostasis by Cu. *Proc. Natl. Acad. Sci. U.S.A.* **2013,** *110,* 14771–14776

7. Goure, W. F.; Krafft, G. A.; Jerecic, J.; Hefti, F. Targeting the Proper Amyloid-Beta Neuronal Toxins: A Path Forward for Alzheimer's Disease Immunotherapeutics. *Alzheimer's Res. Ther*. **2014**, *6*, 42.

8. Chafekar, S. M.; Baas, F.; Scheper, W. Oligomer-Specific A*β* Toxicity in Cell Models is Mediated by Selective Uptake. *Biochim. Biophys. Acta, Mol. Basis Dis*. **2008**, *1782*, 523–531.

9. Zhao, L. N.; Long, H. W.; Mu, Y.; Chew, L. Y. The Toxicity of Amyloid *β* Oligomers. *Int. J. Mol. Sci*. **2012**, *13*, 7303–7327.

10. Danielsson, J.; Pierattelli, R.; Banci, L.; Graslund, A. High-Resolution NMR Studies of the Zinc-Binding Site of the Alzheimer's Amyloid *β*-Peptide. *FEBS J*. **2007**, *274*, 46–59.

11. Jun, S.; Gillespie, J. R.; Shin, B.; Saxena, S. The Second Cu(II)-Binding Site in a Proton-rich Environment Interferes with the Aggregation of Amyloid-*β*(1–40) into Amyloid Fibrils. *Biochemistry* **2009**, *48*, 10724–10732.

12. Eisenberg, D.; Jucker, M. The Amyloid State of Proteins in Human Diseases. *Cell* **2012**, *148*, 1188–1203.

13. Minicozzi, V.; Stellato, F.; Comai, M.; Serra, M. D.; Potrich, C.; Meyer-Klaucke, W.; Morante, S. Identifying the Minimal Copper- and Zinc-Binding Site Sequence in Amyloid-*β* Peptides. *J. Biol. Chem*. **2008**, *283*, 10784–10792.

14. Xiao, Y.; Ma, B.; McElheny, D.; Parthasarathy, S.; Long, F.; Hoshi, M.; Nussinov, R.; Ishii, Y. Aβ(1–42) Fibril Structure Illuminates Self-Recognition and Replication of Amyloid in Alzheimer's Disease. *Nat. Struct. Mol. Biol*. **2015**, *22*, 499–505.

15. Streltsov, V. X-ray Absorption and Diffraction Studies of the Metal Binding Sites in Amyloid β-Peptide. *Eur. Biophys. J*. **2008**, *37*, 257–263.

16. Karr, J. W.; Kaupp, L. J.; Szalai, V. A. Amyloid-Beta Binds Cu^{2+} in a Mononuclear Metal Ion Binding Site. *J. Am. Chem. Soc*. **2004**, *126*, 13534–13538.

17. Hane, F.; Tran, G.; Attwood, S. J.; Leonenko, Z. Cu^{2+} Affects Amyloid-β (1–42) Aggregation by Increasing Peptide-Peptide Binding Forces. *PLoS One* **2013**, *8*, e59005.

18. Kepp, K. P. Bioinorganic Chemistry of Alzheimer's Disease. *Chem. Rev*. **2012**, *112*, 5193–5239.

19. Miller, Y.; Ma, B.; Nussinov, R. Metal Binding Sites in Amyloid Oligomers: Complexes and Mechanisms. *Coord. Chem. Rev*. **2012**, *256*, 2245–2252.

20. Faller, P.; Hureau, C.; La Penna, G. Metal Ions and Intrinsically Disordered Proteins and Peptides: From Cu/Zn Amyloid-β to General Principles. *Acc. Chem. Res*. **2014**, *47*, 2252–2259.

21. Claridge, S. A.; Thomas, J. C.; Silverman, M. A.; Schwartz, J. J.; Yang, Y.; Wang, C.; Weiss, P. S. Differentiating Amino Acid Residues and Side Chain Orientations in Peptides Using Scanning Tunneling Microscopy. *J. Am. Chem. Soc*. **2013**, *135*, 18528–18535.

22. Atwood, C. S.; Moir, R. D.; Huang, X.; Scarpa, R. C.; Bacarra, N. M.; Romano, D. M.; Hartshorn, M. A.; Tanzi, R. E.; Bush, A. I. Dramatic Aggregation of Alzheimer Abeta by Cu(II) is Induced by Conditions Representing Physiological Acidosis. *J. Biol. Chem*. **1998**, *273*, 12817–12826.

23. Viet, M. H.; Li, M. S. Amyloid Peptide Aβ40 Inhibits Aggregation of Aβ42: Evidence from Molecular Dynamics Simulations. *J. Chem. Phys*. **2012**, *136*, 245105.

24. Yu, X.; Zheng, J. Polymorphic Structures of Alzheimer's β-Amyloid Globulomers. *PLoS One* **2011**, *6*, e20575.

25. Miller, Y.; Ma, B.; Nussinov, R. Zinc Ions Promote Alzheimer Aβ Aggregation *via* Population Shift of Polymorphic States. *Proc. Natl. Acad. Sci. U. S. A*. **2010**, *107*, 9490–9495.

26. Wang, Q.; Wang, Y.; Lu, P. Revealing the Secondary Structural Changes of Amyloid β Peptide by Probing the Spectral Fingerprint Characters. *J. Raman Spectrosc*. **2013**, *44*, 670–674.

27. Luhrs, T.; Ritter, C.; Adrian, M.; Riek-Loher, D.; Bohrmann, B.; Dobeli, H.; Schubert, D.; Riek, R. 3D Structure of Alzheimer's Amyloid-β(1–42) Fibrils. *Proc. Natl. Acad. Sci. U.S.A*. **2005**, *102*, 17342–17347.

28. Syme, C. D.; Nadal, R. C.; Rigby, S. E. J.; Viles, J. H. Copper Binding to the Amyloid-β (Aβ) Peptide Associated with Alzheimer's Disease. *J. Biol. Chem*. **2004**, *279*, 18169–18177.

29. Ma, Q.; Hu, J.; Wu, W.; Liu, H.; Du, J.; Fu, Y.; Wu, Y.; Lei, P.; Zhao, Y.; Li, Y. Characterization of Copper Binding to the Peptide Amyloid-β(1–16) Associated with Alzheimer's Disease. *Biopolymers* **2006**, *83*, 20–31.

30. Claridge, S. A.; Schwartz, J. J.; Weiss, P. S. Electrons, Photons, and Force: Quantitative Single-Molecule Measurements from Physics to Biology. *ACS Nano* **2011**, *5*, 693–729.

31. Liu, L.; Niu, L.; Xu, M.; Han, Q.; Duan, H.; Dong, M.; Besenbacher, F.; Wang, C.; Yang, Y. Molecular Tethering Effect of C-Terminus of Amyloid Peptide Aβ42. *ACS Nano* **2014**, *8*, 9503–9510.

32. Kowalewski, T.; Holtzman, D. M. *In Situ* Atomic Force Microscopy Study of Alzheimer's β-Amyloid Peptide on Different Substrates: New Insights into Mechanism of β-sheet Formation. *Proc. Natl. Acad. Sci. U. S. A*. **1999**, *96*, 3688–3693.

33. Mattson, M. P.; Cheng, B.; Davis, D.; Bryant, K.; Lieberburg, I.; Rydel, R. E. β-Amyloid Peptides Destabilize Calcium Homeostasis and Render Human Cortical Neurons Vulnerable to Excitotoxicity. *J. Neurosci*. **1992**, *2*, 376–389.

34. Adzhubei, A. A.; Sternberg, M. J. Left-Handed Polyproline II Helices Commonly Occur in Globular Proteins. *J. Mol. Biol*. **1993**, *229*, 472–493.

35. Stapley, B. J.; Creamer, T. P. A Survey of Left-Handed Polyproline II Helices. *Protein Sci.* **1999**, *8*, 587–595.

36. Rucker, A. L.; Creamer, T. P. Polyproline II Helical Structure in Protein Unfolded States: Lysine Peptides Revisited. *Protein Sci*. **2002**, *11*, 980–985.

37. White, C. J.; Yudin, A. K. Contemporary Strategies for Peptide Macrocyclization. *Nat. Chem.* **2011**, *3*, 509–524.

38. Han, W. G.; Jalkanen, K. J.; Elstner, M.; Suhai, S. Theoretical Study of Aqueous *N*-Acetyl-L-alanine *N*′-Methylamide: Structures and Raman, VCD and ROA Spectra. *J. Phys. Chem.B* **1998**, *102*, 2587–2602.

39. Westhof, E. *Water and Biological Macromolecules*; CRC Press: Boca Raton, FL, 1993; Chapter 5, pp 148–162.

40. Blanch, E. W.; Morozova-Roche, L. A.; Hecht, L.; Noppe, W.; Barron, L. D. Raman Optical Activity Characterization of Native and Molten Globule States of Equine Lysozyme: Comparison with Hen Lysozyme and Bovine α-Lactalbumin. *Biopolymers* **2000**, *57*, 235–248.

41. Blanch, E. W.; Morozova-Roche, L. A.; Cochran, D. A.; Doig, A. J.; Hecht, L.; Barron, L. D. A Raman Optical Activity Study of the Amyloidogenic Prefibrillar Intermediate of Human Lysozyme. *J. Mol. Biol*. **2000**, *301*, 553–563.

42. Fandrich, M.; Meinhardt, J.; Grigorieff, N. Structural Polymorphism of Alzheimer A*β* and Other Amyloid Fibrils. *Prion* **2009**, 3, 89–93.

43. Chen, Y. R.; Huang, H. B.; Chyan, C. L.; Shiao, M. S.; Lin, T. H.; Chen, Y. C. The Effect of A*β* Conformation on the Metal Affinity and Aggregation Mechanism Studied by Circular Dichroism Spectroscopy. *J. Biochem*. **2006**, *139*, 733–740.

44. Baldassarre, M.; Barth, A. Pushing the Detection Limit of Infrared Spectroscopy for Structural Analysis of Dilute Protein Samples. *Analyst* **2014**, *139*, 5393–5399.

45. Goldberg, M. E.; Chaffotte, A. F. Undistorted Structural Analysis of Soluble Proteins by Attenuated Total Reflectance Infrared Spectroscopy. *Protein Sci*. **2005**, *14*, 2781–2792.

46. Berhanu, W. M.; Hansmann, U. H. Structure and Dynamics of Amyloid-*β* Segmental Polymorphisms. *PLoS One* **2012**, *7*, e41479.

47. Baia, M.; Astilean, S.; IIiescu, T. *Raman and SERS Investigations of Pharmaceuticals*; Springer: Berlin, 2008; Chapter 1, pp 9–35.

48. Wang, P.; Zhang, W.; Liang, O.; Pantoja, M.; Katzer, J.; Schroeder, T.; Xie, Y. Giant Optical Response from Graphene-Plasmonic System. *ACS Nano* **2012**, *6*, 6244–6249.

49. Radziuk, D.; Möhwald, H. Prospects for Plasmonic Hot Spots in Single Molecule SERS Towards the Chemical Imaging of Live Cells. *Phys. Chem. Chem. Phys*. **2015**, *17*, 21072–21093.

50. Kumar, C. S. S. R. *Raman Spectroscopy for Nanomaterials Characterization*; Springer: Berlin, 2012; Chapter 10, pp 215–261.

51. Schweitzer-Stenner, R. Advances in Vibrational Spectroscopy as a Sensitive Probe of Peptide and Protein Structure a Critical Review. *Vib. Spectrosc*. **2006**, *42*, 98–117.

52. Ayas, S.; Cinar, G.; Ozkan, A. D.; Soran, Z.; Ekiz, O.; Kocaay, D.; Tomak, A.; Toren, P.; Kaya, Y.; Tunc, I.; Zareie, H.; Tekinay, T.; Tekinay, A. B.; Guler, M. O.; Dana, A. Label-Free Nanometer-Resolution Imaging of Biological Architectures through Surface Enhanced Raman Scattering. *Sci. Rep*. **2013**, *3*, 2624.

53. Ferrari, A. C. Raman Spectroscopy of Graphene and Graphite: Disorder, Electron-Phonon Coupling, Doping and Nonadiabatic Effects. *Solid State Commun*. **2007**, *143*, 47–57.

54. Jorio, A.; Martins Ferreira, E. H.; Moutinho, M. V. O.; Stavale, F.; Achete, C. A.; Capaz, R. B. Measuring Disorder in Graphene with G and D Bands. *Phys. Status Solidi B* **2010**, *247*, 2980–2982.

55. Siddhanta, S.; Naray, C. Surface Enhanced Raman Spectroscopy of Proteins: Implications for Drug Designing. *Nanomater. Nanotechnol*. **2012**, *2*, 1.

56. Barth, A. Infrared Spectroscopy of Proteins. *Biochim. Biophys. Acta, Bioenerg*. **2007**, *1767*, 1073–1101.

57. Siddhanta, S.; Karthigeyan, D.; Kundu, P. P.; Kundu, T. K.; Narayana, C. Surface Enhanced Raman Spectroscopy of Aurora Kinases: Direct, Ultrasensitive Detection of Autophosphorylation. *RSC Adv*. **2013**, *3*, 4221–4230.

58. Podstawka, E.; Ozaki, Y.; Proniewicz, L. M. Part II: Surface-Enhanced Raman Spectroscopy Investigation of Methionine Containing Heterodipeptides Absorbed on Colloidal Silver. *Appl. Spectrosc*. **2004**, *58*, 581–590.

59. Schmidt, E. A. Spectroscopic Investigation of the Beta-Amyloid Peptide. Ph.D. Dissertation, University of Missouri, Columbia, MO, 2008.

60. Di Foggia, M.; Taddei, P.; Torreggiani, A.; Dettin, M.; Tinti, A. Interaction between Oligopeptides and Oxidised Titanium Surfaces Detected by Vibrational Spectroscopy. *J. Raman Spectrosc*. **2011**, *42*, 276–285.

61. Shashilov, V.; Xu, M.; Makarava, N.; Savtchenko, R.; Baskakov, I. V.; Lednev, I. K. Dissecting Structure of Prion Amyloid Fibrils by Hydrogen-Deuterium Exchange Ultraviolet Raman Spectroscopy. *J. Phys. Chem*. *B* **2012**, *116*, 7926–7930.

62. Oladepo, S. A.; Xiong, K.; Hong, Z.; Asher, S. A.; Handen, J.; Lednev, I. K. UV Resonance Raman Investigations of Peptide and Protein Structure and Dynamics. *Chem. Rev*. **2012**, *112*, 2604–2628.

63. Ahmed, Z.; Beta, I. A.; Mikhonin, A. V.; Asher, S. A. UV-Resonance Raman Thermal Unfolding Study of Trp-Cage Shows That It Is Not A Simple Two State Miniprotein. *J. Am. Chem. Soc*. **2005**, *127*, 10943–10950.

64. Mikhonin, A. V.; Myshakina, N. S.; Bykov, S. V.; Asher, S. A. UV-Resonance Raman Determination of Polyproline II, Extended 2.5_1-Helix, and β-Sheet Ψ Angle Energy Landscape in Poly-L-Lysine and Poly-L-Glutamic Acid. *J. Am. Chem. Soc*. **2005**, *127*, 7712–7720.

65. Ma, C. Y.; Rout, M. K.; Chan, W. M.; Phillips, D. L. Raman Spectroscopic Study of Oat Globulin Conformation. *J. Agric. Food Chem*. **2000**, *48*, 1542–1547.

66. Camerlingo, C.; d'Apuzzo, F.; Grassia, V.; Perillo, L.; Lepore, M. Micro-Raman Spectroscopy for Monitoring Changes in Periodontal Ligaments and Gingival Crevicular Fluid. *Sensors* **2014**, *14*, 22552–22563.

67. Kurouski, D.; Van Duyne, R. P.; Lednev, I. K. Exploring the Structure and Formation Mechanism of Amyloid Fibrils by Raman Spectroscopy: A Review. *Analyst* **2015**, *140*, 4967–4980.

68. Phillips, J. C. Thermodynamic Description of Beta Amyloid Formation Using Physicochemical Scales and Fractal Bioinformatic Scales. *ACS Chem. Neurosci*. **2015**, *6*, 745–750.

69. Mao, X.; Guo, Y.; Luo, Y.; Niu, L.; Liu, L.; Ma, X.; Wang, H.; Yang, Y.; Wei, G.; Wang, C. Sequence Effects on Peptide Assembly Characteristics Observed by Using Scanning Tunneling Microscopy. *J. Am. Chem. Soc*. **2013**, *135*, 2181–2187.

70. Nelson, R.; Sawaya, M. R.; Balbirnie, M.; Madsen, A. O.; Riekel, C.; Grothe, R.; Eisenberg, D. Structure of the Cross-*β* Spine of Amyloid-Like Fibrils. *Nature* **2005**, *435*, 773–778.

71. Shaytan, A. K.; Schillinger, E. K.; Mena-Osteritz, E.; Schmid, S.; Khalatur, P. G.; Bauerle, P.; Khokhlov, A. R. Self-Organizing Bioinspired Oligothiophene-Oligopeptide Hybrids. *Beilstein J. Nanotechnol*. **2011**, *2*, 525–544.

72. Mao, X. B.; Wang, C. X.; Wu, X. K.; Ma, X. J.; Liu, L.; Zhang, L.; Niu, L.; Guo, Y. Y.; Li, D. H.; Yang, Y. L.; Wang, C. Beta Structure Motifs of Islet Amyloid Polypeptides Identified Through Surface-Mediated Assemblies. *Proc. Natl. Acad. Sci. U. S. A*. **2011**, *108*, 19605–19610.

73. Paravastu, A. K.; Leapman, R. D.; Yau, W. M.; Tycko, R. Molecular Structural Basis for Polymorphism in Alzheimer's *β*-Amyloid Fibrils. *Proc. Natl. Acad. Sci. U. S. A*. **2008**, *105*, 18349–18354.

74. Makin, O. S.; Atkins, E.; Sikorski, P.; Johansson, J.; Serpell, L. C. Molecular Basis for Amyloid Fibril Formation and Stability. *Proc. Natl. Acad. Sci. U. S. A*. **2005**, *102*, 315–320.

75. Dong, J.; Lu, K.; Lakdawala, A.; Mehta, A. K.; Lynn, D. G. Controlling Amyloid Growth in Multiple Dimensions. *Amyloid* **2006**, *13*, 206–215.

76. Morgan, D. M.; Lynn, D. G.; Lakdawala, A. S.; Snyder, J. P.; Liotta, D. C. Amyloid Structure: Models and Theoretical Considerations in Fibrous Aggregates. *J. Chin. Chem. Soc*. **2002**, *49*, 459–466.

77. Lakdawala, A. S.; Morgan, D. M.; Liotta, D. C.; Lynn, D. G.; Snyder, J. P. Dynamics and Fluidity of Amyloid Fibrils: A Model of Fibrous Protein Aggregates. *J. Am. Chem. Soc*. **2002**, *124*, 15150–15151.

78. Liao, S. M.; Du, Q. S.; Meng, J. Z.; Pang, Z. W.; Huang, R. B. The Multiple Roles of Histidine in Protein Interactions. *Chem. Cent. J*. **2013**, *7*, 44.

79. Jones, C. E.; Abdelraheim, S. R.; Brown, D. R.; Viles, J. H. Preferential Cu^{2+} Coordination by His^{96} and His^{111} Induces β-Sheet Formation in the Unstructured Amyloidogenic Region of the Prion Protein. *J. Biol. Chem*. **2004**, *279*, 32018–32027.

80. Gamez, P.; Caballero, A. B. Copper in Alzheimer's Disease: Implications in Amyloid Aggregation and Neurotoxicity. *AIP Adv*. **2015**, *5*, 092503.

81. Morgan, D. M.; Dong, J.; Jacob, J.; Lu, K.; Apkarian, R. P.; Thiyagarajan, P.; Lynn, D. G. Metal Switch for Amyloid Formation: Insight into the Structure of the Nucleus. *J. Am. Chem. Soc*. **2002**, *124*, 12644–12645.

82. Faller, P. Copper and Zinc Binding to Amyloid-Beta: Coordination, Dynamics, Aggregation, Reactivity and Metal-Ion Transfer. *ChemBioChem* **2009**, *10*, 2837–2845.

83. Rufo, C. M.; Moroz, Y. S.; Moroz, O. V.; Stohr, J.; Smith, T. A.; Hu, X.; DeGrado, W. F.; Korendovych, I. V. Short Peptides Self-Assemble to Produce Catalytic Amyloids. *Nat. Chem*. **2014**, *6*, 303–309.

84. Istrate, A. N.; Kozin, S. A.; Zhokhov, S. S.; Mantsyzov, A. B.; Kechko, O. I.; Pastore, A.; Makarov, A. A.; Polshakov, V. I. Interplay of Histidine Residues of the Alzheimer's Disease Aβ Peptide Governs Its Zn-induced Oligomerization. *Sci. Rep*. **2016**, *6*, 21734.

85. Hernández-Guzmán, J.; Sun, Li.; Mehta, A. K.; Dong, J.; Lynn, D. G.; Warncke, K. Copper(II)-bis-Histidine Coordination Structure in Fibrillar Amyloid-β Peptide Fragment and Model Complexes Revealed by using Electron Spin Echo Envelope Modulation Spectroscopy. *ChemBioChem* **2013**, *14*, 1762–1771.

86. Dong, J.; Canfield, J.; Mehta, A. K.; Shokes, J. E.; Tian, B.; Childers, S.; Simmons, J. A.; Mao, Z.; Scott, R. A.; Warncke, K.; Lynn, D. G. Engineering Metal Ion Coordination to Regulate Amyloid Fibril Assembly and Toxicity. *Proc. Natl. Acad. Sci. U. S. A*. **2007**, *104*, 13313–13318.

87. Yu, Y.; Yang, Y.; Wang, C. Site-Specific Analysis of Amyloid Assemblies by Using Scanning Tunneling Microscopy. *Chin. J. Chem*. **2015**, *33*, 24–34.

88. Nečas, D.; Klapetek, P. Gwyddion: An Open-Source Software for SPM Data Analysis. *Cent. Eur. J. Phys*. **2012**, *10*, 181–188.

89. Ma, X.; Liu, L.; Mao, X.; Niu, L.; Deng, K.; Wu, W.; Li, Y.; Yang, Y.; Wang, C. Amyloid β (1–42) Folding Multiplicity and Single Molecule Binding Behavior Studied with STM. *J. Mol. Biol.* **2009**, *388*, 894–901.

CHAPTER 3

Metal-Ion-Induced Structural Rearrangements of β-Amyloid Peptides

3.1 Introduction

Alzheimer's disease (AD) is the most common cause of dementia, constituting 60-80% of all dementia cases.[1,2] In addition, AD is the third most costly disease in the US after cancer and heart disease.[3] This global health problem will only be exacerbated as the population continues to age. It is estimated that there were 4.7 million cases of AD in the US in 2010; this number is projected to increase to 13.8 million by 2050.[4] The scientific community has yet to understand the etiology and pathogenesis of AD, but one of the hallmarks of the disease is the accumulation in the brain of senile plaques, which are primarily composed of fibrillar β-Amyloid (Aβ) peptides.[5,6] The fibrillar structure of a full-length Aβ, which consists of 42 amino acids, has been reported.[7] Yet, despite substantial research over the past several years, there is still scarce information about the structural, physical, chemical, and biological properties of natively disordered and soluble precursors to insoluble Aβ fibrils, which are known as Aβ oligomers. Characteristic features of fibril intermediates include high solubility and high structural polymorphism;[8-10] as such, Aβ oligomers have versatile structural and mechanical properties. Information about the secondary structure and metal ion (M^{2+}) binding sites of oligomeric Aβ peptides remains limited and poorly understood. It is known that the secondary structure and thus the metal ion binding site can be highly dependent on the type of metal ion ligand.[11,12] In addition, it is established that M^{2+} binding site is in the vicinity of the N-terminus of the full length Aβ,[11,12] and that there are strong correlations between Aβ fibrillar deposits in AD brains and elevated concentrations of M^{2+}, specifically Zn^{2+} and Cu^{2+}, around senile plaques.[13-15] The interactions of Aβ with M^{2+} are not only detrimental due to Aβ plaque accumulation but also contribute to generation of reactive oxygen species, which ultimately lead to neuronal death.[16,17]

For these reasons, we are interested in understanding the interactions of the Aβ oligomer with Zn^{2+} and Cu^{2+} ions.

Previously, scanning tunneling microscopy (STM) has been employed to probe biomolecular structures[18,19] and the effect of Cu^{2+} within the first 16 amino acids (1-16) of the full length Aβ ($Aβ_{1-16}$).[20] Using this method we elucidated a copper binding site within the peptide fragment and demonstrated that the non-fibrillar, natively disordered $Aβ_{1-16}$ assembles into β-sheet oligomers upon coordination with Cu^{2+}. These results only fueled our interest in understanding the structural characteristics of the β-sheets formed and the interactions that drive the transformations from disordered to ordered structures.

The ideal interstrand distance of a β-sheet secondary structure is 4.5−5.0 Å.[18,21-26] Our previously reported interstrand distance of $Aβ_{1-16}$ coordinated with Cu^{2+} as measured by STM was 4.6 ± 0.3 Å,[20] which is consistent with other reported values for amyloidogenic peptides as measured *via* X-ray diffraction (XRD),[22,25] solid-state nuclear magnetic resonance (ssNMR),[21,23] and STM.[18,24,26] However, in the case of XRD and ssNMR, these reports only provide average values across the entire assembly and even in STM studies, where real space measurements were made, these results do not fully take into account the variations in structural behavior along the lengths of the peptide strands. Thus, important information about precise structure of the $Aβ_{1-16}$-Cu^{2+} complixies formed and other amyloidogenic peptides with β-sheet secondary structures are undetermined. Specifically, how the interactions of individual amino acids with other residues or other components, such as metals ions, drive the assembly of long-range ordered structures requires further study. Critical structural aspects that need to be addressed are the extent of conformational variations of pseudo β-sheets and identification of regions with higher and lower propensities for β-sheet formation.

Herein, we experimentally establish and elucidate interstrand binding of Zn^{2+} ions to $A\beta_{1-16}$, which to our knowledge has not previously been reported. We quantitatively address changes in the backbones of assemblies of $A\beta_{1-16}$ with either interstrand binding of Zn^{2+} or Cu^{2+} ions (Figures 3.1 and 3.2). These measurements enable us to observe similarities and differences between oligomers of $A\beta_{1-16}$ coordinated with Cu^{2+} *vs.* Zn^{2+} ions. Furthermore, we address structural variations between different types of $A\beta_{1-16}$ peptides within the assemblies, which were classified based on their proximity to the bound M^{2+}.

These $A\beta_{1-16}$ peptide strands within the β-sheet were categorized into three types of interactions with the metal ion (M^{2+}) binding site: direct interaction, adjacent, or distantly affiliated (Scheme 3.1). Scanning tunneling micrographs were analyzed with novel image segmentation tools that enabled us to measure interstrand distance continuously along the length of the peptide to understand the influence of metal ion binding on each amino acid residue.

3.2 Results and Discussion

In this study, we imaged the $A\beta_{1-16}$ system in either the presence of Zn^{2+} or Cu^{2+} ions (Figure 3.1). In the analyses of these images, we discretized the peptide β-sheet into three types of areas (Scheme 3.1). The first type is pairs of strands with a metal ion in between and interacting with both strands, *i.e.*, the ion forming a histidine bridge with the His_{13} and His_{14} of the respective strands ($A\beta_{1-16}$-M^{2+}). The second group is composed of pairs of strands that are adjacent to the previous type, where one strand is interacting with a metal ion but the second strand is not (M^{2+}-Adj). The last group is composed of pairs of strands that do not fall in either of the previous categories; as such, they are still affiliated with the metal ion but lack direct interactions (M^{2+}-Aff). For each of these three groups, we measured the interstrand distances

continuously along the length of pair, determining interstrand separations for each amino acid residue. Both metal ions create distinct and local effects on a secondary structure of $A\beta_{1-16}$ (Figure 3.3). Interstrand distances of specific amino acids changes based on the distance of the residue to the M^{2+} binding site and between the different $A\beta_{1-16}$ categories. Self-assembly of $A\beta_{1-16}$ peptides in the presence of metal ions (M^{2+}-Global) appears dictated by the behavior of strands in the $A\beta_{1-16}$-M^{2+} and M^{2+}-Adj categories. If we examine the interstrand distance globally, as an average of $A\beta_{1-16}$-M^{2+}, M^{2+}-Adj, and M^{2+}-Aff interstrand distances, we see that Zn^{2+}-Global is larger than in Cu^{2+}-Global: 5.2 ± 0.03 Å and 4.8 ± 0.01 Å, respectively (Table 3.2). The difference between the Zn^{2+}-Global and Cu^{2+}-Global becomes significant and apparent towards N-termini located away from M^{2+} binding site (Figure 3.3d, Tables 3.2 and 3.3). The difference globally in interstrand distance between Zn^{2+} and Cu^{2+} is consistent with the differences of $A\beta_{1-16}$-M^{2+} and M^{2+}-Adj, but we do not observe similar behavior in M^{2+}-Aff. In M^{2+}-Aff strands, there is a high degree of variability in the interstrand distances and structural behavior for both Zn^{2+} and Cu^{2+}, with no apparent distinction in structure based on the metal ion present in the system (Figure 3.3c). This result further supports the conclusion that the global behavior is driven by the behavior of $A\beta_{1-16}$-M^{2+} and M^{2+}-Adj in the system.

The binding of a metal ion to $A\beta_{1-16}$ results in a significant decrease in the interstrand distance. In $A\beta_{1-16}$-M^{2+} strands, the backbone deformation increases the most after residue 11, reaching its maximum deformation at the position of the histidine residues, His_{13} and His_{14} (Figure 3.3a,b). When the average interstrand distance of amino acids in the vicinity of the C-terminus (from residue 12 to residue 16) is compared to the average interstrand distance of amino acids in the vicinity of the N-terminus (first 11 residues) we observe that the interstrand distance *decreases* by 11% in $A\beta_{1-16}$-Zn^{2+} and 7% in $A\beta_{1-16}$-Cu^{2+} peptide categories (Table 3.4).

In contrast, in M^{2+}-Adj strands, metal ion binding to the $A\beta_{1-16}$-M^{2+} strands create local regions of *increased* interstrand distance, which is adjacent to metal ion binding site (Figure 3.3a,b). Due to only indirect interactions with metal ions, a β-sheet structure of M^{2+}-Adj is less ordered (higher variability of interstrand distances per residue and per strand pair). Interstrand separation between β-strands greater than the 5.0 Å, which is observed in M^{2+}-Adj in the vicinity of the C-terminus, signifies broken hydrogen bonding between parallel β-strands and thus further supports higher flexibility observed in M^{2+}-Adj strands.[27-29]

Comparing the effects of Zn^{2+} *vs.* Cu^{2+} ions on $A\beta_{1-16}$, we see that Cu^{2+} leads to more peptide-peptide interactions and thus, more ordered β-sheet structure. The average interstrand distances of $A\beta_{1-16}$-Cu^{2+}, Cu^{2+}-Adj, and Cu^{2+}-Aff along the first 11 residues from N-terminus are all within the region for ideal β-sheet separation (4.8 ± 0.03 Å, 4.8 ± 0.02 Å, and 5.0 ± 0.05 Å, respectively) (Table 3.4). The interstrand distance is slightly larger in Cu^{2+}-Aff and in particular, it increases in the region of aspartate, serine, and glycine at positions seven (Asp7), eight (Ser8), and nine (Gly9), respectively (Figure 3.3c). It is generally recognized that amino acids such as Asp and Gly are flexible, unstable, and thus, have low β-sheet forming propensity;[30-34] hence, it could explain the slightly larger interstrand distance in that region. The average interstrand distances of $A\beta_{1-16}$-Zn^{2+}, Zn^{2+}-Adj, and Zn^{2+}-Aff along the first 11 residues are all above the ideal β-sheet region (5.2 ± 0.02 Å, 5.3 ± 0.03 Å, and 5.1 ± 0.01 Å, respectively) (Table 3.4). The absence of the pristine β-sheet arrangement suggests irregular H-bonding between the strands (hence, all categories along the first 11 residues deviate from the ideal β-sheet region).[35-37] Within the strands, residue-residue alignment is more irregular in Zn^{2+}-Adj than in $A\beta_{1-16}$-Zn^{2+} or Zn^{2+}-Aff, and it increases towards the N-terminus of peptides. Yet, in $A\beta_{1-16}$-Zn^{2+}, some residues show higher β-sheet character. Overall Zn^{2+} ions, compared to Cu^{2+} ions, facilitate less ordered

β-sheet alignment of $A\beta_{1-16}$, however comparing both of these system to intrinsically disordered $A\beta_{1-16}$ free of metal ions, all categories of $A\beta_{1-16}$ in the presence of metal ions show greater β-sheet character.[20] Furthermore, $A\beta_{1-16}$-M^{2+} peptide strands, compared to M^{2+}-Adj, and M^{2+}-Aff, self-assemble into the most compact lamellar structures (Figure 3.3a-c).

We expect the binding of both Zn^{2+} and Cu^{2+} metal ions to be in inter-strand fashion with His_{13} and His_{14} bridging neighboring strands and our findings, as shown in Figures 3.1 and 3.3, support this premise. Therefore, the smallest interstrand distance between the two adjacent $A\beta_{1-16}$ strands with the bound Zn^{2+} and Cu^{2+} has to be either at His_{13}, His_{14}, or between the two residues. The observed results show that the smallest interstrand distance changes based on participating metal ion, for $A\beta_{1-16}$-Zn^{2+} is at His_{13}, while for $A\beta_{1-16}$-Cu^{2+} is at His_{14} (Figure 3.3a,b). This difference indicates that the two metal ions have distinct effects on the $A\beta_{1-16}$ backbone in the vicinity of C-terminus upon binding to His_{13} and His_{14} from adjacent strands. Binding modes of Zn^{2+} and Cu^{2+} onto Aβ have been previously studied and reported and those findings suggest that Cu^{2+} is more rigid than Zn^{2+} in its binding geometry,[38] where the preferred coordination number of Zn^{2+} in Aβ is four[39,40] and of Cu^{2+} is three.[41] Herein, we report how both metal ions affect $A\beta_{1-16}$-M^{2+} when they are coordinated with $A\beta_{1-16}$ in a geometrically similar manner. In order to study the effects and to understand the reasons behind a shift in one amino acid between $A\beta_{1-16}$-Zn^{2+} and $A\beta_{1-16}$-Cu^{2+}, we examined the distance between the M^{2+} binding site and the C-termini of $A\beta_{1-16}$-M^{2+}.

The standard inter-residue spacing in parallel β-sheets is 3.25 Å.[26,42-45] Assuming that our previous findings[20] hold true for *both* metal ions and that *both* metal ions bind to $A\beta_{1-16}$-M^{2+} between His_{13} and His_{14}. Then, in an idealized situation the predicted total length (P) from metal

ion binding site to C-terminus (M^{2+}-C_{term}) in case of Zn^{2+} and Cu^{2+} should be identical (and equivalent to 8.12 Å, Figure 3a).

The ideal inter-residue spacing assumes a linear/geometrically perfect β-strand. It excludes local deformations that might be present in β-strands due to metal ion interactions. Thus, the measured (M) length of M^{2+}-$C_{term}{}^{M}$, which is free of local deformations and perturbations/distortions due to M^{2+} binding between $A\beta_{1-16}$ strands is expected to be similar to the predicted ideal length. Yet, the measured lengths of Zn^{2+}-$C_{term}{}^{M}$ and Cu^{2+}-$C_{term}{}^{M}$ are significantly different, 9.52 ± 0.3 Å and 8.14 ± 0.2 Å, respectively.

When we compare Cu^{2+}-$C_{term}{}^{M}$ and Cu^{2+}-$C_{term}{}^{P}$, we observe that both lengths are similar, and thus we conclude that Cu^{2+} ions have greater stabilizing effects on the C-terminus of $A\beta_{1-16}$-Cu^{2+} strands. However, when the analogous comparison is made for Zn^{2+} ions, we observe that Zn^{2+}-$C_{term}{}^{M}$ is longer than Zn^{2+}-$C_{term}{}^{P}$ by 1.4 Å. The difference between measured and predicted lengths of Zn^{2+}-C_{term} signify that, in contrast to Cu^{2+} ions, Zn^{2+} ions create a strong, local effect on the Zn^{2+}-C_{term} and distort the C-terminus of $A\beta_{1-16}$-Zn^{2+}.

Perhaps due to destabilizing effects of Zn^{2+} on the C-terminus of $A\beta_{1-16}$-M^{2+}, we additionally see a greater fractional change in interstrand distance between N and C-terminus when the participating metal ion is Zn^{2+} rather than Cu^{2+} (11% *vs.* 7%, respectively; as discussed above).

In Figure 3.4c, we further analyze the effects of both metal ions on the different categories and segments of $A\beta_{1-16}$. These segments are based on whether the residues are away from the binding site and mostly homogenous in structure or in the vicinity of the binding site and distorted by the metal ion binding. In this manner, we observe the effects of metal ions on the backbone and inter-residue separation of $A\beta_{1-16}$ and find that these factors are highly distance

and metal ion dependent. Based on the inter-residue separation of M^{2+}-Aff, and the first 13 residues of M^{2+}-Adj and $A\beta_{1-16}$-M^{2+} (Figure 3.4c; Panels 1-3), we see that all these categories and segments show slightly smaller than predicted inter-residue separations. The inter-residue separation in these cases does not vary based on category or segment. However, in M^{2+}-Adj, in the vicinity of the binding site (residues 14-16), we observe the destabilization of inter-residue separation (Figure 3.4c, Panel 4). It is likely that vacancies created upon M^{2+} binding in $A\beta_{1-16}$-M^{2+} strands results in the entropic increase of M^{2+}-Adj strands around residues 14 to 16.[46,47] This change results in the readjustment of residue-residue interaction, which ultimately contributes to destabilization of inter-residue separation around that region. Finally, the destabilization of inter-residue separation due to M^{2+} can also be observed in Figure 3.4c, Panel 5. We see that inter-residue separation in residues 14 to 16 of $A\beta_{1-16}$-Zn^{2+} is significantly larger (p=0.0117) than $A\beta_{1-16}$-Cu^{2+}, 3.81 ± 0.1 Å and 3.26 ± 0.1 Å, respectively.

From here, we see that Cu^{2+} ions upon binding to Aβ have strong stabilizing effects on the $A\beta_{1-16}$-M^{2+} strands. The result of this stabilization is ideal inter-residue separation, small variability in interstrand distance between the N and C-terminus of participating residues, and, as shown in Figure 3.5a,c, long-range effects of Cu^{2+} on $A\beta_{1-16}$-Cu^{2+}.

In regard to the Zn^{2+} ions, we see that Zn^{2+} ions, similarly to Cu^{2+} ions, have strong effects on the assembly of $A\beta_{1-16}$, but contrary to Cu^{2+} ions their effect is *destabilizing* on the peptidyl arrangement. This difference is seen in the larger than ideal inter-residue separations as well as the large change in interstrand distance between the N and C-termini of participating residues. Additionally, by comparing the frequencies of different types of interstrand arrangements, we see that the Zn^{2+} effect on $A\beta_{1-16}$-Zn^{2+} is local, *i.e.*, short range (Figure 3.5a,b).

To access the predominant structural and relative stability of $A\beta_{1-16}$ peptides upon their interactions with metal ions, we compared $A\beta_{1-16}$ categories and their corresponding frequencies of residues in those categories (Figure 3.5). The predominant structural change of $A\beta_{1-16}$ upon Zn^{2+} and Cu^{2+} binding is that the peptides assemble towards small (≤4.4 Å) interstrand distances. Both $A\beta_{1-16}$-Zn^{2+} and $A\beta_{1-16}$-Cu^{2+} show that His_{13} and His_{14} undergo significant structural changes upon metal ion binding. These distances are significantly smaller than in the other two $A\beta_{1-16}$ categories – M^{2+}-Adj and M^{2+}-Aff.

A comparison of the structural changes of individual residues between $A\beta_{1-16}$ categories shows long- and short-range effects of Zn^{2+} and Cu^{2+} on the $A\beta_{1-16}$ sequence. In $A\beta_{1-16}$-Cu^{2+}, the residues with significant small interstrand distance to Cu^{2+}-Aff are glutamic acid at the position three (Glu_3) and histidine at position six (His_6). Both residues are charged amino acids that are located in the vicinity of the N-terminus. The change of interstrand distance in the vicinity of the N-terminus upon Cu^{2+} binding in the vicinity of C-terminus signifies long-range effects of Cu^{2+} ions on $A\beta_{1-16}$ structure. In juxtaposition, we observe that the long-range effects in $A\beta_{1-16}$-M^{2+} are less prevalent upon Zn^{2+} binding. In $A\beta_{1-16}$-Zn^{2+}, the only residue in the vicinity of the N-terminus that deviates from pristine towards a significantly small interstrand distance is aspartic acid at position seven (Asp_7) (*vs.* two residues in $A\beta_{1-16}$-Cu^{2+}). In addition, Asp_7 is closer to the metal ion binding site than Glu_3 and His_6. Since Asp_7 is a charged residue, we again see relative instability of charged amino acids in $A\beta_{1-16}$ peptide.[33,34,48]

Residues with changes in interstrand distance in the vicinity of the C-terminus show the short-range effects on the $A\beta_{1-16}$ structure. In $A\beta_{1-16}$-Zn^{2+} the glutamine as position 15 (Gln_{15}) appears effected and in $A\beta_{1-16}$-Cu^{2+} Gln_{15} and the lysine at position 16 (Lys_{16}) appears significantly influenced by metal ion binding. Residues proximate to the metal ion binding site

are expected to arrange into small (≤4.4 Å) interstrand distances in $A\beta_{1-16}$-M^{2+} with significant differences from M^{2+}-Aff. However, not all residues proximate to the metal ion binding site undergo significant changes in interstrand distances. For example, valine at position 12 (Val_{12}), even though adjacent to the metal ion binding site, lacks significant structural change upon metal ions binding to His_{13} and His_{14} (Figure 3.2 and Table 3.4).

It appears that significant changes in interstrand distances towards smaller (≤4.4 Å) configurations in $A\beta_{1-16}$-M^{2+} residues increase if: 1) the residues are directly involved in the metal ion binding site, 2) the residues are positively/negatively charged, or 3) the residues are polar and adjacent to the metal ion binding site. The enhanced fibrillogenesis due to charged and polar amino acids has also been described by Lopez de la Paz *et al*.[49,50] Although it is known that fibrillogenesis is sequence specific, the mechanism of the nucleating process of similarly charged residues during β-sheet lamination is not established.

3.3 Conclusions and Prospects

In recent years, many research groups have used computational and mathematical modeling as well as experimental methods to establish that M^{2+} ions intercalate between amyloidogenic peptide strands *via* coordination with His residues in an interstrand fashion. [20,51] In 2016, by employing STM, our group experimentally elucidated the position of Cu^{2+} within $A\beta_{1-16}$. This report is consistent with and extends our previous findings and expands the capabilities of STM coupled with mathematical modeling techniques as a useful tool to study secondary structures and interactions of biological systems with host molecules that cannot be accessed otherwise. Herein, by employing STM we imaged self-assembled $A\beta_{1-16}$ peptides while employing mathematical modeling to measure and to reconstruct precise interstrand

measurements of three structural categories of $A\beta_{1-16}$ oligomers intercalated with Zn^{2+} and Cu^{2+}. To our knowledge, the structural versatility of a single amyloidogenic system comprised of individual structural subcategories that we identified in lamellar assemblies of Aβ has not previously been accessed and addressed.

Though ligand kinetics were not part of this study, based on $A\beta_{1-16}$ self-assembly with M^{2+}, which resulted in different interstrand distances and inter-residue separations for Zn^{2+} and Cu^{2+}, we conclude that $A\beta_{1-16}$ Cu^{2+} interactions are stronger than Zn^{2+}. The binding strength influences $A\beta_{1-16}$ structure. From $A\beta_{1-16}$-M^{2+} intercalated with Zn^{2+} and Cu^{2+} ions, we observed that peptides intercalated with Zn^{2+} have higher structural variability. We also showed that Cu^{2+} ions induce pristine β-sheet alignment within the N-terminus, yet they distort that alignment at the C-terminus (by creating smaller than ideal interstrand distances in the vicinity of the C-terminus). Finally, we learned that Zn^{2+} ions cause β-sheet character to dissipate as distance from the M^{2+} binding site increases. We showed that the global behavior of $A\beta_{1-16}$ systems intercalated with M^{2+} is dictated by the participating metal ions. Additionally, we determined the structural differences that Zn^{2+} and Cu^{2+} create in the backbone of $A\beta_{1-16}$-M^{2+} on the single residue level. From our analyses of inter-residue separations and different types of residue frequencies, we showed that Zn^{2+} and Cu^{2+} have opposite effects onto $A\beta_{1-16}$ backbone. The distortion of the C-terminus is due to <u>strong and local</u> effects of Zn^{2+} on the $A\beta_{1-16}$ peptides, whereas Cu^{2+} stabilizes peptidyl interactions creating <u>strong and long-range</u> effects on $A\beta_{1-16}$.

We mapped Zn^{2+}– and Cu^{2+}– induced structural rearrangements in $A\beta_{1-16}$ *via* STM and image segmentation. However, outlined differences are thus far only in regards to the first 16 amino acids of the full length β-Amyloid peptide. In the next step, it will be necessary to investigate the structural arrangements of the full-length β-Amyloid and its interactions with

metal ions while the peptide is in its oligomeric form; ultimately, this study will lead to understanding and explanation of residues that are involved in the formation of reactive oxygen species – the product of metal ion and β-Amyloid interaction that is hypothesized to be detrimental to healthy brain activity.

3.4 Materials and Methods

3.4.1 Scanning Tunneling Microscopy Sample Preparation

Solutions were prepared in a glass vial with a final total volume of 400 μL for both samples ($A\beta_{1-16}$-Zn^{2+} and $A\beta_{1-16}$-Cu^{2+}). $A\beta_{1-16}$ molarity was kept constant between samples: 2.5×10^{-7} M. In the $A\beta_{1-16}$-Cu^{2+} and $A\beta_{1-16}$-Zn^{2+} samples, the final Cu^{2+} and Zn^{2+} concentrations were 2.5×10^{-5} M and 7.5×10^{-5} M, respectively. The $A\beta_{1-16}$-Zn^{2+} solution mixture was prepared by mixing 20 μL of phosphate-buffered saline at pH 7.4, 30 μL of Zn^{2+} (Sigma-Aldrich Fluka Analytical, Zinc Standard for ICP 1000 ± 2 mg/L), 200 μL of acetonitrile (Sigma-Aldrich Fluka Analytical, St. Louis, MO, purity >99.9%), 149 μL of double-distilled water, and 1 μL of $A\beta_{1-16}$ (American Peptide Company, Inc., Sunnyvale, CA, 95.4% purity). Before depositing $A\beta_{1-16}$-Zn^{2+} solution onto HOPG (SPI supplies, size: 10 mm × 10 mm × 2 mm) the surface of HOPG was cleaved with scotch tape to clean the surface and to eliminate any preexisting flakes. Both, $A\beta_{1-16}$-Zn^{2+} and $A\beta_{1-16}$-Cu^{2+}, solutions were deposited onto HOPG for a 1 min and blown off using nitrogen gas. The $A\beta_{1-16}$-Cu^{2+} solution mixture was prepared by mixing 20 μL of phosphate-buffered saline at pH 7.4, 10 μL of Cu^{2+} (Sigma-Aldrich Fluka Analytical, Copper Standard for ICP 1001 ± 2 mg/L), 200 μL of acetonitrile, 169 μL of double-distilled water, and 1 μL of $A\beta_{1-16}$ solution.

3.4.2 Scanning Tunneling Microscopy Measurements

For STM measurements, a mechanically cut Pt−Ir (80%− 20%) (Goodfellow Corp., Oakdale, PA) wire was used as the STM tip. The STM observations were carried out on a Pico SPM microscope head (Molecular Imaging, now Agilent, Santa Clara, CA) controlled by a low-noise controller (RHK Model R9, RHK Technology, Troy, MI) under ambient conditions.

3.4.3 Scanning Tunneling Microscopy Image Processing

Scanning tunneling microscopy images were processed by STM software (RHK Model R9, RHK Technology, Troy, MI) and by GWYDDION[53] (free scanning probe microscopy data analysis software). $A\beta_{1-16}$-Cu^{2+} and $A\beta_{1-16}$-Zn^{2+} peptide strands distance measurements were carried out using MATLAB (Mathworks, Natick, MA) software_distance_peptide MATLAB code.

3.4.4 Scanning Tunneling Microscopy Image Analysis

Results of software_distance_peptide MATLAB code for peptide strand distance measurements, $A\beta_{1-16}$-Cu^{2+} and $A\beta_{1-16}$-Zn^{2+}, peptide strand distance data analyses were carried out using Microsoft Office Excel.

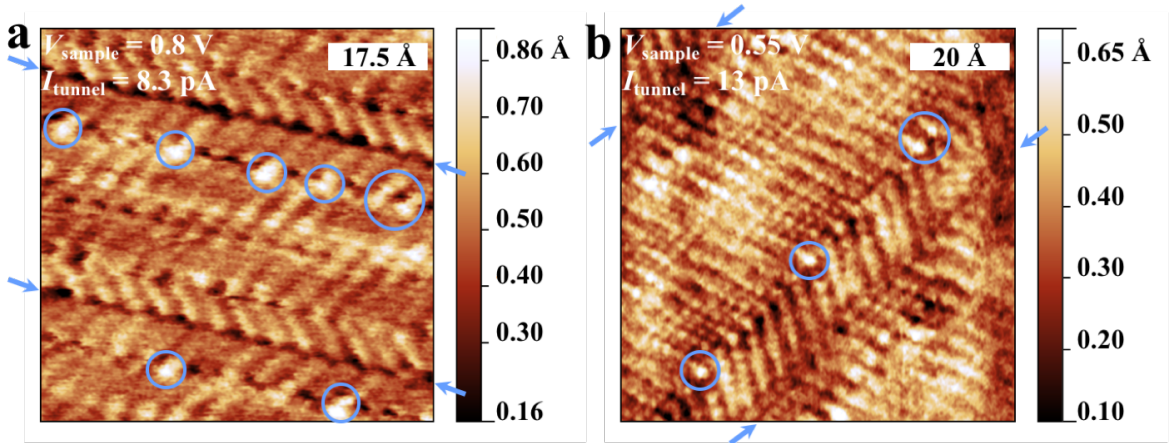

Figure 3.1. Scanning tunneling micrographs of assemblies of the 1-16 amino acid fragment of β-Amyloid ($A\beta_{1\text{-}16}$) coordinated with (a) Zn^{2+} metal ions and (b) Cu^{2+} metal ions. Blue circles highlight the non-periodic, high-intensity protrusions indicative of bound metal ions. Blue arrows highlight the boundaries of the $A\beta_{1\text{-}16}$ strands. The average interstrand distance of the assemblies was 5.17 ± 0.03 Å in the presence of Zn^{2+} and 4.82 ± 0.01 Å in the presence of Cu^{2+}, indicating that metal ion binding induces β-sheet formation in the case of Cu^{2+}, but not in the case of Zn^{2+}.

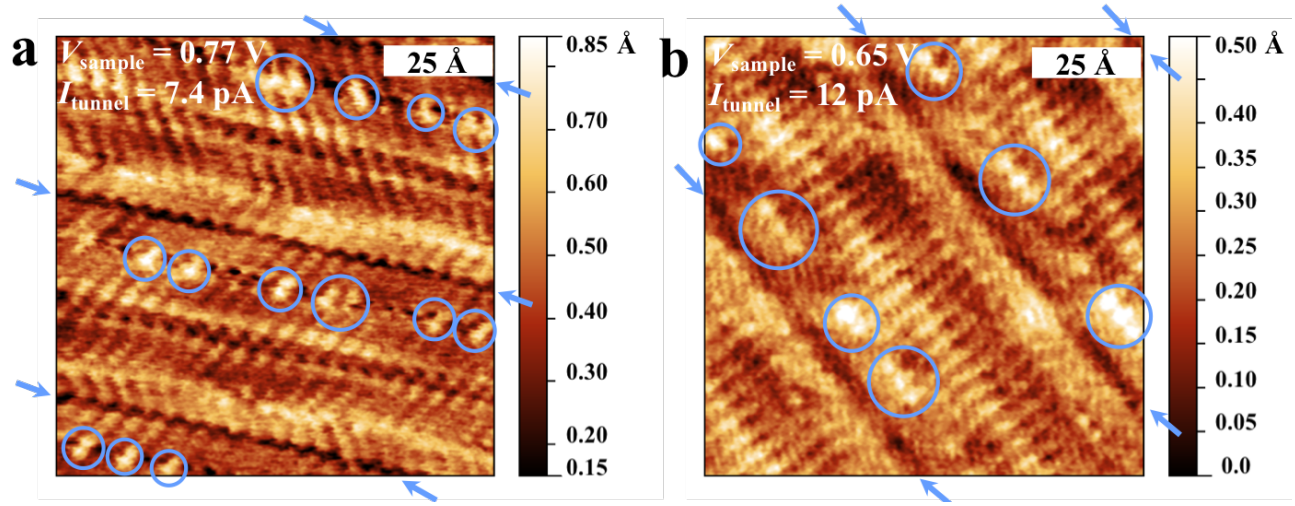

Figure 3.2. Scanning tunneling micrographs of assemblies of the 1-16 amino acid fragment of β-Amyloid ($A\beta_{1-16}$) coordinated with (a) Zn^{2+} metal ions and (b) Cu^{2+} metal ions. Blue circles highlight the non-periodic, high-intensity protrusions indicative of bound metal ions. Blue arrows highlight the boundaries of the $A\beta_{1-16}$ strands.

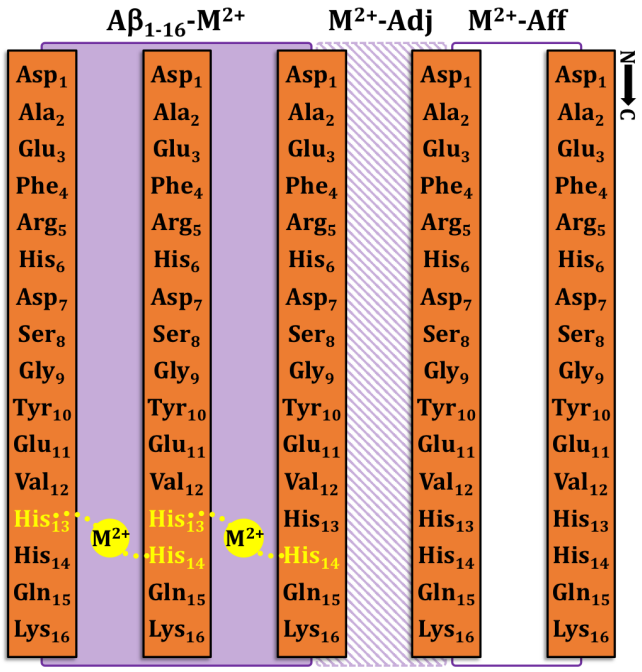

Scheme 3.1. Schematic of the study design. To analyze structural changes in $A\beta_{1\text{-}16}$ due to interactions with Zn^{2+} and Cu^{2+} ions (M^{2+}), the lamellar arrangement of the peptides was categorized into three distinct groups. The first group ($A\beta_{1\text{-}16}$-M^{2+}, shaded box on the left) consists of strands with bound metal ions in an interstrand arrangement. The histidines at position 13 (His_{13}) and 14 (His_{14}) (yellow) are the residues with a propensity to bind metal ions (M^{2+}) with an interstrand bridge. The second group (M^{2+}-Adj, dashed box in the middle) consists of pairs of strands with one strand in direct contact with M^{2+} and the second strand in an adjacent location, but not directly bound. The third group (M^{2+}-Aff, clear box on the right) consists of strands that are affiliated but lack direct contact with M^{2+} and placed a minimum of one strand away from $A\beta_{1\text{-}16}$-M^{2+}.

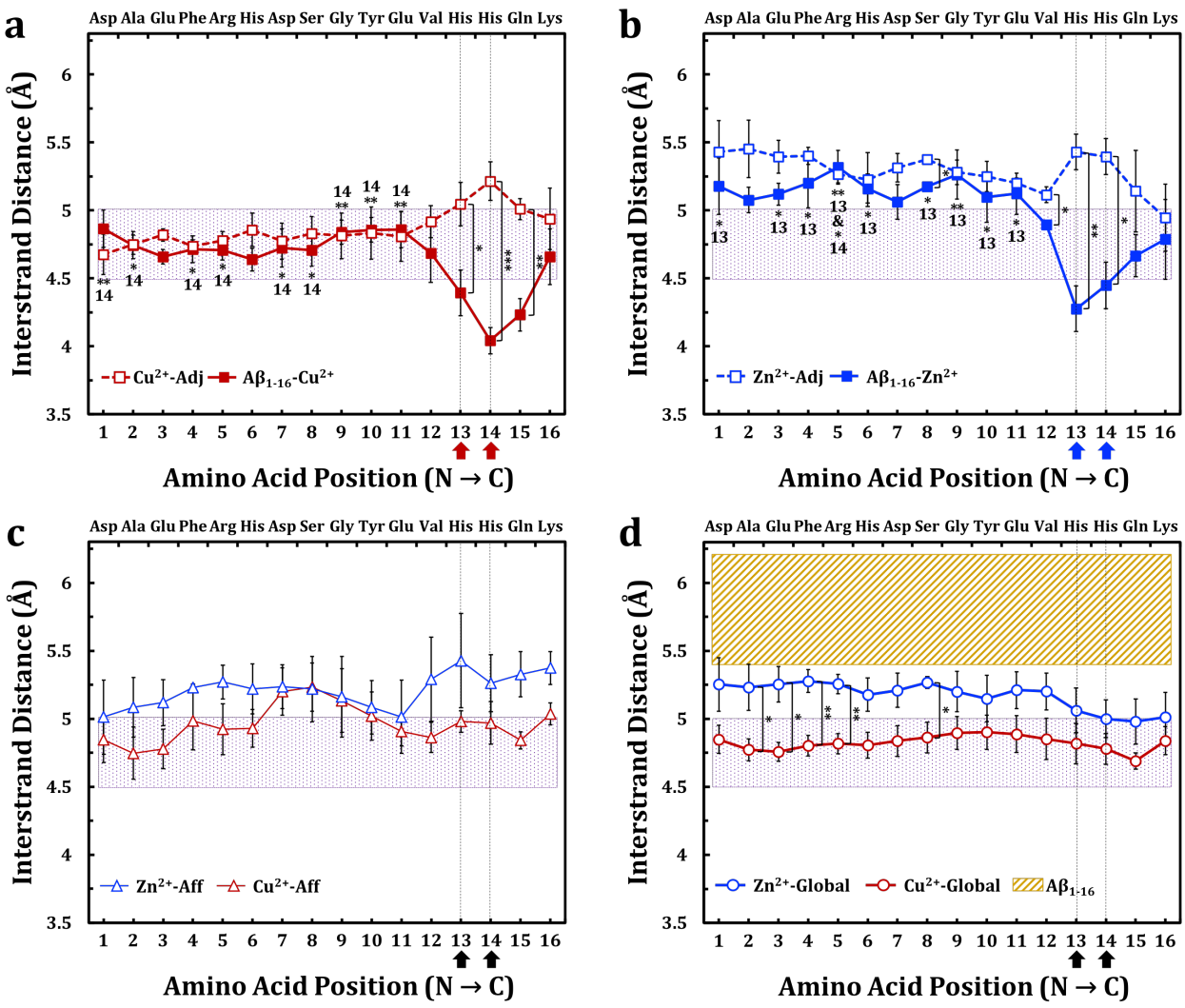

Figure 3.3. Effects of metal ions on interstrand distance in each category of $A\beta_{1\text{-}16}$ (Scheme 3.1) as measured *via* scanning tunneling microscopy. $A\beta_{1\text{-}16}$-M^{2+} (square-solid line) and M^{2+}-Adj (square-dashed line) are compared for (a) Cu^{2+} and (b) Zn^{2+}. The distinguishing feature of M^{2+}-Adj and $A\beta_{1\text{-}16}$-M^{2+} is the marginal fluctuation in interstrand distance between Asp_1 and Val_{12} followed by the pronounced increase (M^{2+}-Adj) and decrease ($A\beta_{1\text{-}16}$-M^{2+}) in interstrand separations after Val_{12}. This observation is consistent with Zn^{2+} and Cu^{2+} binding to $A\beta_{1\text{-}16}$ in interstrand fashion at the His_{13} and His_{14} positions. The ideal interstrand distance of β-sheet secondary structure is 4.5−5.0 Å (purple region).[18,21-24,26,52] Interstrand distance measurements

were collected from at least three independent experiments. Error bars represent standard error (S.E.); Tukey's HSD test was used in conjunction with one-way Anova to determine significance. Significance in $A\beta_{1-16}$-M^{2+} between specific amino acids and His_{13} (13) and His_{14} (14) are indicated (Table 3.1). Results are shown as *, $p < 0.05$; **, $p < 0.01$; and ***, $p < 0.001$. (c) Interstrand distances of $A\beta_{1-16}$ affiliated with Zn^{2+} (triangle-blue line) and Cu^{2+} (triangle-red line). Due to the absence of direct interaction with metal ions these peptides lack structural homogeneity. (d) $A\beta_{1-16}$ intercalated with Zn^{2+} (circle-blue line) and Cu^{2+} (circle-red line) metal ions. Global interstrand distance as average of $A\beta_{1-16}$-M^{2+}, M^{2+}-Adj, and M^{2+}-Aff interstrand distances. Previous studies found that the interstrand distance of $A\beta_{1-16}$ without the presence of metal ions is 5.8 ± 0.4 Å (brown region).[20]

$A\beta_{1\text{-}16}$-Zn^{2+}

	Asp_1	Ala_2	Glu_3	Phe_4	Arg_5	His_6	Asp_7	Ser_8	Gly_9	Tyr_{10}	Glu_{11}	Val_{12}	His_{13}	His_{14}	Gln_{15}	Lys_{16}
Mean (Å)	5.2	5.1	5.1	5.2	5.3	5.2	5.1	5.2	5.3	5.1	5.1	4.9	4.3	4.4	4.7	4.8
N	3	3	3	3	3	3	3	3	3	3	3	3	3	3	3	3
df	2	2	2	2	2	2	2	2	2	2	2	2	2	2	2	2
SS	0.2607	0.0533	0.0385	0.1977	0.0921	0.0670	0.0975	0.0014	0.1956	0.2053	0.1384	0.0055	0.1667	0.1730	0.1462	0.5208
SSB	4.0241	**dfb**	15	**MSB**	0.2683		**HSD for 0.05 = 5.244 →**			0.822						
SSW	2.3598	**dfw**	32	**MSW**	0.0737		**HSD for 0.01 = 6.155 →**			0.965						
k	16	**Gbl Mean**	5.0	**F**	$p < 0.05$											

Absolute Differences of the Means

	Asp_1	Ala_2	Glu_3	Phe_4	Arg_5	His_6	Asp_7	Ser_8	Gly_9	Tyr_{10}	Glu_{11}	Val_{12}	His_{13}	His_{14}	Gln_{15}	Lys_{16}
Asp_1	0	0.102	0.059	0.023	0.138	0.018	0.117	0.001	0.084	0.080	0.055	0.285	0.902	0.730	0.511	0.391
Ala_2			0.043	0.125	0.240	0.084	0.015	0.101	0.186	0.022	0.047	0.183	0.800	0.628	0.409	0.289
Glu_3				0.082	0.197	0.041	0.058	0.057	0.143	0.021	0.004	0.226	0.843	0.671	0.453	0.332
Phe_4					0.115	0.041	0.140	0.025	0.061	0.103	0.078	0.308	0.925	0.753	0.534	0.414
Arg_5						0.157	0.255	0.140	0.054	0.218	0.194	0.423	1.040	0.868	0.650	0.530
His_6							0.099	0.017	0.103	0.062	0.037	0.267	0.884	0.712	0.493	0.373
Asp_7								0.116	0.201	0.037	0.062	0.168	0.785	0.613	0.394	0.274
Ser_8									0.086	0.079	0.054	0.283	0.900	0.729	0.510	0.390
Gly_9										0.164	0.140	0.369	0.986	0.815	0.596	0.476
Tyr_{10}											0.025	0.205	0.822	0.650	0.431	0.311
Glu_{11}												0.230	0.847	0.675	0.456	0.336
Val_{12}													0.617	0.445	0.226	0.106
His_{13}														0.172	0.391	0.511
His_{14}															0.219	0.339
Gln_{15}																0.120
Lys_{16}																0

$A\beta_{1\text{-}16}$-Cu^{2+}

	Asp_1	Ala_2	Glu_3	Phe_4	Arg_5	His_6	Asp_7	Ser_8	Gly_9	Tyr_{10}	Glu_{11}	Val_{12}	His_{13}	His_{14}	Gln_{15}	Lys_{16}
Mean (Å)	4.9	4.7	4.7	4.7	4.7	4.6	4.7	4.7	4.8	4.9	4.9	4.7	4.4	4.0	4.2	4.7
N	4	4	4	4	4	4	4	4	4	4	4	4	4	4	4	4
df	3	3	3	3	3	3	3	3	3	3	3	3	3	3	3	3
SS	0.2284	0.1187	0.0333	0.1150	0.0611	0.0857	0.2358	0.1646	0.0950	0.0994	0.2129	0.5504	0.3355	0.1098	0.1708	0.5024
SSB	3.2231	**dfb**	15	**MSB**	0.2149		**HSD for 0.05 = 5.109 →**			0.651						
SSW	3.1187	**dfw**	48	**MSW**	0.0650		**HSD for 0.01 = 5.926 →**			0.755						
k	16	**Gbl Mean**	4.6	**F**	$p < 0.05$											

Absolute Differences of the Means

	Asp_1	Ala_2	Glu_3	Phe_4	Arg_5	His_6	Asp_7	Ser_8	Gly_9	Tyr_{10}	Glu_{11}	Val_{12}	His_{13}	His_{14}	Gln_{15}	Lys_{16}
Asp_1	0	0.121	0.206	0.151	0.158	0.227	0.143	0.157	0.027	0.008	0.008	0.181	0.473	0.824	0.634	0.207
Ala_2			0.085	0.030	0.037	0.105	0.022	0.036	0.094	0.113	0.113	0.060	0.351	0.703	0.513	0.085
Glu_3				0.054	0.047	0.021	0.063	0.049	0.179	0.198	0.198	0.025	0.267	0.619	0.428	0.001
Phe_4					0.007	0.075	0.009	0.006	0.124	0.143	0.143	0.030	0.321	0.673	0.482	0.055
Arg_5						0.068	0.016	0.001	0.131	0.150	0.150	0.023	0.314	0.666	0.476	0.048
His_6							0.084	0.069	0.200	0.218	0.218	0.045	0.246	0.598	0.407	0.020
Asp_7								0.014	0.116	0.135	0.135	0.038	0.330	0.682	0.491	0.064
Ser_8									0.130	0.149	0.149	0.024	0.315	0.667	0.477	0.049
Gly_9										0.019	0.019	0.154	0.445	0.797	0.607	0.179
Tyr_{10}											0.000	0.173	0.464	0.816	0.626	0.198
Glu_{11}												0.173	0.464	0.816	0.626	0.198
Val_{12}													0.291	0.643	0.453	0.025
His_{13}														0.352	0.161	0.266
His_{14}															0.190	0.618
Gln_{15}																0.427
Lys_{16}																0

Table 3.1. Tukey's HSD test was used to determine statistical significance of interstrand distances between amino acid pairs of $A\beta_{1\text{-}16}$-Zn^{2+} and $A\beta_{1\text{-}16}$-Cu^{2+}. In $A\beta_{1\text{-}16}$-Zn^{2+} – Asp_1, Glu_3, Phe_4, Arg_5, His_6, Ser_8, Gly_9, Tyr_{10}, Glu_{11} are significantly different to His_{13} and His_{14}; while in $A\beta_{1\text{-}16}$-Cu^{2+} – Asp_1, Ala_2, Phe_4, Arg_5, Asp_7, Ser_8, Gly_9, Tyr_{10}, Glu_{11}, Val_{12} are significantly

different to His_{14}. Underlined values represent confidence interval of 0.01, red values represent confidence intervals of 0.05.

Amino Acids	Mean (Å)	S.D.	S.E.	Mean (Å)	S.D.	S.E.	Mean (Å)	S.D.	S.E.	Mean (Å)	S.D.	S.E.
	$A\beta_{1-16}$-Zn^{2+}			Zn^{2+}-Adj			Zn^{2+}-Aff			Zn^{2+}-Global		
Asp_1	5.2	0.36	0.21	5.4	0.40	0.23	5.0	0.47	0.27	5.3	0.34	0.20
Ala_2	5.1	0.16	0.09	5.5	0.36	0.21	5.1	0.38	0.22	5.2	0.29	0.17
Glu_3	5.1	0.14	0.08	5.4	0.21	0.12	5.1	0.29	0.17	5.3	0.23	0.13
Phe_4	5.2	0.31	0.18	5.4	0.11	0.06	5.2	0.05	0.03	5.3	0.14	0.08
Arg_5	5.3	0.21	0.12	5.3	0.11	0.06	5.3	0.21	0.12	5.3	0.12	0.07
His_6	5.2	0.18	0.11	5.2	0.34	0.20	5.2	0.32	0.18	5.2	0.21	0.12
Asp_7	5.1	0.22	0.13	5.3	0.18	0.11	5.2	0.28	0.16	5.2	0.22	0.13
Ser_8	5.2	0.03	0.02	5.4	0.05	0.03	5.2	0.42	0.24	5.3	0.07	0.04
Gly_9	5.3	0.31	0.18	5.3	0.16	0.09	5.2	0.51	0.30	5.2	0.26	0.15
Tyr_{10}	5.1	0.32	0.18	5.2	0.19	0.11	5.1	0.34	0.20	5.1	0.30	0.17
Glu_{11}	5.1	0.26	0.15	5.2	0.07	0.04	5.0	0.47	0.27	5.2	0.23	0.13
Val_{12}	4.9	0.05	0.03	5.1	0.10	0.06	5.3	0.54	0.31	5.2	0.24	0.14
His_{13}	4.3	0.29	0.17	5.4	0.23	0.13	5.4	0.60	0.35	5.1	0.28	0.16
His_{14}	4.4	0.29	0.17	5.4	0.23	0.13	5.3	0.36	0.21	5.0	0.24	0.14
Gln_{15}	4.7	0.27	0.16	5.1	0.52	0.30	5.3	0.29	0.17	5.0	0.29	0.17
Lys_{16}	4.8	0.51	0.29	4.9	0.43	0.25	5.4	0.21	0.12	5.0	0.31	0.18
Mean	5.0	0.30	0.07	5.3	0.14	0.03	5.2	0.12	0.03	5.2	0.10	0.03
	$A\beta_{1-16}$-Cu^{2+}			Cu^{2+}-Adj			Cu^{2+}-Aff			Cu^{2+}-Global		
Asp_1	4.9	0.28	0.14	4.7	0.30	0.15	4.8	0.29	0.17	4.8	0.21	0.10
Ala_2	4.7	0.20	0.10	4.7	0.14	0.07	4.7	0.33	0.19	4.8	0.16	0.08
Glu_3	4.7	0.11	0.05	4.8	0.09	0.05	4.8	0.25	0.15	4.8	0.14	0.07
Phe_4	4.7	0.20	0.10	4.7	0.10	0.05	5.0	0.37	0.21	4.8	0.15	0.08
Arg_5	4.7	0.14	0.07	4.8	0.13	0.07	4.9	0.32	0.19	4.8	0.15	0.07
His_6	4.6	0.17	0.08	4.9	0.25	0.12	4.9	0.24	0.14	4.8	0.19	0.10
Asp_7	4.7	0.28	0.14	4.8	0.26	0.13	5.2	0.30	0.18	4.8	0.23	0.11
Ser_8	4.7	0.23	0.12	4.8	0.25	0.12	5.2	0.31	0.18	4.9	0.23	0.11
Gly_9	4.8	0.18	0.09	4.8	0.34	0.17	5.1	0.41	0.23	4.9	0.24	0.12
Tyr_{10}	4.9	0.18	0.09	4.8	0.38	0.19	5.0	0.31	0.18	4.9	0.25	0.13
Glu_{11}	4.9	0.27	0.13	4.8	0.37	0.18	4.9	0.18	0.11	4.9	0.27	0.13
Val_{12}	4.7	0.43	0.21	4.9	0.24	0.12	4.9	0.19	0.11	4.9	0.31	0.15
His_{13}	4.4	0.33	0.17	5.0	0.32	0.16	5.0	0.14	0.08	4.8	0.30	0.15
His_{14}	4.0	0.19	0.10	5.2	0.29	0.14	5.0	0.27	0.16	4.8	0.23	0.11
Gln_{15}	4.2	0.24	0.12	5.0	0.15	0.08	4.8	0.11	0.06	4.7	0.12	0.06
Lys_{16}	4.7	0.41	0.20	4.9	0.45	0.23	5.0	0.14	0.08	4.8	0.21	0.10
Mean	4.6	0.23	0.06	4.9	0.14	0.03	5.0	0.14	0.04	4.8	0.06	0.01

Table 3.2. Statistical results (Mean, standard deviation, S.D., of the mean, and standard error, S.E., of the mean) of interstrand distance measurements per each amino acid for all studied $A\beta_{1-16}$ categories.

Amino Acids	Zn^{2+}-Global *vs.* Cu^{2+}-Global		Zn^{2+}-Aff *vs.* Cu^{2+}-Aff		$A\beta_{1-16}$-Zn^{2+} *vs.* Zn^{2+}-Adj		$A\beta_{1-16}$-Cu^{2+} *vs.* Cu^{2+}-Adj		$A\beta_{1-16}$-Zn^{2+} *vs.* $A\beta_{1-16}$-Cu^{2+}		Zn^{2+}-Adj *vs.* Cu^{2+}-Adj	
Asp_1	0.1058	ns	0.6317	ns	0.4652	ns	0.4652	ns	0.2477	ns	0.0345	*
Ala_2	0.0438	*	0.3100	ns	0.1770	ns	0.1770	ns	0.0663	ns	0.0154	*
Glu_3	0.0148	*	0.2012	ns	0.1300	ns	0.1300	ns	0.0040	**	0.0040	**
Phe_4	0.0086	**	0.3149	ns	0.3543	ns	0.3543	ns	0.0512	ns	0.0004	***
Arg_5	0.0086	**	0.1972	ns	0.7379	ns	0.7379	ns	0.0061	**	0.0037	**
His_6	0.0591	ns	0.2765	ns	0.7798	ns	0.7798	ns	0.0114	*	0.1556	ns
Asp_7	0.0802	ns	0.8900	ns	0.2008	ns	0.2008	ns	0.1470	ns	0.0299	*
Ser_8	0.0338	*	0.9645	ns	0.0038	**	0.0038	**	0.0200	*	0.0147	*
Gly_9	0.1686	ns	0.9459	ns	0.9344	ns	0.9344	ns	0.0695	ns	0.0797	ns
Tyr_{10}	0.2865	ns	0.8217	ns	0.5228	ns	0.5228	ns	0.2580	ns	0.1510	ns
Glu_{11}	0.1588	ns	0.7273	ns	0.6432	ns	0.6432	ns	0.2467	ns	0.1332	ns
Val_{12}	0.1633	ns	0.2640	ns	0.0270	*	0.0270	*	0.4493	ns	0.2362	ns
His_{13}	0.3218	ns	0.2758	ns	0.0055	**	0.0055	**	0.6497	ns	0.1378	ns
His_{14}	0.2684	ns	0.3256	ns	0.0118	*	0.0118	*	0.0753	ns	0.4123	ns
Gln_{15}	0.1200	ns	0.0523	ns	0.2328	ns	0.2328	ns	0.0731	ns	0.6397	ns
Lys_{16}	0.4164	ns	0.0825	ns	0.6999	ns	0.6999	ns	0.7264	ns	0.9816	ns
Mean	0.0518	ns	0.2534	ns	0.0501	*	0.0501	*	0.0584	ns	0.0165	*

Table 3.3. Comparison of interstrand distance measurements of different $A\beta_{1-16}$ categories per each amino acid pair *via* one-way Anova; amino acids with significant difference are outlined in red. Measurements were collected from at least three independent sets of experiments. Results are shown as *, $p < 0.05$; **, $p < 0.01$; and ***, $p < 0.001$.

Segment	Mean (Å)	SD	SE	*vs.* Ideal (upper limit: 5.0 Å)	*vs.* Ideal (lower limit: 4.5 Å)	*vs.* mean of 1-16	*vs.* mean of 1-11
				$A\beta_{1-16}$-Cu^{2+}			
1-16	4.6	0.23	0.06	-7%	3%	-	-2%
1-11	4.8	0.08	0.03	-5%	6%	2%	-
12-16	4.4	0.28	0.14	-12%	-2%	-5%	-7%
His_{13}	4.4	0.33	0.17	-12%	-2%	-5%	-8%
His_{14}	4.0	0.19	0.10	-19%	-10%	-13%	-15%
				Cu^{2+}-Adj			
1-16	4.9	0.14	0.03	-3%	8%	-	2%
1-11	4.8	0.05	0.02	-4%	6%	-2%	-
12-16	5.0	0.12	0.06	-	12%	3%	5%
His_{13}	5.0	0.32	0.16	1%	12%	4%	5%
His_{14}	5.2	0.29	0.14	4%	16%	7%	9%
				Cu^{2+}-Aff			
1-16	5.0	0.14	0.04	-1%	10%	-	-
1-11	5.0	0.16	0.05	-1%	11%	-	-
12-16	4.9	0.08	0.04	-1%	10%	-0.5%	-1%
His_{13}	5.0	0.14	0.08	-	11%	-	-
His_{14}	5.0	0.27	0.16	-1%	10%	-	-
				Cu^{2+}-Global			
1-16	4.8	0.06	0.01	-4%	7%	-	-
1-11	4.8	0.05	0.01	-3%	7%	-	-
12-16	4.8	0.07	0.03	-4%	7%	-1%	-1%
His_{13}	4.8	0.30	0.15	-4%	7%	-	-
His_{14}	4.8	0.23	0.11	-4%	6%	-1%	-1%
				$A\beta_{1-16}$-Zn^{2+}			
1-16	5.0	0.30	0.07	-	11%	-	-3%
1-11	5.2	0.08	0.02	3%	15%	3%	-
12-16	4.6	0.25	0.13	-8%	3%	-8%	-11%
His_{13}	4.3	0.29	0.17	-14%	-5%	-14%	-17%
His_{14}	4.4	0.29	0.17	-11%	-1%	-11%	-14%
				Zn^{2+}-Adj			
1-16	5.3	0.14	0.03	6%	18%	-	-1%
1-11	5.3	0.09	0.03	7%	18%	1%	-
12-16	5.2	0.20	0.10	4%	16%	-2%	-2%
His_{13}	5.4	0.23	0.13	9%	21%	3%	2%
His_{14}	5.4	0.23	0.13	8%	20%	2%	1%
				Zn^{2+}-Aff			
1-16	5.2	0.12	0.03	4%	16%	-	1%
1-11	5.1	0.09	0.03	3%	14%	-1%	-
12-16	5.3	0.07	0.03	7%	19%	2%	4%
His_{13}	5.4	0.60	0.35	9%	21%	4%	5%
His_{14}	5.3	0.36	0.21	5%	17%	1%	2%
				Zn^{2+}-Global			
1-16	5.2	0.10	0.03	3%	15%	-	-1%
1-11	5.2	0.04	0.01	5%	16%	1%	-
12-16	5.1	0.09	0.04	1%	12%	-2%	-3%
His_{13}	5.1	0.28	0.16	1%	12%	-2%	-3%
His_{14}	5.0	0.24	0.14	-	11%	-3%	-4%

Table 3.4. Comparison of average interstrand distance values of the full length $A\beta_{1-16}$ peptide (1-16), first 11 residues from the N-terminus (1-11), last 4 residues of C-terminus (12-16), His13 and His 14 to ideal interstrand distance (upper 5.0 Å and lower values 4.5 Å), average of 1-16 and 1-11 residues of $A\beta_{1-16}$ peptide. Positive values represent increases in interstrand distance while negative values represent decreases in interstrand distance between examined pairs.

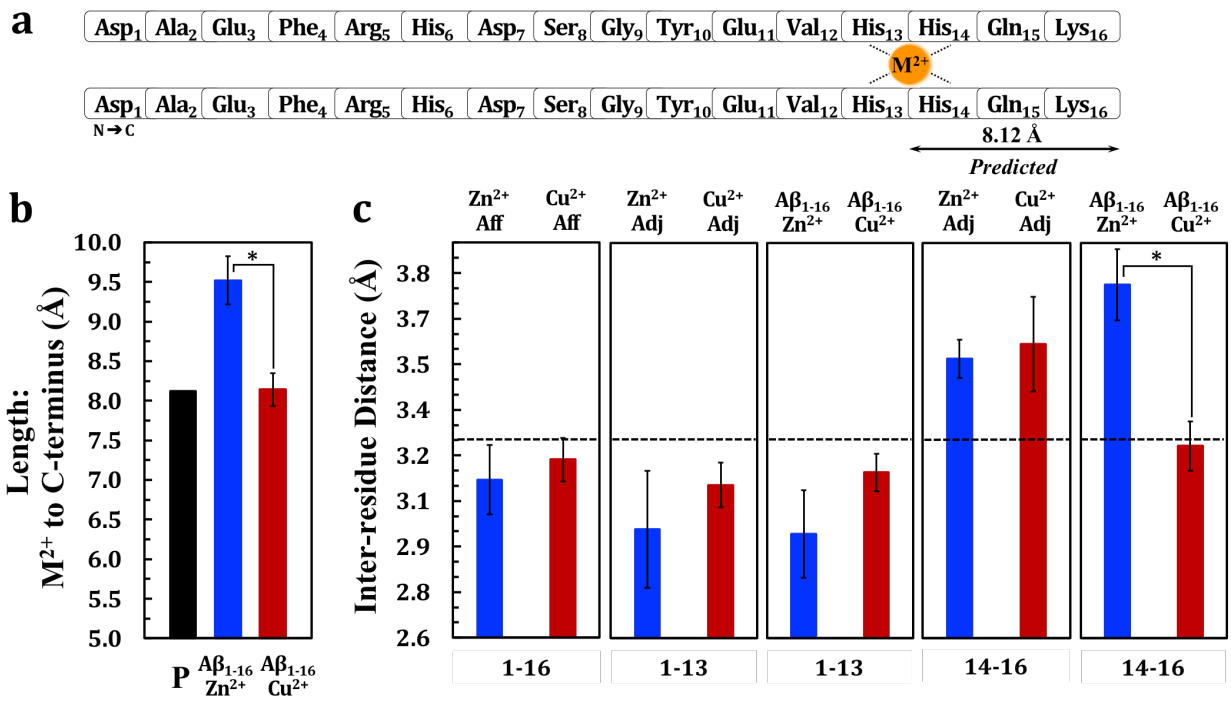

Figure 3.4. (a) Scheme of $A\beta_{1\text{-}16}$ sequence with a bound metal ion. Predicted distance from the metal ion binding site to the C-terminus is 8.12 Å. (b) Comparison between length from the metal ion binding site to the C-terminus of predicted (P) $A\beta_{1\text{-}16}$ (black) and measured $A\beta_{1\text{-}16}$-Zn^{2+} (blue) and $A\beta_{1\text{-}16}$-Cu^{2+} (red). Total length of $A\beta_{1\text{-}16}$-Zn^{2+} is significantly ($p = 0.0117$) greater in comparison to $A\beta_{1\text{-}16}$-Cu^{2+}, 9.52 ± 0.3 Å and 8.14 ± 0.2 Å, respectively. (c) Comparison of inter-residue distances of the three $A\beta_{1\text{-}16}$ strand categories (Scheme 3.1) and two segments based on deformation due to ion binding (residues 1-13 *vs.* residues 14-16). Residues that are not in direct contact with M^{2+} show compact, less than ideal, inter-residue separations of 3.25 Å – dashed black line (Panels 1-3). Residues adjacent to M^{2+} binding site show distorted, larger than ideal residue-residue distances. This distortion is most likely due to vacancies created by the metal ion binding between strands of $A\beta_{1\text{-}16}$-M^{2+} and M^{2+}-Adj. These peptides, in the residue 14-16 segment, show higher than ideal inter-residue separations (Panel 4). Zn^{2+} (blue) and Cu^{2+} (red) have different effects on the C-terminus of $A\beta_{1\text{-}16}$-M^{2+} (Panel 5). This difference can be

observed from significantly larger (p = 0.0117) inter-residue distances of $A\beta_{1\text{-}16}$-Zn^{2+} than $A\beta_{1\text{-}16}$-Cu^{2+} in residues 14-16. Zn^{2+} ions create a strong, local effect on the C-terminus of $A\beta_{1\text{-}16}$-M^{2+}, which ultimately leads to a distortion of the C-terminus. Cu^{2+} ions, in contrast to Zn^{2+}, show a strong and long-range effect on $A\beta_{1\text{-}16}$-M^{2+}. This effect ultimately contributes to the stabilizing interactions between neighboring peptide strands that results in the overall greater β-sheet character. Measurements were collected from at least three independent sets of experiments. Error bars represent standard error (S.E.); to determine significance one-way Anova was used. Results are shown as *, $p < 0.05$; **, $p < 0.01$; and ***, $p < 0.001$.

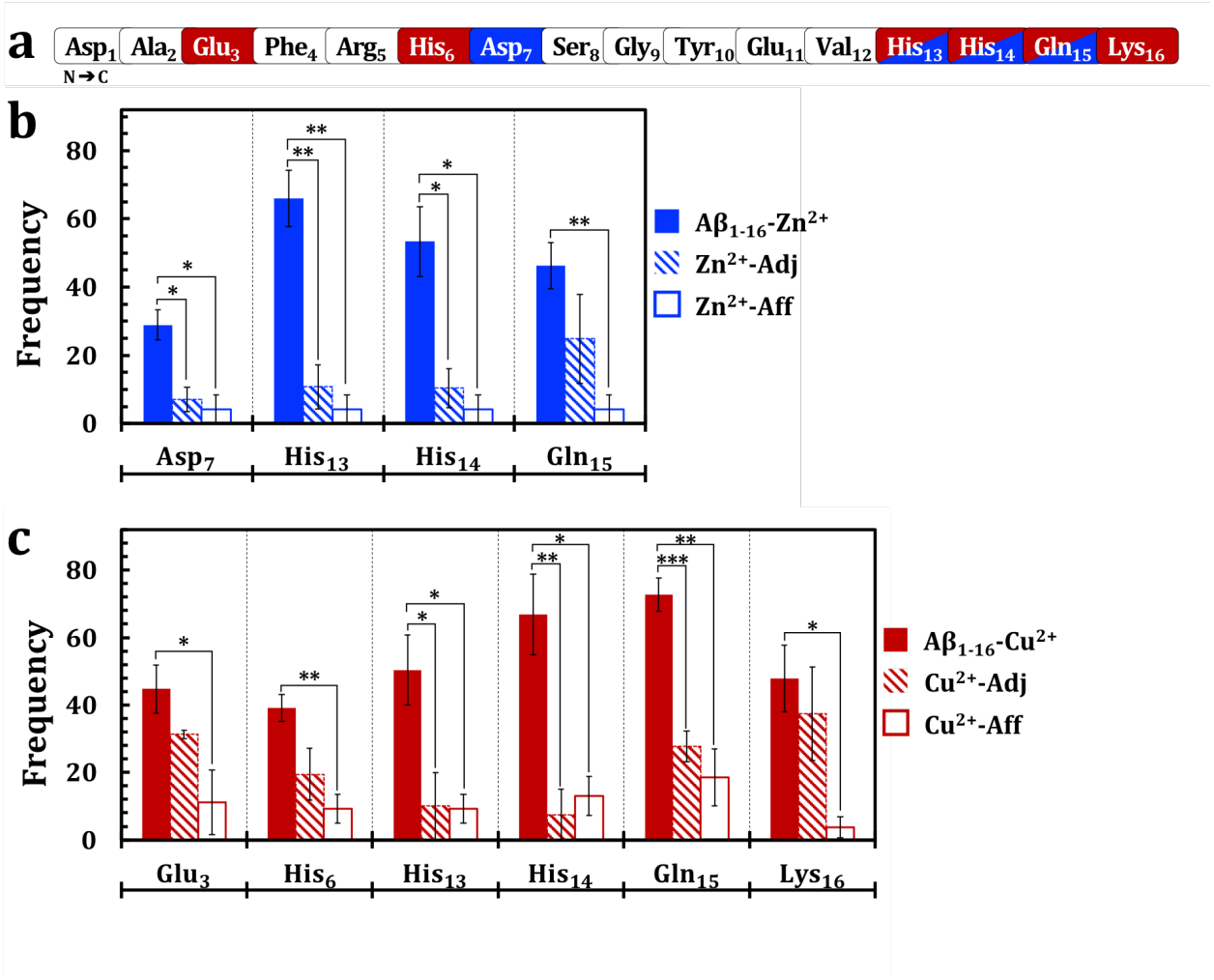

Figure 3.5. (a) $A\beta_{1-16}$ sequence; upon Cu^{2+} (red) and Zn^{2+} (blue) binding to $A\beta_{1-16}$ in interstrand fashion between His_{13} and His_{14} the highlighted amino acids undergo structural deformation acquiring interstrand distances smaller (≤4.4 Å) than the ideal β-sheet range (4.5−5.0 Å). Both metal ions have prominent structural effects on certain residues (highlighted), which ultimately lead to global ordering of $A\beta_{1-16}$ peptides (for more details see Figure 3.6 and Table 3.5). (b) Residues prone to structural deformation upon $A\beta_{1-16}$ interaction with Zn^{2+}, besides His_{13} and His_{14}, are Asp_7 and Gln_{15}. (c) Affected residues, besides His_{13} and His_{14}, in $A\beta_{1-16}$ due to Cu^{2+} binding are Glu_3, His_6, Gln_{15}, and Lys_{16}. Compared to Cu^{2+}-Aff these residues undergo significant strand-to-strand deformation towards adapting small (≤4.4 Å) interstrand distance

with similar residues from adjacent strands. Measurements were collected from at least three independent experiments. Error bars represent standard error (S.E.); to determine significance, one-way Anova was used. Results are shown as *, $p < 0.05$; **, $p < 0.01$; and ***, $p < 0.001$.

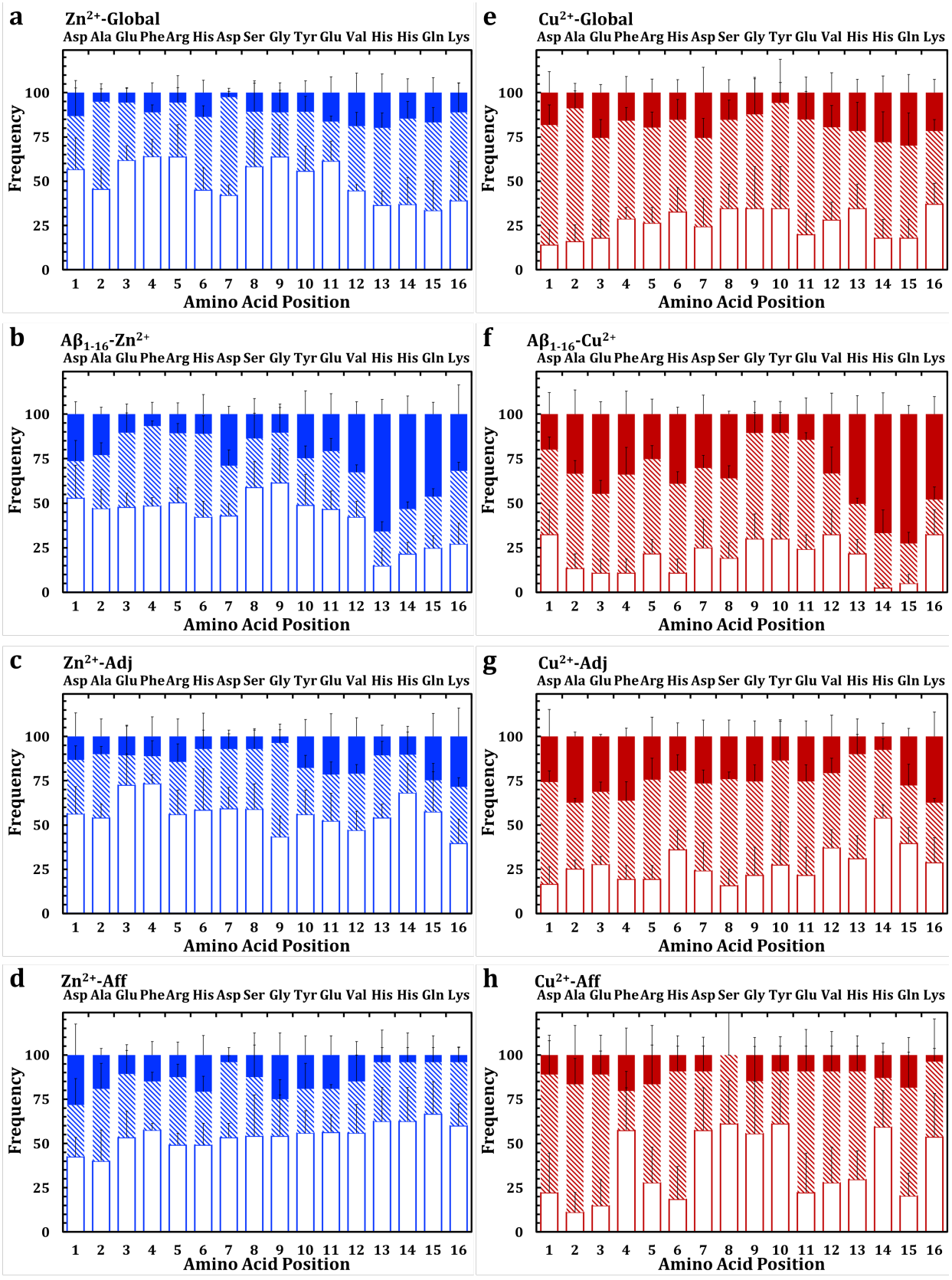
a
Zn2+-Global
e
Cu2+-Global
b
Aβ1-16-Zn2+
f
Aβ1-16-Cu2+
c
Zn2+-Adj
g
Cu2+-Adj
d
Zn2+-Aff
h
Cu2+-Aff
Asp Ala Glu Phe Arg His Asp Ser Gly Tyr Glu Val His His Gln Lys
Frequency
0
25
50
75
100
1 2 3 4 5 6 7 8 9 10 11 12 13 14 15 16
Amino Acid Position
Zn2+ Cu2+
Small (≤4.4 Å)
Normal (4.5–5.0 Å)
Large (≥5.1 Å)

Figure 3.6. Amino acid frequencies in three interstrand distance categories: small (≤4.4 Å), ideal β-sheet range (4.5−5.0 Å), and large (≥5.1 Å) for $A\beta_{1\text{-}16}$ categories and their corresponding frequencies of residues in those categories. Error bars represent standard error (S.E.)

	Small (≤4.4 Å)						Normal (4.5 Å–5.0 Å)						Large (≥5.1 Å)					
	$A\beta_{1-16}$-Cu^{2+} *vs.* Cu^{2+}-Aff		$A\beta_{1-16}$-Cu^{2+} *vs.* Cu^{2+}-Adj		Cu^{2+}-Adj *vs.* Cu^{2+}-Aff		$A\beta_{1-16}$-Cu^{2+} *vs.* Cu^{2+}-Aff		$A\beta_{1-16}$-Cu^{2+} *vs.* Cu^{2+}-Adj		Cu^{2+}-Adj *vs.* Cu^{2+}-Aff		$A\beta_{1-16}$-Cu^{2+} *vs.* Cu^{2+}-Aff		$A\beta_{1-16}$-Cu^{2+} *vs.* Cu^{2+}-Adj		Cu^{2+}-Adj *vs.* Cu^{2+}-Aff	
Asp_1	0.628	ns	0.780	ns	0.504	ns	0.342	ns	0.332	ns	0.632	ns	0.694	ns	0.379	ns	0.809	ns
Ala_2	0.466	ns	0.792	ns	0.205	ns	0.263	ns	0.092	ns	0.040	*	0.875	ns	0.256	ns	0.252	ns
Glu_3	0.043	*	0.110	ns	0.084	ns	0.093	ns	0.729	ns	0.051	ns	0.807	ns	0.112	ns	0.383	ns
Phe_4	0.524	ns	0.870	ns	0.302	ns	0.167	ns	0.581	ns	0.219	ns	0.090	ns	0.465	ns	0.146	ns
Arg_5	0.641	ns	0.956	ns	0.701	ns	0.911	ns	0.837	ns	0.979	ns	0.763	ns	0.844	ns	0.679	ns
His_6	0.005	**	0.062	ns	0.356	ns	0.286	ns	0.647	ns	0.223	ns	0.688	ns	0.111	ns	0.426	ns
Asp_7	0.175	ns	0.804	ns	0.199	ns	0.556	ns	0.682	ns	0.427	ns	0.293	ns	0.972	ns	0.281	ns
Ser_8	0.000	***	0.250	ns	0.080	ns	0.799	ns	0.110	ns	0.355	ns	0.122	ns	0.798	ns	0.106	ns
Gly_9	0.736	ns	0.237	ns	0.458	ns	0.223	ns	0.679	ns	0.295	ns	0.428	ns	0.706	ns	0.322	ns
Tyr_{10}	0.890	ns	0.811	ns	0.732	ns	0.223	ns	0.986	ns	0.389	ns	0.288	ns	0.932	ns	0.383	ns
Glu_{11}	0.674	ns	0.413	ns	0.207	ns	0.742	ns	0.435	ns	0.522	ns	0.930	ns	0.892	ns	0.984	ns
Val_{12}	0.159	ns	0.481	ns	0.472	ns	0.316	ns	0.659	ns	0.375	ns	0.847	ns	0.794	ns	0.669	ns
His_{13}	0.024	*	0.031	*	0.955	ns	0.112	ns	0.038	*	0.923	ns	0.648	ns	0.557	ns	0.946	ns
His_{14}	0.017	*	0.006	**	0.625	ns	0.891	ns	0.609	ns	0.491	ns	0.023	*	0.001	***	0.798	ns
Gln_{15}	0.003	**	0.001	***	0.390	ns	0.088	ns	0.476	ns	0.251	ns	0.269	ns	0.015	*	0.262	ns
Lys_{16}	0.014	*	0.557	ns	0.099	ns	0.340	ns	0.105	ns	0.684	ns	0.453	ns	0.856	ns	0.388	ns
	$A\beta_{1-16}$-Zn^{2+} *vs.* Zn^{2+}-Aff		$A\beta_{1-16}$-Zn^{2+} *vs.* Zn^{2+}-Adj		Zn^{2+}-Adj *vs.* Zn^{2+}-Aff		$A\beta_{1-16}$-Zn^{2+} *vs.* Zn^{2+}-Aff		$A\beta_{1-16}$-Zn^{2+} *vs.* Zn^{2+}-Adj		Zn^{2+}-Adj *vs.* Zn^{2+}-Aff		$A\beta_{1-16}$-Zn^{2+} *vs.* Zn^{2+}-Aff		$A\beta_{1-16}$-Zn^{2+} *vs.* Zn^{2+}-Adj		Zn^{2+}-Adj *vs.* Zn^{2+}-Aff	
Asp_1	0.919	ns	0.438	ns	0.531	ns	0.680	ns	0.532	ns	0.947	ns	0.649	ns	0.896	ns	0.505	ns
Ala_2	0.514	ns	0.293	ns	0.438	ns	0.536	ns	0.510	ns	0.762	ns	0.749	ns	0.622	ns	0.504	ns
Glu_3	0.958	ns	0.968	ns	0.992	ns	0.746	ns	0.276	ns	0.421	ns	0.757	ns	0.265	ns	0.448	ns
Phe_4	0.457	ns	0.749	ns	0.787	ns	0.044	*	0.033	*	0.303	ns	0.205	ns	0.022	*	0.068	ns
Arg_5	0.864	ns	0.769	ns	0.881	ns	0.954	ns	0.473	ns	0.528	ns	0.914	ns	0.747	ns	0.680	ns
His_6	0.568	ns	0.744	ns	0.299	ns	0.283	ns	0.618	ns	0.850	ns	0.668	ns	0.547	ns	0.738	ns
Asp_7	0.015	*	0.018	*	0.627	ns	0.207	ns	0.674	ns	0.403	ns	0.372	ns	0.303	ns	0.704	ns
Ser_8	0.941	ns	0.519	ns	0.696	ns	0.810	ns	0.733	ns	0.974	ns	0.871	ns	1.000	ns	0.871	ns
Gly_9	0.348	ns	0.387	ns	0.178	ns	0.704	ns	0.234	ns	0.104	ns	0.820	ns	0.466	ns	0.698	ns
Tyr_{10}	0.756	ns	0.688	ns	0.928	ns	0.940	ns	1.000	ns	0.940	ns	0.761	ns	0.766	ns	0.996	ns
Glu_{11}	0.926	ns	0.968	ns	0.897	ns	0.342	ns	0.562	ns	0.824	ns	0.536	ns	0.781	ns	0.837	ns
Val_{12}	0.166	ns	0.418	ns	0.664	ns	0.811	ns	0.371	ns	0.874	ns	0.503	ns	0.746	ns	0.674	ns
His_{13}	0.003	**	0.006	**	0.439	ns	0.500	ns	0.180	ns	0.930	ns	0.090	ns	0.035	*	0.703	ns
His_{14}	0.011	*	0.021	*	0.433	ns	0.660	ns	0.797	ns	0.603	ns	0.112	ns	0.058	ns	0.834	ns
Gln_{15}	0.006	**	0.218	ns	0.207	ns	0.987	ns	0.356	ns	0.559	ns	0.098	ns	0.242	ns	0.766	ns
Lys_{16}	0.180	ns	0.892	ns	0.216	ns	0.624	ns	0.262	ns	0.714	ns	0.125	ns	0.524	ns	0.331	ns

Table 3.5. Comparison of interstrand distance frequencies (Figures 3.5 and 3.6) of different $A\beta_{1-16}$ categories per each amino acid pair *via* one-way Anova; amino acids with significant difference are outlined in red. Measurements were collected from at least three independent experiments. Results are shown as *, $p < 0.05$; **, $p < 0.01$; and ***, $p < 0.001$.

3.5 References

1. Goldman, L.; Schaffer, A. I., *Goldman's Cecil Medicine*. Elsevier Saunders: Philadelphia, PA, 2011.

2. Alzheimer's Association. 2018 Alzheimer's Disease Facts and Figures. *Alzheimers Dement* **2018,** *14,* 367−425.

3. Zhu, C. W.; Sano, M. Economic Considerations in the Management of Alzheimer's Disease. *Clin Interv Aging* **2006,** *1,* 143−154.

4. Hebert, L. E.; Weuve, J.; Scherr, P. A.; Evans, D. A. Alzheimer Disease in the United States (2010–2050) Estimated Using the 2010 Census. *Neurology* **2013,** *80,* 1778−1783.

5. Butterfield, D. A.; Halliwell, B. Oxidative Stress, Dysfunctional Glucose Metabolism and Alzheimer Disease. *Nat Rev Neurosci* **2019,** *20,* 148−160.

6. Goldsworthy, M. R.; Vallence, A. M. The Role of β-Amyloid in Alzheimer's Disease-Related Neurodegeneration. *J Neurosci* **2013,** *33,* 12910−12911.

7. Gremer, L.; Scholzel, D.; Schenk, C.; Reinartz, E.; Labahn, J.; Ravelli, R. B. G.; Tusche, M.; Lopez-Iglesias, C.; Hoyer, W.; Heise, H.; Willbold, D.; Schroder, G. F. Fibril Structure of Amyloid-β(1-42) by Cryo-Electron Microscopy. *Science* **2017,** *358,* 116−119.

8. Fandrich, M.; Meinhardt, J.; Grigorieff, N. Structural Polymorphism of Alzheimer Aβ and Other Amyloid Fibrils. *Prion* **2009,** *3,* 89−93.

9. Colletier, J. P.; Laganowsky, A.; Landau, M.; Zhao, M.; Soriaga, A. B.; Goldschmidt, L.; Flot, D.; Cascio, D.; Sawaya, M. R.; Eisenberg, D. Molecular Basis for Amyloid-β Polymorphism. *Proc Natl Acad Sci USA* **2011,** *108,* 16938−16943.

10. Brody, D. L.; Jiang, H.; Wildburger, N.; Esparza, T. J. Non-Canonical Soluble Amyloid-β Aggregates and Plaque Buffering: Controversies and Future Directions for Target Discovery in Alzheimer's Disease. *Alzheimers Res Ther* **2017,** *9,* 62.

11. del Barrio, M.; Borghesani, V.; Hureau, C.; Faller, P., Chapter 14 - Metal-Binding to Amyloid-β Peptide: Coordination, Aggregation, and Reactive Oxygen Species Production. In *Biometals in Neurodegenerative Diseases*, White, A. R.; Aschner, M.; Costa, L. G.; Bush, A. I., Eds. Academic Press: 2017; pp 265−281.

12. Rana, M.; Sharma, A. K. Cu and Zn Interactions with Aβ Peptides: Consequence of Coordination on Aggregation and Formation of Neurotoxic Soluble Aβ Oligomers. *Metallomics* **2019,** *11,* 64−84.

13. Gerber, H.; Wu, F.; Dimitrov, M.; Garcia Osuna, G. M.; Fraering, P. C. Zinc and Copper Differentially Modulate Amyloid Precursor Protein Processing by γ-Secretase and Amyloid-β Peptide Production. *J Biol Chem* **2017,** *292,* 3751−3767.

14. Lovell, M. A.; Robertson, J. D.; Teesdale, W. J.; Campbell, J. L.; Markesbery, W. R. Copper, Iron and Zinc in Alzheimer's Disease Senile Plaques. *J Neurol Sci* **1998,** *158,* 47−52.

15. Roberts, B. R.; Ryan, T. M.; Bush, A. I.; Masters, C. L.; Duce, J. A. The Role of Metallobiology and Amyloid-β Peptides in Alzheimer's Disease. *J Neurochem* **2012,** *120 Suppl 1,* 149−166.

16. Cheignon, C.; Tomas, M.; Bonnefont-Rousselot, D.; Faller, P.; Hureau, C.; Collin, F. Oxidative Stress and the Amyloid β Peptide in Alzheimer's Disease. *Redox Biol* **2018,** *14,* 450−464.

17. Yang, J.; Zhang, X.; Yuan, P.; Yang, J.; Xu, Y.; Grutzendler, J.; Shao, Y.; Moore, A.; Ran, C. Oxalate-Curcumin-Based Probe for Micro- and Macroimaging of Reactive Oxygen Species in Alzheimer's Disease. *Proc Natl Acad Sci USA* **2017,** *114,* 12384−12389.

18. Claridge, S. A.; Thomas, J. C.; Silverman, M. A.; Schwartz, J. J.; Yang, Y.; Wang, C.; Weiss, P. S. Differentiating Amino Acid Residues and Side Chain Orientations in Peptides Using Scanning Tunneling Microscopy. *J Am Chem Soc* **2013,** *135,* 18528−18535.

19. Wang, C.; Yang, A.; Li, X.; Li, D.; Zhang, M.; Du, H.; Li, C.; Guo, Y.; Mao, X.; Dong, M.; Besenbacher, F.; Yang, Y.; Wang, C. Observation of Molecular Inhibition and Binding Structures of Amyloid Peptides. *Nanoscale* **2012,** *4,* 1895−1909.

20. Yugay, D.; Goronzy, D. P.; Kawakami, L. M.; Claridge, S. A.; Song, T.-B.; Yan, Z.; Xie, Y.-H.; Gilles, J.; Yang, Y.; Weiss, P. S. Copper Ion Binding Site in β-Amyloid Peptide. *Nano Lett* **2016,** *16,* 6282−6289.

21. Tycko, R. Characterization of Amyloid Structures at the Molecular Level by Solid State Nuclear Magnetic Resonance Spectroscopy. *Method Enzymol* **2006,** *413,* 103−122.

22. Tayeb-Fligelman, E.; Tabachnikov, O.; Moshe, A.; Goldshmidt-Tran, O.; Sawaya, M. R.; Coquelle, N.; Colletier, J. P.; Landau, M. The Cytotoxic *Staphylococcus Aureus* PSMα3 Reveals a Cross-α Amyloid-Like Fibril. *Science* **2017,** *355,* 831−833.

23. Paravastu, A. K.; Leapman, R. D.; Yau, W. M.; Tycko, R. Molecular Structural Basis for Polymorphism in Alzheimer's β-Amyloid Fibrils. *Proc Natl Acad Sci USA* **2008,** *105,* 18349−18354.

24. Mao, X. B.; Wang, C. X.; Wu, X. K.; Ma, X. J.; Liu, L.; Zhang, L.; Niu, L.; Guo, Y. Y.; Li, D. H.; Yang, Y. L.; Wang, C. β Structure Motifs of Islet Amyloid Polypeptides Identified through Surface-Mediated Assemblies. *Proc Natl Acad Sci USA* **2011,** *108,* 19605−19610.

25. Nelson, R.; Sawaya, M. R.; Balbirnie, M.; Madsen, A. O.; Riekel, C.; Grothe, R.; Eisenberg, D. Structure of the Cross-β Spine of Amyloid-Like Fibrils. *Nature* **2005,** *435,* 773−778.

26. Mao, X.; Guo, Y.; Luo, Y.; Niu, L.; Liu, L.; Ma, X.; Wang, H.; Yang, Y.; Wei, G.; Wang, C. Sequence Effects on Peptide Assembly Characteristics Observed by Using Scanning Tunneling Microscopy. *J Am Chem Soc* **2013,** *135,* 2181−2187.

27. Sheu, S. Y.; Yang, D. Y.; Selzle, H. L.; Schlag, E. W. Energetics of Hydrogen Bonds in Peptides. *Proc Natl Acad Sci USA* **2003,** *100,* 12683−12687.

28. Dou, J.; Vorobieva, A. A.; Sheffler, W.; Doyle, L. A.; Park, H.; Bick, M. J.; Mao, B.; Foight, G. W.; Lee, M. Y.; Gagnon, L. A.; Carter, L.; Sankaran, B.; Ovchinnikov, S.; Marcos, E.; Huang, P. S.; Vaughan, J. C.; Stoddard, B. L.; Baker, D. De Novo Design of a Fluorescence-Activating β-Barrel. *Nature* **2018,** *561,* 485−491.

29. Schrader, T. E.; Schreier, W. J.; Cordes, T.; Koller, F. O.; Babitzki, G.; Denschlag, R.; Renner, C.; Loweneck, M.; Dong, S. L.; Moroder, L.; Tavan, P.; Zinth, W. Light-Triggered β-Hairpin Folding and Unfolding. *Proc Natl Acad Sci USA* **2007,** *104,* 15729−15734.

30. Minor, D. L.; Kim, P. S. Measurement of the β-Sheet-Forming Propensities of Amino-Acids. *Nature* **1994,** *367,* 660−663.

31. Bhattacharjee, N.; Biswas, P. Position-Specific Propensities of Amino Acids in the β-Strand. *BMC Struct Biol* **2010,** *10*.

32. FarzadFard, F.; Gharaei, N.; Pezeshk, H.; Marashi, S. A. β-Sheet Capping: Signals That Initiate and Terminate β-Sheet Formation. *J Struct Biol* **2008,** *161,* 101−110.

33. Street, A. G.; Mayo, S. L. Intrinsic β-Sheet Propensities Result from Van Der Waals Interactions between Side Chains and the Local Backbone. *Proc Natl Acad Sci USA* **1999,** *96,* 9074−9076.

34. Fujiwara, K.; Toda, H.; Ikeguchi, M. Dependence of α-Helical and β-Sheet Amino Acid Propensities on the Overall Protein Fold Type. *BMC Struct Biol* **2012,** *12,* 18.

35. Richardson, J. S.; Richardson, D. C. Natural β-Sheet Proteins Use Negative Design to Avoid Edge-to-Edge Aggregation. *Proc Natl Acad Sci USA* **2002,** *99,* 2754−2759.

36. Worth, C. L.; Blundell, T. L. On the Evolutionary Conservation of Hydrogen Bonds Made by Buried Polar Amino Acids: The Hidden Joists, Braces and Trusses of Protein Architecture. *BMC Evol Biol* **2010,** *10*.

37. Craveur, P.; Joseph, A. P.; Rebehmed, J.; de Brevern, A. G. β-Bulges: Extensive Structural Analyses of β-Sheets Irregularities. *Protein Sci* **2013,** *22,* 1366−1378.

38. Matheou, C. J.; Younan, N. D.; Viles, J. H. The Rapid Exchange of Zinc^{2+} Enables Trace Levels to Profoundly Influence Amyloid-β Misfolding and Dominates Assembly Outcomes in Cu^{2+}/Zn^{2+} Mixtures. *J Mol Biol* **2016,** *428,* 2832−2846.

39. Furlan, S.; La Penna, G. Modeling of the Zn^{2+} Binding in the 1-16 Region of the Amyloid β Peptide Involved in Alzheimer's Disease. *Phys Chem Chem Phys* **2009,** *11,* 6468−6481.

40. Tsvetkov, P. O.; Kulikova, A. A.; Golovin, A. V.; Tkachev, Y. V.; Archakov, A. I.; Kozin, S. A.; Makarov, A. A. Minimal Zn^{2+} Binding Site of Amyloid-β. *Biophys J* **2010,** *99,* L84−86.

41. Minicozzi, V.; Stellato, F.; Comai, M.; Dalla Serra, M.; Potrich, C.; Meyer-Klaucke, W.; Morante, S. Identifying the Minimal Copper- and Zinc-Binding Site Sequence in Amyloid-β Peptides. *J Biol Chem* **2008,** *283,* 10784−10792.

42. Liu, L.; Niu, L.; Xu, M.; Han, Q. S.; Duan, H. Y.; Dong, M. D.; Besenbacher, F.; Wang, C.; Yang, Y. L. Molecular Tethering Effect of C-Terminus of Amyloid Peptide Aβ42. *ACS Nano* **2014,** *8,* 9503−9510.

43. Schmidt, M.; Rohou, A.; Lasker, K.; Yadav, J. K.; Schiene-Fischer, C.; Fandrich, M.; Grigorieff, N. Peptide Dimer Structure in an Aβ(1-42) Fibril Visualized with Cryo-EM. *Proc Natl Acad Sci USA* **2015,** *112,* 11858−11863.

44. Balbirnie, M.; Grothe, R.; Eisenberg, D. S. An Amyloid-Forming Peptide from the Yeast Prion Sup35 Reveals a Dehydrated β-Sheet Structure for Amyloid. *Proc Natl Acad Sci USA* **2001,** *98,* 2375−2380.

45. Pauling, L.; Corey, R. B. Two Rippled-Sheet Configurations of Polypeptide Chains, and a Note About the Pleated Sheets. *Proc Natl Acad Sci USA* **1953,** *39,* 253−256.

46. Camilloni, C.; Bonetti, D.; Morrone, A.; Giri, R.; Dobson, C. M.; Brunori, M.; Gianni, S.; Vendruscolo, M. Towards a Structural Biology of the Hydrophobic Effect in Protein Folding. *Sci Rep* **2016,** *6,* 28285.

47. Narayanan, C.; Dias, C. L. Hydrophobic Interactions and Hydrogen Bonds in β-Sheet Formation. *J Chem Phys* **2013,** *139,* 115103.

48. Zhang, S. G. Emerging Biological Materials through Molecular Self-Assembly. *Biotechnol Adv* **2002,** *20,* 321−339.

49. Lopez de la Paz, M.; Serrano, L. Sequence Determinants of Amyloid Fibril Formation. *Proc Natl Acad Sci USA* **2004,** *101,* 87−92.

50. Zhou, H. X.; Pang, X. D. Electrostatic Interactions in Protein Structure, Folding, Binding, and Condensation. *Chem Rev* **2018,** *118,* 1691−1741.

51. Lee, M.; Wang, T.; Makhlynets, O. V.; Wu, Y. B.; Polizzi, N. F.; Wu, H. F.; Gosavi, P. M.; Stohr, J.; Korendovych, I. V.; DeGrado, W. F.; Hong, M. Zinc-Binding Structure of a Catalytic Amyloid from Solid-State NMR. *Proc Natl Acad Sci USA* **2017,** *114,* 6191−6196.

52. Nelson, R.; Sawaya, M. R.; Balbirnie, M.; Madsen, A. O.; Riekel, C.; Grothe, R.; Eisenberg, D. Structure of the Cross-β Spine of Amyloid-Like Fibrils. *Nature* **2005,** *435,* 773−778.

53. Nečas, D.; Klapetek, P. Gwyddion: An Open-Source Software for SPM Data Analysis. *Cent. Eur. J. Phys.* **2012,** *10,* 181−188.

CHAPTER 4

Copper Ion Interactions with the C-terminus of the β-Amyloid Peptide

4.1 Introduction

The last 26 amino acid residues of the C-terminus of β-amyloid (Aβ) are known as $A\beta_{17-42}$ or p3; this segment is generated via the non-amyloidogenic pathway. Therefore, $A\beta_{17-42}$ has been considered non-pathogenic and, thus, a *benign* form of Aβ.[1] The *benign* nature of $A\beta_{17-42}$ was questioned after it was found in cerebral pre-amyloid plaques in patients with Alzheimer's disease (AD) and pre-amyloid lesions (neuritic plaques) in patients with Down syndrome (DS).[2,3] Nevertheless, until now, its role and its function remain undefined.

The structural information available about $A\beta_{17-42}$ indicates that it does not form stable oligomers; nevertheless, it is a structural determinant for Aβ fibril assembly. The main feature of the segment is an intrastrand salt bridge. The salt bridge can be formed either between aspartic acid at position 23 and lysine at position 28 (Asp_{23}-Lys_{28})[4-6] or between glutamic acid at position 22 and lysine at position 28 (Glu_{22}-Lys_{28}).[7,8] The purpose of the salt bridge is hypothesized to be stabilization of the hairpin-like hook structure of Aβ, facilitation of $A\beta_{17-42}$ oligomer formation, and consequent propagation of Aβ to fibrils.[9]

Previous studies have investigated disruption of the salt bridge by subjecting $A\beta_{17-42}$ to mutations, host molecules, and zinc ions.[5,10-12] In these studies, salt bridge disruption resulted in the formation of amorphous aggregates instead of fibrils. It has also been found that although the non-salt-bridge conformation of Aβ has a similar cross-β structure, it has distinct fibrillar morphology compared with Aβ with a salt bridge present in its conformation.[5,13] In addition, experimental results showed that Zn^{2+} ions disrupt the salt bridge in $A\beta_{17-42}$ without altering its hairpin secondary structure.[5]

The effects of salt bridge disruption and formation *versus* consequent Aβ structural changes have been extensively investigated by employing molecular dynamics (MD)

simulations; based on these MD simulations, different models of Zn^{2+} and Cu^{2+} interactions with Aβ peptides have been proposed. Interestingly, in those models, it is predicted that Cu^{2+} ions have the opposite effect on $A\beta_{17-42}$ than Zn^{2+} ions do. Specifically, Cu^{2+} ions promote salt bridge formation, whereas Zn^{2+} ions disrupt it. Nevertheless, so far, there are no experimental reports to test these MD simulation results.[7,14]

Finally, the crystal structure of the C-terminus of Aβ – specifically, $A\beta_{18-41}$ – was determined in 2011 by Streltsov *et al.*[15] Based on their crystal data, we know that the C-terminus of Aβ forms two distinct motifs. The first motif (Val_{18}-Ile_{31}) has a β-α structure, and the second motif (Ile_{32}-Ile_{41}) has a β-hairpin structure, comprising two anti-parallel β-strands. It is critical to realize that the only available crystal structure of $A\beta_{18-41}$ has been determined by fusing/complexing $A\beta_{18-41}$ with other proteins for crystallization purposes. Moreover, to our knowledge, the native structure of the C-terminus of Aβ remains unresolved.

The goal of the present study is to investigate the effects of Cu^{2+} ions on the secondary structure of $A\beta_{17-42}$, including potential alterations in the salt bridge in $A\beta_{17-42}$ due to Cu^{2+} ions and potential Cu^{2+} binding to $A\beta_{17-42}$. To observe the interaction of Cu^{2+} ions with $A\beta_{17-42}$, we employed cyclic voltammetry (CV), surface-enhanced Raman spectroscopy (SERS), atomic force microscopy (AFM), scanning tunneling microscopy (STM), and X-ray photoelectron spectroscopy (XPS).

4.2 Results and Discussion

4.2.1 Cyclic Voltammetry

Voltammetry of free Cu^{2+} and $A\beta_{17-42}$ incubated with Cu^{2+} ($A\beta_{17-42}$-Cu^{2+}) showed oxidation and reduction peaks within the ranges 0.3–0.7 V and 0–0.2 V, respectively (Figure

4.1). These peaks correspond to oxidation and reduction of Cu^{2+} ions, respectively. The current values corresponding to these voltammetry peaks are smaller in $A\beta_{17-42}$-Cu^{2+} because the Cu^{2+} ions in $A\beta_{17-42}$-Cu^{2+} are complexed or bound to the peptide. Consequently, Cu^{2+} ions in the complexed or bound state have lower diffusion coefficients because they do not move as easily as free Cu^{2+} ions do.

Furthermore, the literature based on *in-vitro* experiments indicates that Cu^{2+} upon binding to Aβ, due to electron transfer, gets reduced to Cu^{+} ($Cu^{2+} \rightarrow Cu^{+}$). Cu^{2+} reduction leads to changes in the binding configuration of the Aβ-Cu^{2+} complex from a four-coordination (distorted square planar Cu^{2+}) arrangement to two-coordination (linear Cu^{+}) arrangement.[16-19] Ultimately, this internal reorganization of Aβ-Cu^{2+} complex induced by Cu^{+} electron transfer activity can be deduced through differences in cathodic-to-anodic peak separation.[20]

For $A\beta_{17-42}$-Cu^{2+}, voltammetry showed peak-to-peak separation of 0.23 V (0.37 V - 0.14 V = 0.23 V). The presence of this cathodic-to-anodic peak separation exhibited in the voltammetry of $A\beta_{17-42}$-Cu^{2+} indicates that the rapid heterogeneous electron transfer rate of Cu^{2+} had an effect on the structure of $A\beta_{17-42}$ and caused rearrangements in $A\beta_{17-42}$-Cu^{2+} binding configuration.

In $A\beta_{17-42}$ voltammetry, we observed broad bands resembling oxidation and reduction peaks; however, these peaks are different from the ones which we observed in $A\beta_{17-42}$-Cu^{2+} and Cu^{2+} voltammetries, and thus, we conclude they are not related to Cu^{2+} oxidation. According to the literature, small and broad oxidation and reduction bands that are present in $A\beta_{17-42}$ voltammetry originate from cycling of redox-active residues, which are present in $A\beta_{17-42}$ segment, such as methionine residue at position 35 (Met_{35}), respectively.[21,22] Additionally, owing to the absence of Cu^{2+} ions, there is a lack of cathodic-to-anodic peak separation in $A\beta_{17-42}$

voltammetry, unlike in $A\beta_{17-42}$-Cu^{2+} voltammetry, which indicates that there is no structural change in $A\beta_{17-42}$.

4.2.2 Surface-Enhanced Raman Spectroscopy

Surface-enhanced Raman spectroscopy results indicated that in the presence of Cu^{2+} ions, the $A\beta_{17-42}$-Cu^{2+} peptide complex adopts a secondary structure that is a mixture of α-helical and β-sheet character (Table 4.1 and Figure 4.2). A mixture of α-helical and β-sheet elements in $A\beta_{17-42}$-Cu^{2+} was deduced from the bands located in the amide I region (1600–1700 cm^{-1}).[32,78] Specifically, one band each at 1705 cm^{-1} and 1646 cm^{-1} indicated β-sheet and α-helical secondary structures, respectively.[23-26] Furthermore, the presence of both secondary structures in $A\beta_{17-42}$-Cu^{2+} was confirmed based on bands found in the amide III region (1200–1300 cm^{-1}).[25,26,31,79] Specifically, bands at both 1219 and 1236 cm^{-1} correspond to β-sheet secondary structure;[28,44,60,61] whereas, a band at 1285 cm^{-1} corresponds to α-helical secondary structure.[28,58] Finally, a band at 946 cm^{-1}, which is considered to be a signature of an α-helix, confirmed the presence of this secondary structure.[30,60,77]

Similar to $A\beta_{17-42}$-Cu^{2+}, $A\beta_{17-42}$ showed the presence of both α-helical and β-sheet elements in its secondary structure, as deduced on the basis of bands located in the amide I region. Specifically, bands at 1705 and 1623 cm^{-1} indicated the presence of both β-sheet and α-helical structures, respectively.[23,24,27,28] The latter was confirmed by the bands located in the amide III region at 1308 cm^{-1} and 1287 cm^{-1}, which also corresponds to an α-helical secondary structure.[53-59] However, in contrast to $A\beta_{17-42}$-Cu^{2+}, $A\beta_{17-42}$ did not show a band in the amide III region corresponding to a β-sheet secondary structure.

To summarize our vibrational spectroscopy findings, in $A\beta_{17-42}$-Cu^{2+}, both regions – amide I and amide III – showed bands that corresponded to α-helical and β-sheet secondary structures, respectively. Thus, we conclude that the $A\beta_{17-42}$-Cu^{2+} complex retains both these secondary structures. In contrast to $A\beta_{17-42}$-Cu^{2+}, in $A\beta_{17-42}$, SERS results based on bands in the amide I region indicated the presence of both α-helical and β-sheet secondary structures (Table 4.1 and Figure 4.2). However, a band corresponding to the latter secondary structure was absent in the amide III region, whereas it was present in the case of $A\beta_{17-42}$-Cu^{2+}. Therefore, we conclude that in comparison with $A\beta_{17-42}$-Cu^{2+}, in $A\beta_{17-42}$, α-helical character is more pronounced than β-sheet character.

The above results indicating the presence of β-sheet secondary structure character in $A\beta_{17-42}$ are in agreement with literature results. This secondary structure in $A\beta_{17-42}$ results from the salt bridge between Asp_{23} and Lys_{28}[4-6] (or Glu_{22} and Lys_{28}[7,8]). Additionally, based on SERS spectral analyses of $A\beta_{17-42}$ and $A\beta_{17-42}$-Cu^{2+}, it is apparent that 1) $A\beta_{17-42}$ is structurally different from $A\beta_{17-42}$-Cu^{2+}; thus, Cu^{2+} ions alter the secondary structure of $A\beta_{17-42}$; and 2) Cu^{2+} ions promote β-sheet secondary structure character within the $A\beta_{17-42}$-Cu^{2+} system. However, based on the SERS results, it remains undetermined whether the enhancement of the β-sheet element within $A\beta_{17-42}$-Cu^{2+} is due to increased β-sheet character within single molecules or to increased overall lamination of $A\beta_{17-42}$ peptides (*i.e.,* peptide-peptide interactions).

4.2.3 Atomic Force Microscopy

Although it is now possible to utilize AFM to examine structural states of adsorbed molecules and biomolecules with sub-molecular resolution,[80,81] we employed STM, which has higher spatial resolution except under special circumstances (specific non-contact modes of

AFM), to investigate structural states of $A\beta_{17-42}$ and its interaction with Cu^{2+} ions (covered in section 4.2.4). Herein, we utilized AFM to investigate the overall aggregation state of $A\beta_{17-42}$ *vs.* $A\beta_{17-42}$-Cu^{2+} based on parameters such as size and frequency of aggregates and overall surface roughness due to aggregate size. In the present study, the following two outcomes were possible: first, if Cu^{2+} ions do not structurally influence $A\beta_{17-42}$, then the aggregation states of $A\beta_{17-42}$ and $A\beta_{17-42}$-Cu^{2+} would be similar. Second, if Cu^{2+} ions structurally influence $A\beta_{17-42}$, then the aggregation states of $A\beta_{17-42}$ and $A\beta_{17-42}$-Cu^{2+} would be different. Generally, binding of Cu^{2+} to Aβ results in rapid Aβ aggregation.[82-84] Thus, we were interested to investigate whether Cu^{2+} ions result in enhanced aggregation of $A\beta_{17-42}$; ultimately, such results would signify alteration of the structural state of $A\beta_{17-42}$ due to Cu^{2+} ions.

The atomic force microscopy results presented in Figure 4.3 indicate different aggregation states of $A\beta_{17-42}$ after incubating peptides for 1 hr with ($A\beta_{17-42}$-Cu^{2+}) and without Cu^{2+} ($A\beta_{17-42}$) ions. Specifically, $A\beta_{17-42}$-Cu^{2+}, in comparison with $A\beta_{17-42}$, results in larger aggregate size and more significant surface coverage. In addition, we confirmed that Cu^{2+} ions result in more extensive aggregation of $A\beta_{17-42}$ *via* surface roughness analysis, which indicated that $A\beta_{17-42}$-Cu^{2+} and $A\beta_{17-42}$ result in roughness average values (Ra) of 0.524 nm and 0.364 nm, respectively (Figure 4.4).

According to the protein and amyloid aggregation pathways, the β-sheet secondary structure is a requirement for protein and amyloid aggregation. The general aggregation trend proceeds from disordered species (molecules rich in random coil and α-helical elements) to partially folded species (species that are a mixture of α-helices and β-sheets) to oligomers (species with β-sheet secondary structure) and finally to fibrils (proteins/amyloids composed of organized and stacked β-sheets).[85,86] The SERS results indicated a higher β-sheet content in

$A\beta_{17-42}$-Cu^{2+} than in $A\beta_{17-42}$. Furthermore, AFM results indicated higher aggregation of $A\beta_{17-42}$-Cu^{2+} than of $A\beta_{17-42}$. Based on SERS and AFM results, we conclude that $A\beta_{17-42}$-Cu^{2+} must be further in the aggregation pathway than $A\beta_{17-42}$. Thus, Cu^{2+} ions interact with $A\beta_{17-42}$ peptides. These interactions ultimately lead to the higher aggregation state of $A\beta_{17-42}$-Cu^{2+} than $A\beta_{17-42}$.

4.2.4 Scanning Tunneling Microscopy

The secondary structure of biological molecules and their interaction with metal ions are distinguishable with STM. Considering the apparent effect of Cu^{2+} ions on the aggregation of $A\beta_{17-42}$, we employed STM to investigate the structural conformation of $A\beta_{17-42}$-Cu^{2+} and its putative metal ion-binding site (Figure 4.5). Because the secondary structure of $A\beta_{18-41}$ has been elucidated *via* X-ray diffraction (XRD) analysis,[15] $A\beta_{17-42}$ without the presence of metal ions was not a subject of interest to us in investigating its structure *via* STM. Thus, herein, we analyzed collected STM micrographs of $A\beta_{17-42}$-Cu^{2+} for peptidyl length as well as interstrand separation. Disordered molecular assemblies elucidated *via* STM, due to the absence of periodicity, are observed as disordered mesh structures;[87,88] *i.e.,* we expect that if $A\beta_{17-42}$-Cu^{2+} has a random coil conformation, then the molecular assembly of $A\beta_{17-42}$-Cu^{2+} will not be determined using STM. In contrast to a random coil conformation, α-helical or β-sheet conformations of biological molecules, owing to their specific surface arrangements, are easily distinguishable in STM micrographs.[89-92] Finally, if $A\beta_{17-42}$ has a metal ion-binding site, then in the $A\beta_{17-42}$-Cu^{2+} system, it would be observed as a non-periodic protruding feature.[92,93]

Figure 4.5 shows an STM micrograph of $A\beta_{17-42}$-Cu^{2+} deposited on highly oriented pyrolytic graphite (HOPG). We excluded the likelihood of $A\beta_{17-42}$-Cu^{2+} having a random coil

conformation because, as mentioned above, the molecular structure of $A\beta_{17-42}$-Cu^{2+} of the random coil conformation would be elucidated *via* STM as a disordered mesh structure; additionally, the signature of random coil conformation would be observed in SERS.

The average measured peptidyl length and interstrand separation of $A\beta_{17-42}$-Cu^{2+} peptides are 54.8 ± 1.3 Å and 5.5 ± 0.2 Å, respectively. Based on the interstrand separation of 5.5 ± 0.2 Å, laminated $A\beta_{17-42}$-Cu^{2+} peptides cannot be classified either as α-helical or β-sheet secondary structures. Biological molecules with α-helical and β-sheet secondary structures arrange into assemblies with interstrand separations of ~10.5 Å and ~4.7 Å, respectively.[89-92,94,95] Taking into consideration that SERS results indicating the presence of *both* α-helical and β-sheet elements in $A\beta_{17-42}$-Cu^{2+}, we hypothesize that the interstrand separation of $A\beta_{17-42}$-Cu^{2+} is neither β-sheet nor α-helix owing to the presence of both secondary structure elements in $A\beta_{17-42}$-Cu^{2+} strands. Rather, the interstrand separation of 5.5 ± 0.2 Å indicates mix of α-helical and β-sheet elements of $A\beta_{17-42}$-Cu^{2+} assemblies on the surface.

Based on the measured peptidyl length of 54.8 ± 1.3 Å, there are two potential surface arrangements for $A\beta_{17-42}$-Cu^{2+} peptides. First, owing to the presence of a salt bride between Asp_{23} and Lys_{28} (or Glu_{22} and Lys_{28}), $A\beta_{17-42}$-Cu^{2+} could have a folded conformation. Second, owing to the yet unknown proportions of α-helix and β-sheet elements per $A\beta_{17-42}$-Cu^{2+} complex, it is possible that the length of 54.8 ± 1.3 Å is due to a linear configuration of $A\beta_{17-42}$-Cu^{2+}. However, the latter cannot be verified since the proportions of the α-helix and β-sheet elements per $A\beta_{17-42}$-Cu^{2+} complex are unknown.

4.2.5 X-Ray Photoelectron Spectroscopy

We have determined the effects of Cu^{2+} ions on $A\beta_{17-42}$ structure using both SERS and AFM. However, direct binding of metal ions to $A\beta_{17-42}$ peptides was not observed dirrectly *via* STM. Nevertheless, the lack of protruding features in STM images, which would suggest direct Cu^{2+} binding to $A\beta_{17-42}$, does not indicate the absence of such interactions. For instance, if Cu^{2+} ions bind to $A\beta_{17-42}$ but conformationally stay underneath the backbone of the peptide or if Cu^{2+} ions bind between two $A\beta_{17-42}$ strands in the direction of Z-axis, then their presence in either of those cases would not necessary have been observed *via* ambient STM.

Thus, to investigate the presence of Cu^{2+} in STM samples of $A\beta_{17-42}$-Cu^{2+}, we employed XPS (Figure 4.6). However, because all tested samples, even those that were incubated in excess Cu^{2+}, showed negative results for the presence of Cu^{2+} ions, we conclude that the negative results were obtained owing to the limited sensitivity of XPS and not to the absence of Cu^{2+} ions in the tested samples.

4.3 Conclusions and Prospects

In this study, we investigated the effects of Cu^{2+} ions on the structure of $A\beta_{17-42}$. Both SERS and AFM showed complementary results, the findings of which indicated that Cu^{2+} ions affect the aggregation of $A\beta_{17-42}$ peptides. Specifically, Cu^{2+} ions enhance the aggregation of $A\beta_{17-42}$ peptides. With increased aggregation, we also observed changes in the secondary structures of the $A\beta_{17-42}$ peptides. Specifically, in the presence of Cu^{2+} ions, $A\beta_{17-42}$ peptides shift from an α-helical secondary structure to a β-sheet secondary structure. The presence of both secondary structures has also been confirmed by STM measurements of interstrand separation.

However, more single-molecule experiments are required in order to investigate the reasons underlying the structural changes in $A\beta_{17-42}$ in the presence of Cu^{2+} ions.

4.4 Materials and Methods

4.4.1 Cyclic Voltammetry Sample Preparation

Solutions were prepared in a glass vial with final total volume of 400 μL for all samples (Cu^{2+}, $A\beta_{17\text{-}42,}$ and $A\beta_{17\text{-}42}$-Cu^{2+}). $A\beta_{17–42}$ molarity was kept constant between samples: 6.4×10^{-7} M. The $A\beta_{17\text{-}42}$ solution mixture was prepared by mixing 20 μL of phosphate-buffered saline at pH 6.8, 200 μL of acetonitrile (Sigma-Aldrich Fluka Analytical, St. Louis, MO, purity >99.9%), 179 μL of double-distilled water, and 1 μL of $A\beta_{17\text{-}42}$ (rPeptide, Premiere Peptide Solutions, Bogart, GA, >90% purity). Before depositing $A\beta_{17\text{-}42}$ solution onto gold substrates, the surface of the gold substrate was cleaned with ethanol and oxygen plasma. The $A\beta_{17\text{-}42}$-Cu^{2+} solution mixture was prepared by mixing 20 μL of phosphate-buffered saline at pH 6.8, 10 μL of Cu^{2+} (Sigma-Aldrich Fluka Analytical Copper Standard for ICP 1001 ± 2 mg/L), 200 μL of acetonitrile, 169 μL of double-distilled water, and 1 μL of $A\beta_{17\text{-}42}$ solution. $A\beta_{17\text{-}42}$ and $A\beta_{17\text{-}42}$-Cu^{2+} solution were incubated before deposition onto the substrate and dried in a vacuum desiccator. The samples were immersed in double-distilled water for final cleaning.

4.4.2 Cyclic Voltammetry Measurements

Electrochemical experiments were performed using Gamry Reference 600 using a plastic electrochemical cell. A saturated calomel electrode, isolated from Ag/AgCl solution by a glass frit, and a platinum wire were used as reference and counter electrodes, respectively. The working electrode was a gold O-ring electrode washed with water and ethanol before and placed on top of the gold substrate with the deposited sample. The electrolyte solution was 5 mM phosphate-buffered saline at pH 6.8. Before each experiment, the electrolyte solutions were degassed by bubbling nitrogen gas into them. The potential was cycled at 50 mV/s at room

temperature. Cyclic voltammetry was performed in the potential range of -0.3 to 1.0 V *vs.* Ag/AgCl.

4.4.3 Surface-Enhanced Raman Spectroscopy Sample Preparation

Silver–coated gold nanostars for $A\beta_{17-42}$ and $A\beta_{17-42}$-Cu^{2+} SERS measurements were prepared, as described previously.[99] $A\beta_{17–42}$ and $A\beta_{17–42}$-Cu^{2+} solutions were prepared in a glass vial with a final total volume of 400 μL for both samples. $A\beta_{17–42}$ molarity was kept constant between samples: 6.4×10^{-7} M. In the $A\beta_{17–42}$-Cu^{2+} samples, the final Cu^{2+} concentration was 7.8×10^{-6} M. The $A\beta_{17–42}$ solution mixture was prepared by mixing 20 μL of phosphate-buffered saline at pH 6.8, 200 μL of acetonitrile (Sigma-Aldrich Fluka Analytical, St. Louis, MO, purity >99.9%), 172 μL silver–coated gold nanostars solution 7 μL of double-distilled water, and 1 μL of $A\beta_{17–42}$ (rPeptide, Premiere Peptide Solutions, Bogart, GA, > 90% purity). Both solutions upon preparation were incubated for 10 min at room temperature. Afterwards, $A\beta_{17–42}$ solution was deposited onto glass substrate for 5 min and spin cast at 7000 rpm to get rid of excess solution from the glass substrate. The $A\beta_{17–42}$-Cu^{2+} solution mixture was prepared by mixing 20 μL of phosphate-buffered saline at pH 6.8, 2 μL of Cu^{2+} (Sigma Aldrich Fluka Analytical, Copper Standard for ICP 1001 ± 2 mg/L), 200 μL of acetonitrile, 172 μL silver–coated gold nanostars solution 5 μL of double-distilled water, and 1 μL of $A\beta_{17–42}$ solution.

4.4.4 Surface-Enhanced Raman Spectroscopy Measurements

A Renishaw inVia Raman system (Renishaw, IL) operating under ambient conditions was employed for Raman analyses. Spectral analyses were performed *via* WiRE spectral acquisition wizard. During SERS measurements, a 633 nm edge (mode: regular) He−Ne laser was used as

the Raman excitation source to match the resonant wavelength of the substrate. Laser power, slit opening, and objective were ~0.25%, ~50 μm (centre 1733 μm), and 50x respectively. Spectra were acquired as a single-scan measurement. Exposure time of each measurement was 2 s.

4.4.5 Atomic Force Microscopy Sample Preparation

$A\beta_{17–42}$ and $A\beta_{17–42}$-Cu^{2+} solutions were prepared in a glass vial with a final total volume of 400 μL for both samples. $A\beta_{17–42}$ molarity was kept constant between samples: 6.4×10^{-7} M. In the $A\beta_{17–42}$-Cu^{2+} samples, the final Cu^{2+} concentration was 7.8×10^{-6} M. The $A\beta_{17–42}$ solution mixture was prepared by mixing 20 μL of phosphate-buffered saline at pH 6.8, 200 μL of acetonitrile (Sigma-Aldrich Fluka Analytical, St. Louis, MO, purity >99.9%), 179 μL of double-distilled water, and 1 μL of $A\beta_{17–42}$ (rPeptide, Premiere Peptide Solutions, Bogart, GA, >90% purity). Both solutions upon preparation were incubated for 1 hr at room temperature. Afterwards, $A\beta_{17–42}$ solution was deposited onto HOPG for a 1 min and blown off using nitrogen gas. The $A\beta_{17–42}$-Cu^{2+} solution mixture was prepared by mixing 20 μL of phosphate-buffered saline at pH 6.8, 2 μL of Cu^{2+} (Sigma Aldrich Fluka Analytical, Copper Standard for ICP 1001 ± 2 mg/L), 200 μL of acetonitrile, 177 μL of double-distilled water, and 1 μL of $A\beta_{17–42}$ solution.

4.4.6 Atomic Force Microscopy Measurements

All AFM measurements were performed under ambient conditions at the California NanoSystems Institute (NanoPico Characterization laboratory) using a Bruker FastScan system (Bruker, Billerica, MA) under PeakForce tapping mode with a ScanAsyst-Air cantilevers (Bruker, spring constant = 0.4 ± 0.1 N/m).

4.4.7 Scanning Tunneling Microscopy Sample Preparation

Scanning tunneling microscopy sample preparation was identical to AFM sample preparation with the exception of solution deposition onto HOPG. Both solutions, $A\beta_{17-42}$ and $A\beta_{17-42}$-Cu^{2+}, were deposited onto HOPG for 1 min and blown dry using nitrogen gas.

4.4.8 Scanning Tunneling Microscopy Measurements

For STM measurements, a mechanically cut Pt−Ir (80%− 20%) (Goodfellow Corp., Oakdale, PA) wire was used as the STM tip. The STM observations were carried out on a Pico SPM microscope head (Molecular Imaging, now Agilent, Santa Clara, CA) controlled by a low-noise controller (RHK Model R9, RHK Technology, Troy, MI) under ambient conditions.

4.4.9 X-Ray Photoelectron Spectroscopy Sample Preparation

X-ray photoelectron spectroscopy $A\beta_{17-42}$ and $A\beta_{17-42}$-Cu^{2+} sample preparation was identical to AFM and STM sample preparation with the exception of the time period that the solution was deposited onto HOPG. Both solutions, $A\beta_{17-42}$ and $A\beta_{17-42}$-Cu^{2+} were deposited onto HOPG for 10 min and blown dry using nitrogen gas. HOPG washed with excess of Cu^{2+} sample was prepared by depositing concentrated Cu^{2+} solution (Sigma Aldrich Fluka Analytical, Copper Standard for ICP 1001 ± 2 mg/L) onto HOPG for 10 min and blowing off using nitrogen gas.

4.4.10 X-Ray Photoelectron Spectroscopy Measurements

X-ray photoelectron spectroscopy was performed using an AXIS Ultra DLD photoelectron spectrometer (Kratos Analytical Inc., Chestnut Ridge, NY) and a monochromatic Al K_α X-ray source with a 200 μm circular spot size under ultrahigh vacuum (10^{-9} Torr). Spectra were

acquired at a pass energy of 20 eV using a 300 ms dwell time. For all scans, 15 kV was applied with an emission of 15 mA. X-Ray photoelectron spectra were fit with the CasaXPS Software.

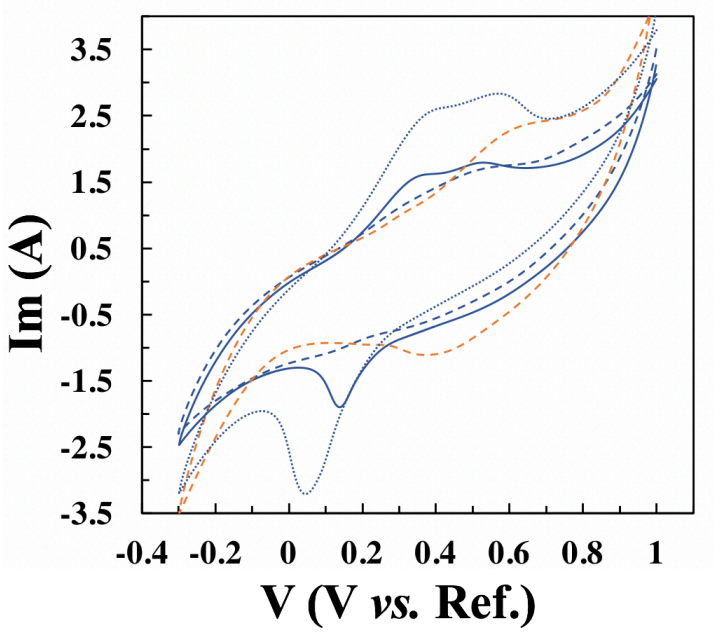

Figure 4.1. An overlay of the redox potentials measured by cyclic voltammetry. Cyclic voltammetric responses represent: substrate – gold on silica (dashed orange line), free Cu^{2+} (dotted blue line), $A\beta_{17-42}$ (dashed blue line), and $A\beta_{17-42}$ with Cu^{2+} (solid blue line). Bands with positive current in the range of 0.2 V to 0.7 V represent oxidized state of copper (Cu^{2+}; $Cu \rightarrow Cu^{2+} + 2e^-$) while bands with negative current in the range of -0.1 V to 0.3 V represent reduced state of copper (Cu^+; $Cu^{2+} + 2e^- \rightarrow Cu$).

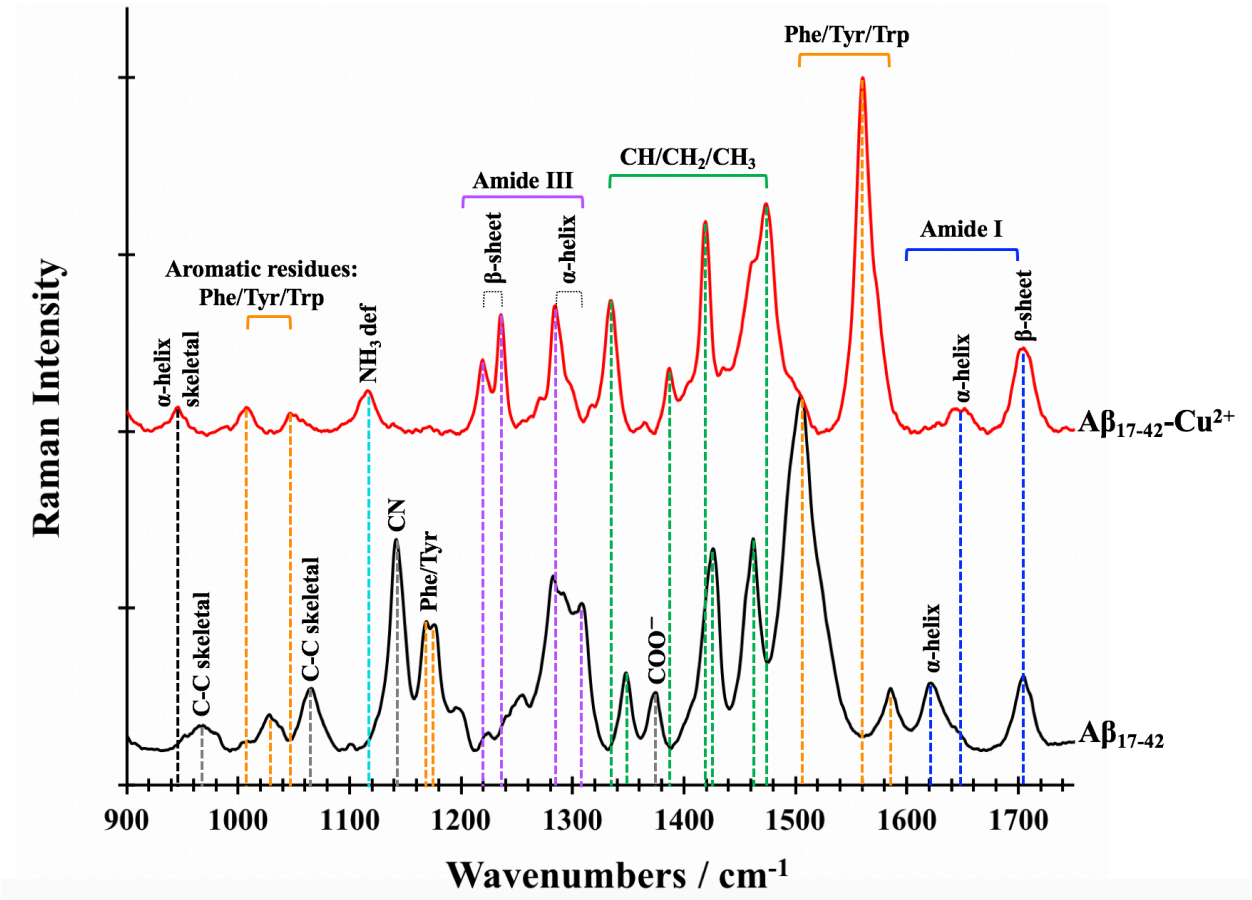

Figure 4.2. Surface-enhanced Raman spectrum of $A\beta_{17-42}$ (bottom spectra) and $A\beta_{17-42}$-Cu^{2+} (top spectra) obtained by depositing $A\beta_{17-42}$ and $A\beta_{17-42}$-Cu^{2+} solutions on the SERS substrate composed of silver–coated gold nanostars. Amide I and Amide III indicate structural differences between $A\beta_{17-42}$ and $A\beta_{17-42}$-Cu^{2+}. $A\beta_{17-42}$ is more in α-helical configuration because it lacks bands that would indicate β-sheet component in Amide III region.

Table 4.1. Surface-Enhanced Raman Spectroscopy Band Assignment for Acquired Spectra of $A\beta_{17-42}$ and $A\beta_{17-42}$-Cu^{2+} at 633 nm excitation

Raman Shift (cm^{-1})	**Assignment**	**Reference**
[a,b]1705*	Amide I: β-sheet	23,24
[a]1646*	Amide I: α-helix	23-26
[b]1623*	Amide I: α-helix	27,28
[b]1585	Phe/Tyr	29-31
[a]1560	Trp	23,32-34
[b]1504	Tyr/Phe	35,36
[a]1474	CH_3/CH_2	32,37
[b]1462	$CH_3/CH_2/CH$	29,38
[b]1425	CH_2	39-41
[a]1419	CH_2	42,43
[a]1386	CH_2/CH	40,44,45
[b]1375	COO^-	46-48
[b]1338	CH_2	40,41,49
[a]1334	CH_2/CH_3/ CH_2/CH	36,50-52
[b]1308**	Amide III: α-helix	53-57
[b]1287**	Amide III: α-helix	58,59
[a]1285**	Amide III: α-helix	28,58
[a]1236**	Amide III: β-sheet	28,60,61
[a]1219**	Amide III: β-sheet	44,61
[b]1176	Tyr/Phe/Benzene ring	62,63
[b]1168	Tyr/Phe	36,64,65
[b]1143	CCαN/CN	30,66,67
[a]1115	NH^{3+} (amino moiety)	36,68,69
[b]1065	C-C (skeletal)	36,70,71
[a]1046	Trp/Tyr	23,72
[b]1028	Phe	67,73
[a]1007	Trp/Phe	23,32,33,74
[b]967	C-C (skeletal)	52,75,76
[a]946	α-helix signature	30,60,77

[a] = $A\beta_{17-42}$-Cu^{2+}; [b] = $A\beta_{17-42}$; * = amide I; ** = amide III;

Phe = Phenylalanine; Tyr = Tyrosine; Trp = Tryptophan

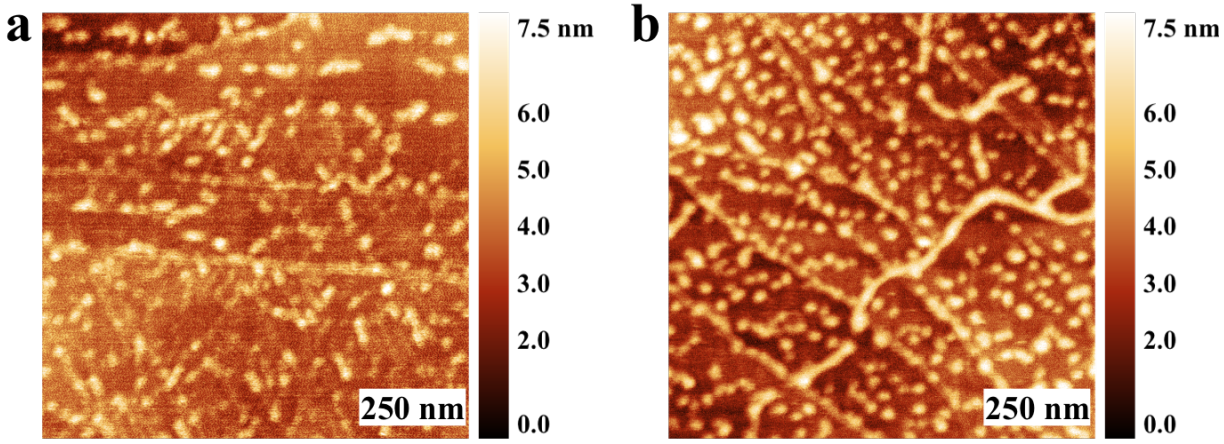

Figure 4.3. Atomic force microscopy images of $A\beta_{17-42}$ (a) and $A\beta_{17-42}$-Cu^{2+} (b) incubated for 1 hr in the absence and in the presence of Cu^{2+} ions, respectively. Both conditions result in aggregation of the peptide, however, in contrast to $A\beta_{17-42}$, aggregates of $A\beta_{17-42}$-Cu^{2+} are larger in size and result in denser surface coverages than $A\beta_{17-42}$. In addition, $A\beta_{17-42}$ and $A\beta_{17-42}$-Cu^{2+} images were analyzed for average surface roughness (see Figure 4.4 for more details). Average surface roughness of $A\beta_{17-42}$ is lower than for $A\beta_{17-42}$-Cu^{2+} specifically, 0.364 nm and 0.524 nm, respectively. This result indicates means that $A\beta_{17-42}$ results in smoother surface than $A\beta_{17-42}$-Cu^{2+}. Overall, AFM results signify that Cu^{2+} ions enhance aggregation of $A\beta_{17-42}$ segment.

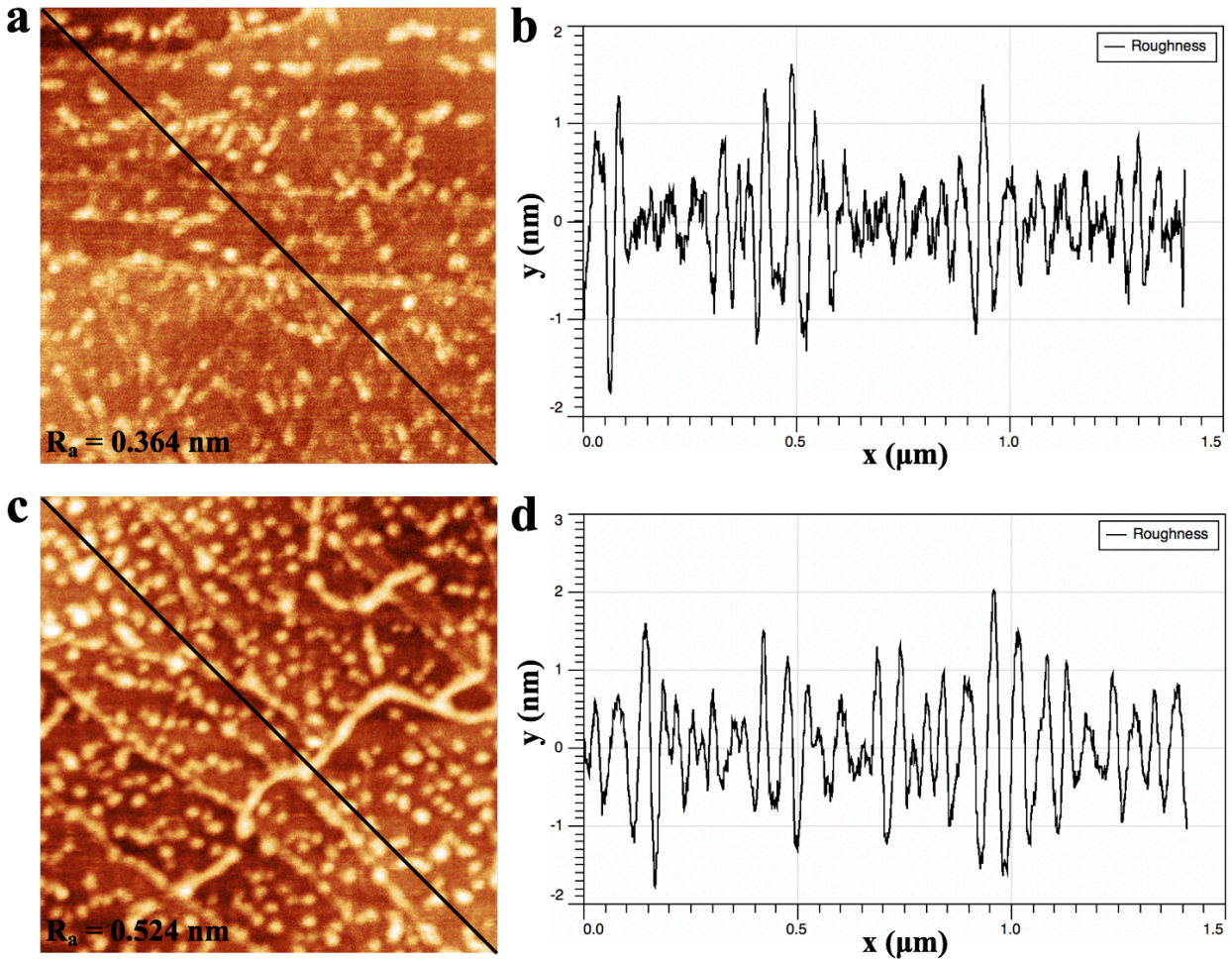

Figure 4.4. Atomic force microscopy analyses of average surface roughness (Ra) of (a) $A\beta_{17-42}$ and (b) $A\beta_{17-42}$-Cu^{2+}. Average surface roughness of $A\beta_{17-42}$ and $A\beta_{17-42}$-Cu^{2+} is 0.364 nm and 0.524 nm, respectively. (a,c) Diagonal lines represent (b,d) the cross sections of the Ra analysis. (b,d) Corresponding graphs of the Ra analysis of $A\beta_{17-42}$ and $A\beta_{17-42}$-Cu^{2+}, respectively.

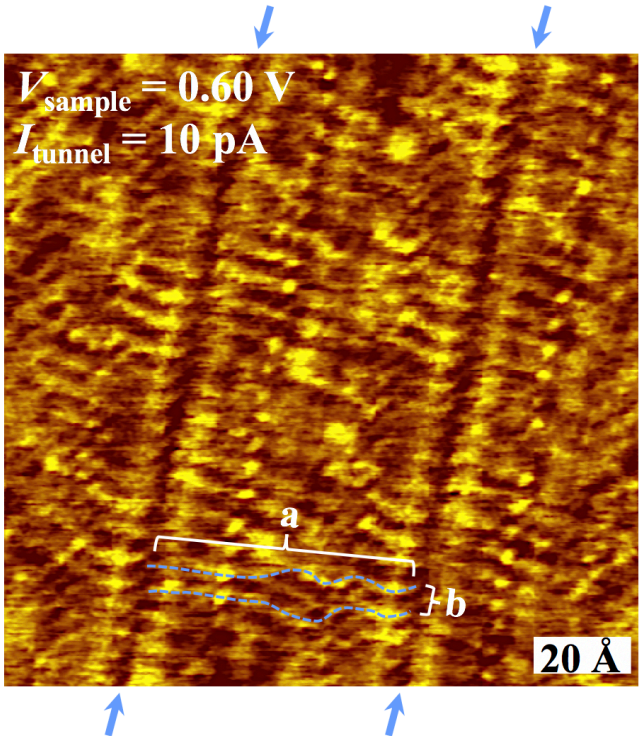

Figure 4.5. Scanning tunneling micrograph of $A\beta_{17-42}$-Cu^{2+}. Blue arrows signify boundaries of laminated $A\beta_{17-42}$-Cu^{2+} peptides. For clarity, two $A\beta_{17-42}$-Cu^{2+} strands are outlined as blue dashed lines. (a) Measured average strand length is 54.8 ± 1.3 Å while, (b) measured average interstrand separation is 5.5 ± 0.2 Å.

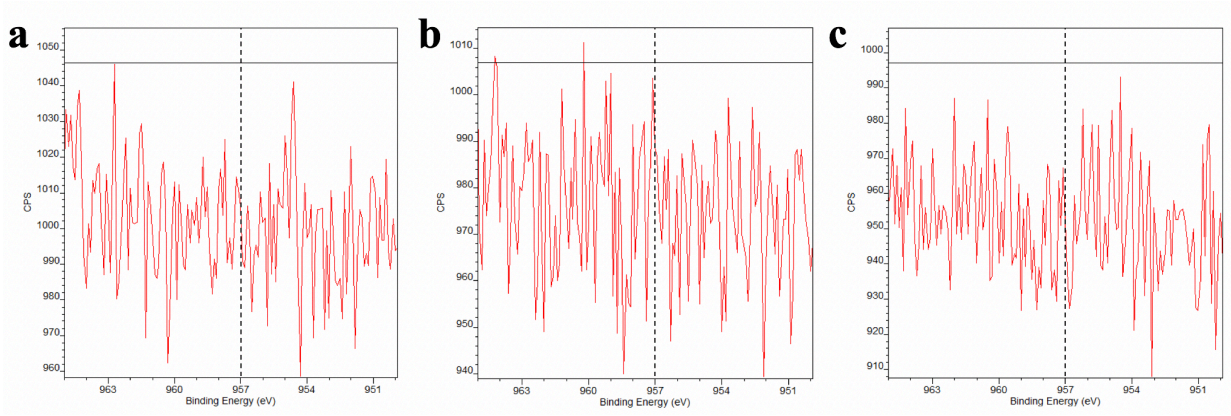

Figure 4.6. X-ray photoelectron spectroscopy of (a) $A\beta_{17-42}$ (b) $A\beta_{17-42}$ incubated with excess of Cu^{2+} (c) HOPG washed with excess of Cu^{2+}. All conditions show negative results for presence of Cu^{2+}. Copper band (Cu $2p_{1/2}$) was expected at ~957 eV (dashed line).[96-98]

4.5 References

1. Pearson, H. A.; Peers, C. Physiological Roles for Amyloid β Peptides. *J Physiol* **2006,** *575,* 5–10.

2. Lalowski, M.; Golabek, A.; Lemere, C. A.; Selkoe, D. J.; Wisniewski, H. M.; Beavis, R. C.; Frangione, B.; Wisniewski, T. The "Nonamyloidogenic" p3 Fragment (Amyloid β 17-42) is a Major Constituent of Down's Syndrome Cerebellar Preamyloid. *J Biol Chem* **1996,** *271,* 33623–33631.

3. Wei, W.; Norton, D. D.; Wang, X.; Kusiak, J. W. Aβ 17-42 in Alzheimer's Disease Activates Jnk and Caspase-8 Leading to Neuronal Apoptosis. *Brain* **2002,** *125,* 2036–2043.

4. Miller, Y.; Ma, B.; Nussinov, R. Polymorphism of Alzheimer's Aβ17-42 (p3) Oligomers: The Importance of the Turn Location and Its Conformation. *Biophys J* **2009,** *97,* 1168–1177.

5. Mithu, V. S.; Sarkar, B.; Bhowmik, D.; Chandrakesan, M.; Maiti, S.; Madhu, P. K. Zn^{++} Binding Disrupts the Asp(23)-Lys(28) Salt Bridge without Altering the Hairpin-Shaped Cross-β Structure of Aβ(42) Amyloid Aggregates. *Biophys J* **2011,** *101,* 2825–2832.

6. Villalobos Acosta, D. M. A.; Chimal Vega, B.; Correa Basurto, J.; Fragoso Morales, L. G.; Rosales Hernandez, M. C. Recent Advances by in Silico and in Vitro Studies of Amyloid-β 1-42 Fibril Depicted a S-Shape Conformation. *Int J Mol Sci* **2018,** *19*.

7. Boopathi, S.; Kolandaivel, P. Role of Zinc and Copper Metal Ions in Amyloid β-Peptides Aβ(1-40) and Aβ(1-42) Aggregation. *RSC Adv* **2014,** *4,* 38951–38965.

8. Khandogin, J.; Brooks, C. L., 3rd. Linking Folding with Aggregation in Alzheimer's β-Amyloid Peptides. *Proc Natl Acad Sci USA* **2007,** *104,* 16880–16885.

9. Dulin, F.; Leveille, F.; Ortega, J. B.; Mornon, J. P.; Buisson, A.; Callebaut, I.; Colloc'h, N. p3 Peptide, a Truncated Form of Aβ Devoid of Synaptotoxic Effect, Does Not Assemble into Soluble Oligomers. *FEBS Lett* **2008,** *582,* 1865–1870.

10. Baumketner, A.; Bernstein, S. L.; Wyttenbach, T.; Lazo, N. D.; Teplow, D. B.; Bowers, M. T.; Shea, J. E. Structure of the 21-30 Fragment of Amyloid β-Protein. *Protein Sci* **2006,** *15,* 1239–1247.

11. Chandra, B.; Mithu, V. S.; Bhowmik, D.; Das, A. K.; Sahoo, B.; Maiti, S.; Madhu, P. K. Curcumin Dictates Divergent Fates for the Central Salt Bridges in Amyloid-β40 and Amyloid-β42. *Biophys J* **2017,** *112,* 1597–1608.

12. Mithu, V. S.; Sarkar, B.; Bhowmik, D.; Das, A. K.; Chandrakesan, M.; Maiti, S.; Madhu, P. K. Curcumin Alters the Salt Bridge-Containing Turn Region in Amyloid β(1-42) Aggregates. *J Biol Chem* **2014,** *289,* 11122–11131.

13. Ma, B.; Nussinov, R. Stabilities and Conformations of Alzheimer's β-Amyloid Peptide Oligomers (Aβ 16-22, Aβ 16-35, and Aβ 10-35): Sequence Effects. *Proc Natl Acad Sci USA* **2002,** *99,* 14126–14131.

14. Mutter, S. T.; Turner, M.; Deeth, R. J.; Platts, J. A. Metal Binding to Amyloid-β 1-42: A Ligand Field Molecular Dynamics Study. *ACS Chem Neurosci* **2018,** *9,* 2795–2806.

15. Streltsov, V. A.; Varghese, J. N.; Masters, C. L.; Nuttall, S. D. Crystal Structure of the Amyloid-β p3 Fragment Provides a Model for Oligomer Formation in Alzheimer's Disease. *J Neurosci* **2011,** *31,* 1419–1426.

16. Himes, R. A.; Park, G. Y.; Barry, A. N.; Blackburn, N. J.; Karlin, K. D. Synthesis and X-Ray Absorption Spectroscopy Structural Studies of Cu(I) Complexes of Histidylhistidine Peptides: The Predominance of Linear 2-Coordinate Geometry. *J Am Chem Soc* **2007,** *129,* 5352–5353.

17. Le Clainche, L.; Giorgi, M.; Reinaud, O. Synthesis and Characterization of a Novel Calix[4]Arene-Based Two-Coordinate Copper(I) Complex That Is Unusually Resistant to Dioxygen. *Eur J Inorg Chem* **2000,** 1931–1933.

18. Sanyal, I.; Karlin, K. D.; Strange, R. W.; Blackburn, N. J. Chemistry and Structural Studies on the Dioxygen-Binding Copper-1,2-Dimethylimidazole System. *J Am Chem Soc* **1993,** *115,* 11259–11270.

19. Sorrell, T. N.; Jameson, D. L. Synthesis, Structure, and Reactivity of Monomeric 2-Coordinate Copper(I) Complexes. *J Am Chem Soc* **1983,** *105,* 6013–6018.

20. Balland, V.; Hureau, C.; Saveant, J. M. Electrochemical and Homogeneous Electron Transfers to the Alzheimer Amyloid-β Copper Complex Follow a Preorganization Mechanism. *P Natl Acad Sci USA* **2010,** *107,* 17113–17118.

21. Jiang, D. L.; Men, L. J.; Wang, J. X.; Zhang, Y.; Chickenyen, S.; Wang, Y. S.; Zhou, F. M. Redox Reactions of Copper Complexes Formed with Different β-Amyloid Peptides and Their Neuropathalogical Relevance. *Biochemistry-US* **2007,** *46,* 9270–9282.

22. Vestergaard, M.; Kerman, K.; Saito, M.; Nagatani, N.; Takamura, Y.; Tamiya, E. A Rapid Label-Free Electrochemical Detection and Kinetic Study of Alzheimer's Amyloid β Aggregation. *J Am Chem Soc* **2005,** *127,* 11892–11893.

23. Wang, J.; Lin, D.; Lin, J. Q.; Yu, Y.; Huang, Z. F.; Chen, Y. P.; Lin, J. Y.; Feng, S. Y.; Li, B. H.; Liu, N. R.; Chen, R. Label-Free Detection of Serum Proteins Using Surface-Enhanced Raman Spectroscopy for Colorectal Cancer Screening. *J Biomed Opt* **2014,** *19*.

24. Nguyen, A. H.; Peters, E. A.; Schultz, Z. D. Bioanalytical Applications of Surface-Enhanced Raman Spectroscopy: De Novo Molecular Identification. *Rev Anal Chem* **2017,** *36*.

25. Kurouski, D.; Deckert-Gaudig, T.; Deckert, V.; Lednev, I. K. Structure and Composition of Insulin Fibril Surfaces Probed by Ters. *J Am Chem Soc* **2012,** *134,* 13323–13329.

26. Kurouski, D.; Van Duyne, R. P.; Lednev, I. K. Exploring the Structure and Formation Mechanism of Amyloid Fibrils by Raman Spectroscopy: A Review. *Analyst* **2015,** *140,* 4967–4980.

27. Kumar, G. V. P.; Reddy, B. A. A.; Arif, M.; Kundu, T. K.; Narayana, C. Surface-Enhanced Raman Scattering Studies of Human Transcriptional Coactivator P300. *J Phys Chem B* **2006,** *110,* 16787–16792.

28. D'Urso, L.; Condorelli, M.; Puglisi, O.; Tempra, C.; Lolicato, F.; Compagnini, G.; La Rosa, C. Detection and Characterization at nM Concentration of Oligomers Formed by hIAPP, Aβ(1-40) and Their Equimolar Mixture Using SERS and MD Simulations. *Phys Chem Chem Phys* **2018,** *20,* 20588–20596.

29. Krysmann, M. J.; Castelletto, V.; Kelarakis, A.; Hamley, I. W.; Hule, R. A.; Pochan, D. J. Self-Assembly and Hydrogelation of an Amyloid Peptide Fragment. *Biochemistry-US* **2008,** *47,* 4597–4605.

30. Fazio, B.; D'Andrea, C.; Foti, A.; Messina, E.; Irrera, A.; Donato, M. G.; Villari, V.; Micali, N.; Marago, O. M.; Gucciardi, P. G. SERS Detection of Biomolecules at Physiological pH via Aggregation of Gold Nanorods Mediated by Optical Forces and Plasmonic Heating. *Sci Rep-UK* **2016,** *6*.

31. Tabatabaei, M.; Caetano, F. A.; Pashee, F.; Ferguson, S. S. G.; Lagugne-Labarthet, F. Tip-Enhanced Raman Spectroscopy of Amyloid β at Neuronal Spines. *Analyst* **2017,** *142,* 4415–4421.

32. Schwenk, N.; Mizaikoff, B.; Cardenas, S.; Lopez-Lorente, A. I. Gold-Nanostar-Based SERS Substrates for Studying Protein Aggregation Processes. *Analyst* **2018,** *143,* 5103–5111.

33. Alvarez-Puebla, R. A.; Agarwal, A.; Manna, P.; Khanal, B. P.; Aldeanueva-Potel, P.; Carbo-Argibay, E.; Pazos-Perez, N.; Vigderman, L.; Zubarev, E. R.; Kotov, N. A.; Liz-Marzan, L. M. Gold Nanorods 3D-Supercrystals as Surface Enhanced Raman Scattering Spectroscopy Substrates for the Rapid Detection of Scrambled Prions. *P Natl Acad Sci USA* **2011,** *108,* 8157–8161.

34. Zavatski, S.; Khinevich, N.; Girel, K.; Redko, S.; Kovalchuk, N.; Komissarov, I.; Lukashevich, V.; Semak, I.; Mamatkulov, K.; Vorobyeva, M.; Arzumanyan, G.; Bandarenka, H. Surface Enhanced Raman Spectroscopy of Lactoferrin Adsorbed on Silvered Porous Silicon Covered with Graphene. *Biosensors-Basel* **2019,** *9*.

35. Swiech, D.; Ozaki, Y.; Kim, Y.; Proniewicz, E. Surface- and Tip-Enhanced Raman Scattering of Bradykinin onto the Colloidal Suspended Ag Surface. *Phys Chem Chem Phys* **2015,** *17,* 19672–19672.

36. Di Foggia, M.; Ottani, S.; Torreggiani, A.; Zamuner, A.; Dettin, M.; Sanchez-Cortes, S.; Cesini, D.; Tinti, A. Surface Enhanced Raman Scattering and Quantum-Mechanical Calculations on Self-Assembling Oligopeptides. *J Raman Spectrosc* **2018,** *49,* 982–996.

37. Guo, T. J.; Ding, F. S.; Li, D. L.; Zhang, W.; Cao, L. R.; Liu, Z. M. Full-Scale Label-Free Surface-Enhanced Raman Scattering Analysis of Mouse Brain Using a Black Phosphorus-Based Two-Dimensional Nanoprobe. *Appl Sci-Basel* **2019,** *9*.

38. Accardo, A.; Shalabaeva, V.; Cotte, M.; Burghammer, M.; Krahne, R.; Riekel, C.; Dante, S. Amyloid β Peptide Conformational Changes in the Presence of a Lipid Membrane System. *Langmuir* **2014,** *30,* 3191–3198.

39. Shende, C.; Inscore, F.; Huang, H.; Farquharson, S.; Sengupta, A. Detection of Bacillus Spores within 15 Minutes by Surface-Enhanced Raman Spectroscopy. *Proc SPIE* **2012,** *8358*.

40. Ngo, Y. H.; Then, W. L.; Shen, W.; Garnier, G. Gold Nanoparticles Paper as a SERS Bio-Diagnostic Platform. *J Colloid Interf Sci* **2013,** *409,* 59–65.

41. Ooka, A. A.; Garrell, R. L. Surface-Enhanced Raman Spectroscopy of Dopa-Containing Peptides Related to Adhesive Protein of Marine Mussel, Mytilus Edulis. *Biopolymers* **2000,** *57,* 92–102.

42. Ma, C. X.; Harris, J. M. Surface-Enhanced Raman Scattering Study of the Kinetics of Self-Assembly of Carboxylate-Terminated N-Alkanethiols on Silver. *Langmuir* **2012,** *28,* 2628–2636.

43. Castro, J. L.; Lopez-Ramirez, M. R.; Arenas, J. F.; Otero, J. C. Surface-Enhanced Raman Scattering of 3-Mercaptopropionic Acid Adsorbed on a Colloidal Silver Surface. *J Raman Spectrosc* **2004,** *35,* 997–1000.

44. Demeritte, T.; Nellore, B. P. V.; Kanchanapally, R.; Sinha, S. S.; Pramanik, A.; Chavva, S. R.; Ray, P. C. Hybrid Graphene Oxide Based Plasmonic-Magnetic Multifunctional Nanoplatform for Selective Separation and Label-Free Identification of Alzheimer's Disease Biomarkers. *ACS Appl Mater Inter* **2015,** *7,* 13693–13700.

45. Kho, K. W.; Dinish, U. S.; Kumar, A.; Olivo, M. Frequency Shifts in SERS for Biosensing. *ACS Nano* **2012,** *6,* 4892–4902.

46. Malek, K.; Krolikowska, A.; Bukowska, J. pH and Substrate Effect on Adsorption of Peptides Containing Z and E Dehydrophenylalanine. Surface-Enhanced Raman Spectroscopy Studies on Ag Nanocolloids and Electrodes. *J Phys Chem B* **2014,** *118,* 4025–4036.

47. Orendorff, C. J.; Gole, A.; Sau, T. K.; Murphy, C. J. Surface-Enhanced Raman Spectroscopy of Self-Assembled Monolayers: Sandwich Architecture and Nanoparticle Shape Dependence. *Anal Chem* **2005,** *77,* 3261–3266.

48. Singha, A.; Dasgupta, S.; Roy, A. Comparison of Metal-Amino Acid Interaction in Phe-Ag and Tyr-Ag Complexes by Spectroscopic Measurements. *Biophys Chem* **2006,** *120,* 215–224.

49. Madzharova, F.; Heiner, Z.; Kneipp, J. Surface Enhanced Hyper-Raman Scattering of the Amino Acids Tryptophan, Histidine, Phenylalanine, and Tyrosine. *J Phys Chem C* **2017,** *121,* 1235–1242.

50. Jarvis, R. M.; Law, N.; Shadi, L. T.; O'Brien, P.; Lloyd, J. R.; Goodacre, R. Surface-Enhanced Raman Scattering from Intracellular and Extracellular Bacterial Locations. *Anal Chem* **2008,** *80,* 6741–6746.

51. Paccotti, N.; Boschetto, F.; Horiguchi, S.; Marin, E.; Chiado, A.; Novara, C.; Geobaldo, F.; Giorgis, F.; Pezzotti, G. Label-Free SERS Discrimination and in Situ Analysis of Life Cycle in Escherichia Coli and Staphylococcus Epidermidis. *Biosensors-Basel* **2018,** *8*.

52. Monfared, A. M. T.; Tiwari, V. S.; Trudeau, V. L.; Anis, H. Surface-Enhanced Raman Scattering Spectroscopy for the Detection of Glutamate and Gamma-Aminobutyric Acid in Serum by Partial Least Squares Analysis. *IEEE Photonics J* **2015,** *7*.

53. Barron, L. D.; Hecht, L.; Blanch, E. W.; Bell, A. F. Solution Structure and Dynamics of Biomolecules from Raman Optical Activity. *Prog Biophys Mol Bio* **2000,** *73,* 1–49.

54. Nawrocka, A. Conformational Changes in Wheat Gluten after Using Ag-Nanoparticles. *Int Agrophys* **2014,** *28,* 311–317.

55. Mikhonin, A. V.; Ahmed, Z.; Ianoul, A.; Asher, S. A. Assignments and Conformational Dependencies of the Amide III Peptide Backbone UV Resonance Raman Bands. *J Phys Chem B* **2004,** *108,* 19020–19028.

56. Li, S. S.; Guan, Q. Y.; Meng, G.; Chang, X. F.; Wei, J. W.; Wang, P.; Kang, B.; Xu, J. J.; Chen, H. Y. Revealing Chemical Processes and Kinetics of Drug Action within Single Living Cells via Plasmonic Raman Probes. *Sci Rep-UK* **2017,** *7*.

57. Serban, D.; Arcineigas, S. F.; Vorgias, C. E.; Thomas, G. J. Structure and Dynamics of the DNA-Binding Protein Hu of B-Stearothermophilus Investigated by Raman and Ultraviolet-Resonance Raman Spectroscopy. *Protein Sci* **2003,** *12,* 861–870.

58. Panikkanvalappil, S. R.; Hira, S. M.; Mahmoud, M. A.; El-Sayed, M. A. Unraveling the Biomolecular Snapshots of Mitosis in Healthy and Cancer Cells Using Plasmonically-Enhanced Raman Spectroscopy. *J Am Chem Soc* **2014,** *136,* 15961–15968.

59. Podstawka, E.; Ozaki, Y.; Proniewicz, L. M. Adsorption of S-S Containing Proteins on a Colloidal Silver Surface Studied by Surface-Enhanced Raman Spectroscopy. *Appl Spectrosc* **2004,** *58,* 1147–1156.

60. Wen, Z. Q. Raman Spectroscopy of Protein Pharmaceuticals. *J Pharm Sci-US* **2007,** *96,* 2861–2878.

61. Krasnoslobodtsev, A. V.; Deckert-Gaudig, T.; Zhang, Y. L.; Deckert, V.; Lyubchenko, Y. L. Polymorphism of Amyloid Fibrils Formed by a Peptide from the Yeast Prion Protein Sup35: AFM and Tip-Enhanced Raman Scattering Studies. *Ultramicroscopy* **2016,** *165,* 26–33.

62. Wu, J. W.; Zhang, L. X.; Bu, X. F.; Li, P.; Zhao, B.; Tian, Y. Determination of the Illegal Adulteration of Natural Healthcare Products with Chemical Drugs Using Surface-Enhanced Raman Scattering. *Analyst* **2018,** *143,* 5202–5209.

63. Chowdhury, M. H.; Gant, V. A.; Trache, A.; Baldwin, A.; Meininger, G. A.; Cote, G. L. Use of Surface-Enhanced Raman Spectroscopy for the Detection of Human Integrins. *J Biomed Opt* **2006,** *11*.

64. Podstawka-Proniewicz, E.; Kosior, M.; Kim, Y.; Rolka, K.; Proniewicz, L. M. Nociceptin and its Natural and Specifically-Modified Fragments: Structural Studies. *Biopolymers* **2010,** *93,* 1039–1054.

65. Cottat, M.; Yasukuni, R.; Homma, Y.; Lidgi-Guigui, N.; Varin-Blank, N.; de la Chapelle, M. L.; Le Roy, C. Phosphorylation Impact on Spleen Tyrosine Kinase Conformation by Surface Enhanced Raman Spectroscopy. *Sci Rep-UK* **2017,** *7*.

66. Ren, H.; Zhang, Y.; Guo, S. B.; Lin, N.; Deng, L.; Yue, T. T.; Huang, F. Identifying Cu(II)-Amyloid Peptide Binding Intermediates in the Early Stages of Aggregation by Resonance Raman Spectroscopy: A Simulation Study. *Phys Chem Chem Phys* **2017,** *19,* 31103–31112.

67. Costas, C.; Lopez-Puente, V.; Bodelon, G.; Gonzalez-Bello, C.; Perez-Juste, J.; Pastoriza-Santos, I.; Liz-Marzan, L. M. Using Surface Enhanced Raman Scattering to Analyze the Interactions of Protein Receptors with Bacterial Quorum Sensing Modulators. *ACS Nano* **2015,** *9,* 5567–5576.

68. vandenAkker, C. C.; Deckert-Gaudig, T.; Schleeger, M.; Velikov, K. P.; Deckert, V.; Bonn, M.; Koenderink, G. H. Nanoscale Heterogeneity of the Molecular Structure of Individual hIAPP Amyloid Fibrils Revealed with Tip-Enhanced Raman Spectroscopy. *Small* **2015,** *11,* 4131–4139.

69. Aliaga, A. E.; Osorio-Roman, I.; Garrido, C.; Leyton, P.; Carcamo, J.; Clavijo, E.; Gomez-Jeria, J. S.; Diaz, G.; Campos-Vallette, M. M. Surface Enhanced Raman Scattering Study of L-Lysine. *Vib Spectrosc* **2009,** *50,* 131–135.

70. Asiala, S. M.; Schultz, Z. D. Surface Enhanced Raman Correlation Spectroscopy of Particles in Solution. *Anal Chem* **2014,** *86,* 2625–2632.

71. Wang, Q.; Wang, Y. M.; Lu, H. P. Revealing the Secondary Structural Changes of Amyloid β Peptide by Probing the Spectral Fingerprint Characters. *J Raman Spectrosc* **2013,** *44,* 670–674.

72. Subaihi, A.; Xu, Y.; Muhamadali, H.; Mutter, S. T.; Blanch, E. W.; Ellis, D. I.; Goodacre, R. Towards Improved Quantitative Analysis Using Surface-Enhanced Raman Scattering Incorporating Internal Isotope Labelling. *Anal Methods-UK* **2017,** *9,* 6636–6644.

73. Karaballi, R. A.; Merchant, S.; Power, S. R.; Brosseau, C. L. Electrochemical Surface-Enhanced Raman Spectroscopy (EC-SERS) Study of the Interaction between Protein Aggregates and Biomimetic Membranes. *Phys Chem Chem Phys* **2018,** *20,* 4513–4526.

74. Xu, L. J.; Zong, C.; Zheng, X. S.; Hu, P.; Feng, J. M.; Ren, B. Label-Free Detection of Native Proteins by Surface-Enhanced Raman Spectroscopy Using Iodide-Modified Nanoparticles. *Anal Chem* **2014,** *86,* 2238–2245.

75. Leyton, P.; Lizama-Vergara, P. A.; Campos-Vallette, M. M.; Becker, M. I.; Clavijo, E.; Reyes, I. C.; Vera, M.; Jerez, C. A. Surface Enhanced Raman Spectrum of Nanometric Molecular Systems. *J Chil Chem Soc* **2005,** *50,* 725–730.

76. Podstawka, E.; Ozaki, Y.; Proniewicz, L. M. Part III: Surface-Enhanced Raman Scattering of Amino Acids and Their Homodipeptide Monolayers Deposited onto Colloidal Gold Surface. *Appl Spectrosc* **2005,** *59,* 1516–1526.

77. Dolui, S.; Roy, A.; Pal, U.; Saha, A.; Maiti, N. C. Structural Insight of Amyloidogenic Intermediates of Human Insulin. *ACS Omega* **2018,** *3,* 2452–2462.

78. Yu, X. K.; Hayden, E. Y.; Xia, M.; Liang, O.; Cheah, L.; Teplow, D. B.; Xie, Y. H. Surface Enhanced Raman Spectroscopy Distinguishes Amyloid β-Protein Isoforms and Conformational States. *Protein Sci* **2018,** *27,* 1427–1438.

79. Kuhar, N.; Sil, S.; Verma, T.; Umapathy, S. Challenges in Application of Raman Spectroscopy to Biology and Materials. *RSC Adv* **2018,** *8,* 25888–25908.

80. Dufrene, Y. F. Atomic Force Microscopy, a Powerful Tool in Microbiology. *J Bacteriol* **2002,** *184,* 5205–5213.

81. Feng, L.; Watanabe, H.; Molino, P.; Wallace, G.G.; Phung, S.L.; Uchihashi, T.; Higgins, M.J. Dynamics of Inter-Molecular Interactions Between Single Aβ42 Oligomeric and Aggregate Species by High-Speed Atomic Force Microscopy. *J Mol Biol* **2019,** *431,* 2687–2699

82. Atwood, C. S.; Moir, R. D.; Huang, X. D.; Scarpa, R. C.; Bacarra, N. M. E.; Romano, D. M.; Hartshorn, M. K.; Tanzi, R. E.; Bush, A. I. Dramatic Aggregation of Alzheimer Aβ by Cu(II) Is Induced by Conditions Representing Physiological Acidosis. *J Biol Chem* **1998,** *273,* 12817–12826.

83. Dai, X.; Sun, Y.; Gao, Z.; Jiang, Z. Copper Enhances Amyloid-β Peptide Neurotoxicity and Non β-Aggregation: A Series of Experiments Conducted Upon Copper-Bound and Copper-Free Amyloid-β Peptide. *J Mol Neurosci* **2010,** *41,* 66–73.

84. Gamez, P.; Caballero, A. B. Copper in Alzheimer's Disease: Implications in Amyloid Aggregation and Neurotoxicity. *AIP Adv* **2015,** *5*.

85. Adamcik, J.; Mezzenga, R. Amyloid Polymorphism in the Protein Folding and Aggregation Energy Landscape. *Angew Chem Int Ed Engl* **2018,** *57,* 8370–8382.

86. Lin, Y.; Sahoo, B. R.; Ozawa, D.; Kinoshita, M.; Kang, J.; Lim, M. H.; Okumura, M.; Huh, Y. H.; Moon, E.; Jang, J. H.; Lee, H. J.; Ryu, K. Y.; Ham, S.; Won, H. S.; Ryu, K. S.; Sugiki, T.; Bang, J. K.; Hoe, H. S.; Fujiwara, T.; Ramamoorthy, A.; Lee, Y. H. Diverse Structural Conversion and Aggregation Pathways of Alzheimer's Amyloid-β (1-40). *ACS Nano* **2019,** *13,* 8766–8783.

87. Cai, Z. F.; Dong, W. L.; Chen, T.; Yan, H. J.; Wang, D.; Xu, W.; Wan, L. J. Directed Assembly of Fullerene on Modified Au(111) Electrodes. *Chem Commun (Camb)* **2018,** *54,* 8052–8055.

88. Yang, Z. Y.; Zhang, H. M.; Yan, C. J.; Li, S. S.; Yan, H. J.; Song, W. G.; Wan, L. J. Scanning Tunneling Microscopy of the Formation, Transformation, and Property of Oligothiophene Self-Organizations on Graphite and Gold Surfaces. *Proc Natl Acad Sci USA* **2007,** *104,* 3707–3712.

89. Claridge, S. A.; Thomas, J. C.; Silverman, M. A.; Schwartz, J. J.; Yang, Y. L.; Wang, C.; Weiss, P. S. Differentiating Amino Acid Residues and Side Chain Orientations in Peptides Using Scanning Tunneling Microscopy. *J Am Chem Soc* **2013,** *135,* 18528–18535.

90. Mao, X. B.; Wang, C. X.; Wu, X. K.; Ma, X. J.; Liu, L.; Zhang, L.; Niu, L.; Guo, Y. Y.; Li, D. H.; Yang, Y. L.; Wang, C. Beta Structure Motifs of Islet Amyloid Polypeptides Identified through Surface-Mediated Assemblies. *P Natl Acad Sci USA* **2011,** *108,* 19605–19610.

91. Mcmaster, T. J.; Carr, H. J.; Miles, M. J.; Cairns, P.; Morris, V. J. Scanning Tunneling Microscopy of Poly(Gamma-Benzyl L-Glutamate). *Macromolecules* **1991,** *24,* 1428–1430.

92. Yugay, D.; Goronzy, D. P.; Kawakami, L. M.; Claridge, S. A.; Song, T. B.; Yan, Z.; Xie, Y. H.; Gilles, J.; Yang, Y.; Weiss, P. S. Copper Ion Binding Site in β–Amyloid Peptide. *Nano Lett* **2016,** *16,* 6282–6289.

93. Chi, Q. J.; Farver, O.; Ulstrup, J. Long-Range Protein Electron Transfer Observed at the Single-Molecule Level: In Situ Mapping of Redox-Gated Tunneling Resonance. *P Natl Acad Sci USA* **2005,** *102,* 16203–16208.

94. Nelson, R.; Sawaya, M. R.; Balbirnie, M.; Madsen, A. O.; Riekel, C.; Grothe, R.; Eisenberg, D. Structure of the Cross-β Spine of Amyloid-Like Fibrils. *Nature* **2005,** *435,* 773–778.

95. Tayeb-Fligelman, E.; Tabachnikov, O.; Moshe, A.; Goldshmidt-Tran, O.; Sawaya, M. R.; Coquelle, N.; Colletier, J. P.; Landau, M. The Cytotoxic Staphylococcus Aureus PSMα3 Reveals a Cross-α Amyloid-Like Fibril. *Science* **2017,** *355,* 831–833.

96. Choudhary, S.; Sarma, J. V. N.; Pande, S.; Ababou-Girard, S.; Turban, P.; Lepine, B.; Gangopadhyay, S. Oxidation Mechanism of Thin Cu Films: A Gateway Towards the Formation of Single Oxide Phase. *AIP Adv* **2018,** *8*.

97. Mondal, P.; Sinha, A.; Salam, N.; Roy, A. S.; Jana, N. R.; Islam, S. M. Enhanced Catalytic Performance by Copper Nanoparticle-Graphene Based Composite. *RSC Adv* **2013,** *3,* 5615–5623.

98. Shimizu, Y.; Yamamoto, S.; Takase, S. A Thick-Film Impedancemetric Carbon Monoxide Sensor Using Layered Perovskite-Type Cuprate. *Sensor Actuat B-Chem* **2017,** *249,* 667–672.

99. Fales, A. M.; Yuan, H. K.; Vo-Dinh, T. Development of Hybrid Silver-Coated Gold Nanostars for Nonaggregated Surface-Enhanced Raman Scattering. *J Phys Chem C* **2014,** *118,* 3708–3715.

CHAPTER 5

Summary and Outlook

5.1 Scanning Tunneling Microscopy: Past and Future

The advantages of scanning tunneling microscopy (STM) include, but are not limited to, its ability to determine structural information without the requirement of biomolecular crystallinity that plagues other techniques used for structural determination, such as X-ray diffraction (XRD). Furthermore, while other techniques rely on ensemble measurements, STM is capable of imaging unique and non-periodic features. Additionally, the use of multi-modal imaging techniques allows us to extract chemical as well as structural information.[1,2] Using STM and mathematical modeling algorithms, we demonstrated that it is possible 1) to differentiate between side-chain amino acid residues in peptides,[3] 2) to visualize in real space the metal ion-binding sites in non-crystalline biological molecules,[4] 3) to map and to differentiate between assemblies of biological molecules based on their interaction with two different metal ions (*manuscript in preparation*), and 4) to map buried hydrogen-bonding networks within the buried interfaces of amide-containing surface assemblies.[5]

In the above studies, we evaluated the potential of STM as a technique to resolve secondary structures of biological molecules, specifically, structures of simple model peptides and fragments of amyloidogenic peptides. Unique physical properties of amyloidogenic peptides, such as conformational flexibility and non-crystallinity, is an interest to us because, by using STM in amyloidogenic systems, we not only explore and expand STM as a tool for studying biological molecules and assemblies and their interactions with their surroundings but we also contribute to understanding the fundamental processes behind amyloid-related diseases such as Alzheimer's disease (AD).

In initial studies, we focused on either simple oligopeptide systems – linear peptide chains with five histidines and five alanines[3] – or self-assembled amide-containing alkanethiolate

monolayers[5] as models to resolve biological structures *via* STM (not included in this dissertation). Further studies examined the short chain segment containing the first 16 amino acid residues of β-amyloid ($A\beta_{1-16}$) and its interactions with Cu^{2+} ions[4] and Zn^{2+} ions (included in Chapters 2 and 3). Based on the analyses of the STM images, we were able to elucidate the peptide-peptide interactions as well as the peptide-metal ion interactions with submolecular resolution.[3-5]

Using our expertise in studying biological molecules *via* STM, we aim 1) to increase the scope of our imaging techniques to effectively study more complex biological molecules and changes in their structures due to post-translational modifications (PTMs) and 2) to expand STM potential by employing different STM imaging modalities – alternating current coupled to the STM (ACSTM or microwave STM) and electrochemical STM (ECSTM). These STM modalities would enable us to examine specific biomolecular and metal ion/modulator interactions based on their properties, such as local variations in chemical, dielectric, magnetic, and electrochemical properties.

5.2 Visualization of Buried Metal Ion-Binding Sites

The structure of the last 26 amino acid residues of Aβ ($A\beta_{17-42}$) was discovered using steady-state nuclear magnetic resonance and XRD.[6,7] However, the location of a second, lower affinity binding site in the vicinity of the C-terminus of the peptide remains undetermined.[8,9] Thus, our ongoing project examines the buried metal-ion binding site of $A\beta_{17-42}$. To explore the peptide interactions within this system, it is necessary to use both ambient STM and STM with additional imaging modalities such as ACSTM.

As discussed in Chapter 4, our preliminary results of surface-enhanced Raman spectroscopy (SERS), and cyclic voltammetry (CV), confirm the interaction of $A\beta_{17-42}$ with Cu^{2+} ions. The scanning tunneling microscopy results show that $A\beta_{17-42}$ incubated with Cu^{2+} ions self-assemble into β-sheets with an interstrand distance of 5.5 ± 0.2 Å, and the strands are 54.8 ± 1.3 Å in length. This strand length corresponds to approximately ~17 amino acids; because this peptide has 26 amino acids, the data suggest that $A\beta_{17-42}$ must be in a folded conformation. Taking into consideration the preliminary SERS and CV data that suggest interactions of $A\beta_{17-42}$ with Cu^{2+} ions and the absence of non-periodic protruding features – which would correspond to Cu^{2+} sites – in STM data, we hypothesize that the $A\beta_{17-42}$ copper-binding sites are at a buried interface underneath the peptide backbone.

To image locations and interfaces of the buried metal ion-binding sites of $A\beta_{17-42}$ effectively, advanced imaging techniques such as polarized STM will be used. These multi-modal imaging techniques are powerful tools for extracting chemical and structural information even from buried interfaces (Figure 5.1).[1,2]

5.3 Detection of Buried Metal Ion-Binding Sites

Detection of buried metal ion-binding site within $A\beta_{17-42}$ will demonstrate that it is possible 1) to explore biological systems *via* ACSTM and 2) to explore buried amino acids residues and interaction of those residues with inorganic molecules. After completing the studies on $A\beta_{17-42}$, the next step in our research is to investigate full-length Aβ, which contains 42 amino acid residues ($A\beta_{1-42}$). Both the crystal structure and its adsorbed self-assembled structures have been studied by ambient STM and XRD.[10,11] It has been established that $A\beta_{1-42}$ folds twice onto itself.[10] However, despite recent advances in determining peptide folding and structures of $A\beta_{1-42}$

in its fibrillar form as well as extensive literature on interactions of $A\beta_{1-42}$ with metal ions, there is still a lack of studies on experimental visualization of the position of metal ions bound to $A\beta_{1-42}$. Thus, the second part of the project has two ultimate goals – 1) to elucidate the position of the buried metal ion-binding sites in $A\beta_{1-42}$ and 2) to establish whether the binding sites in $A\beta_{1-42}$ show preferential metal ion binding, by incubating $A\beta_{1-42}$ with a solution containing both Zn^{2+} and Cu^{2+}.

5.4 Resolving Structures and Interactions between Post-Translationally Modified Amyloidogenic Peptides

Apart from recent interest in the correlation between metal ions and AD, there is growing interest in how PTMs in the form of glycosylation affect the structure and function of Aβ and its link to AD pathogenesis. Studies have suggested correlations between glycosylation malfunction and AD.[12,13] Halim *et al.* examined glycosylation of Aβ in the cerebrospinal fluid of healthy patients versus patients with AD.[14] They found that Aβ peptides in diseased patients were glycosylated 2.5 times more frequently than those in the control group. One of the most abundant glycopeptides they found was an Aβ segment containing the first 15 amino acid residues ($A\beta_{1-15}$) with the glycan group attached to the tyrosine residue at position 10 (Tyr10). Wang *et al.* have synthesized $A\beta_{1-15}$ with α-linked and β-linked glycan attachments at the Tyr10 position, Figure 5.2.[15] However, the effect of these glycan attachments on the structure, interaction with metal ions, and aggregation of Aβ in the brain remains unclear.

This project involves studying post-translationally modified $A\beta_{1-15}$ *via* STM. This Aβ segment has a glycan group attached at the Tyr10. Our preliminary results based on atomic force microscopy (AFM) (Figure 5.3) suggest that glycosylation does not affect the ability of the

peptides to self-assemble into β-sheets. We also noted that the self-assembly of the post-translationally modified $A\beta_{1-15}$ into β-sheets is not affected by the presence or absence of Cu^{2+} ions. However, the preliminary peak force AFM results suggest that the β-sheet surface of $A\beta_{1-15}$ deposited with Cu^{2+} ions is more adhesive than the surface of $A\beta_{1-15}$ without Cu^{2+} ions. However, owing to the resolution limits of AFM, we cannot make any structural conclusions about how glycosylation affects $A\beta_{1-15}$ peptides on a structural and sub-molecular level. Because our group has previously shown that STM is a powerful new tool for elucidating the structures of biomolecules, we propose to utilize our expertise in this area to study the structure of glycopeptides such as glycosylated $A\beta_{1-15}$, to determine the locations of glycosylated bonds, and to study its interaction with adjacent glycopeptides and metal ions. This project presents certain new challenges because, in the case of post-translationally modified peptides, the molecular attachment (glycan) is a bulky group that can freely rotate around the attachment bond and thus, constrain STM imaging. If we are successful in imaging and analyzing post-translationally modified $A\beta_{1-15}$, then it would be a stepping stone towards studying complicated PTM systems such as systems with multiple glycosylation sites and peptides with multi-glycan chain attachments. Such studies, of complicated biological systems, would be broadly applicable to the study of biomolecular structures and more representative of *in vivo* biomolecules.

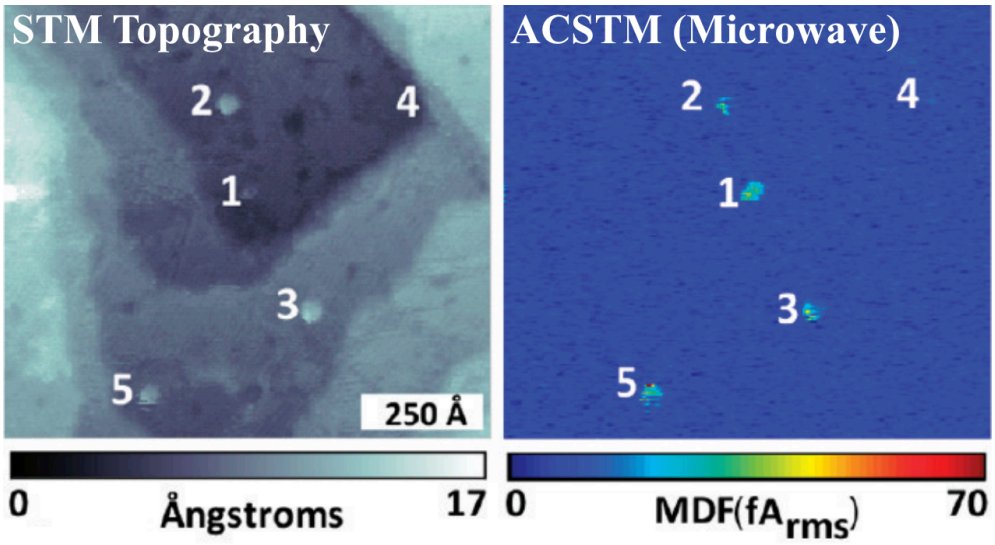

Figure 5.1. Scanning tunneling microscopy image showing molecular polarizability of highly polarizable 4,4'-di(ethynylphenyl)-1-benzenethiol (OPE) molecules inserted into dodecanethiolate (C12) self-assembled monolayer (SAM). In the ACSTM microwave image, OPE molecules appear as high-contrast protruding features (numbered 1–5) against a dark background (C12 SAM); contrast between OPE and C12 is more intense in the ACSTM image than in the STM topography image. Adapted from ref. 2. Copyright 2010, ACS Nano.

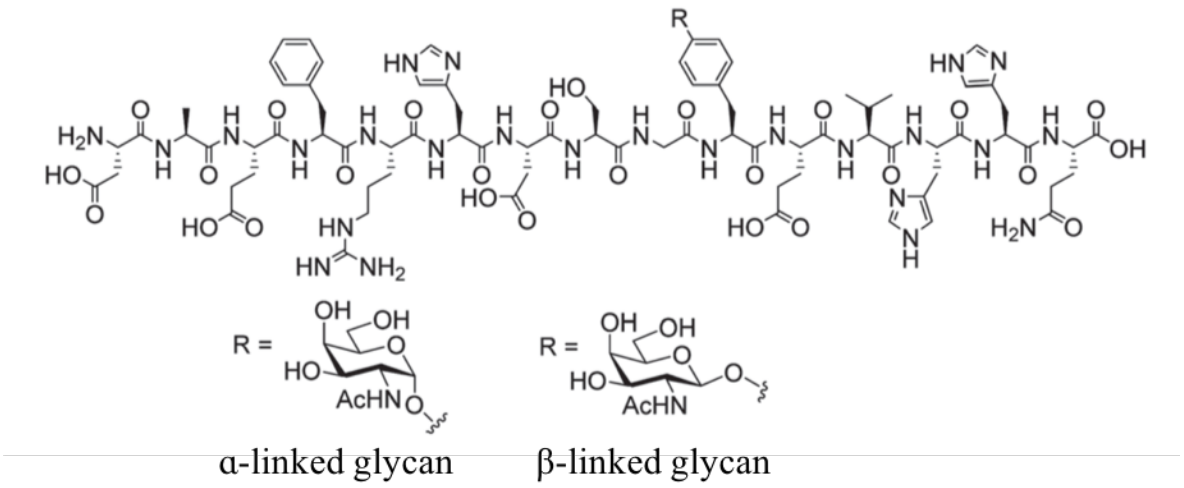

Figure 5.2. Primary structure of glycosylated $A\beta_{1\text{-}15}$. The R group on the tyrosine residue indicates an α-linked glycan attachment (bottom, left) or a β-linked glycan attachment (bottom, right). Adapted from ref. 15. Copyright 2014, Chemical Communications.

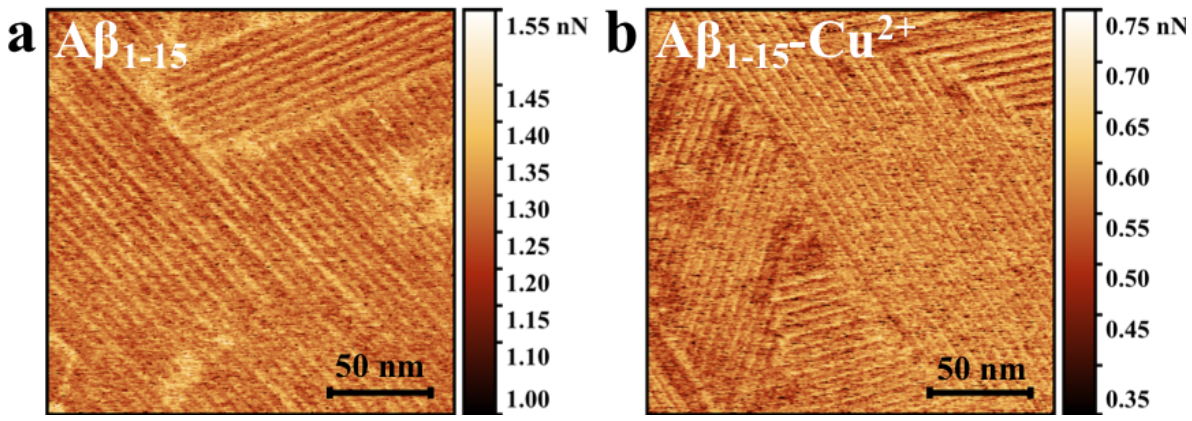

Figure 5.3. Images of adhesion measurements with atomic force microscopy (a) $A\beta_{1-15}$ without Cu^{2+} and (b) $A\beta_{1-15}$ incubated with Cu^{2+} ions. $A\beta_{1-15}$ without Cu^{2+} has higher adhesive properties; therefore, laminated β-sheets are more flexible ("sticky") compared to β-sheets of $A\beta_{1-15}$ when incubated with Cu^{2+} ions.

5.5 References

1. Bang, J. J.; Russell, S. R.; Rupp, K. K.; Claridge, S. A. Multimodal Scanning Probe Imaging: Nanoscale Chemical Analysis from Biology to Renewable Energy. *Anal Methods-UK* **2015,** *7,* 7106–7127.

2. Moore, A. M.; Yeganeh, S.; Yao, Y.; Claridge, S. A.; Tour, J. M.; Ratner, M. A.; Weiss, P. S. Polarizabilities of Adsorbed and Assembled Molecules: Measuring the Conductance through Buried Contacts. *ACS Nano* **2010,** *4,* 7630–7636.

3. Claridge, S. A.; Thomas, J. C.; Silverman, M. A.; Schwartz, J. J.; Yang, Y. L.; Wang, C.; Weiss, P. S. Differentiating Amino Acid Residues and Side Chain Orientations in Peptides Using Scanning Tunneling Microscopy. *J Am Chem Soc* **2013,** *135,* 18528–18535.

4. Yugay, D.; Goronzy, D. P.; Kawakami, L. M.; Claridge, S. K.; Song, T. B.; Yan, Z. B.; Xie, Y. H.; Gilles, J.; Yang, Y.; Weiss, P. S. Copper Ion Binding Site in β-Amyloid Peptide. *Nano Lett* **2016,** *16,* 6282–6289.

5. Thomas, J. C.; Goronzy, D. P.; Dragomiretskiy, K.; Zosso, D.; Gilles, J.; Osher, S. J.; Bertozzi, A. L.; Weiss, P. S. Mapping Buried Hydrogen-Bonding Networks. *ACS Nano* **2016,** *10,* 5446–5451.

6. Miller, Y.; Ma, B.; Nussinov, R. Polymorphism of Alzheimer's A$\beta_{17\text{-}42}$ (p3) Oligomers: The Importance of the Turn Location and Its Conformation. *Biophys J* **2009,** *97,* 1168–1177.

7. Streltsov, V. A.; Varghese, J. N.; Masters, C. L.; Nuttall, S. D. Crystal Structure of the Amyloid-β P3 Fragment Provides a Model for Oligomer Formation in Alzheimer's Disease. *J Neurosci* **2011,** *31,* 1419–1426.

8. Danielsson, J.; Pierattelli, R.; Banci, L.; Graslund, A. High-Resolution NMR Studies of the Zinc-Binding Site of the Alzheimer's Amyloid β-Peptide. *FEBS J* **2007,** *274,* 46–59.

9. Jun, S.; Gillespie, J. R.; Shin, B. K.; Saxena, S. The Second Cu(II)-Binding Site in a Proton-Rich Environment Interferes with the Aggregation of Amylold-β(1-40) into Amyloid Fibrils. *Biochemistry-US* **2009,** *48,* 10724–10732.

10. Gremer, L.; Scholzel, D.; Schenk, C.; Reinartz, E.; Labahn, J.; Ravelli, R. B. G.; Tusche, M.; Lopez-Iglesias, C.; Hoyer, W.; Heise, H.; Willbold, D.; Schroder, G. F. Fibril Structure of Amyloid-β(1-42) by Cryo-Electron Microscopy. *Science* **2017,** *358,* 116–119.

11. Wang, Z.; Zhou, C.; Wang, C.; Wan, L.; Fang, X.; Bai, C. AFM and STM Study of β-Amyloid Aggregation on Graphite. *Ultramicroscopy* **2003,** *97,* 73–79.

12. Frenkel-Pinter, M.; Shmueli, M. D.; Raz, C.; Yanku, M.; Zilberzwige, S.; Gazit, E.; Segal, D. Interplay between Protein Glycosylation Pathways in Alzheimer's Disease. *Sci Adv* **2017,** *3,* e1601576.

13. Schedin-Weiss, S.; Winblad, B.; Tjernberg, L. O. The Role of Protein Glycosylation in Alzheimer Disease. *FEBS J* **2014,** *281,* 46–62.

14. Halim, A.; Brinkmalm, G.; Ruetschi, U.; Westman-Brinkmalm, A.; Portelius, E.; Zetterberg, H.; Blennow, K.; Larson, G.; Nilsson, J. Site-Specific Characterization of Threonine, Serine, and Tyrosine Glycosylations of Amyloid Precursor Protein/Amyloid β-Peptides in Human Cerebrospinal Fluid. *P Natl Acad Sci USA* **2011,** *108,* 11848–11853.

15. Wang, P.; Nilsson, J.; Brinkmalm, G.; Larson, G.; Huang, X. Synthesis Aided Structural Determination of Amyloid-β(1-15) Glycopeptides, New Biomarkers for Alzheimer's Disease. *Chem Commun* **2014,** *50,* 15067–15070.

Appendix A

A.1 Chapter 2 MATLAB Code

Unstripping Matlab Code:

```
function [out,D]=Unstripping(I0,rt,winsize)

%=========================================================
% function out=Unstripping(I0,rt,winsize)
%
% This function removes horizontal stripes and
% saturation segments for nanoimaging
%
% Inputs:
%  -I0: image
%  -rt: detection ratio (0<rt<1) (0.3 seems working)
%  -winsize: size of the window on which the median filter is computed
%
% Output:
%  -out: processed image
%
%=========================================================

if((rt<0)||(rt>1))
   rt=0.5;
end

% Take the vertical second order-derivative
C=zeros(size(I0));
C(2:end-1,:)=I0(1:end-2,:)+I0(3:end,:)-2*I0(2:end-1,:);

% detection by thresholding
D=zeros(size(C));
thresh =rt*max(C(:));
D= double(abs(C)>thresh);
% for c=1:size(C,2)
%    for r=1:size(C,1)
%       if abs(C(r,c))>thresh
%          D(r,c)=1;
%       end
%   end
% end

% vertical median
out=I0;
% winsize=3; for
```

```
c=1:size(D,2)
   for r=1:size(D,1)
     if abs(D(r,c)) == 1
        if r<(winsize+1)
           top=1;
           bot=r+winsize;
        elseif r>(size(D,1)-winsize-1)
           top=r-winsize;
           bot=size(D,1);
        else
           top=r-winsize;
           bot=r+winsize;
        end out(r,c)=median(I0(top:bot,c));
     end
  end
end
```

A.2 Chapter 3 MATLAB Code and Computation

Interstrand Distance Peptide Measurement Matlab Code (software_distance_peptide):

```
function varargout = software_distance_peptide(varargin)
% Last Modified by GUIDE v2.5 07-Sep-2017 17:06:31
% Begin initialization code - DO NOT EDIT
gui_Singleton = 1;
gui_State = struct('gui_Name',       mfilename, ...
                   'gui_Singleton',  gui_Singleton, ...
                   'gui_OpeningFcn', @software_distance_peptide_OpeningFcn, ...
                   'gui_OutputFcn',  @software_distance_peptide_OutputFcn, ...
                   'gui_LayoutFcn',  [] , ...
                   'gui_Callback',   []);
if nargin && ischar(varargin{1})
   gui_State.gui_Callback = str2func(varargin{1});
end

if nargout
   [varargout{1:nargout}] = gui_mainfcn(gui_State, varargin{:});
else
   gui_mainfcn(gui_State, varargin{:});
end
% End initialization code - DO NOT EDIT


% --- Executes just before software_distance_peptide is made visible.
function software_distance_peptide_OpeningFcn(hObject, ~, handles, varargin)
% This function has no output args, see OutputFcn.
% hObject    handle to figure
% eventdata  reserved - to be defined in a future version of MATLAB
% handles    structure with handles and user data (see GUIDATA)
% varargin   command line arguments to software_distance_peptide (see VARARGIN)
% Choose default command line output for software_distance_peptide
handles.output = hObject;
% Update handles structure
guidata(hObject, handles);

% Initialisation of all variables
setappdata(0,'step_find_curve',0);
setappdata(0,'step_im_load',0);
setappdata(0,'step_select_ROI',0);
setappdata(0,'step_dist',0);
setappdata(0,'im',[]);
setappdata(0,'ratio',[]);
setappdata(0,'nb_direction_edit',nan);
```

```
setappdata(0,'unit','');
setappdata(0,'x_curve',[]);
setappdata(0,'smoothing_spline',[]);
setappdata(0,'nb_curve',nan);
setappdata(0,'im',[]);
setappdata(0,'im_init',[]);
setappdata(0,'filename',[]);
set(handles.checkbox_rotate,'Value',0);
set(handles.checkbox_line_distance,'Value',0);
set(handles.checkbox_bright_spots_line,'Value',0);
set(handles.checkbox_bright_spot_points,'Value',0);
set(handles.checkbox_segment,'Value',0);
set(handles.checkbox_curve,'Value',0);
set(handles.checkbox_rotate,'Value',0);
set(handles.uipanel_transformation,'Visible','Off');
set(handles.uipanel_region_of_interest_selection,'Visible','Off');
set(handles.uipanel_peptide_detection,'Visible','Off');
set(handles.uipanel_curve_modification,'Visible','Off');
set(handles.uipanel_distance_computation,'Visible','Off');
set(handles.Save_picture,'Visible','Off');


% --- Outputs from this function are returned to the command line.
function varargout = software_distance_peptide_OutputFcn(~, ~, handles)
% varargout  cell array for returning output args (see VARARGOUT);
% hObject    handle to figure
% eventdata  reserved - to be defined in a future version of MATLAB
% handles    structure with handles and user data (see GUIDATA)

% Get default command line output from handles structure
varargout{1} = handles.output;


% --- Executes on button press in load_image.
function load_image_Callback(~, ~, handles)
% Load the new image, a new box is opened to find the file, we save the
% filename to print the title and the pathname to create the new folder.
% It converts a color image in grayscale thanks to the rgb2gray function.
% New picture means to initialize variables.

% OUTPUT :
% - im : transformed image
% - im_init : loaded image
% - filename : sting
% - pathname : sting
```

```
% Open new box to load image
[filename, pathname] = uigetfile('*.png', 'Select a file');
if isequal(filename,0)
   disp('User selected Cancel')
else
    pathname = pathname(1:end-1);
    str = fullfile(pathname);
    addpath (str)
    im = imread(filename);
  % Convert in gray scale
    if size(im,3)~=1
        im = rgb2gray(im);
    end
    im = imadjust(im);
    hold off;
    imshow(im)
    title(filename)
    setappdata(0,'im',im);
    setappdata(0,'im_init',im);
    setappdata(0,'filename',filename)
    setappdata(0,'pathname',pathname)
  % If we push again this button, we initialize all variable as default
    setappdata(0,'scatter_IC_1',[]);
    setappdata(0,'scatter_IC_2',[]);
    setappdata(0,'plot_IC_1',[]);
    setappdata(0,'plot_IC_2',[]);
    setappdata(0,'step_find_curve',0);
    setappdata(0,'step_im_load',1);
    setappdata(0,'step_select_ROI',0);
    setappdata(0,'x_curve',[]);
    setappdata(0,'x_curve_area',[]);
    set(handles.edit_nb_direction,'string','');
    set(handles.edit_nb_curve,'string','');
    set(handles.checkbox_line_distance,'Value',0);
    set(handles.checkbox_bright_spots_line,'Value',0);
    set(handles.checkbox_bright_spot_points,'Value',0);
    set(handles.checkbox_segment,'Value',0);
    set(handles.checkbox_curve,'Value',0);
    set(handles.checkbox_rotate,'Value',0);
    set(handles.uipanel_transformation,'Visible','On');
    set(handles.uipanel_region_of_interest_selection,'Visible','On');
    set(handles.uipanel_peptide_detection,'Visible','Off');
    set(handles.uipanel_curve_modification,'Visible','Off');
    set(handles.uipanel_distance_computation,'Visible','Off');
    set(handles.Save_picture,'Visible','On');
end
```

```
% --- Executes on button press in checkbox_rotate.
function checkbox_rotate_Callback(hObject, ~, handles)
% Rotate the image of 90 degrees in the clockwise if yes, or show the
% initial image if no

% INPOUT :
% - check_rotate : boolean
% - im_init : loaded image
% - filename : string

% OUTPUT :
% - im : transformed image

step_im_load = getappdata(0,'step_im_load');
if step_im_load
    set(handles.uipanel_curve_modification,'Visible','Off');
    set(handles.uipanel_distance_computation,'Visible','Off');
    check_rotate = get(hObject,'Value');
    filename = getappdata(0,'filename');
    im = getappdata(0,'im');
    if check_rotate
        im = imrotate(im,-90);
    else
        im = imrotate(im,90);
    end
    hold off
    imshow(im);
    title(filename);
    setappdata(0,'im',im)
    set(handles.edit_nb_direction,'string','');
    set(handles.edit_nb_curve,'string','');
    set(handles.checkbox_line_distance,'Value',0);
    set(handles.checkbox_bright_spots_line,'Value',0);
    set(handles.checkbox_bright_spot_points,'Value',0);
    set(handles.checkbox_segment,'Value',0);
    set(handles.checkbox_curve,'Value',0);
    set(handles.uipanel_transformation,'Visible','On');
    set(handles.uipanel_region_of_interest_selection,'Visible','On');
    set(handles.uipanel_peptide_detection,'Visible','Off');
    set(handles.uipanel_curve_modification,'Visible','Off');
    set(handles.uipanel_distance_computation,'Visible','Off');
    set(handles.Save_picture,'Visible','On');
else
    set(handles.checkbox_rotate,'Value',0);
```

```
end


% --- Executes on button press in reload_transformed_image.
function reload_transformed_image_Callback(~, ~, handles)
% Show the last loaded/rotated/zoomed picture.

% INPUT :
% - im : transformed image
% - filename (string)

step_im_load = getappdata(0,'step_im_load');
if step_im_load
    set(handles.uipanel_peptide_detection,'Visible','Off');
    set(handles.uipanel_curve_modification,'Visible','Off');
    set(handles.uipanel_distance_computation,'Visible','Off');
    im=getappdata(0,'im');
    filename=getappdata(0,'filename');
    if isempty(im)==0
        if size(im,3)~=1
            im = rgb2gray(im);
        end
        setappdata(0,'im',im);
        axes(handles.axes1);
        hold off;
        imshow(im)
        title(filename)
    end
    setappdata(0,'scatter_IC_1',[]);
    setappdata(0,'scatter_IC_2',[]);
    setappdata(0,'plot_IC_1',[]);
    setappdata(0,'plot_IC_2',[]);
    setappdata(0,'step_find_curve',0)
    setappdata(0,'step_select_ROI',0)
    setappdata(0,'x_curve',[]);
    setappdata(0,'x_curve_area',[]);
    set(handles.edit_nb_direction,'string','');
    set(handles.edit_nb_curve,'string','');
    set(handles.checkbox_line_distance,'Value',0);
    set(handles.checkbox_bright_spots_line,'Value',0);
    set(handles.checkbox_bright_spot_points,'Value',0);
    set(handles.checkbox_segment,'Value',0);
    set(handles.checkbox_curve,'Value',0);
end
```

```
% --- Executes on button press in reload_image.
function reload_image_Callback(~, ~, handles)
% Show the loaded image.

% INPUT :
% - im_init : loaded image
% - filename : string

step_im_load = getappdata(0,'step_im_load');
if step_im_load
    set(handles.uipanel_peptide_detection,'Visible','Off');
    set(handles.uipanel_curve_modification,'Visible','Off');
    set(handles.uipanel_distance_computation,'Visible','Off');
    im_init=getappdata(0,'im_init');
    filename=getappdata(0,'filename');
    if isempty(im_init)==0
        if size(im_init,3)~=1
            im_init = rgb2gray(im_init);
        end
        setappdata(0,'im',im_init);
        axes(handles.axes1);
        hold off;
        imshow(im_init)
        title(filename)
    end
    setappdata(0,'scatter_IC_1',[]);
    setappdata(0,'scatter_IC_2',[]);
    setappdata(0,'plot_IC_1',[]);
    setappdata(0,'plot_IC_2',[]);
    setappdata(0,'step_find_curve',0)
    setappdata(0,'step_select_ROI',0)
    setappdata(0,'x_curve',[]);
    setappdata(0,'x_curve_area',[]);
    set(handles.edit_nb_direction,'string','');
    set(handles.edit_nb_curve,'string','');
    set(handles.checkbox_rotate,'Value',0);
    set(handles.checkbox_line_distance,'Value',0);
    set(handles.checkbox_bright_spots_line,'Value',0);
    set(handles.checkbox_bright_spot_points,'Value',0);
    set(handles.checkbox_segment,'Value',0);
    set(handles.checkbox_curve,'Value',0);
end


% --- Executes on button press in Zoom.
function Zoom_Callback(~, ~, handles)
```

```
% Use the mouse to click and drag the desired rectangle.
% If we drag outside, it is ok

% INPUT :
% - im : tranformed image
% - filename : string
% - step_im_load : boolean

% OUTPUT :
% - im : tranformed image

step_im_load = getappdata(0,'step_im_load');
if step_im_load
    set(handles.uipanel_region_of_interest_selection,'Visible','Off');
    set(handles.uipanel_peptide_detection,'Visible','Off');
    set(handles.uipanel_curve_modification,'Visible','Off');
    set(handles.uipanel_distance_computation,'Visible','Off');
    im =getappdata(0,'im');
    filename=getappdata(0,'filename');

    im = run_zoom(im,filename);

    setappdata(0,'im',im);
    setappdata(0,'scatter_IC_1',[]);
    setappdata(0,'scatter_IC_2',[]);
    setappdata(0,'plot_IC_1',[]);
    setappdata(0,'plot_IC_2',[]);
    setappdata(0,'step_find_curve',0)
    setappdata(0,'step_select_ROI',0)
    setappdata(0,'x_curve',[]);
    setappdata(0,'x_curve_area',[]);
    set(handles.edit_nb_direction,'string','');
    set(handles.edit_nb_curve,'string','');
    set(handles.checkbox_line_distance,'Value',0);
    set(handles.checkbox_bright_spots_line,'Value',0);
    set(handles.checkbox_bright_spot_points,'Value',0);
    set(handles.checkbox_segment,'Value',0);
    set(handles.checkbox_curve,'Value',0);
    set(handles.uipanel_region_of_interest_selection,'Visible','On');
end


% --- Executes on button press in Save_picture.
function Save_picture_Callback(~, ~, handles)
% Save the picture as we see.
```

```
% INPUT :
% - step_im_load : boolean

step_im_load = getappdata(0,'step_im_load');
if step_im_load
%    Open new box
   [filename, pathname] = uiputfile({'*.png','.png Files' });
%   The user write something
   if isequal(filename,0)==0
      F = getframe(handles.axes1);
      Image = frame2im(F);
      imwrite(Image,[pathname filename]);
   end
end


% --- Executes on edit edit_nb_direction
function edit_nb_direction_Callback(hObject, ~, handles)
% The users write a number, it has to be an integer to be save.

% OUTPUT :
% - nb_direction_edit : number of direction from the edit box

nb_direction_edit = str2double(get(hObject,'String'));
if nb_direction_edit<0 || floor(nb_direction_edit) - nb_direction_edit ~= 0 || nb_direction_edit ==
0
   nb_direction_edit = nan;
%   Delete the number in the box
   set(handles.edit_nb_direction,'string','');
end
setappdata(0,'nb_direction_edit',nb_direction_edit);


% --- Executes during object creation, after setting all properties.
function edit_nb_direction_CreateFcn(hObject, ~, ~)
if ispc && isequal(get(hObject,'BackgroundColor'), get(0,'defaultUicontrolBackgroundColor'))
   set(hObject,'BackgroundColor','white');
end


% --- Executes on button press in roi_selection.
function roi_selection_Callback(~, ~, handles)
% The user has to delimited the ROI where he wants to detect peptides by
% giving 2 piecewises curves composed of straight lines. The first initial
% condition is IC_1 and the second is IC_2.
% To pass from the first to the second initial condition, it is
```

```
% automatically detected by comparing the abscissa, if the abscissa is
% shorter than the previous point, so we pass from the first to the second.
% In case of the user click outside, it is automatically fixed by
% putting the new point in the intersection between the picture and the
% straight line created by the new point and the previous one. If the first
% point is outside, the algorithm waits the second point and fixes it by
% the same method
% We estimate the number of curve at the end

% INPUT :
% - scatter_IC_1 : scatter of IC_1
% - scatter_IC_2 : scatter of IC_2
% - plot_IC_1 : plot of IC_1
% - plot_IC_2 : plot of IC_2
% - im : tranformed image
% - nb_direction_edit : number of direction from the edit box

% OUTPUT :
% - IC_1 : first initial condition
% - IC_2 : second initial condition
% - scatter_IC_1 : scatter of IC_1
% - scatter_IC_2 : scatter of IC_2
% - plot_IC_1 : plot of IC_1
% - plot_IC_2 : plot of IC_2
% - nb_direction_edit : number of direction

step_im_load = getappdata(0,'step_im_load');
if step_im_load
    set(handles.uipanel_peptide_detection,'Visible','Off');
    set(handles.uipanel_curve_modification,'Visible','Off');
    set(handles.uipanel_distance_computation,'Visible','Off');
    nb_direction_edit = str2double(get(handles.edit_nb_direction,'String'));
    scatter_IC_1 = getappdata(0,'scatter_IC_1');
    scatter_IC_2 = getappdata(0,'scatter_IC_2');
    plot_IC_1 = getappdata(0,'plot_IC_1');
    plot_IC_2 = getappdata(0,'plot_IC_2');
    im = getappdata(0,'im');
    filename = getappdata(0,'filename');

    [IC_1, IC_2, scatter_IC_1, scatter_IC_2, plot_IC_1, plot_IC_2, nb_direction, plot_IC_edge] =
run_select_ROI(scatter_IC_1, scatter_IC_2, plot_IC_1, plot_IC_2, im,
nb_direction_edit,handles.edit_nb_direction,filename);
    drawnow;
    nb_curve = find_nb_curve(im,IC_1,IC_2);

    setappdata(0,'IC_1',IC_1);
```

```
    setappdata(0,'IC_2',IC_2);
    setappdata(0,'scatter_IC_1',scatter_IC_1);
    setappdata(0,'scatter_IC_2',scatter_IC_2);
    setappdata(0,'plot_IC_1',plot_IC_1);
    setappdata(0,'plot_IC_2',plot_IC_2);
    setappdata(0,'step_select_ROI',1);
    setappdata(0,'nb_direction',nb_direction);
    setappdata(0,'plot_IC_edge',plot_IC_edge);
    set(handles.edit_nb_curve,'string',nb_curve);
    set(handles.checkbox_line_distance,'Value',0);
    set(handles.checkbox_bright_spots_line,'Value',0);
    set(handles.checkbox_bright_spot_points,'Value',0);
    set(handles.checkbox_segment,'Value',0);
    set(handles.checkbox_curve,'Value',0);
    set(handles.uipanel_peptide_detection,'Visible','On');
end


% --- Executes on button press in modify_points.
function modify_points_Callback(~, ~, handles)
% The closest point is replaced by the new one.
% We estimate again the number of curve at the end

% INPUT :
% - IC_1 : first initial condition
% - IC_2 : second initial condition
% - im : tranformed image

% OUTPUT :
% - IC_1 : first initial condition
% - IC_2 : second initial condition
% - scatter_IC_1 : scatter of IC_1
% - scatter_IC_2 : scatter of IC_2
% - plot_IC_1 : plot of IC_1
% - plot_IC_2 : plot of IC_2
% - plot_IC_edge : plot of ROI edge

step_select_ROI=getappdata(0,'step_select_ROI');
if step_select_ROI
    set(handles.uipanel_peptide_detection,'Visible','Off');
    set(handles.uipanel_curve_modification,'Visible','Off');
    set(handles.uipanel_distance_computation,'Visible','Off');
    IC_1=getappdata(0,'IC_1');
    IC_2=getappdata(0,'IC_2');
    im=getappdata(0,'im');
    hold on;
```

```
    imshow(im);
    scatter_IC_1 = scatter(IC_1(:,1),IC_1(:,2),'b','x','Linewidth',2);
    scatter_IC_2 = scatter(IC_2(:,1),IC_2(:,2),'b','x','Linewidth',2);
    plot_IC_1 = zeros(size(IC_1,1)-1,1);
    plot_IC_2 = zeros(size(IC_1,1)-1,1);
    plot_IC_edge = zeros(2);
    for i=1:size(IC_1,1)-1
      plot_IC_1(i) = plot([IC_1(i,1) IC_1(i+1,1)],[IC_1(i,2) IC_1(i+1,2)],'b','Linewidth',2);
      plot_IC_2(i) = plot([IC_2(i,1) IC_2(i+1,1)],[IC_2(i,2) IC_2(i+1,2)],'b','Linewidth',2);
    end
    plot_IC_edge(1) = plot([IC_1(1,1) IC_2(1,1)],[IC_1(1,2) IC_2(1,2)],'blue','LineWidth',2.);
    plot_IC_edge(2) = plot([IC_1(end,1) IC_2(end,1)],[IC_1(end,2)
IC_2(end,2)],'blue','LineWidth',2.);

    [IC_1,IC_2,scatter_IC_1,scatter_IC_2,plot_IC_1,plot_IC_2,plot_IC_edge] =
run_modify_points_ROI(IC_1,IC_2,im,scatter_IC_1,scatter_IC_2,plot_IC_1,plot_IC_2,plot_IC_
edge);
    nb_curve = find_nb_curve(im,IC_1,IC_2);

    setappdata(0,'IC_1',IC_1);
    setappdata(0,'IC_2',IC_2);
    setappdata(0,'scatter_IC_1',scatter_IC_1);
    setappdata(0,'scatter_IC_2',scatter_IC_2);
    setappdata(0,'plot_IC_1',plot_IC_1);
    setappdata(0,'plot_IC_2',plot_IC_2);
    setappdata(0,'plot_IC_edge',plot_IC_edge);
    set(handles.edit_nb_curve,'string',nb_curve);
    set(handles.checkbox_line_distance,'Value',0);
    set(handles.checkbox_bright_spots_line,'Value',0);
    set(handles.checkbox_bright_spot_points,'Value',0);
    set(handles.checkbox_segment,'Value',0);
    set(handles.checkbox_curve,'Value',0);
    set(handles.uipanel_peptide_detection,'Visible','On');
end


% --- Executes on button press in erase_selection.
function erase_selection_Callback(~, ~, handles)
% Delete the direction plots and variables is equivqlent to show the last
% image

% INPUT:
%  - im : transformed image

step_select_ROI=getappdata(0,'step_select_ROI');
if step_select_ROI
```

```
    set(handles.uipanel_peptide_detection,'Visible','Off');
    set(handles.uipanel_curve_modification,'Visible','Off');
    set(handles.uipanel_distance_computation,'Visible','Off');
    im=getappdata(0,'im');
    imshow(im);
    set(handles.edit_nb_direction,'string','');
    set(handles.edit_nb_curve,'string','');
    set(handles.checkbox_line_distance,'Value',0);
    set(handles.checkbox_bright_spots_line,'Value',0);
    set(handles.checkbox_bright_spot_points,'Value',0);
    set(handles.checkbox_segment,'Value',0);
    set(handles.checkbox_curve,'Value',0);
    setappdata(0,'step_select_ROI',0)
end


% --- Executes on button press in Find_curve.
function Find_curve_Callback(~, ~, handles)
% We crop image by area.
% For each image, we compute the scale space of the image.
% For each step we save the position of all local maxima, it give us curve
% We compute the length of curves
% We find the threshold thanks to the Otsu method
% We have our points of all bright spot
% We crop each area in nb_curve part
% We join all points by part and join them in all areas
% We compute the smoothing spline of these points
% We plot these curves

% INPUT :
% - im : tranformed image
% - nb_direction : number of peptide direction
% - IC_1 : first initial condition
% - IC_2 : second initial condition
% - step_im_load : boolean
% - step_select_ROI : boolean
% - nb_curve : number of curve

% OUTPUT :
% - nb_curve : number of curve
% - x_curve_area : abscissa of all whole curves by area
% - y_curve_area : ordinate of all whole curves by area
% - points : coordinate of meaningfull maximum
% - step_find_curve : boolean
% - x_curve : abscissa of all whole curves
% - y_curve : ordinate of all whole curves
```

```
% - smoothing_spline : fit object of all curves
% - plot_spline : plot of the smoothing_spline
% - txt_curve : number of curve

hold on;
im = getappdata(0,'im');
nb_direction = getappdata(0,'nb_direction');
IC_1 = getappdata(0,'IC_1');
IC_2 = getappdata(0,'IC_2');
step_im_load = getappdata(0,'step_im_load');
step_select_ROI = getappdata(0,'step_select_ROI');
nb_curve = str2double(get(handles.edit_nb_curve,'String'));
if step_im_load && step_select_ROI
    set(handles.checkbox_curve,'Value',1);
    set(handles.checkbox_line_distance,'Value',0);
    set(handles.checkbox_bright_spots_line,'Value',0);
    set(handles.checkbox_bright_spot_points,'Value',0);
    set(handles.checkbox_segment,'Value',0);
    hold on;
    imshow(im);
    plot_IC_1 = zeros(size(IC_1,1)-1,1);
    plot_IC_2 = zeros(size(IC_1,1)-1,1);
    plot_IC_edge = zeros(2);
    scatter_IC_1 = scatter(IC_1(:,1),IC_1(:,2),'b','x','Linewidth',2);
    scatter_IC_2 = scatter(IC_2(:,1),IC_2(:,2),'b','x','Linewidth',2);
    for i=1:size(IC_1,1)-1
      plot_IC_1(i) = plot([IC_1(i,1) IC_1(i+1,1)],[IC_1(i,2) IC_1(i+1,2)],'b','Linewidth',2);
      plot_IC_2(i) = plot([IC_2(i,1) IC_2(i+1,1)],[IC_2(i,2) IC_2(i+1,2)],'b','Linewidth',2);
    end
    plot_IC_edge(1) = plot([IC_1(1,1) IC_2(1,1)],[IC_1(1,2) IC_2(1,2)],'blue','LineWidth',2.);
    plot_IC_edge(2) = plot([IC_1(end,1) IC_2(end,1)],[IC_1(end,2)
IC_2(end,2)],'blue','LineWidth',2.);
    setappdata(0,'scatter_IC_1',scatter_IC_1);
    setappdata(0,'scatter_IC_2',scatter_IC_2);
    setappdata(0,'plot_IC_1',plot_IC_1);
    setappdata(0,'plot_IC_2',plot_IC_2);

    [x_curve,
y_curve,smoothing_spline,plot_spline,points,x_curve_area,y_curve_area,nb_curve,txt_curve] =
run_find_curve(im, nb_direction, IC_1, IC_2,nb_curve,handles.edit_nb_curve);

    hold off;
    step_find_curve = 1;
    setappdata(0,'nb_curve',nb_curve)
    setappdata(0,'x_curve_area',x_curve_area)
    setappdata(0,'y_curve_area',y_curve_area)
```

```
    setappdata(0,'points',points)
    setappdata(0,'step_find_curve',step_find_curve)
    setappdata(0,'x_curve',x_curve)
    setappdata(0,'y_curve',y_curve)
    setappdata(0,'smoothing_spline',smoothing_spline)
    setappdata(0,'plot_spline',plot_spline)
    setappdata(0,'txt_curve',txt_curve)
    set(handles.uipanel_curve_modification,'Visible','On');
    set(handles.uipanel_distance_computation,'Visible','On');
end


% --- Executes on edit edit_nb_curve
function edit_nb_curve_Callback(hObject, ~, handles)
% The users write a number, it has to be a positive integer to be save.

% OUTPUT :
% - nb_curve : number of curve from the edit box

nb_curve = str2double(get(hObject,'String'));
if nb_curve<=0 || floor(nb_curve) - nb_curve ~= 0
    nb_curve = nan;
%   Delete the number in the box
    set(handles.edit_nb_curve,'string','');
end
setappdata(0,'nb_curve',nb_curve);


% --- Executes during object creation, after setting all properties.
function edit_nb_curve_CreateFcn(hObject, ~, ~)
if ispc && isequal(get(hObject,'BackgroundColor'), get(0,'defaultUicontrolBackgroundColor'))
    set(hObject,'BackgroundColor','white');
end


% --- Executes on button press in checkbox_bright_spot_points.
function checkbox_bright_spot_points_Callback(hObject, ~, handles)
% Plot or delete all points detected

% INPUT :
% - step_find_curve : boolean
% - nb_direction : number of direction
% - check_points : boolean
% - points : coordinate of meaningfull maximum
% - scatter_Otsu : scatter of meaningfull maximum
```

```
% OUTPUT :
% - scatter_Otsu : scatter of meaningfull maximum
% - check_points : boolean

step_find_curve = getappdata(0,'step_find_curve');
nb_direction = getappdata(0,'nb_direction');
check_points = get(hObject,'Value');
setappdata(0,'check_points',check_points)
scatter_Otsu = cell(nb_direction,1);
% Usable only if we run 'find_curve'
if step_find_curve == 1
   if check_points == 1
      for niter=1:nb_direction
         points = getappdata(0,'points');
         x = points{niter}(:,2);
         y = points{niter}(:,1);
         hold on;
         scatter_Otsu{niter} = scatter(x,y,'x','red','LineWidth',2.);
         setappdata(0,'scatter_Otsu',scatter_Otsu)
         hold off;
      end
   else
      scatter_Otsu = getappdata(0,'scatter_Otsu');
      for i=1:size(scatter_Otsu,1)
         delete(scatter_Otsu{i});
      end
   end
else
   set(handles.checkbox_bright_spot_points,'Value',0);
end


% --- Executes on button press in checkbox_segment.
function checkbox_segment_Callback(hObject, ~, handles)
% Plot or delete segment between all point joined by area.

% INPUT :
% - check_seg : boolean
% - plot_seg  : plot of the segments
% - x_curve : abscissa of all whole curves
% - y_curve : ordinate of all whole curves

% OUTPUT :
% - plot_seg  : plot of the segments
% - check_seg : boolean
```

```
check_seg = get(hObject,'Value');
x_curve = getappdata(0,'x_curve');
y_curve = getappdata(0,'y_curve');

x_curve_area = getappdata(0,'x_curve_area');
y_curve_area = getappdata(0,'y_curve_area');

if isempty(x_curve) == 0
   if check_seg==1
      cpt = 0;
      hold on
      for i_area = 1:size(x_curve_area,2)
         for i_curve=1:size(x_curve_area,1)
            for i_point=1:size(x_curve_area{i_curve,i_area},1)-1
               cpt = cpt + 1;
               plot_seg(cpt) = plot([x_curve_area{i_curve,i_area}(i_point)
x_curve_area{i_curve,i_area}(i_point+1)],[y_curve_area{i_curve,i_area}(i_point)
y_curve_area{i_curve,i_area}(i_point+1)],'b', 'Linewidth',2.);
            end
         end
      end
%       for i_curve=1:size(x_curve,1)
%          for i_point=1:size(x_curve{i_curve},1)-1
%             cpt = cpt + 1;
%            plot_seg(cpt) = plot([x_curve{i_curve}(i_point)
x_curve{i_curve}(i_point+1)],[y_curve{i_curve}(i_point)
y_curve{i_curve}(i_point+1)],'b','Linewidth',2.);
%          end
%       end
      hold off
      setappdata(0,'plot_seg',plot_seg)
   else
      plot_seg = getappdata(0,'plot_seg');
      delete(plot_seg);
   end
else
   set(handles.checkbox_segment,'Value',0);
end
setappdata(0,'check_seg',check_seg);


% --- Executes on button press in checkbox_curve.
function checkbox_curve_Callback(hObject, ~, handles)
% Plot or delete curves
```

```
% INPUT :
% - x_curve : abscissa of all whole curves
% - y_curve : ordinate of all whole curves
% - check_curve : boolean
% - smoothing_spline : fit object of all curves
% - txt_curve : number of curve

% OUTPUT :
% - plot_spline : plot of the smoothing_spline
% - check_curve : boolean


x_curve = getappdata(0,'x_curve');
txt_curve = getappdata(0,'txt_curve');
check_curve = get(hObject,'Value');
hold on
if isempty(x_curve) == 0
   if check_curve == 1
      y_curve = getappdata(0,'y_curve');
      txt_curve = getappdata(0,'txt_curve');
      smoothing_spline = getappdata(0,'smoothing_spline');
      plot_spline = cell(size(x_curve,1),1);
      for i = 1 : size(x_curve,1)
         hold on;
         plot_spline{i} = plot(smoothing_spline{i},x_curve{i},y_curve{i});
         set(plot_spline{i},'LineWidth',2.,'MarkerSize',10);
         legend('off');
         xlabel([]);
         ylabel([]);
         txt_curve{i} = text(x_curve{i}(1)-10,y_curve{i}(1)-10,num2str(i),'color','red');
      end
      setappdata(0,'plot_spline',plot_spline);
      setappdata(0,'txt_curve',txt_curve);
   else
      plot_spline = getappdata(0,'plot_spline');
      for i = 1 : size(plot_spline,1)
         delete(plot_spline{i});
         for i_txt = 1:size(txt_curve,1)
            delete(txt_curve{i_txt})
         end
      end
   end
else
   set(handles.checkbox_curve,'Value',0);
end
setappdata(0,'check_curve',check_curve)
```

```
% --- Executes on button press in checkbox_line_distance.
function checkbox_line_distance_Callback(hObject, ~, handles)
% Plot or delete some segment showing how the distance is computed

% INPUT :
% - nb_direction : number of peptide direction
% - IC_1 : first initial condition
% - IC_2 : second initial condition
% - smoothing_spline : fit object of all curves
% - x_curve : abscissa of all whole curves
% - y_curve : ordinate of all whole curves
% - x_curve_area : abscissa of all whole curves by area
% - y_curve_area : ordinate of all whole curves by area
% - check_line_distance : boolean
% - plot_line_distance : plot of distance line

% OUTPUT :
% - plot_line_distance : plot of distance line

check_line_distance = get(hObject,'Value');

if check_line_distance == 1
   x_curve = getappdata(0,'x_curve');
   if isempty(x_curve) == 0
      nb_direction = getappdata(0,'nb_direction');
      IC_1 = getappdata(0,'IC_1');
      IC_2 = getappdata(0,'IC_2');
      smoothing_spline = getappdata(0,'smoothing_spline');
      x_curve = getappdata(0,'x_curve');
      y_curve = getappdata(0,'y_curve');
      x_curve_area = getappdata(0,'x_curve_area');
      y_curve_area = getappdata(0,'y_curve_area');

      [plot_line_distance] =
run_checkbox_line_distance(nb_direction,IC_1,IC_2,smoothing_spline,x_curve,y_curve,x_curv
e_area,y_curve_area);

      setappdata(0,'plot_line_distance',plot_line_distance);
   else
      set(handles.checkbox_line_distance,'Value',0);
   end
else
   plot_line_distance = getappdata(0,'plot_line_distance');
   delete(plot_line_distance);
```

```
end


% --- Executes on button press in checkbox_bright_spots_line.
function checkbox_bright_spots_line_Callback(hObject, ~, handles)
% Plot or delete the curve passing through the same corresponding bright
% spot of each curve

% INPUT :
% - check_bright_spot_line : boolean
% - x_curve_area : abscissa of all whole curves by area
% - y_curve_area : ordinate of all whole curves by area
% - IC_1 : first initial condition
% - IC_2 : second initial condition
% - nb_direction : number of peptide direction
% - plot_bright_spot_line : plot of all bright spot lines

% OUTPUT :
% - plot_bright_spot_line : plot of all bright spot lines


check_bright_spot_line = get(hObject,'Value');

if check_bright_spot_line == 1
   x_curve_area = getappdata(0,'x_curve_area');
   if isempty(x_curve_area) == 0
      IC_1 = getappdata(0,'IC_1');
      nb_direction = getappdata(0,'nb_direction');
      IC_2 = getappdata(0,'IC_2');
      y_curve_area = getappdata(0,'y_curve_area');

      plot_bright_spot_line =
run_checkbox_bright_spot_line(nb_direction,IC_1,IC_2,x_curve_area,y_curve_area);

      setappdata(0,'plot_bright_spot_line',plot_bright_spot_line);
   else
      set(handles.checkbox_bright_spots_line,'Value',0);
   end
else
   plot_bright_spot_line = getappdata(0,'plot_bright_spot_line');
   for i = 1 : size(plot_bright_spot_line,1)
      for j = 1:size(plot_bright_spot_line{i},1)
         delete(plot_bright_spot_line{i}{j})
      end
   end
end
```

```
% --- Executes on button press in add_point.
function add_point_Callback(~, ~, handles)

% NOT USE AND NOT UPDATED, SEE run_add_delete_points TO THE UPDATED
VERSION

% Add unlimited points, the user clicks to delete a point, to find the area,
% we test if the point is in the area.
% To find the curve, we find the distance between all curve and the straight
% line given by the point and the slope joining the left points of the initial
% condition of the area. The shortest distance gives the nearest curve.
% After we find the local and global position of the point by computing the
% substract in abscissa between each points of the curve and the new point.
% The first which is positive gives the position.
% We adjust all variables and delete the curve's plot and plot the new
% curve.
% To stop to add points, just click outside.

% INPUT :
% - x_curve : abscissa of all whole curves
% - y_curve : ordinate of all whole curves
% - x_curve_area : abscissa of all whole curves by area
% - y_curve_area : ordinate of all whole curves by area
% - smoothing_spline : fit object of all curves
% - IC_1 : first initial condition
% - IC_2 : second initial condition
% - plot_spline : plot of the smoothing_spline
% - im : tranformed image

% OUTPUT
% - x_curve : abscissa of all whole curves
% - y_curve : ordinate of all whole curves
% - x_curve_area : abscissa of all whole curves by area
% - y_curve_area : ordinate of all whole curves by area
% - smoothing_spline : fit object of all curves
% - plot_spline : plot of the smoothing_spline

if get(handles.checkbox_curve,'Value') == 1
    hold on;
    smoothing_spline = getappdata(0,'smoothing_spline');
    x_curve = getappdata(0,'x_curve');
    y_curve = getappdata(0,'y_curve');
    x_curve_area = getappdata(0,'x_curve_area');
    y_curve_area = getappdata(0,'y_curve_area');
```

```
    IC_1 = getappdata(0,'IC_1');
    IC_2 = getappdata(0,'IC_2');
    plot_spline = getappdata(0,'plot_spline');
    im = getappdata(0,'im');
    txt_curve = getappdata(0,'txt_curve');

    [x_curve,y_curve,smoothing_spline,plot_spline,x_curve_area,y_curve_area,txt_curve] =
run_add_point(smoothing_spline,x_curve,y_curve,IC_1,IC_2,plot_spline,im,x_curve_area,y_cur
ve_area,txt_curve);

    setappdata(0,'txt_curve',txt_curve)
    setappdata(0,'x_curve',x_curve)
    setappdata(0,'y_curve',y_curve)
    setappdata(0,'x_curve_area',x_curve_area)
    setappdata(0,'y_curve_area',y_curve_area)
    setappdata(0,'smoothing_spline',smoothing_spline)
    setappdata(0,'plot_spline',plot_spline)
    hold off;
end


% --- Executes on button press in Delete_points.
function Delete_points_Callback(~, ~, handles)

% NOT USE AND NOT UPDATED, SEE run_add_delete_points TO THE UPDATED
VERSION

% Delete unlimited points, the user clicks to delete a point, to find the area,
% we test if the point is in the area.
% To find the curve, we find the distance between all curve and the straight
% line given by the point and the slope joining the left points of the initial
% condition of the area. The shortest distance gives the nearest curve.
% To find the local and global position of the point, it computes the absolute
% value of the offset in abscissa between the new point and all the points
% of the curve. The minimum is the nearest point.
% It deletes it
% We adjust all variables and delete the curve's plot and plot the new
% curve.
% To stop to add points, just click outside.

% INPUT :
% - x_curve : abscissa of all whole curves
% - y_curve : ordinate of all whole curves
% - x_curve_area : abscissa of all whole curves by area
% - y_curve_area : ordinate of all whole curves by area
% - smoothing_spline : fit object of all curves
```

```
% - IC_1 : first initial condition
% - IC_2 : second initial condition
% - plot_spline : plot of the smoothing_spline
% - im : tranformed image

% OUTPUT
% - x_curve : abscissa of all whole curves
% - y_curve : ordinate of all whole curves
% - x_curve_area : abscissa of all whole curves by area
% - y_curve_area : ordinate of all whole curves by area
% - smoothing_spline : fit object of all curves
% - plot_spline : fit object of all curves

if get(handles.checkbox_curve,'Value') == 1
   hold on;
   smoothing_spline = getappdata(0,'smoothing_spline');
   x_curve = getappdata(0,'x_curve');
   y_curve = getappdata(0,'y_curve');
   x_curve_area = getappdata(0,'x_curve_area');
   y_curve_area = getappdata(0,'y_curve_area');
   IC_1 = getappdata(0,'IC_1');
   IC_2 = getappdata(0,'IC_2');
   plot_spline = getappdata(0,'plot_spline');
   im = getappdata(0,'im');
   txt_curve = getappdata(0,'txt_curve');

   [x_curve,y_curve,smoothing_spline,plot_spline,x_curve_area,y_curve_area,txt_curve] =
run_delete_point(smoothing_spline,x_curve,y_curve,IC_1,IC_2,plot_spline,im,x_curve_area,y_c
urve_area,txt_curve);

   setappdata(0,'txt_curve',txt_curve)
   setappdata(0,'x_curve',x_curve)
   setappdata(0,'y_curve',y_curve)
   setappdata(0,'x_curve_area',x_curve_area)
   setappdata(0,'y_curve_area',y_curve_area)
   setappdata(0,'smoothing_spline',smoothing_spline)
   setappdata(0,'plot_spline',plot_spline)
   hold off;
end


% --- Executes on button press in pushbutton21.
function Add_Delete_points_Callback(~, ~, handles)
% Right click to delete a point
% Left click to add a point
% outside click to stop
```

```
% To delete a point, we find the closest point, delete it and adjust
% variable and plot
% To add a point, if the new point is not an extrema, we find the closest
% curve, find the good position to add the point, adjust variable and plot.
% If the new point is an extrema, we compute the slope between the new
% point and the closest extrema of each curve, the slope closest to the
% initial condition in this area corresponds to the curve to add the point.
% If check_bright_spot_line == 1, so we compute the new curve passing
% through the same bright spot and adjust the plot.

% INPUT :
% - smoothing_spline : fit object of all curves
% - x_curve : abscissa of all whole curves
% - y_curve : ordinate of all whole curves
% - x_curve_area : abscissa of all whole curves by area
% - y_curve_area : ordinate of all whole curves by area
% - IC_1 : first initial condition
% - IC_2 : second initial condition
% - plot_spline : plot of the smoothing_spline
% - im : tranformed image
% - txt_curve : number of curve
% - plot_bright_spot_line : plot of all bright spot lines
% - check_bright_spot_line : boolean

% OUTPUT :
% - txt_curve : number of curve
% - x_curve : abscissa of all whole curves
% - y_curve : ordinate of all whole curves
% - x_curve_area : abscissa of all whole curves by area
% - y_curve_area : ordinate of all whole curves by area
% - smoothing_spline : fit object of all curves
% - plot_spline : plot of the smoothing_spline
% - plot_bright_spot_line : plot of all bright spot lines

if get(handles.checkbox_curve,'Value') == 1
    hold on;
    smoothing_spline = getappdata(0,'smoothing_spline');
    x_curve = getappdata(0,'x_curve');
    y_curve = getappdata(0,'y_curve');
    x_curve_area = getappdata(0,'x_curve_area');
    y_curve_area = getappdata(0,'y_curve_area');
    IC_1 = getappdata(0,'IC_1');
    IC_2 = getappdata(0,'IC_2');
    plot_spline = getappdata(0,'plot_spline');
    im = getappdata(0,'im');
    txt_curve = getappdata(0,'txt_curve');
```

```
    plot_bright_spot_line = getappdata(0,'plot_bright_spot_line');
    check_bright_spot_line = get(handles.checkbox_bright_spots_line,'Value');
    set(handles.text_add_delete_point,'Visible','On');


[x_curve,y_curve,smoothing_spline,plot_spline,x_curve_area,y_curve_area,txt_curve,plot_brigh
t_spot_line] =
run_add_delete_points(smoothing_spline,x_curve,y_curve,IC_1,IC_2,plot_spline,im,x_curve_ar
ea,y_curve_area,txt_curve,check_bright_spot_line,plot_bright_spot_line);

    setappdata(0,'txt_curve',txt_curve)
    setappdata(0,'x_curve',x_curve)
    setappdata(0,'y_curve',y_curve)
    setappdata(0,'x_curve_area',x_curve_area)
    setappdata(0,'y_curve_area',y_curve_area)
    setappdata(0,'smoothing_spline',smoothing_spline)
    setappdata(0,'plot_spline',plot_spline)
    setappdata(0,'plot_bright_spot_line',plot_bright_spot_line)
    set(handles.text_add_delete_point,'Visible','Off');
    hold off;
end


% --- Executes on button press in add_curve.
function add_curve_Callback(~, ~, handles)
% After giving the initial conditions or after ploting the curve, the user
% can add one curve by one curve.
% He can add unlimited points to the new curve, to stop he has to click
% outside the picture.
% The first point gives the position of the curve following the other and
% after it is the same as add a point.

% INPUT :
% - x_curve : abscissa of all whole curves
% - y_curve : ordinate of all whole curves
% - x_curve_area : abscissa of all whole curves by area
% - y_curve_area : ordinate of all whole curves by area
% - smoothing_spline : fit object of all curves
% - IC_1 : first initial condition
% - IC_2 : second initial condition
% - plot_spline : plot of the smoothing_spline
% - im : tranformed image
% - txt_curve : number of curve

% OUTPUT :
% - x_curve_add : abscissa of all whole curves
```

```
% - y_curve_add : ordinate of all whole curves
% - x_curve_area_add : abscissa of all whole curves by area
% - y_curve_area_add : ordinate of all whole curves by area
% - smoothing_spline_add : fit object of all curves
% - plot_spline_add : plot of the smoothing_spline
% - txt_curve_add : number of curve

x_curve = getappdata(0,'x_curve');
if (get(handles.checkbox_curve,'Value') == 1 && isempty(x_curve) == 0) ||
(get(handles.checkbox_curve,'Value') == 0 && isempty(x_curve) == 1)
    hold on;
    smoothing_spline = getappdata(0,'smoothing_spline');
    y_curve = getappdata(0,'y_curve');
    x_curve_area = getappdata(0,'x_curve_area');
    y_curve_area = getappdata(0,'y_curve_area');
    IC_1 = getappdata(0,'IC_1');
    IC_2 = getappdata(0,'IC_2');
    plot_spline = getappdata(0,'plot_spline');
    step_select_ROI = getappdata(0,'step_select_ROI');
    txt_curve = getappdata(0,'txt_curve');
    im = getappdata(0,'im');

    if step_select_ROI == 1
        [x_curve,y_curve,smoothing_spline,plot_spline,x_curve_area,y_curve_area,txt_curve] =
run_add_curve(smoothing_spline,x_curve,y_curve,IC_1,IC_2,plot_spline,im,x_curve_area,y_cu
rve_area,txt_curve);
    end
    set(handles.checkbox_curve,'Value',1)
    setappdata(0,'x_curve',x_curve)
    setappdata(0,'y_curve',y_curve)
    setappdata(0,'x_curve_area',x_curve_area)
    setappdata(0,'y_curve_area',y_curve_area)
    setappdata(0,'smoothing_spline',smoothing_spline)
    setappdata(0,'plot_spline',plot_spline)
    setappdata(0,'txt_curve',txt_curve)
end


% --- Executes on button press in delete_curve.
function delete_curve_Callback(~, ~, handles)
% The user can delete one curve by clicking on it.
% It is the same as to delete a point but here it is the whole curve.

% INPUT :
% - x_curve : abscissa of all whole curves
% - y_curve : ordinate of all whole curves
```

```
% - x_curve_area : abscissa of all whole curves by area
% - y_curve_area : ordinate of all whole curves by area
% - smoothing_spline : fit object of all curves
% - IC_1 : first initial condition
% - IC_2 : second initial condition
% - plot_spline : plot of the smoothing_spline
% - im : tranformed image

% OUTPUT
% - x_curve : abscissa of all whole curves
% - y_curve : ordinate of all whole curves
% - x_curve_area : abscissa of all whole curves by area
% - y_curve_area : ordinate of all whole curves by area
% - smoothing_spline : fit object of all curves
% - plot_spline : fit object of all curves

if get(handles.checkbox_curve,'Value') == 1
   hold on;
   smoothing_spline = getappdata(0,'smoothing_spline');
   x_curve = getappdata(0,'x_curve');
   y_curve = getappdata(0,'y_curve');
   IC_1 = getappdata(0,'IC_1');
   IC_2 = getappdata(0,'IC_2');
   plot_spline = getappdata(0,'plot_spline');
   x_curve_area = getappdata(0,'x_curve_area');
   y_curve_area = getappdata(0,'y_curve_area');
   txt_curve = getappdata(0,'txt_curve');
   im = getappdata(0,'im');

   [x_curve,y_curve,smoothing_spline,plot_spline,x_curve_area,y_curve_area,txt_curve] =
run_delete_curve(smoothing_spline,x_curve,y_curve,IC_1,IC_2,plot_spline,im,x_curve_area,y_
curve_area,txt_curve);

   if isempty(x_curve) == 1
      set(handles.checkbox_curve,'Value',0)
      set(handles.uipanel_curve_modification,'Visible','Off');
      set(handles.uipanel_distance_computation,'Visible','Off');
   end
   setappdata(0,'x_curve',x_curve)
   setappdata(0,'y_curve',y_curve)
   setappdata(0,'smoothing_spline',smoothing_spline)
   setappdata(0,'plot_spline',plot_spline)
   setappdata(0,'x_curve_area',x_curve_area)
   setappdata(0,'y_curve_area',y_curve_area)
   setappdata(0,'txt_curve',txt_curve)
end
```

```
% --- Executes on edit ratio.
function ratio_Callback(hObject, ~, handles)
% The ratio is save if it is positive

% OUTPUT :
% - ratio : conversion from pixel to unit

ratio = str2double(get(hObject,'String'));
if ratio>0
   set(handles.redratio,'BackgroundColor',[0.94 0.94 0.94]);
   set(handles.text_ratio,'BackgroundColor',[0.94 0.94 0.94]);
else
   ratio = nan;
   set(handles.ratio,'string','');
end
setappdata(0,'ratio',ratio);


% --- Executes during object creation, after setting all properties.
function ratio_CreateFcn(hObject, ~, ~)
if ispc && isequal(get(hObject,'BackgroundColor'), get(0,'defaultUicontrolBackgroundColor'))
   set(hObject,'BackgroundColor','white');
end


% --- Executes on selection change in unit_menu.
function unit_menu_Callback(hObject, ~, handles)
% Give the unit

% OUTPUT :
% - unit : string

contents = cellstr(get(hObject,'String'));
unit = contents{get(hObject,'Value')};
set(handles.redunit,'BackgroundColor',[0.94 0.94 0.94]);
set(handles.text4,'BackgroundColor',[0.94 0.94 0.94]);
setappdata(0,'unit',unit);


% --- Executes during object creation, after setting all properties.
function unit_menu_CreateFcn(hObject, ~, ~)
if ispc && isequal(get(hObject,'BackgroundColor'), get(0,'defaultUicontrolBackgroundColor'))
   set(hObject,'BackgroundColor','white');
end
```

```
% --- Executes on button press in Plot_distance.
function Plot_distance_Callback(~, ~, handles)
% By area we compute the bright spot line passing through the same bright
% spot. To compute it, we choose a curve, of all its points, we search if
% there is a point in each others curves close to the straight line passing
% through the point and with slope equal to the mean of a14 a23.
% Of all these line, we compute the linear regression and compute the mean
% of the slope.
% For each curve, we discretize it such as for all points, the straight
% line passing from these points intersects the next curve.
% We compute the distance between all point and the intersection.
% PLot the curve and the histogramm

% INPUT :
% - nb_direction : number of peptide direction
% - IC_1 : first initial condition
% - IC_2 : second initial condition
% - x_curve_area : abscissa of all whole curves by area
% - y_curve_area : ordinate of all whole curves by area
% - x_curve : abscissa of all whole curves
% - y_curve : ordinate of all whole curves
% - smoothing_spline : fit object of all curves
% - ratio : conversion from pixel to unit
% - unit : string

nb_direction = getappdata(0,'nb_direction');
IC_1 = getappdata(0,'IC_1');
IC_2 = getappdata(0,'IC_2');
x_curve_area = getappdata(0,'x_curve_area');
y_curve_area = getappdata(0,'y_curve_area');
x_curve = getappdata(0,'x_curve');
y_curve = getappdata(0,'y_curve');
smoothing_spline = getappdata(0,'smoothing_spline');
ratio = getappdata(0,'ratio');
unit = getappdata(0,'unit');

if isempty(ratio) || isnan(ratio)
    set(handles.redratio,'BackgroundColor','red');
    set(handles.text4,'BackgroundColor','red');
    set(handles.text_ratio,'BackgroundColor','red');
end

if strcmp(unit,'') == 1
    set(handles.redunit,'BackgroundColor','red');
```

```
end

if isempty(x_curve) == 0 && isempty(ratio) == 0 && isnan(ratio) == 0 && strcmp(unit,'') == 0

run_distance(nb_direction,IC_1,IC_2,x_curve_area,y_curve_area,smoothing_spline,x_curve,y_c
urve,ratio,unit);
end


% --- Executes on button press in save_distance.
function save_distance_Callback(~, ~, handles)
% We create a new folder, save all distance in a .txt file
% Save the picture as we seen
% Plot and take a screenshot of the distance's plot

% INPUT :
% - nb_direction : number of peptide direction
% - x_curve_area : abscissa of all whole curves by area
% - y_curve_area : ordinate of all whole curves by area
% - smoothing_spline : fit object of all curves
% - ratio : conversion from pixel to unit
% - unit : string
% - pathname : string
% - filename : string

ratio = getappdata(0,'ratio');
pathname = getappdata(0,'pathname');
filename = getappdata(0,'filename');
unit = getappdata(0,'unit');
smoothing_spline = getappdata(0,'smoothing_spline');
nb_direction = getappdata(0,'nb_direction');
x_curve_area = getappdata(0,'x_curve_area');
y_curve_area = getappdata(0,'y_curve_area');

if isempty(ratio) || isnan(ratio)
   set(handles.redratio,'BackgroundColor','red');
   set(handles.text4,'BackgroundColor','red');
   set(handles.text_ratio,'BackgroundColor','red');
end

if strcmp(unit,'') == 1
   set(handles.redunit,'BackgroundColor','red');
end

if isempty(smoothing_spline) == 0 && isempty(ratio)==0 && isnan(ratio) == 0 &&
strcmp(unit,'') == 0
```

```
    run_save_distance(ratio, pathname, filename, unit, smoothing_spline, nb_direction,
x_curve_area, y_curve_area)
end



% PREPROCESSING
% --- Executes on button press in fft_high.
function fft_high_Callback(~, ~, ~)
im = getappdata(0,'im_init');
im_bandpass = Bandpass_Butterworth_Filter(im, 0, 90);
imshow(im_bandpass);
setappdata(0,'im_bandpass',im_bandpass)


% --- Executes on button press in Correlation_averaging.
function Correlation_averaging_Callback(~, ~, ~)
% im_bandpass = getappdata(0,'im_bandpass_rotate');
im_bandpass = getappdata(0,'im');
im_average_adjust = Correlation_averaging(im_bandpass);
imshow(im_average_adjust,[0 255])
setappdata(0,'im',im_average_adjust)


% --- Executes on slider movement.
function rotate_slider_Callback(hObject, ~, ~)
theta = get(hObject,'Value');
% im_bandpass = getappdata(0,'im_bandpass');
% im_bandpass_rotate = imrotate(im_bandpass,-theta);
% imshow(im_bandpass_rotate)
% setappdata(0,'im_bandpass_rotate',im_bandpass_rotate);
im_init = getappdata(0,'im_init');
im = imrotate(im_init,-theta);
imshow(im)
setappdata(0,'im',im);


% --- Executes during object creation, after setting all properties.
function rotate_slider_CreateFcn(hObject, ~, ~)
if isequal(get(hObject,'BackgroundColor'), get(0,'defaultUicontrolBackgroundColor'))
    set(hObject,'BackgroundColor',[.9 .9 .9]);
end


% --- Executes on button press in Show_image_init.
```

```
function Show_image_init_Callback(~, ~, ~)
im = getappdata(0,'im_init');
imshow(im)
```